Turbine loading and wake model uncertainty

Emmanuel Ardillon, M. Bakhoday Paskyabi, Alexis Cousin, N. Dimitrov, Marine Dupoiron, S. Eldevik, Elias Fekhari, Carla Ferreira, Martin Guiton, Baptiste Jezequel, et al.

HIghly advanced Probabilistic design and Enhanced Reliability methods for high-value, cost-efficient offshore WIND

Title: Turbine loading and wake model uncertainty
Deliverable no: D3.2

Delivery date: 16.12.2022
Lead beneficiary: IFPEN
Dissemination level: Public

This project has received funding from the European Union's Horizon 2020 Research and Innovation Programme under Grant Agreement No. 101006689

Author(s) information (alphabetical):		
Name	**Organisation**	**Email**
E. Ardillon	EDF	emmanuel.ardillon@edf.fr
M. Bakhoday Paskyabi	UiB	mostafa.bakhoday-paskyabi@uib.no
A. Cousin	IFPEN	alexis.cousin@ifpen.fr
N. Dimitrov	DTU	nkdi@dtu.dk
M. Dupoiron.	IFPEN	marine.dupoiron@ifpen.fr
S. Eldevik	DNV	
E. Fekhari	EDF	elias.fekhari@edf.fr
C .Ferreira	DNV	carla.ferreira@dnv.com
M. Guiton	IFPEN	martin.guiton@ifpen.fr
B. Jézéquel	EDF	baptiste.jezequel@edf.fr
P-A. Joulin	IFPEN	pierre-antoine.joulin@ifpen.fr
A. Lovera	EDF	anais.lovera@edf.fr
L. Mayol	IFPEN	
M. M. Penchah	UiB	mohammadreza.penchah@uib.no

Acknowledgements/Contributions:		
Name	**Name**	**Name**

Document information:					
Version	**Date**	**Description**	**Prepared by**	**Reviewed by**	**Approved by**
0	16.12.2022	First official version	Authors listed above	F. Blondel, M. Kelly	Nikolay Dimitrov
1	21.03.2023	Final version	Authors listed above	F. Blondel, M. Kelly	Nikolay Dimitrov
2	27.10.2023	Corrected version	Authors listed above	F. Blondel, M. Kelly	Nikolay Dimitrov

Definitions:

Contents

List of Abbreviations

WT	Wind Turbine
FOWT	Floating Offshore Wind Turbine
BEM	Blade Element Momentum
ASHE	Aero-Servo-Hydro-Elastic
DLW	DeepLines Wind™
DoE	Design of Experiments
DEL	Damage Equivalent Load
AEP	Annual Energy Production
CPU	Central Processing Unit
NTM	Normal Turbulence Model
GP	Gaussian Process
FVW	Free Vortex Wake
GPU	Graphics Processing Unit
CUDA	Compute Unified Device Architecture
LHS	Latin Hypercube Sampling
WP	Work Package
SCADA	Supervisory Control And Data Acquisition
CV	Cross-Validation
RMSE	Root-mean-squared error
CI	Confidence Interval
DWM	Dynamic Wake Meandering
TI	Turbulence Intensity
RBD	Reliability-Based Design
CFD	Computational Fluid Dynamics
RANS	Reynolds-Averaged Navier Stokes
LES	Large-Eddy Simulation
MSL	Mean Sea Level
MMD	Maximum Mean Discrepancy
std	standard deviation
CFL	Courant–Friedrichs–Lewy

1. Executive Summary

The present report addresses HIPERWIND Deliverable 3.2: “Turbine loading and wake model uncertainty”. The following work provides new results to estimate the uncertainty of analytical wake models. Also known as “engineering wake models”, such tools are widely used to predict the production of a wind farm at a given site during the pre-design stage. Their main advantage is a low computational cost, obtained through simplified formulations to describe the behaviour of wakes. Nevertheless, the assumptions considered may lead to limitations. Consequently, such models will be compared in section 2 to medium-fidelity models with Dynamic Wake Meandering (DWM) and high-fidelity models involving Large Eddy Scale (LES) with actuator methods. Wake conditions are not only important for electricity production but also for the load on the turbines, specifically for fatigue loads on blades and towers. The fatigue life of such components may be strongly influenced by the added turbulence, and spatial deviation induced e.g., by yaw misalignment of upwind turbines or meandering. The results of this report are however only limited to the wind conditions seen at different locations within a wind farm which will define the input aerodynamic loading for future reliability-based designs of offshore wind turbines (WT).

These results are documented for the two offshore case studies of HIPERWIND: the 2.3 MW WT on a monopile within the Teesside (United Kingdom) wind farm, and the IEA15MW WT on the UMaine semi-submersible floater in the South Brittany site (France). The latest is a modified version of the original design which was proposed by NREL and UMaine [1] [2][3] [4].

For the floating case, a new wake tool has been developed which takes into account the static position of the floater due to constant mean wind forces on the WT. Section 3 presents the main difference in wake predictions (mean wind speed and turbulence) when compared to a fixed case. It is shown that the influence is small and mainly due to the inclination of the floater. Annual Electricity Production (AEP) is computed for both fixed and floating cases. The conclusion is that the main difference is coming from the rotor tilt of a free WT and that the wake modification is negligible.

The uncertainty of engineering methodology for wake modelling is investigated in section 4. Firstly, a qualitative comparison to high-fidelity LES simulations is conducted for selected representative configurations of the ambient wind conditions. Differences in wake behaviours are noticed, depending on the atmospheric stability and the static inclined position of the floater. If the engineering approach provides fairly good results in neutral conditions, more discrepancies are observed in stable ones (underestimation of speed deficit). Concerning the inclined position of the floater, the vertical wake deflection seems well predicted, but a wider and stronger wake is observed in LES simulations downstream of the first wind turbine. The turbulence intensity shows also good predictions. A slight and overall overestimation underlines the need for further investigations to improve such models. Secondly, a quantitative estimation of uncertainty has been computed with a Kriging approach, considering Dynamic Wake Meandering models as a reference. Once more, the overall differences for wake deficit remain small, while higher discrepancies are evaluated for turbulence intensities. Furthermore, an important uncertainty is identified when the wind turbine is directly downstream of several others, highlighting the need for improved superposition models.

Finally, section 5 is devoted to the uncertainty propagation, from ambient wind conditions to parameters defining the local wind conditions which should be used in a Reliability-Based Design (RBD) of the offshore WT composing a farm. A metric based on Maximum Mean Discrepancy (MMD) is defined to quantify the difference between ambient mean wind speed plus turbulence intensity and the corresponding

quantities modified by the wake. The latter quantities are integrated over the rotor, at each WT of the farm. RBD may require huge computational costs which may be intractable in an industrial context. Such costs are due to the cost of a single multiphysics simulation plus the high number of simulations required to sample the low target failure probability in standard (e.g., 1e-4 for the normal safety class in [5]). To alleviate this problem, a clustering strategy is proposed to group the WT into a reduced number of sets, according to the similarity in the local wind uncertainty metric. A demonstration is given for the Teesside case study with only 5 clusters so that only 5 WT of the farms provide an RBD analysis for the whole set of WT.

References of the Executive Summary

[1] Allen, C., Viscelli, A., Dagher, H., Goupee, A., Gaertner, E., Abbas, N., Hall, M. Barter, G. (2020). "Definition of the UMaine VolturnUS-S reference platform developed for the IEA Wind 15-megawatt offshore reference wind turbine". Tech. Rep. NREL/TP-5000-76773). National Renewable Energy Lab., Golden, CO (USA).

[2] Evan Gaertner, Rinker, J., Sethuraman, L., Zahle, F., Anderson, B., Barter, G., Abbas, N., Meng, F., Bortolloti, P., Skrzypinski, W., Scott, G., Feil, R., Bredmose, H., Dykes, K., Sheilds, M., Allen, C., Viselli, A. (2020). "Definition of the IEA wind 15-megawatt offshore reference wind turbine". Tech. Rep. NREL/TP-5000-75698 National Renewable Energy Lab., Golden, CO (USA).

[3] Capaldo, M., Guiton, M., Huwart, G., Julan, E., Dimitrov, N.K., Kim, T., Lovera, A., Peyrard, C. (2021). "Design brief of HIPERWIND offshore wind turbine cases: bottom fixed 10MW and floating 15MW". Tech. Rep. of HIPERWIND H2020 project (agreement No. 101006689), https://hal-ifp.archives-ouvertes.fr/hal-04033059.

[4] Peyrard, C., Robaux, F., Borras-Nadal, A., Joulin, P.-A., Mayol, L., Eldevik, S., Guiton, M., Cousin, A, Benoit, M., Dimitrov, N.K., Lovera, A., Fereira, C. (2022). Aero-servo-hydroelastic model uncertainty. D3.3. Rep. of HIPERWIND H2020 project (agreement No. 101006689), https://hal-ifp.archives-ouvertes.fr/hal-04033056.

[5] DNV (2013). "Design of Floating Wind Turbine Structures". DNV-OS-J103 standard.

2. Introduction

The feasibility of future Offshore WT farm installations firstly depends on the economic evaluation of the Levelized Cost of Energy (LCOE) by operators when applying to national tenders for a given site. Among the influencing parameters driving the LCOE for Offshore WT, the discount rate is dominating even the turbine or foundation costs (see e.g., the sensitivity analysis of [6] for Floating Offshore WT (FOWT)). This ranking demonstrates the economic role of uncertainty, primarily for the financial investors, and the importance to reduce its impact which is the main objective of the HIPERWIND project.

In the pre-installation evaluation stage, the prospective wind farm operators generally have access to a wind resource assessment. This requires statistical prediction(s) based on multi-year measurements, long-term correction using the nearest applicable time series with a length at least as long as the expected turbine lifetime, and possibly complemented by spatially interpolated/downscaled time series from reanalysis or mesoscale simulation [7]. They must also take into account the expected power specifications plus site constraints like an allowable space for the layout, and finally a model of WT. The latter is often upscaled from existing ones due to the continual upscaling of Offshore WT during the last decade, which is expected to continue until 2030 [8]. From these data, the estimate of the future plant performance firstly depends on the Annual Energy Production (AEP) which requires efficient numerical tools enabling the optimization of turbine siting (layout). It is worth mentioning that only a few per cent of misprediction on the mean (expected) AEP can have an impact of several million euros on the net value [7] and that there often is still significant overprediction of wind plant performance [9].

This need for the planning phase of an offshore wind farm has motivated the development of numerous wake analysis approaches since the pioneering work of [10], to predict both the wind deficit and the added turbulence downstream of WTs, propagating into the farm. The general mathematical framework for this problem is the Navier Stokes (NS) equations for a turbulent flow, modified by the aerodynamic interaction of the WTs. Without giving an exhaustive list of these models, we can distinguish different groups according to their fidelity, which indicates their level of simplification of the flow physics to save computational costs. The reader can find more details and references on several of these models in the comparative benchmark of [11].

Following the classification of [12], we first distinguish low-fidelity analytical models which compute the steady-state wake. Thanks to their low computational cost, these models enable the industry to use them to seek a layout of a wind farm optimizing the productions under site constraints. For this reason, they are also often referred to as “engineering” models. These models assume different spatial distributions of wake deficit, according to the downstream distance to the rotor and distance in the transverse direction. Given these assumptions, their formulation derives generally from mass and momentum conservation. The models were initially designed to predict far-wake conditions, typically at distances downstream larger than 5 times the rotor diameter D. However, with increasing constraints on the layout and upscaling tendencies, the inter-turbine distance may be smaller, especially for specific wind directions. Thus, it motivates the need to enrich the model in the near-wake zone. For the latter, the rotor influence is greater, mainly due to the generation of the blade tip vortex. When going downstream these tip vortices break down while the transition to far wake is driven by turbulent mixing with the ambient flow [13] of the Atmospheric Boundary Layer (ABL), see Figure 1. The result is a wind deficit profile in the cross-stream direction varying from top-hat in the near wake to Gaussian in the far wake [14]. An important parameter to evaluate the deficit is the thrust coefficient, normalizing the thrust force of the rotor by the total amount of the wind force:

$$C_T = \frac{8T}{\pi \rho D^2 \bar{u}^2};$$

Eq 1

here ρ denotes the air density, T denotes the aerodynamic thrust (force) on the rotor, and $\bar{u}$ denotes the time-averaged wind speed at hub height. It is to be noticed that these analytical models are empirical and thus other parameters are needed and require a fitting against experimental or in situ measurement [14]. These fittings are assumed to be valid for arbitrary ambient wind conditions given by $\bar{u}$ and its standard deviation σ_u or its normalized measure of Turbulence Intensity (TI) $\frac{\sigma_u}{\bar{u}}$, see e.g.,.

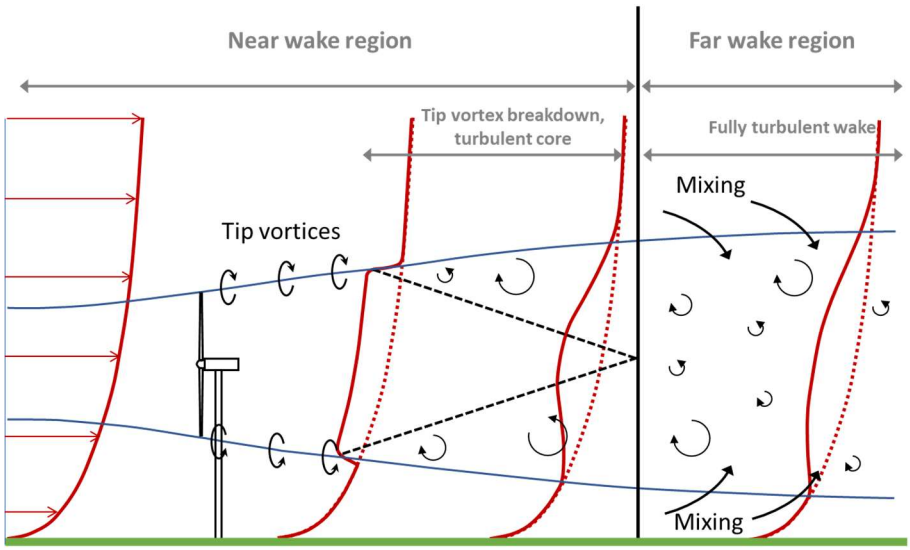

Figure 1: Illustration of the vertical profiles of wind speed (in red) and added turbulence (in black) downwind of a WT, from [15], adapted from [16].

More recently, a second category of medium-fidelity models is composed of Dynamic Wake Meandering (DWM) approaches initially proposed by [17]. They consider an unsteady low-frequency motion of the wake governed by large-scale turbulence structures. It allows enriching wind-box (3D turbulent flow-field) generation necessary for design tools, to simulate a WT within the wake of an upstream one, and study the load variations- specifically for fatigue life constraints [18][19]. Such models are based on a simplified Computational Fluid Dynamics (CFD) solution of NS with an axisymmetric solution in a thin layer inspired by [20], with various eddy viscosity formulations for turbulence closure of equations. A basic assumption of the DWM model is a separation of the scales between the large-scale eddies responsible for the low-frequency meandering (both horizontally and vertically) in the ABL, and the small-scale eddies which produce the wake turbulence that is passively transported in the moving frame of the meandering. Hence, the wake deficit predicted by the DWM model has three components [19]: 1) a steady wake deficit dependent on the operational state of the upwind turbine (the blade pitch and rotor speed leading to a C_T value) and the downwind distance from the source, 2) a wake deficit meandering path obtained from low-pass filtering of the lateral and vertical turbulence components, 3) small-scale wake-added turbulence. In a typical load simulation, the three DWM components are superimposed on a wind box representing ambient turbulence conditions. The initial model was enriched in [21] to represent the atmospheric stability (i.e., mean thermal stratification of the ABL) effect on the turbulence length scale which influences both the wind speed deficit and the meandering. Despite their physical basis, DWM models remain partly empirical, with a few coefficients to calibrate. The turbine aerodynamic interaction with the flow can be either given

only by C_T or evaluated via Blade Element Momentum (BEM) theory, which is commonly found in Aero-Servo-Hydro-Elastic solvers (ASHE) like DTU's HAWC2 (https://www.hawc2.dk/) or NREL's OpenFAST (https://www.nrel.gov/wind/nwtc/openfast.html). Some known limitations of the current DWM model implementations include the approach to combining multiple wakes, which is done by mathematical superposition rules matching empirical evidence [22] rather than concrete physics considerations [23]. Despite its partially empirical formulation the DTU implementation of DWM is considered here as a higher fidelity reference model than the analytical steady-state engineering models since it represents also the transient flow including low-frequency meandering. DWM is also increasingly considered for the design of Offshore WT (see Annex E of [24]). In the domain of dynamic wind farm simulation, recent tools like FAST.Farm and Hawc2Farm are both using DWM for the simulation of wake deficit propagation.

The last category is composed of wake analysis numerical models which are based on CFD and considered high-fidelity models. The fluid dynamics are numerically computed from NS equations, using methods such as the Reynolds Averages Navier Stokes (RANS) approach or the Large Eddy Simulation (LES) approach. These methods are numerically expensive, especially when an entire wind farm is simulated. To alleviate this problem, the flow around the blade is not explicitly solved: body forces approaches are commonly used to implicitly reproduce the aerodynamic interactions. Among these models, one can cite the Actuator Disk without rotation [25], the Actuator Disk with rotation [26], and the Actuator Line [27]. Contrarily to the previous categories, the representativeness of the physic is advanced. Some existing solvers also include ABL phenomena to improve the wind flow modelling, such as the buoyancy effect (due to thermal stratification), the topography effect (due to roughness and orography), or the Coriolis effect; e.g., PALM [28] and Meso-NH [29]. If fewer empirical coefficients or laws are used in these meteorological models, they require an expensive procedure (using precursor simulation) to simulate a specific wind condition (U and TI) combined with a specific thermal stratification.

The validation of the models against real *in situ* measurement remains a challenge which is the topic of ongoing research projects, like the IEA WakeBench project of IEA Wind Task 31. The difficulty comes mainly from the lack of available data, and they are rarely as well equipped as the SWiFT facility in Texas providing Lidar measurements [11]. The latter reference presents a benchmark comparing such measurement, hence for a single WT, and several simulators of the three fidelity categories hereabove introduced for neutral, stable, and unstable atmospheric stability. The results underline an important dispersion of model predictions, particularly in the near-wake (at 2D downwind distance), in terms of wind speed deficit and wake profiles. Interestingly, the error ranking in [11] seems to follow the fidelity of the models, suggesting that LES models may be used as acceptable references to compute the error of low-fidelity models. At the scale of wind farms, a benchmark comparing low-fidelity engineering models against the power production of 5 farms concludes with a small uncertainty, less than 1% when considering the total production of the farm normalized by the optimal one corresponding to the ambient wind [30]. However, the error can rise locally to more than 30% for some WT. Without giving an exhaustive list of published benchmarks, the mentioned references illustrate that wake model uncertainty certainly contributes to the current uncertainty estimate in both AEP and turbine loading predictions which penalizes the targeted massive deployment of offshore wind plants.

The efficiency of low-fidelity models is well established in the industry for predicting the mean wind speed deficit driving the main part of the AEP estimate. However, these models miss important phenomena of the ABL interaction with wake in wind farms. Among these effects, the thermal stability of the ABL is known to play a significant role [31]. The stability can vary from very unstable to very stable during the day, as it depends on the diurnal cycle. For onshore conditions, unstable conditions can be observed near the surface during the day, when the sun heats the surface and become warmer than the air, generating

convective motions, as shown in Figure 2. Stable conditions are more common during the night when the radiative cooldown of the ground leads to a surface cooler than the air. Such conditions have a strong influence on the turbulence length scale and kinetic energy, leading to enhanced wind shear, weaker turbulence intensities, and thus different wake behaviours. One of the major impacts on the wake is the recovery rate: the recovery is much faster in a convective boundary layer compared to a neutral ABL or a stable boundary layer [31]. Several parameters can be used to characterize the stability of the ABL (such as the Richardson number or reciprocal of Obukhov length). They are ratios of thermal turbulence production (due to buoyancy) to mechanical turbulence production (due to shear). A neutral atmosphere neither enhances nor inhibits mechanical turbulence and is usually considered in analytical wake models due to its relative simplicity. An unstable atmosphere enhances turbulence, whereas a stable atmosphere damps mechanical turbulence as buoyancy tends to suppress it.

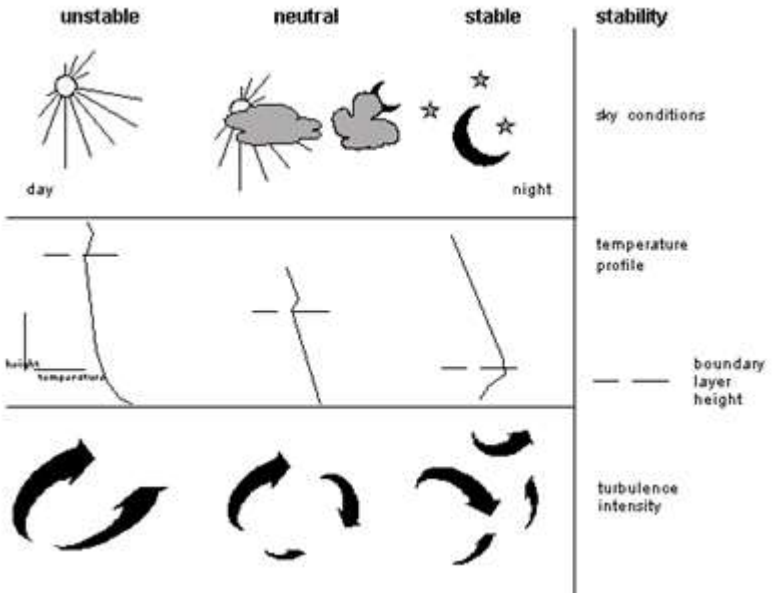

Figure 2: The atmospheric stability categories; neutral, stable, and unstable based on cloudiness and wind speed [32] extracted from [33].

A second important phenomenon may be noted for the specific case of FOWT: the motion of the rotor due to the floating motion might change the downstream wake characteristics. Studies of this problem with high-fidelity CFD solvers have gained increasing interest in recent years, e.g. [34] with RANS, and [35][36] with LES turbulence. However, these papers are either limited to the near-wake region with the interaction of the FOWT and its wake [32][34] or are limited to one or two WT [35] [36]. Also, in [37] the interaction between the NREL 5MW and its wake for different floater concepts is simulated with Free Vortex Wake model (inviscid lifting line theory). The case of multiple rows of WT which may be more representative of conditions in a wind farm remains to be investigated, to the author's knowledge. Simulations with multiple rows of WT have been published about tilt control applications, studying the vertical deflection of wake [38]. Note however that in tilt control, the optimal production focus is on positive tilt (rotor tilt top forward into the wind steers) which produces a downward wake [39], while the steady pitch of the floater under wind force on FOWT turbine will generate an upward deflection of the wake, as explained hereafter.

Floater motion influence on wake depends on the FOWT technology, with varying floater motion under wind and wave solicitation. Also, the FOWT controller will be specifically tuned to optimize the production

and to damp the thrust on the rotor which follows the floater (hence inclined with floater pitch). However, a common result of multiple works using high-fidelity simulations is that the influence on wake velocity deficit is mainly driven by the time-averaged floater position, particularly the pitch that deflects upward the wake (e.g. Figure 3 from [36] and [40]). If the impact on production is not clarified, the previous reference mentions about 10% change in the fatigue design of blades and tower of FOWT.

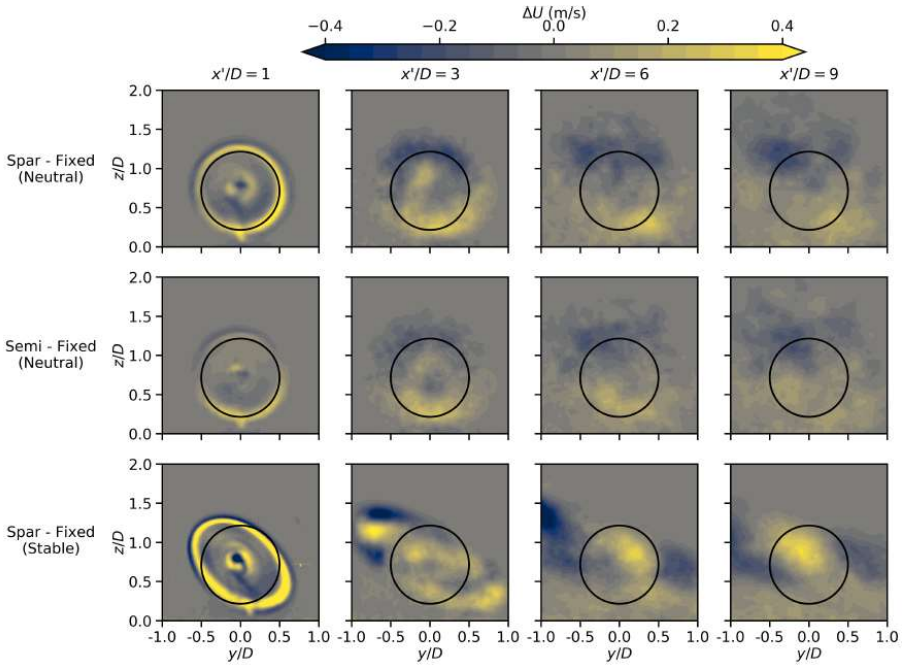

Figure 3: Differences in time-averaged wake velocity between fixed and floating simulations at downstream locations of 1D; 3D; 6D and 9D. The downstream locations are measured from the mean rotor displacement. The initial rotor location is outlined for reference. From [36].

One novelty of the HIPERWIND workflow is in the propagation of uncertainty through all the steps of the wind farm, and WT modelling. Indeed, previous results of WP2 have documented joint probabilistic distributions for wind and wave parameters of two case study sites [41][42]. In this report which collects WP3 activity, the focus is on the uncertainty propagation with wind modification due to wake for specific WT inside a farm. To get a realistic probabilistic distribution of wind parameters, it is also required to account for the wake model uncertainty, which depends on ABL characteristics. HIPERWIND also goes beyond the state of the art for the wake model uncertainty estimate by comparing different fidelity models and considering two wind farms, one real with fixed foundations and one generic with a floating wind turbine. The objective is then to provide stochastic input information to ASHE simulations which will compute, in the next step of the project with WP4, Reliability-Based Design (RBD). One may argue that a more efficient transfer of information would be obtained with a direct chain of model coupling wake analysis results to ASHE solvers like that provided by the coupling of DWM with HAWC2 [43]. Note however that such coupling always implies or demands turbulence box generation. Alternately, the choice we follow here, computing the uncertainty on the local wind parameters only, has the advantage to give more control over the model uncertainty. Besides, it lets the possibility that different people or companies work on wake analysis and WT design, as is often the case in industrial projects.

The structure of the report is as follows. In section 3, a new coupling is introduced for FOWT, between the wind farm wake analysis software of IFPEN (FarmShadow^{TM}) and a hydrostatic solver. The influence of the floater position due to constant mean wind on wake and AEP is documented. In section 4, an estimate of the engineering wake model is presented based on the comparison of FarmShadow^{TM} with LES simulations of Meso-NH and PALM, both including actuator methods for the interaction of WT. This comparison considers the effect of atmospheric stability on the difference between low and high-fidelity wake predictions. Given the huge computational cost of LES, this comparison is made on a few selected representative cases for the two case studies of HIPERWIND: Teesside (monopile 2.3 MW WT in an EDF farm in the UK) and South Brittany (generic farm of 5 x 5 WT composed of a modified version of IEA 15MW WT on UMaine semi-submersible floater). To provide an exhaustive estimate of the uncertainty in the space of wind parameters (U, TI and wind orientation), a more systematic comparison is also made between FarmShadow^{TM} and DWM of DTU in the framework of the Gaussian Process of DNV. Section 5 presents the uncertainty propagation towards U and TI averaged over a WT rotor surface that is performed with OpenTurns platform of EDF R&D, with and without the wake model uncertainty, and for both case studies. This section also suggests a clustering method to reduce the number of representative cases for future RBD expensive simulations.

Last, section 6 concludes with a summary of key results presented in this report and suggests possible perspectives for future research projects and exploitation in the industry.

References of the Introduction

[6] Lerch, M. (2019). “D2.8: Expected LCOE for floating wind turbines 10MW+ for 50m+ water depth”. Report of LifeS50+ H2020 project, Agreement H2020-LCE-2014-1-640741.

[7] Sanz Rodrigo, J., Chávez Arroyo, R. A., Moriarty, P., Churchfield, M., Kosović, B., Réthoré, P.E., Hansen, K.S., Hahmann, A., Mirocha, J.D., Rife, D., (2017). “Mesoscale to microscale wind farm flow modeling and evaluation”. WIREs Energy Environ 2017, 6:e214. doi: 10.1002/wene.214.

[8] Jahani, K., Langlois, R.G., Afagh, F.F. (2022). “Structural dynamics of offshore Wind Turbines: A review”. Ocean Engineering, 251, 111136, https://doi.org/10.1016/j.oceaneng.2022.111136.

[9] Damiani, R. (2018). “Uncertainty and Risk Assessment in the Design Process for Wind”. Tech. Rep. NREL/TP-5000-67499. National Renewable Energy Lab., Golden, CO (United States).

[10] Jensen, N. (1983). “A Note on Wind Generator Interaction”, RISOE-M-2411, Risø National Laboratory, https://books.google.fr/books?id=5w3tvgEACAAJ.

[11] Doubrawa, P., Quon, E., Martinez-Tossas, L.A. et al (2020). “Multimodel validation of single wakes in neutral and stratified atmospheric conditions”. Wind Energy, 23(11):2027–2055.https://doi.org/10.1002/we.2543.

[12] van den Bos, L. Sanderse, B. (2017). “Uncertainty quantification for wind energy applications. Report SC-1701”. Centrum Wiskunde & Informatica.

[13] van der Laan, M. P., Baungaard, M., and Kelly, M. (2022). “Brief communication: A clarification of wake recovery mechanisms”. Wind Energ. Sci. Discuss. [preprint], https://doi.org/10.5194/wes-2022-56, in review.

[14] Blondel, F., Cathelain, M. (2020). “An alternative form of the super-Gaussian wind turbine wake model”. Wind Energ. Sci., 5, 1225–1236, https://doi.org/10.5194/wes-5-1225-2020.

[15] Blondel, F., (2022). “Modélisation des sillages éoliens : de la simulation haute-fidélité à l’application industrielle”. Conference Journées Scientifiques de l’Eolien, Paris.

[16] Uchida, T. (2020). “Effects of Inflow Shear on Wake Characteristics of Wind-Turbines over Flat Terrain”. Energies, 13(14), 3745.

[17] Larsen G.C., Madsen H.A., Thomsen K., Larsen T.J. (2008). “Wake meandering—a pragmatic approach”. Wind Energy, 11:377–395.
[18] Jonkman, J., Annoni, J., Hayman, G., Jonkman, B., Purkayastha, A. (2017). “Development of FAST.Farm: A New Multiphysics Engineering Tool for Wind Farm Design and Analysis”. NREL Conference paper CP-5000-67528.
[19] Reinwardt, I., Schilling, L., Steudel, D., Dimitrov, N., Dalhoff, P., Breuer, M. (2021). “Validation of the dynamic wake meandering model with respect to loads and power production”. Wind Energy Science, 6(2), 441-460. https://doi.org/10.5194/wes-6-441-2021
[20] Ainslie JF. (1988). “Calculating the flow field in the wake of wind turbines”. Journal of Wind Engineering and Industrial Aerodynamics; 27: 213–224.
[21] Keck, R.E., de Maré, M., Churchfield, M.J., Lee, S., Larsen, G., Madsen, H.A., (2014). “On atmospheric stability in the dynamic wake. meandering model”. Wind Energy, 17:1689–1710.
[22] Larsen, T. J., Larsen, G. C., Aagaard Madsen , H., Petersen, S. M. (2015). ”Wake effects above rated wind speed. An overlooked contributor to high loads in wind farms”. In Scientific Proceedings. EWEA Annual Conference and Exhibition 2015 (pp. 95-99). European Wind Energy Association (EWEA).
[23] Bastankhah, M., Welch, B. L., Martínez-Tossas, L. A., King, J., Fleming, P. (2021). “Analytical solution for the cumulative wake of wind turbines in wind farms”. Journal of Fluid Mechanics, 911.
[24] IEC (2019). "Wind energy generation systems – Part 1 : Design requirements”. IEC-61400-1 : 2019 standard.
[25] Jiménez, Á., Crespo, A., Migoya, E. (2010). “Application of a LES technique to characterize the wake deflection of a wind turbine in yaw”. Wind energy, 13(6), 559-572.
[26] Wu, Y. T., Porté-Agel, F. (2011). “Large-eddy simulation of wind-turbine wakes: evaluation of turbine parametrisations”. Boundary-layer meteorology, 138(3), 345-366.
[27] Sorensen, J. N., Shen, W. Z. (2002). “Numerical modeling of wind turbine wakes”. J. Fluids Eng., 124(2), 393-399.
[28] Bakhoday Paskyabi, M., Krutova, M., Nielsen, F.G., Reuder, J., Guernaoui, O.E., (2020). “On Stochastic Reduced-Order and LES-based Models of Offshore Wind Turbine Wakes”. J. Phys.: Conf. Ser. 1669 012018
[29] Joulin, P.A., Mayol, M.L., Blondel, F., Masson, V., Rodier, Q., Lac, C. (2019). “Coupling the actuator line method to the high order meteorological LES model Meso-NH to study wind farm wakes impacts on local meteorology”. Journal of Physics: Conference Series, 1256, pp.012019.
[30] Sanz Rodrigo, J., Borbón Guillén, F., Fernandes Correia, P.M., García Hevia, B., Schlez, W., Schmidt, S., Basu, S., Li, B., Nielsen, P., Cathelain, M., Dall’Ozzo, C., Grignon, L., Pullinger, D., (2020). “Validation of Meso-Wake Models for Array Efficiency Prediction Using Operational Data from Five Offshore Wind Farms”. J. Phys.: Conf. Ser. 1618 062044.
[31] Porté-Agel, F., Bastankhah, M., Shamsoddin, S. (2020). “Wind-turbine and wind-farm flows: a review”. Boundary-Layer Meteorology, 174(1), 1-59.
[32] Pasquill, F. (1961). “The estimation of the dispersion of windborne material”. Met. Mag., 90, 33.
[33] “Meteorological data for Dispersion Modelling”. (n.d.). Retrieved November 14, 2022, from https://www2.dmu.dk/atmosphericenvironment/cost/fisher.htm
[34] Liu, Y., Xiao, Q., Incecik, A., Peyrard, C. (2018). “Aeroelastic analysis of a floating offshore wind turbine in platform-induced surge motion using a fully coupled CFD-MBD method”. Wind Energy. 2018;1–20.
[35] Lee, S., Churchfield, M., Driscoll, F., Sirnivas., S., Jonkman., J., Moriarty, P., Skaare, B., Nielsen, F.G., Byklum, E. (2018). “Load Estimation of OffshoreWind Turbines”. Energies, 11, 1895; doi:10.3390/en11071895.

[36] Johlas, Hannah M.; Martínez-Tossas, Luis A.; Churchfield, Matthew J.; Lackner, Matthew A.; Schmidt, David P. (2021) Floating platform effects on power generation in spar and semisubmersible wind turbines. In : Wind Energy, vol. 24, n° 8, p. 901–916. DOI: 10.1002/we.2608.

[37] Sebastian, T., Lackner, M., (2012). "Analysis of the Induction and Wake Evolution of an Offshore Floating Wind Turbine". Energies, 5, 968-1000; doi:10.3390/en5040968.

[38] Cossu, C. (2021). "Evaluation of tilt control for wind-turbine arrays in the atmospheric boundary layer". Wind Energ. Sci., 6, 663–675, 2021.

[39] Johlas, H.M., Schmidt, D.P., Lackner, M.A., (2022). "Large eddy simulations of curled wakes from tilted wind turbines". Renewable Energy 188, 349-360.

[40] Doubrawa, P., Sirnivas, S., Godvik, M. (2021). "Effects of upstream rotor tilt on a downstream floating wind turbine". J. Phys.: Conf. Ser. 1934 012016.

[41] Vanem, E., Dimitrov, N.K., Kelly, M., Fekhari, E., Cousin, A., Guiton, M. (2022). "A joint probability distribution model for multivariate wind and wave conditions". Proceedings of the ASME 2023 42nd International Conference on Ocean, Offshore and Arctic Engineering, OMAE2023-101961. In review.

[42] M. Kelly, E. Vanem (2022). D2.3 Tech Rep. of "Environmental joint probability distributions and uncertainties ». D2.3 Tech Rep. of HIPERWIND H2020 project, Grant Agreement No. 101006689, https://www.hiperwind.eu/.

[43] Dimitrov, N. (2019). "Surrogate models for parameterized representation of wake induced loads in wind farms". Wind Energy, 22:1371–1389.

3. Accounting for a floater motion for production and load estimate of a floating wind farm

3.1. Short literature review

The effect of platform motion on the wake of a wind turbine is more and more studied with the development of offshore floating farms. In most publications, the wake behind a single turbine supported by a floating structure is studied on its own, using a large diversity of techniques, experimental or numerical. Sometimes a second turbine is added in the wake of the first one to assess the effect of the wake on structural fatigue or production, mainly to assess farm control options. Wise and Bachynsky [44] use the software FAST.Farm to assess the effect of an upstream FWT wake on another FWT placed 8D downstream. They show that the floater pitch has the strongest impact on the wake, moving its vertical centre upwards by up to 0.25D at a distance 8D downwind when comparing the wake of a 10MW turbine on a spar floater with a fixed pitch of 0° and 10° as seen on Figure 4. The computation uses a wake meandering model, but no added turbulence model. The vertical shear exponent was chosen as 0.14, typical of neutral atmospheric stability conditions offshore.

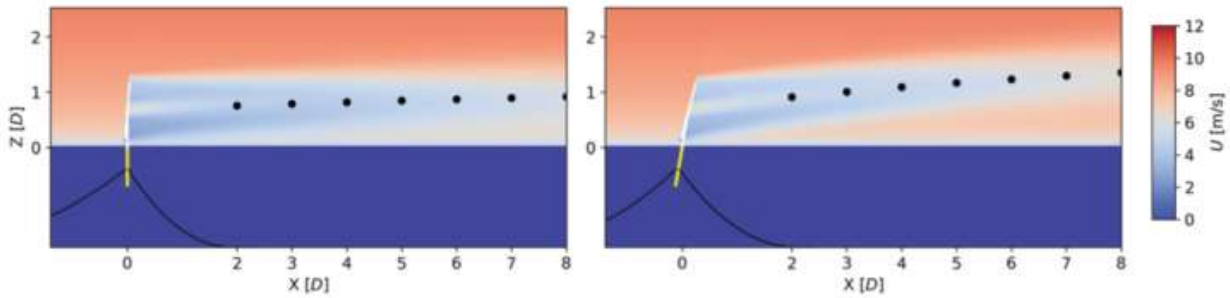

Figure 4: Wake of a 10MW turbine on a spar floater, with 0° (left) and 10° pitch (right). From [44]

Doubrava and Godvik [45] use the same software and observe the effect of pitch on the loads applied on the downstream rotor. With a 6° increase in tilt on a 6MW turbine, the wake centre at x=7D rises by more than 0.2D and the DEL on the tower pitch moment blade root moment increase by up to 10%.

Such a large deflection is not found by Johlas et al. [46][47] when simulating a single turbine using the LES software SOWFA, coupled with OpenFAST for the floater motion. At 6D downwind of the turbine, they found the wake centre rose about 0.05D for a spar (2.5° floater pitch), and 0.03D for a semisubmersible platform (1.8° floater pitch). They also underline that stable atmospheric conditions lead to a larger deviation than neutral ABL.

Shi and al [48] analysed the aerodynamic performances of a single 5MW wind turbine supported by a semi-submersible floater, using the CFD software StarCCM+. They showed that the pitch and surge motion led to an increase in power produced by the tilted turbine, due to the added relative velocity, but also to an increase in power and thrust variations. The floater pitching motion also influences the turbine wake, increasing the recovery rate.

The rotor tilt is also studied independently from the floater motion, as part of a control method to mitigate the wake effect. Fleming et al. [49] use SOWFA to assess whether energy production can be improved using turbine repositioning, rotor yaw or rotor tilt control while minimising the turbine loads. They

simulated two 5MW turbines separated by 7D in a neutral ABL. A positive tilt of 36°, corresponding to the rotor facing downward, led to an increase of total power of 7.1% and an increase in blade out-of-plane bending loads for the tilted and downstream turbines of respectively 5 and 20%, while negative tilts as low as $-15°$ (rotor facing upwards) did not increase the total power and reduced the blade loads. Introducing a load-reducing controller slightly affects the results, leading to a lesser impact of the tilt on the blade loads (1 and 5% respectively).

Scott [50] led an experimental campaign to measure the effect of rotor tilt from –15 to +15° on the wake in a scale-model farm of 12cm diameter model turbines. He demonstrated that secondary steering can occur in these conditions and that the maximum upward wake offset at 6D was 0.2D. A positive tilt (upward-facing rotor) led to a larger effect than a negative tilt. Cossu [51] addressed the impact of the turbine diameter relative to the ABL on tilted rotor wake, in the context of control for maximising the farm power. Two turbines were simulated using SOWFA, separated by 7D in a neutral ABL with capping inversion. The power gain scales with the boundary layer momentum thickness rather than boundary layer height, and there is an optimal diameter where the effect of tilt has the highest impact on total power. Controlling the induction (thrust coefficient) simultaneously with the tilt leads to even better efficiency.

Finally, Kheirabadi and Nagamune [52] present FOWFSim-Dyn, a software based on the low-fidelity wake simulator Floris, which takes into account the floater motion in the wind farm power computation. This software has many similarities with the work presented in this section, except that it does not take the floater pitch motion into account. Aimed at validating control strategies based on turbine repositioning or derating, it includes the modelling of the floater mooring system, to accurately capture its time-averaged surge and sway.

To our knowledge, no published model is computing the time-averaged floaters' pitch and roll in an offshore wind farm, predicting the rotor tilt and its effect on the velocity and turbulence field for the downstream turbines; the purpose of the work presented in this section is to show such.

3.2. Software development

The software objective is to compute the load and production for wind turbines in an offshore floating farm. For given environmental conditions, the position of each turbine is affected by the motion of the supporting floater.

Since the floater surge was shown to have a negligible impact on the wake seen by the subsequent turbine, the hydrodynamic loads due to the current and the waves (drift) were not considered for this software. They could have a second-order effect by altering the stiffness of the mooring system or changing the time-averaged floater pitch. In this study, the mooring system is linearised, which is correct for most of the degrees of freedom except for the surge (see section 3.2.2).

Because the position considered is an average position for specific wind conditions, and the wind conditions vary over timescales of hours rather than minutes, we do not consider the floater yaw as a relevant parameter in this study. The wind turbines align with the average incoming wind, regardless of the floater's motion. It is possible to introduce a yaw misalignment in the software (corresponding to a sensor defect or quickly changing wind conditions), and by design, this misalignment is not affected by the floater yaw.

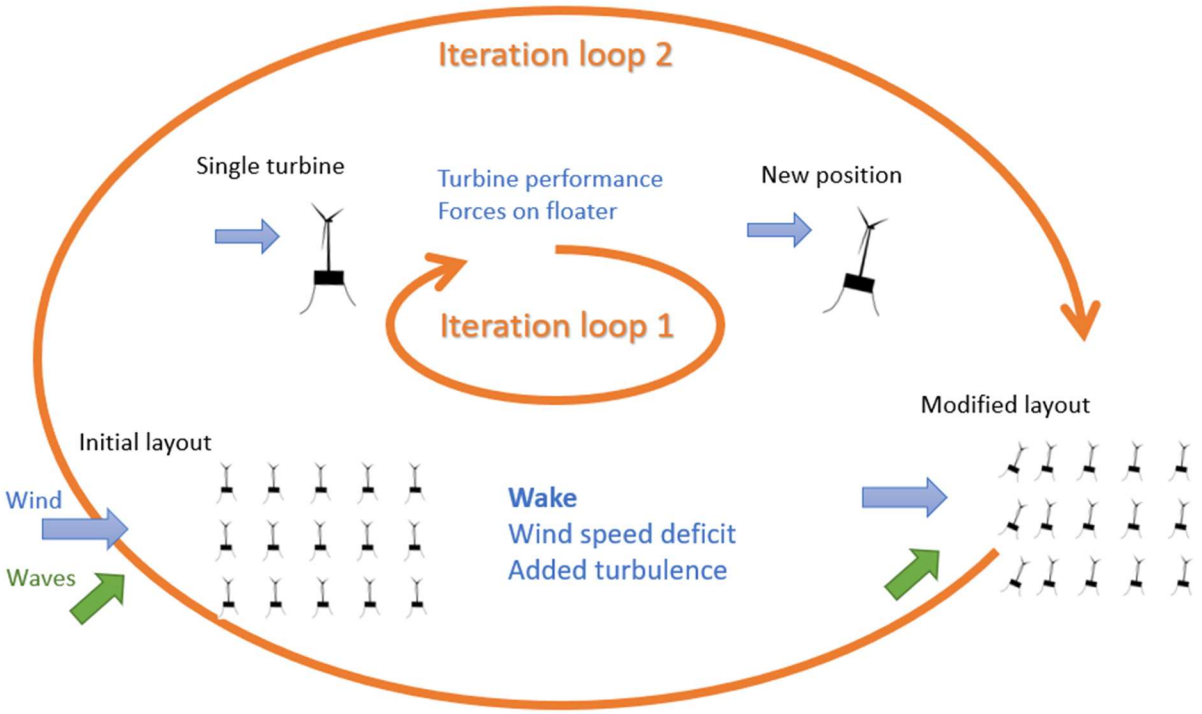

Figure 5: Representation of the two nested iterative loops solving the wind field in the farm

The hydrostatic computation (inner loop in Figure 5, so-called HiperSAMI in the rest of this document) is made by first computing the floater equilibrium position, and then the average aerodynamic load on the rotor over two rotations. This load is used to compute the new equilibrium position. The aerodynamic calculation uses a blade element momentum (BEM) method, with rigid blades. The rotation speed and blade pitch are set at values directly depending on the averaged wind speed over the rotor according to control data shown in Figure 6. The process (compute equilibrium position then calculate aerodynamic load) is iterated until the floater position converges (variation of the position vector norm less than 1%).

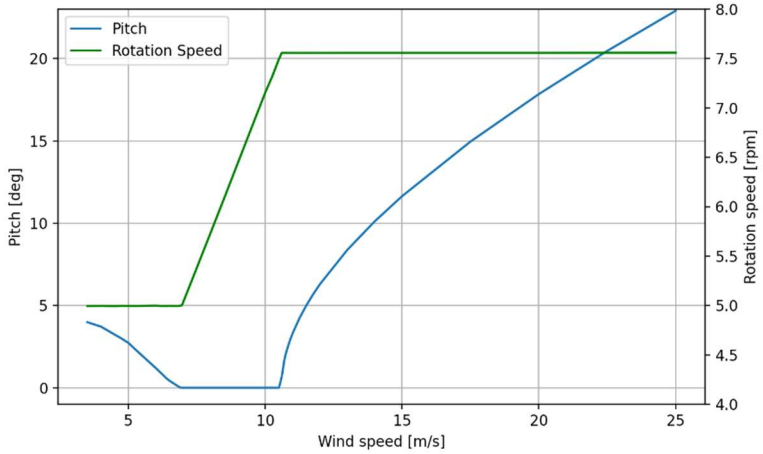

Figure 6: Design rotation speed and blade pitch as a function of wind speed

In the aerodynamic load computations, the wind is constant and uniform, meaning that no turbulence or vertical shear is considered. Only the force on the rotor is computed, neglecting the wind drag on the tower or the floater. However, the tower shadow (upstream influence of the tower) is part of the computation.

The second loop consists of computing the incoming wind on each turbine in the farm and deducing the new position of each turbine. Since the floater pitch is defined in the floater referential, and the rotor tilt is defined according to the wind direction, the rotor tilt $\hat{\beta}$ is derived from the floater roll $\alpha$and pitch β, and the nacelle yaw γ (misalignment between the nacelle and the floater), using the following expression:

$$\hat{\beta} = \tan^{-1}\left(\frac{cos(\gamma)\,sin(\beta) - sin(\gamma)\,cos(\beta)\,sin(\alpha)}{\sqrt{1 - (cos(\gamma)\,sin(\beta) - sin(\gamma)\,cos(\beta)\,sin(\alpha))^2}}\right) + \widehat{\beta_0}\,, \qquad \text{Eq. 1}$$

where $\widehat{\beta_0}$ is the shaft tilt.

Farmshadow™ uses engineering wake models to predict the wind field throughout the whole farm, starting from the most upstream turbine and working downwards. Turbulence and wind vertical shear are considered in this computation, and modelling of the velocity deficit, added turbulence and wake superposition is done through published models. In this study, the models used are super-gaussian for the wake speed deficit [53], Qian for the wake-added turbulence [54] and local-linear-sum for the superposition [55]. No blockage model is used.

The wake is first computed with all turbines in the neutral position, then the average incoming wind U_{mean} is computed for each rotor and HiperSAMI is used to determine the new floater positions. The process is repeated until the average speed at each rotor has converged ($\max(dU_{mean}) / U < 0.5\%$). The convergence usually takes 1 or 2 iterations.

3.2.1. Implementation

The software is based on four major libraries schematically represented in Figure 7:

- SAMI (Simulator for Aerodynamic Models Investigation) is a C++ static library which enables the user to describe a wind turbine (tower, nacelle and blades), generate motion (hub rotation, blade pitch, tower position) and dynamically link to an aerodynamics library.
- AeroDeep is a C++ dynamics library enabling the computation of the aerodynamic force generated by the wind on the rotor, using a BEM (Blade Element Momentum) model.
- Farmshadow™ is a library written in C++ using the interface compiler SWIG, enabling the use of C++ functions within a python script. It lets the user determine the velocity and turbulent fields in a wind farm given the position (six degrees of freedom) of each wind turbine. Several models are available which are described in [53].
- HydroSolver is a C++ static library which enables the user to describe a floating wind turbine and predict its position based on a hydrostatic calculation.

The C++ executable HiperSAMI (associating HydroSolver and SAMI) is used to determine the position of a floating wind turbine given the incoming wind, while a Python script runs a loop over the whole wind farm using Farmshadow™ to determine the incoming wind for each turbine. This is schematically represented in Figure 7.

HiperSAMI suffers some limitations compared to a fully coupled aero-hydro-servo-elastic simulation, namely:

- Rigid blades
- Absence of controller
- Linear hydrostatics

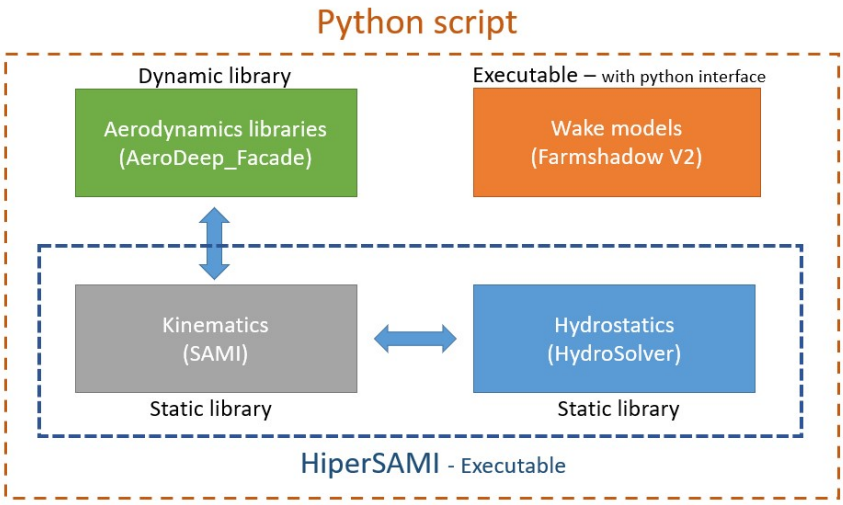

Figure 7: Software architecture

3.2.2. Validation

The libraries existed and were validated independently before starting this work. Here we focus on HiperSAMI, by comparing results with fully coupled simulations using DeeplinesWind™ (DLW, https://www.principia-group.com/blog/product/deeplines-wind/). The model for the UMaine semi-submersible floater and 15MW IEA turbine which will be used in the application was set up in WP1 (cf. section 1). The floater and turbine are presented in Figure 8, with the sign conventions used in the software and the following sections.

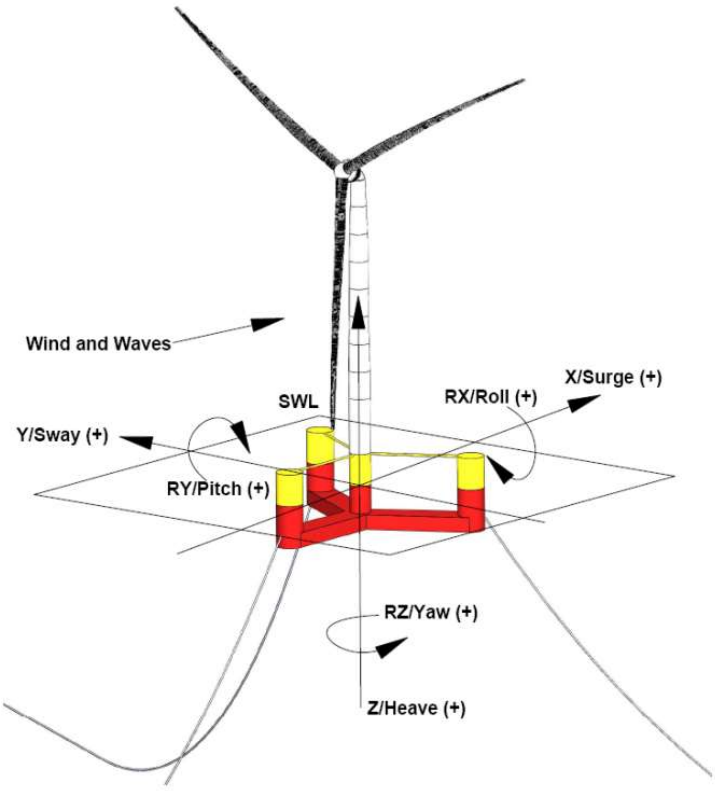

Figure 8: Umaine floater with IEAWind 15MW turbine

The turbine blades are made rigid in DLW, as HiperSAMI does not compute elasticity. For the rigid DLW simulation, the pitch saturation is disabled as it is not supported. We also show the results for the reference elastic DLW simulation. As there is no controller in HiperSAMI, we use a look-up table, giving the blade pitch and rotor rotation speed as a function of the wind speed. The incoming wind is uniform with no turbulence for both HiperSAMI and DLW. HiperSAMI does not support vertical shear because of the absence of a controller (applying vertical shear results in platform oscillations). All simulations are performed with the wind in the X+ direction.

We first compare the aerodynamic forces and moments computed by DLW with the loads computed by SAMI for a fixed turbine. Figure 9 and Figure 10 show respectively the aerodynamic thrust and blade pitch computed by the two software. SAMI and DLW rigid show a good agreement, except at low speed due to the lack of pitch saturation in DLW, but in this region SAMI and DLW elastic match.

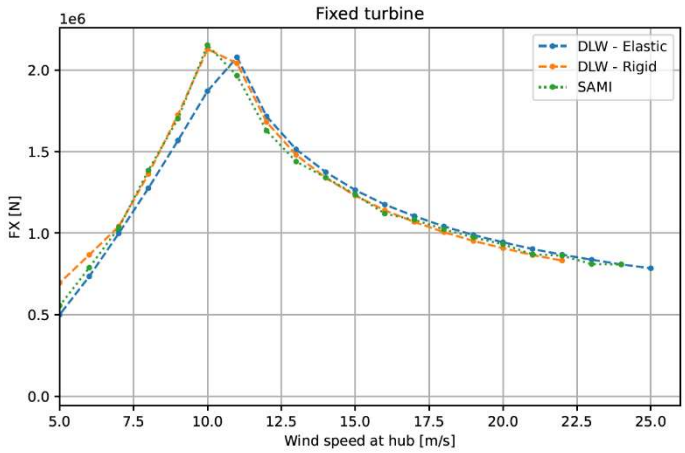

Figure 9: Aerodynamic force on the rotor along X as a function of wind speed for SAMI and DLW simulations

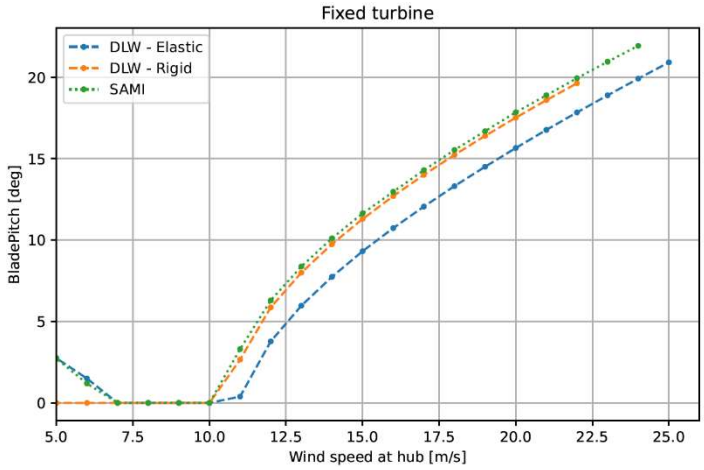

Figure 10: Effective blade pitch as a function of wind speed for SAMI and DLW simulations

The next step is to compare the floater position computed by DLW with the ones computed by HiperSAMI for a floating wind turbine. The surge (Figure 11) is overestimated by HiperSAMI, because of the linearisation of the mooring forces, especially for large displacement. However, the surge has a very small impact on the wake, since the relative displacement between turbines is much smaller than the distance between two turbines.

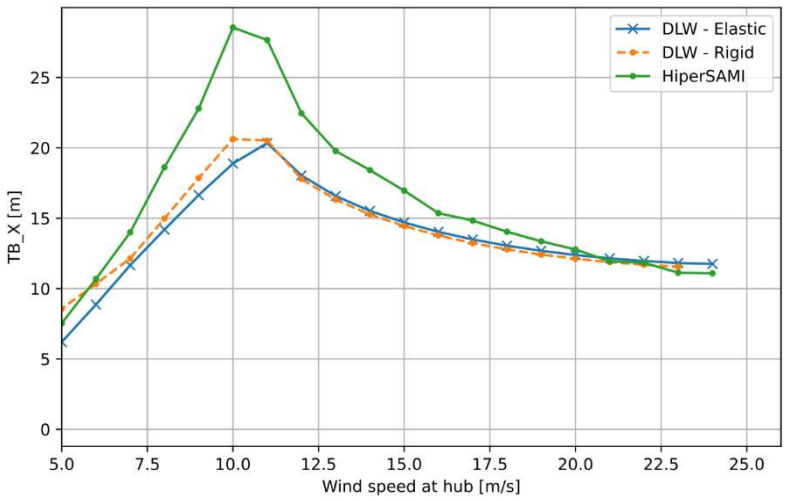

Figure 11: Surge computed by DLW and HiperSAMI for a floating wind turbine

The floater pitch is much more important to our study, and Figure 12 shows a good agreement between DLW and HiperSAMI. The discrepancy at high wind speed (pitch underestimated by 0.5 to 1°) is also due to the linearisation of the mooring forces. To obtain a more accurate result, we recommend using a look-up table in the future, rather than linearised forces.

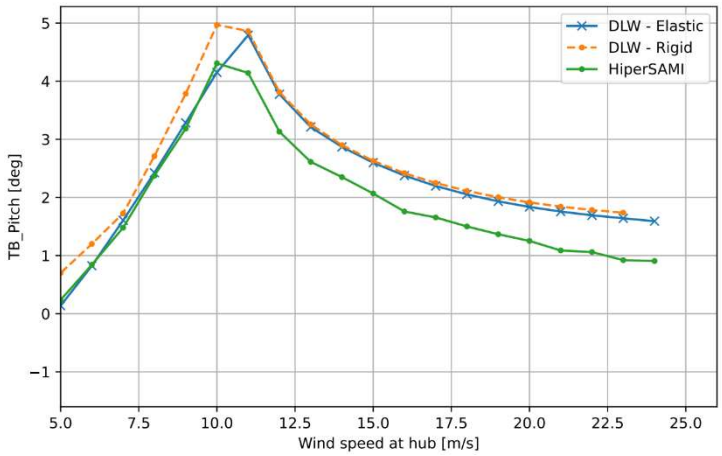

Figure 12: Floater pitch computed by DLW and HiperSAMI for a floating wind turbine

3.3. Application to South Brittany wind farm

This software is aimed at being used on the South Brittany virtual wind farm, so we present a few qualitative and quantitative results below, as well as an AEP calculation.

3.3.1. Input data

The model inputs to the software are:

- Floater mass, inertia, the centre of gravity and junction point with the turbine tower base
- Mooring fairleads position, pre-tension and stiffness matrix

- Floater hydrostatic stiffness matrix (including the effect of change of gravity centre with motion)
- Turbine geometry (total mass, tower, blades, pre-cone, shaft tilt, …)
- Rotor control tables and parameters of the aerodynamics model (only used in SAMI)
- Rotor performance tables: C_p, C_t as a function of the wind speed (used only in Farmshadow^{TM})
- Farm layout

A python function enables one to compute the velocity and turbulence field in the farm, as well as for each turbine, the position, mean wind at the rotor and output power, for any combination of wind speed, direction, turbulence intensity and vertical shear coefficient.

The rotor performance tables are used in Farmshadow^{TM} to compute the thrust, which is an input for the wake models, and the power which is an output of our software. We used the values given by DLW rather than those given by HiperSAMI, to have a more realistic evaluation of the total farm power. Note that the rotor performance depends on the support (fixed or floating), the wind speed but also its turbulent intensity, vertical shear, direction and veer, as well as the amplitude and period of the waves. Here we only consider the wind speed and vertical shear. In Figure 13 we compare the performances of the 15MW IEAWind rotor with a fixed and floating support. Above the rated speed, the pitch control ensures production at nominal power, and below the rated speed, the oscillations of the rotor compensate for the reduction in swept area induced by the tower pitch.

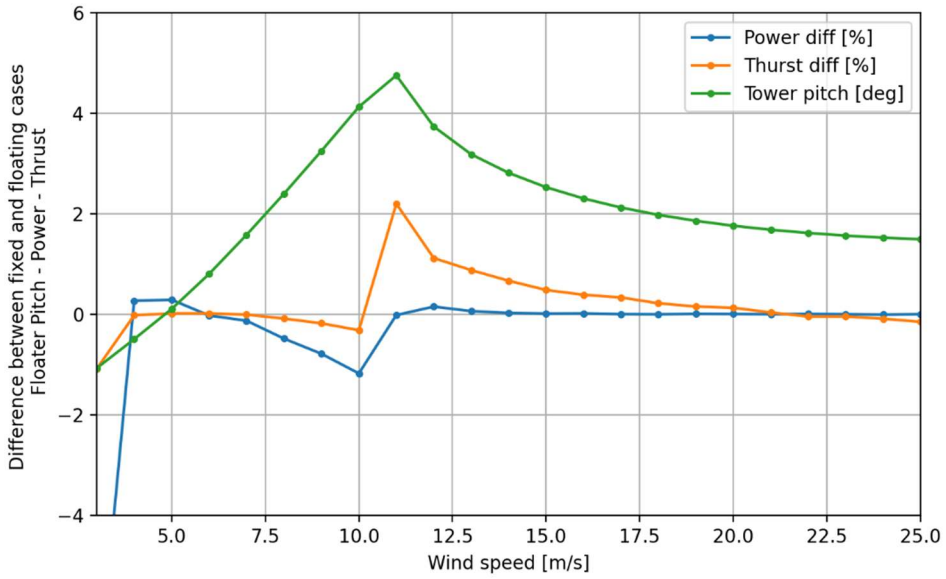

Figure 13: Floater pitch, the relative difference in power and thrust for the fixed and the floating IEAWind 15MW turbine, computed from DLW with a uniform headwind (vertical shear following a power law of coefficient 0.1) and no waves.

3.3.2. Qualitative analysis

For the qualitative study, we consider four test cases summarised in Table 1.

Table 1: Test matrix for the qualitative study

Case	Wind speed [m/s]	Wind direction [degrees, relative to main farm direction]	Turbulence intensity [%]	Wind vertical shear exponent
A	8	0	14	0.1
B	8	90	14	0.1
C	11	90	14	0.1
D	11	90	14	0
E	11	90	21.47	0.1
F	14	90	14	0.1
G	11	180	14	0.1

The farm turbulence and velocity fields are computed using Farmshadow™ and HiperSAMI, for three configurations per test case:

- No tilt: No rotor tilt is taken into account in the wake computation: this is quite standard in low-fidelity wake models.
- Fixed: The shaft tilt is considered in the wake computation, but the floater is considered fixed.
- Floating: Both the shaft tilt and floater time-averaged position (surge, sway, pitch and roll) are taken into account in the wake computation.

For each configuration, the thrust and power curves used are those of a floating turbine, taking into account the shaft tilt and floater motion.

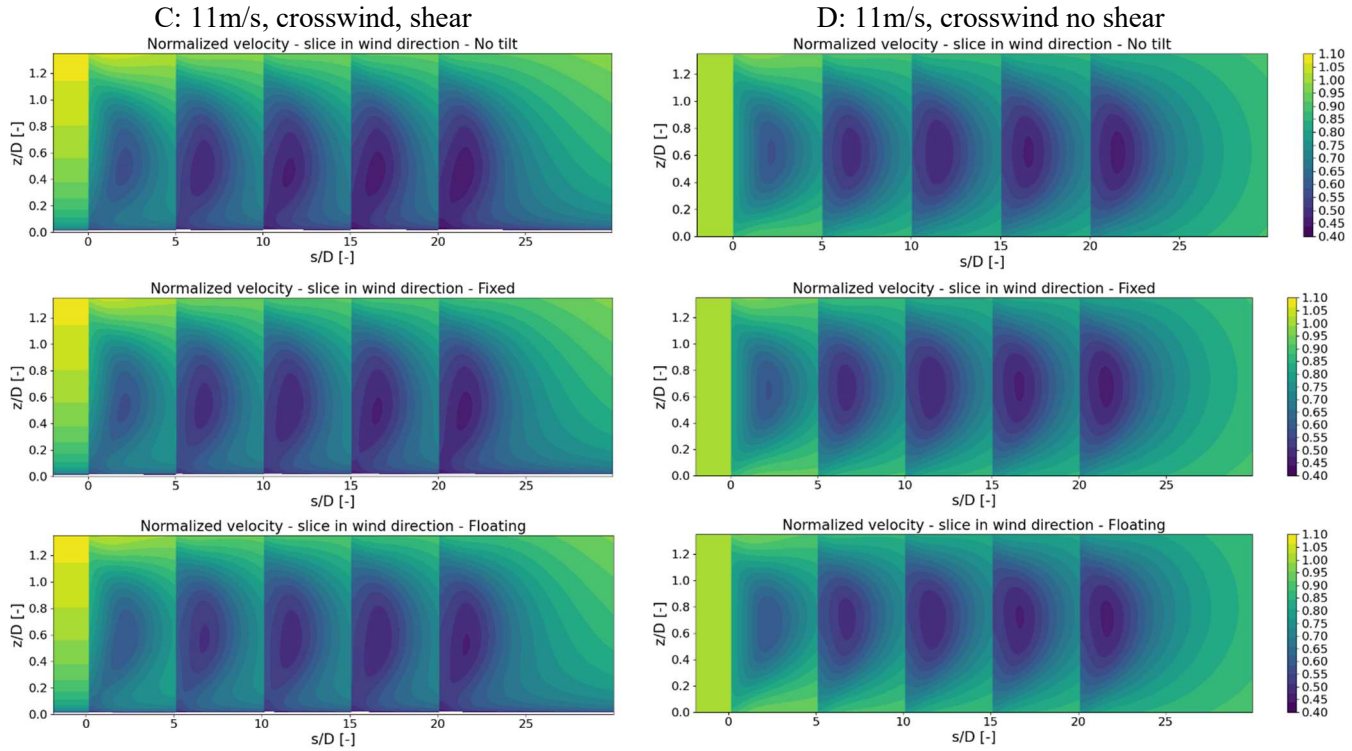

Figure 14: Vertical slice showing the axial wind velocity downwind of the most upwind turbine for cases C (left) and D (right), 11m/s

Figure 14 shows vertical slices of the axial wind velocity in the farm, for cases C (with vertical shear) and D (no shear). The plane is taken at the centre of the rotors in the middle of the farm relative to the wind. In both cases, the total rotor tilt is around 10° (6° shaft tilt, plus 4° floater roll). The wake upwards deflection due to the shaft tilt (Figure 14, second row) and to the tower tilt (Figure 14, third row) is visible, although the vertical shear strongly modifies the wake shape, adding an initial downward deflection.

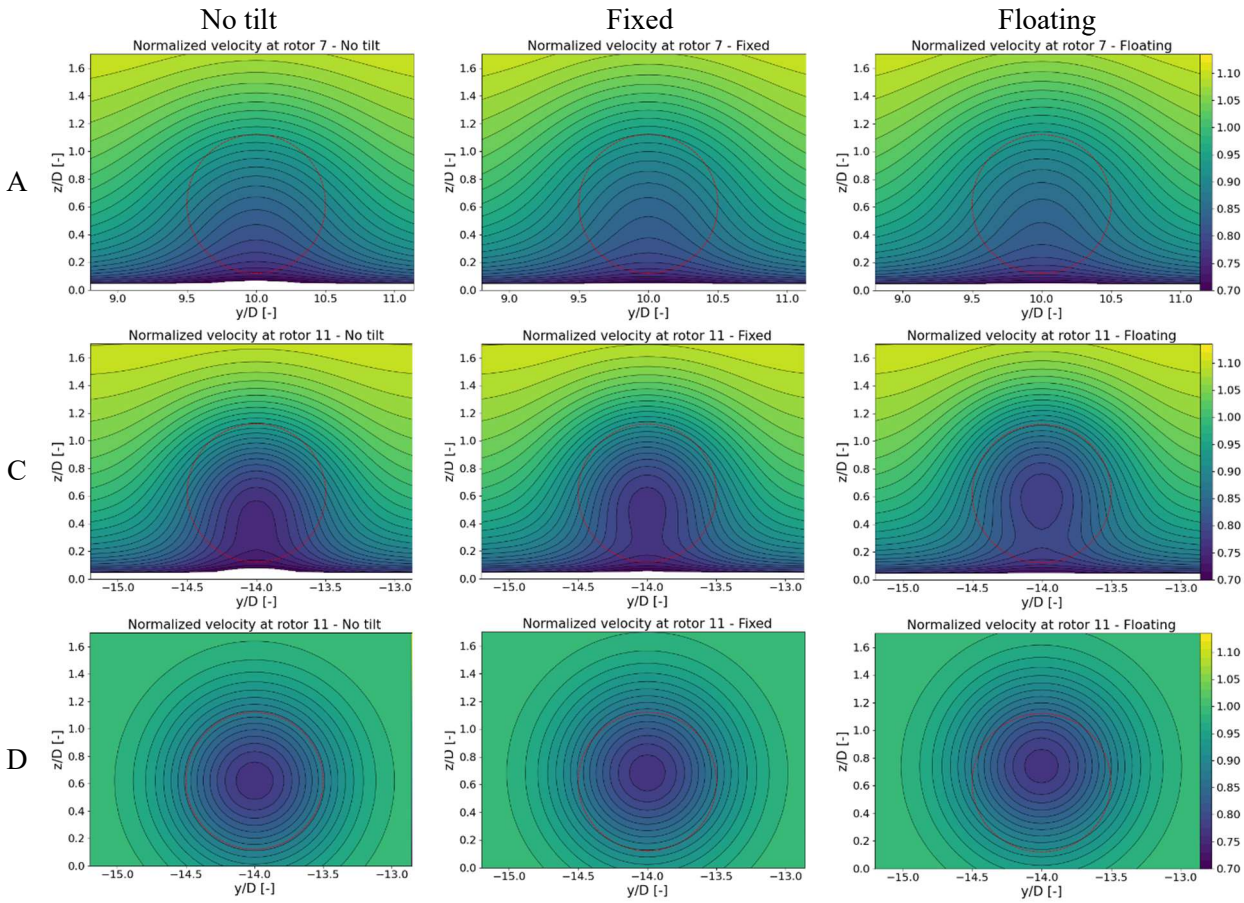

Figure 15: Axial velocity profile ahead of the second rotor in the middle row depending on the wind direction (Rotor 7 for head wind, 11 for crosswind). Case A (top): 8m/s, head-wind with vertical shear. Case C (middle): 11m/s, crosswind with vertical shear, Case D (bottom): 11 m/s crosswind, no vertical shear. The rotor is represented as a red dashed line.

Figure 15 shows the axial velocity profile upstream of the second rotor relative to the wind, in the middle of the farm, for cases A (8m/s headwind with shear), C (11m/s crosswind with shear) and D (11m/s crosswind without shear). For case A, it is difficult to determine the wake centre. This is done numerically in the next section, using [56]. For case C, the wake centre is easier to see, and the upwards deflection is more visible. Without shear (case D), the effect of shaft tilt and floater position is even clearer.

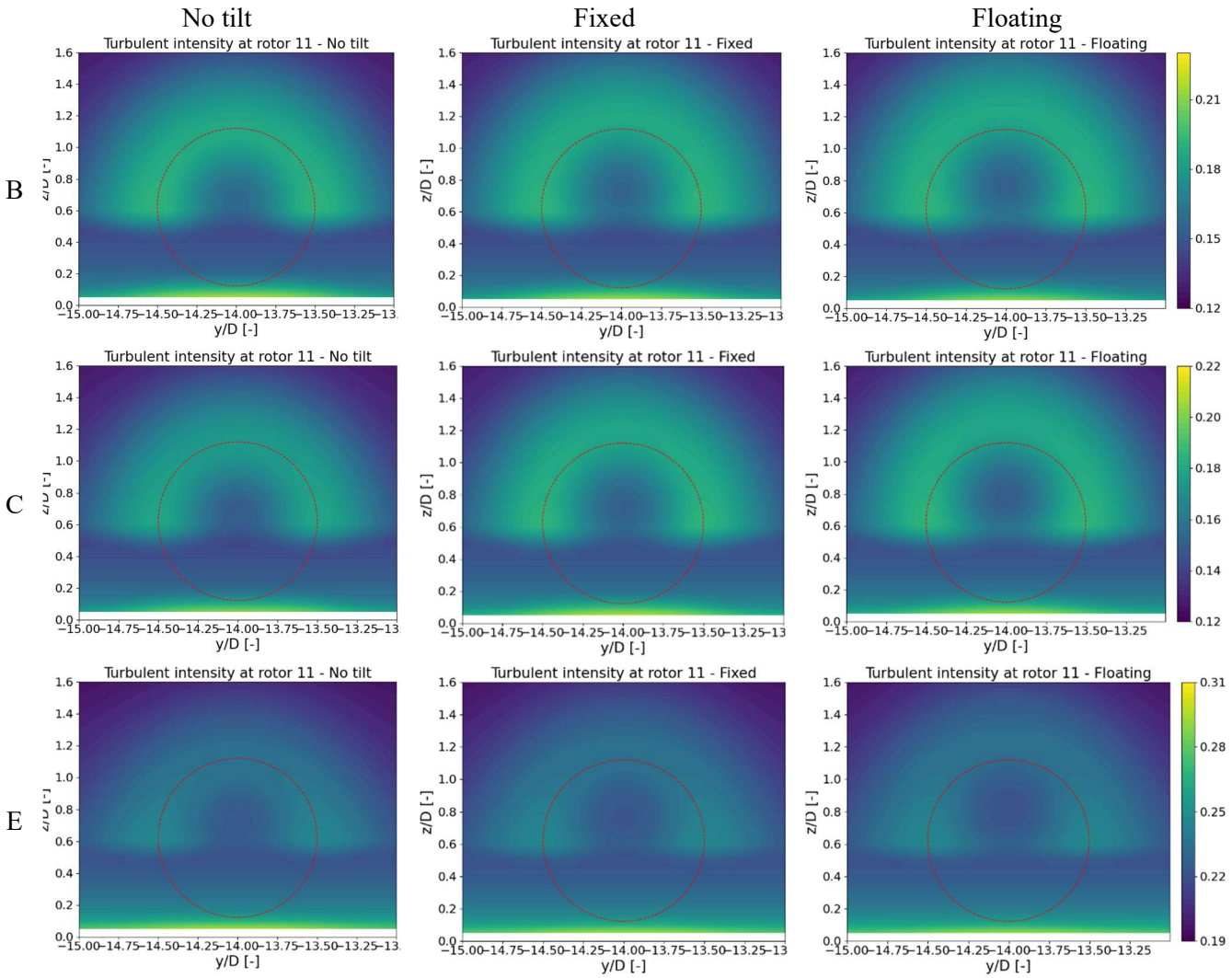

Figure 16: Turbulence intensity profiles ahead of the second rotor in the middle row depending on the wind direction (Rotor 11 for crosswind). Case B (top): 8m/s, crosswind with shear and 14% TI. Case C (middle): 11m/s, crosswind with shear and 14% TI. Case E (bottom): 11m/s, crosswind with shear and 21.47% TI.

Figure 16 represents the turbulence upstream of the second rotor in the middle of the farm for cases B, C and E. The quantity represented is the velocity standard deviation, normalised by the average velocity on the rotor plane. Because the turbulence is higher at the edge of the wake, it makes it easier to visualise the wake centre. Note that the fading of added turbulence below the hub height is due to the correction from [54]. Again, an elevation of the wake centre is visible in all three cases as the shaft tilt, then tower tilt is taken into account. The wake shape is similar when the ambient turbulence intensity increases from 14 to 21.47% (cases C and E).

3.3.3. Quantitative analysis

The power, the averaged wind speed and the averaged TI ahead of each rotor and the wake vertical centre are computed for each of the cases presented in section 3.3.2. They are gathered in the figures and tables below, which show the rotor tilt and incoming wind vertical wake centre as a function of the rotor index (attributed number of the rotor in the farm, see Figure 25).

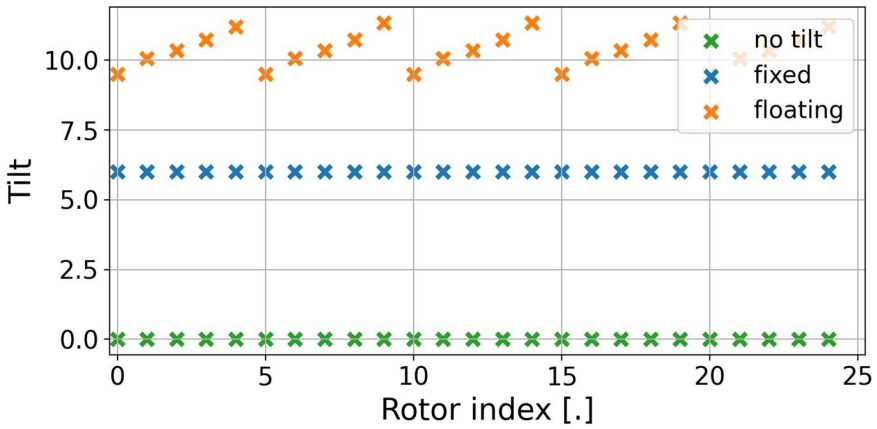

Figure 17: Rotor tilt for Case F: 14m/s crosswind with vertical shear. The rotors most upstream (first row) are indexed 0,5,10,15 and 20.

The rotor tilts are represented in Figure 17 for case F, with a wind speed above rated (11m/s), showing that the tilt is increasing as rotors are deeper in the farm since the wind axial velocity decreases and get close to the rated conditions where the thrust is maximal.

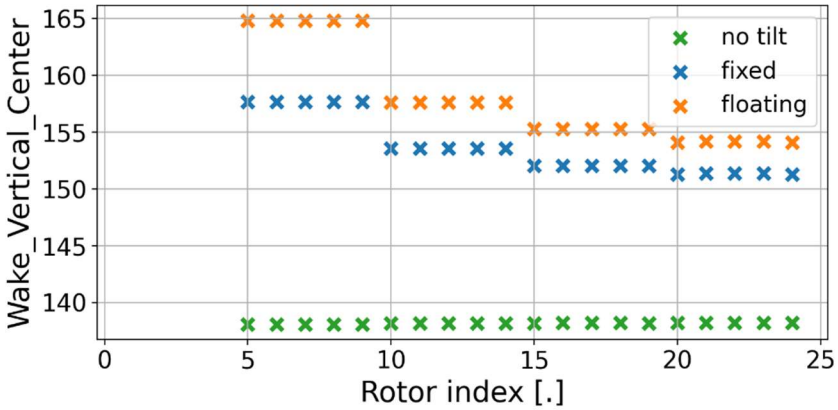

Figure 18: Wake vertical centre for Case A: 8m/s head-wind with vertical shear. The rotors 0-4 (first row) do not have a wake.

Figure 18 represents the wake vertical centre for the rotors across the farm, for an under-rated wind speed along the main farm direction. The difference is maximal for the second row of turbines, as the first-row experiences the highest thrust, therefore the largest rotor tilt.

In Table 2, the farm-averaged power and mean rotor velocity and turbulence intensity are presented for all test cases. The difference is positive when a value is larger in the floating case:

$$\Delta\overline{X} = \left(\overline{X}_{\text{floating}} - \overline{X}_{\text{fixed}}\right)/\overline{X}_{\text{fixed}} .$$

Table 2: Comparison of floating case to fixed case in terms of power, rotor mean wind speed and turbulence intensity, and wake vertical centre for several cases. The average tilt in the farm is reminded for the floating case.

Case	U [m/s]	Dir [°]	TI	Shear	Tilt [°]	$\Delta\bar{P}$ [%]	$\Delta\overline{U_{mean}}$ [%]	$\Delta\overline{TI_{mean}}$ [%]	$\Delta\overline{Z_{wake}}$ [%]
A	8	0	0.14	0.1	7.50	0.27%	0.10%	-0.08%	2.8%
B	8	90	0.14	0.1	8.42	0.63%	0.21%	-0.15%	5.1%
C	11	90	0.14	0.1	10.49	1.09%	0.43%	-0.28%	8.4%
D	11	90	0.14	0.0	10.36	1.05%	0.41%	-0.25%	7.3%
E	11	90	0.2147	0.1	11.01	0.66%	0.26%	-0.17%	6.8%
F	14	90	0.14	0.1	10.39	0.00%	0.24%	-0.23%	4.2%
G	11	180	0.14	0.1	12.30	1.31%	0.50%	-0.15%	10.7%

Numerous simulations were run to prepare the AEP computation, enabling to draw more general and quantitative conclusions on the impact of the floater motion on production. Following the IEC 61400-1 standard the turbulence intensity used for each case is a function of the incoming wind speed U:

$$\bar{ti} = 1.4\,\mathrm{TI_{ref}}\frac{0.75\,U + 3.8}{U}, \qquad \text{Eq. 2}$$

where $\mathrm{TI_{ref}} = 0.14$.

This expression is used as an input for case E (U = 11m/s, TI = 21.47%) and leads to a smaller difference between fixed and floating power, due to a quicker wake recovery.

Figure 19 shows the rotor tilt (sum of shaft tilt and tower tilt obtained from Eq. 1), as a function of the wind direction, shown as compass azimuth (0° means a wind coming from the north), for different incoming wind speeds. The maximal tilt is obtained for 10.75 m/s and 67.5° wind, which corresponds to a tail wind.

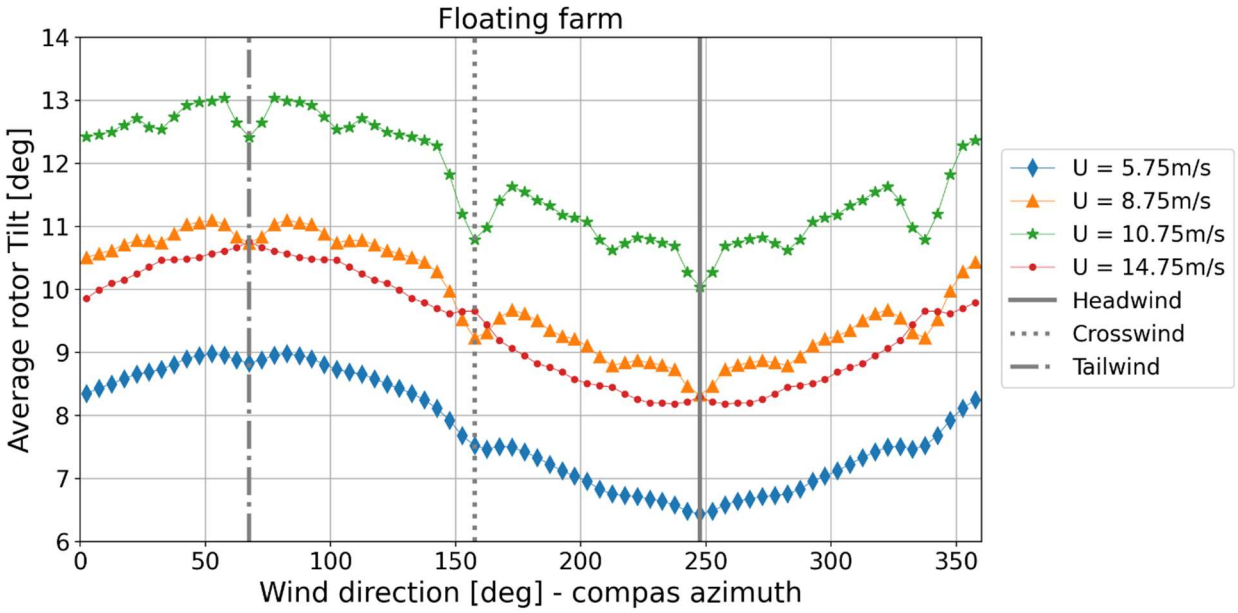

Figure 19: Farm averaged rotor tilt for different wind conditions. Headwind is represented with a grey line and crosswind with a dashed line.

Figure 20 shows the relative difference in power as a function of the wind direction for different wind conditions. The largest differences (0.6%) are found for an ambient wind of 10.75m/s, close to the rated conditions (10.59m/s), and for a tailwind, where the floater pitch is the largest. Above the rated speed, the floater positions do not have an impact on the produced power, as the blade pitch is adjusted by the control system to maximise production.

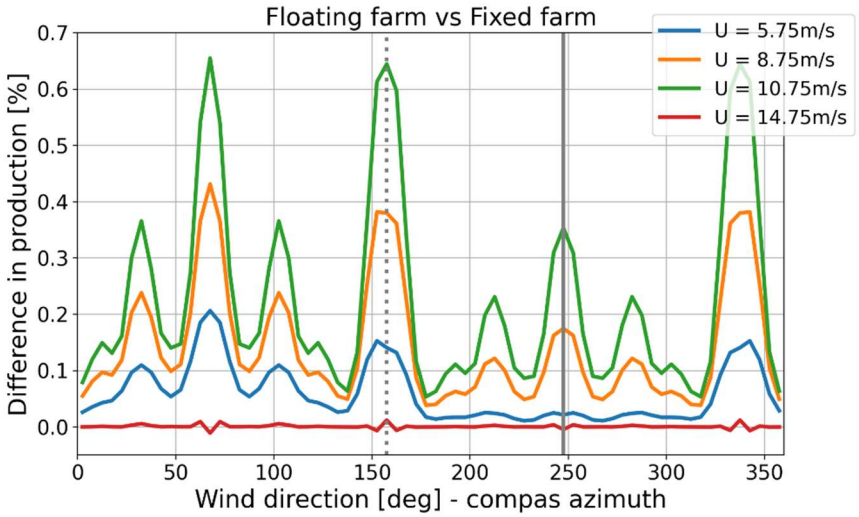

Figure 20: Relative difference in produced power between a fixed (configuration 6) and floating (configuration 7) farm for different wind conditions.

3.3.4. AEP calculation

To compute the annual electrical production for the floating wind farm, we computed the farm power for 3096 cases spread across all possible wind speeds and directions (0.5 m/s step in wind speed, 5° step in direction). A weighted average of the produced power and probability of occurrence of the weather conditions, represented in Figure 21, gives the power production averaged over a year.

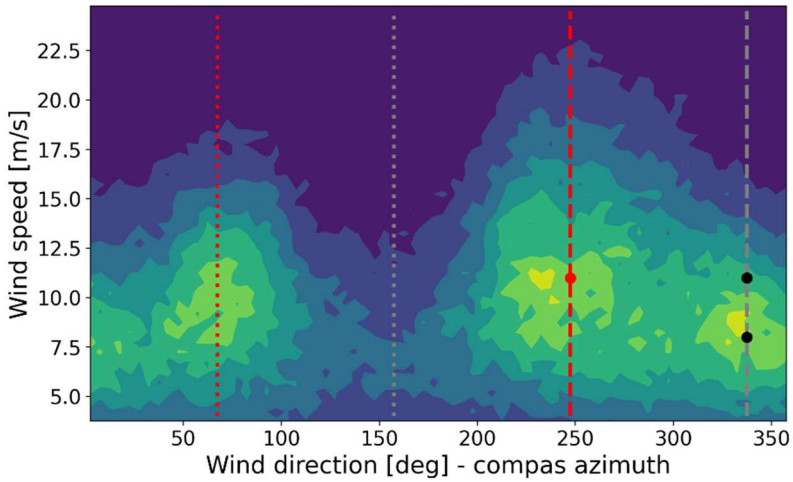

Figure 21: Probability distribution of wind speed and direction for the South Brittany case. The red lines correspond to headwind (247.5°) and tailwind (67.5°), while the grey lines correspond to crosswinds (157.5 and 337.5°). The black and red dots correspond to the test cases presented in section 3.3.2.

Using the farm symmetry, the number of cases could be reduced to 1549 (from 67.5 to 247.5°). To distinguish the effect of the shaft tilt, floater motion, and floater averaged position on the wake, seven AEP were computed, depending on the power and thrust curves taken into account at the turbine level (see section 3.3.1), and the rotor tilt used for the wake computation (see section 3.3.3). These configurations are summarised in Table 3, with the final results in terms of AEP and yearly averaged power. The rated power of the farm is 25×15=375MW. When the effect of wakes is not modelled ("no wake"), all turbines in the farm produce the same power regardless of their position. Standards computation of the AEP usually take into account the shaft tilt at the turbine level (the C_p, C_t curves given by the manufacturer include the shaft tilt), but not at the farm level in the wake. This is represented by case #2. The other configurations add the effect of the floater motion on the turbine performance and the effect of the rotor tilt (separating shaft tilt and tilt due to floater position). The shaft tilt and the tilt due to the floater motion are always included in the performance (C_p, C_t) of the turbine

Table 3: AEP computations for different configurations of floating and fixed wind farms

Configuration	Effect on wake	Effect on turbine performances	AEP [GWh/year]	Yearly averaged power [MW]
1	**No wake**	**Shaft tilt**	**2164**	**246.98**
2	**No tilt**	**Shaft tilt**	**2083**	**237.84**
3	**Shaft tilt**	**Shaft tilt**	**2084**	**237.93**
4	No wake	Shaft tilt + floater motion	2157	246.20
5	No tilt	Shaft tilt + floater motion	2077	237.08
6	**Shaft tilt**	**Shaft tilt + floater motion**	**2078**	**237.16**
7	**Shaft tilt + floater position**	**Shaft tilt + floater motion**	**2079**	**237.34**

The results for configurations 1, 2, 3, 6 and 7 are compared in Figure 22, where the different effects are cumulated from left to right. Beyond the effect of the wake itself, the major impact comes from the performance of each turbine, which is worse on a floater compared to a fixed support (see Figure 13). This is contrary to [47], where a very small but opposite trend for a 6MW turbine on a semi-submersible platform

was found. The relative size of the turbine compared to the floater probably has a strong impact on the maximal pitch and therefore the performance. Also note that [47] were studying a single set of weather conditions, whereas these results compute the AEP based on the condition at a specific location in Brittany.

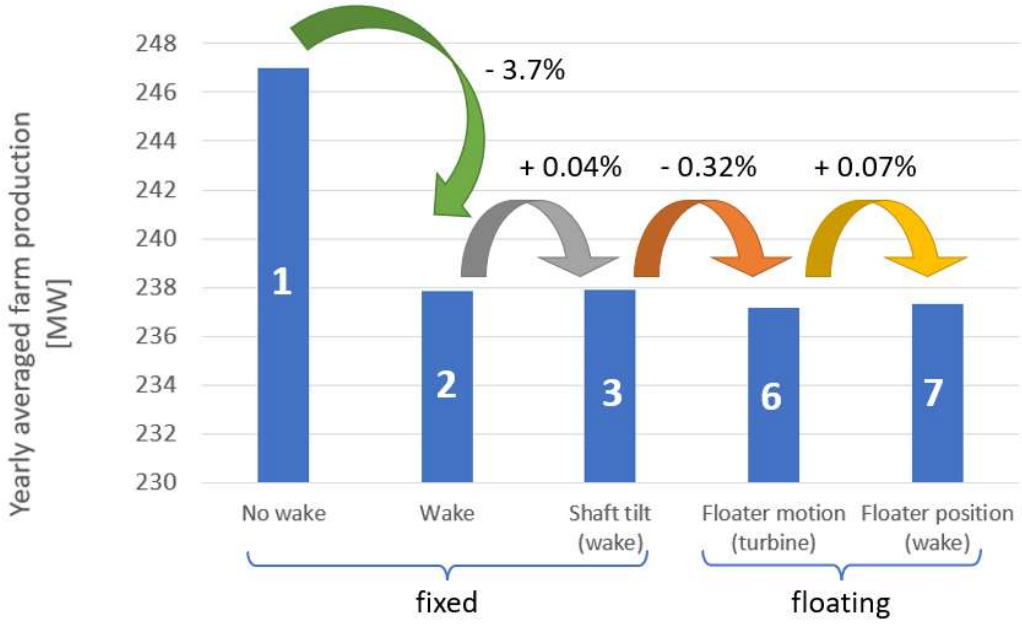

Figure 22- Yearly averaged farm production taking different effects into account. The white numbers refer to Table 3.

The shaft tilt and floater time-averaged pitch and roll deflect the wake upwards but have a relatively small impact on the yearly averaged production (equivalent to AEP): respectively +0.04% and +0.07% compared to a decrease in AEP by 0.32% due to the lower performance of the turbine placed on floating support. The overall impact computed in this work (shaft tilt, turbine performance due to floater motion and effect of the time-averaged floater position on the wake, comparing cases 2 and 7) is an AEP reduction of 0.1%.

In Figure 23, the power difference is mapped as a function of wind speed and direction, to present the combined effect of the turbine performance (left: 2 versus 7) and the change in wake due to the floater position (right: 6 versus 7). The effect of the floater position is more localised and of lesser amplitude compared to the total effect of floating motion.

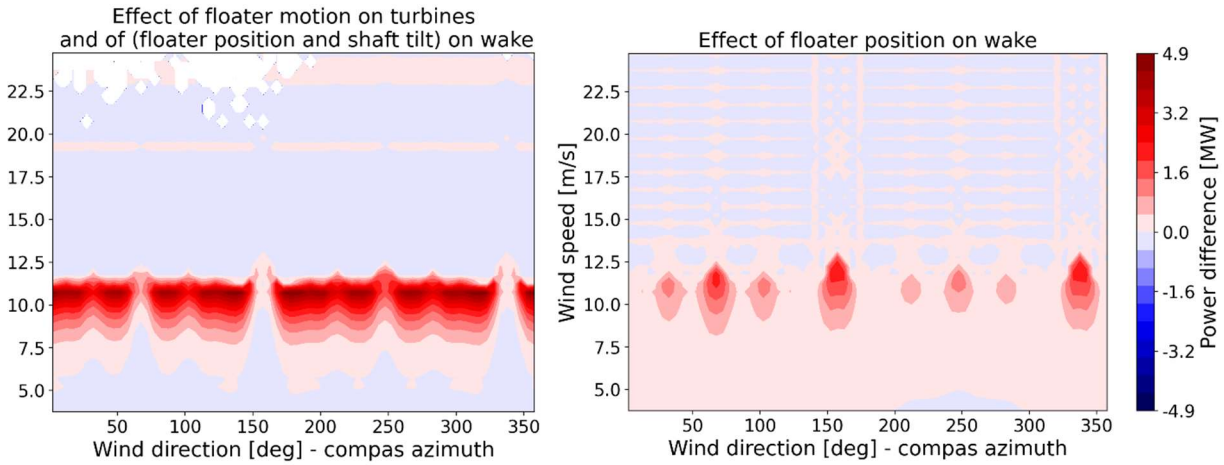

Figure 23: Map of power difference delivered by the farm, between floating and fixed setup. Left: configurations 2 versus 7, Right: configurations 6 versus 7

3.3.5. Conclusions

The tool developed in this work has enabled the computation of the effects on the wake of the time-averaged position of the floater, with some simplifications:

- shear disregarded in the determination of the floater time-average position,
- thrust used for the wake computation depends only on the wind speed,
- low-fidelity model used for the wake computation.

Despite these limitations, it was possible to determine the wake deflection due to the tower tilt, which was consistent with the existing literature (0.04 to 0.1D depending on the wind speed and direction). The impact of the floater position on the wake regarding energy production is small in comparison to the performance change of a single turbine due to the floating motion. The elevation of the wake centre is more significant and will affect the loads applied on the downstream turbines.

References of section 3

[44] Wise, A S.; Bachynski, E E. (2020) ”Wake meandering effects on floating wind turbines”. In : Wind Energy, vol. 23, n° 5, p. 1266–1285. DOI: 10.1002/we.2485.

[45] Doubrawa, P., Sirnivas, S., Godvik, M. (2021). ”Effects of upstream rotor tilt on a downstream floating wind turbine”. In : Journal of Physics: Conference Series, vol. 1934, n° 1, p. 12016. DOI: 10.1088/1742-6596/1934/1/012016.

[46] Johlas, H. M.; Martínez-Tossas, L. A.; Lackner, M. A.; Schmidt, D. P.; Churchfield, M. J. (2020). ”Large eddy simulations of offshore wind turbine wakes for two floating platform types”. In : Journal of Physics: Conference Series, vol. 1452, n° 1, p. 12034. DOI: 10.1088/1742-6596/1452/1/012034.

[47] Johlas, Hannah M.; Martínez-Tossas, L A.; Churchfield, M J.; Lackner, M A.; Schmidt, D P. (2021). ”Floating platform effects on power generation in spar and semisubmersible wind turbines”. In : Wind Energy, vol. 24, n° 8, p. 901–916. DOI: 10.1002/we.2608.

[48] Shi, W; Jiang, J; Sun, K; Ju, Q (2021) ”Aerodynamic performance of semi-submersible floating wind turbine under pitch motion”. In : Sustainable Energy Technologies and Assessments, vol. 48, p. 101556. DOI: 10.1016/j.seta.2021.101556.

[49] Fleming, P, Gebraad, PM.O., Lee, S, van Wingerden, J-W, Johnson, K, Churchfield, M Michalakes, J., Spalart, P., Moriarty, P. (2015). ”Simulation comparison of wake mitigation control strategies for a two-turbine case”. In : Wind Energy, vol. 18, n° 12, p. 2135–2143. DOI: 10.1002/we.1810.

[50] Scott, R., Bossuyt, J., and Cal, R. (2020). “Characterizing tilt effects on wind plants”, J. Renew. Sustain. Ener., 12, 2135–2143, https://doi.org/10.1063/5.0009853.

[51] Cossu, C. (2021). ”Evaluation of tilt control for wind-turbine arrays in the atmospheric boundary layer”. In : Wind Energy Science, vol. 6, n° 3, p. 663–675. DOI: 10.5194/wes-6-663-2021.

[52] Kheirabadi, A C.; Nagamune, R (2021). ”A low-fidelity dynamic wind farm model for simulating time-varying wind conditions and floating platform motion”. In : Ocean Engineering, vol. 234, p. 109313. DOI: 10.1016/j.oceaneng.2021.109313.

[53] Blondel, F., Cathelain, M. (2020). “An alternative form of the super-Gaussian wind turbine wake model”. Wind Energy Science, 5(3), 1225-1236.

[54] Ishihara, T., Qian, G. W. (2018). “A new Gaussian-based analytical wake model for wind turbines considering ambient turbulence intensities and thrust coefficient effects”. Journal of Wind Engineering and Industrial Aerodynamics, 177, 275-292.

[55] Zong, H., Porté-Agel, F. (2020). “A momentum-conserving wake superposition method for wind farm power prediction”. Journal of Fluid Mechanics, 889.

[56] McWilliam, M., Bonfils, N., Dimitrov, N., Dou, S. (2022). “Wind farm parameterization and turbulent wind box generation”. D3.1 Tech Rep. of HIPERWIND H2020 project, Grant Agreement No. 101006689, https://hal-ifp.archives-ouvertes.fr/hal-04033050.

4. Engineering wake model uncertainty

4.1. Presentation of models, methodology, and case studies

4.1.1. Objectives

4.1.2. Methodology

The objective of this task is two-fold. First, the study aims to give a qualitative uncertainty evaluation of engineering wake models (see section 2 for an explanation of this terminology) under specific conditions, such as non-neutral thermal stratification (i.e. atmospheric stability), strong wake interactions, and non-vertical static position of FOWT due to thrust-induced floater pitch. Secondly, the goal is to provide a quantitative uncertainty estimation of engineering wake models with variations of usual wind parameters (mean speed, turbulence, and orientation). This estimation will be provided for the two offshore wind farms. These two case studies are presented in section 1 and detailed in section 4.1.4.

To fulfil the above-mentioned objectives, successive steps have been proposed.

Section 4.2 is dedicated to the first objective, with a comparison between wake simulations with the engineering software FarmShadow™ and the corresponding results obtained with the high-fidelity models Meso-NH and PALM based on an LES framework (see section 4.1.3 and 4.1.3.4 for details on the model settings). As a preliminary study, for validation purposes, a comparison between numerical results and SCADA data from the Teesside wind farm is given first (section 4.2.1.2). As the simulation cost of high-fidelity tools is high, only reduced wind farms will be studied (a few rows are considered, using cyclic conditions on each side of the domain). Then engineering wake models are compared to high-fidelity simulations over cases where they might show limitations. In this way, the effect of different thermal stratifications (stability) on the wake and the strong wake interactions are analysed for the Teesside wind farm (section 4.2.1.3), while the effect of the static position (mean drift and pitch of the floater) on the wake is studied for the floating South Brittany wind farm (section 4.2.2).

The second objective of a quantitative estimation is documented in section 4.3. FarmShadow™ is compared to the DWM coupled with HAWC2, which is more affordable in terms of computational cost than LES simulations and enables the estimation over an exhaustive Design of Experiment (DoE) covering an entire set of ambient wind conditions (see section 4.3.1). The uncertainty estimation is then computed for the Teesside and the South Brittany wind farms (section 4.3.2).

4.1.3. Numerical models

4.1.3.1. FarmShadow™

FarmShadow™ is an engineering steady-state farm wake model developed by IFPEN [57][58], allowing wind farm design and layout optimization. It considers several stationary analytical wake models, based on

wind velocity deficit [59][60][57], added turbulence [61][62], and wake superposition [63]. Different sub-model combinations will be studied in this report (see

Table 9). Velocity deficit and wake-added turbulence induced by upstream rotors are evaluated at every point on the discretized rotor disks. Then, mean velocity and turbulence intensity are computed and used as input for the wake models and rotor operating state (i.e., the power and thrust coefficients are given as a function of wind speed). A blockage correction based on the vortex cylinder flow model is used [64].

4.1.3.2. Meso-NH

Meso-NH is a meteorological model developed by the National Centre of Meteorological Research of Météo France and the laboratory of aerology of French "Centre National de la Recherche Scientifique" (CNRS), using a Large Eddy Simulation (LES) framework [65]. It is based on a non-hydrostatic equation system and uses 1.5-order closure to evaluate the 3D (sub-grid) turbulence. A prognostic equation is used for the sub-grid kinetic energy, and the mixing length is parameterized and dependent on resolution.

Aerodynamic models of a WT have been implemented, such as the Actuator Line model [66]. It enables comparisons and calibrations of engineering wake models. In the present study, this tool will be considered as a reference high-fidelity model, allowing the quantification of engineering wake model uncertainties for different stability conditions [67], and non-vertical floating positions [68]. A simple controller, based on a pitch and omega look-up table, can be used for wind farm simulations: the wind speed averaged over 2sec in an area upstream the wind turbine is used to impose the pitch angle and the rotation speed.

4.1.3.3. DWM-HAWC2

The Dynamic Wake Meandering (DWM) model is an engineering model for dynamic wake simulation developed by DTU. Based on a simplified CFD solver and using the assumption that the wake is advected downwind as a passive tracer (via Taylor's hypothesis), the DWM model provides a computationally efficient solution for carrying out dynamic load simulations with wakes embedded in the input wind fields. The DWM model implementation in DTU's aeroelastic HAWC2 code consists of generating three turbulence boxes [69]: 1) a large turbulence box covering the entire wind farm defines the low-frequency wake meandering paths through the wind farm; 2) a smaller microscale turbulence box that simulates the wake-added turbulence; and 3) a turbulence box representing the ambient wind. Using the simple CFD solver, the static wake deficit is estimated based on the operating conditions of the turbines (defined by two input parameters, rotor speed and blade pitch) and the atmospheric conditions (wind shear and stability). A meandering wake deficit is then simulated by combining the static deficit shape with the microturbulence box, and superimposing this combination on the ambient turbulence box, with the deficit centre location determined by the wake meandering path obtained from low-pass filtering of the farm-wide turbulence box.

As already mentioned in section 2, the DTU implementation of the DWM model remains partly empirical and thus shares with FarmShadow™ wake models the need for fitting against in-situ monitoring data or high-fidelity (LES) data. This also concerns the wake superposition rules, for which [70] indicates that a sum of all deficits is preferable for above rated wind speeds, while a single deficit from the closest WT is preferable for wind speeds below rated.

4.1.3.4. PALM

The Parallelized Large Eddy Simulation Model (PALM) [71] is an LES model developed at the Leibniz Universität Hannover, Germany. PALM uses the Boussinesq approximation to solve the non-hydrostatic, incompressible Navier–Stokes equations, and it parameterizes the subgrid-scale turbulence using a 1.5-order closure [72][73][74].

Wind turbines are represented by an Actuator Disc Model with Rotation (ADM-R) that acts as an axial momentum sink and an angular momentum source (inducing wake rotation) [75]. ADM-R reduces the computational cost when compared to ADL and produces almost the same results [76][77]. In actuator disc models without rotation, the thrust force has a uniform distribution across the disc (e.g. it does not account for the effect of turbine-induced rotation on thrust). This is improved in the ADM-R by including the effect of turbine rotation. In this method, the wind turbine is presented as a disk with several rings and segments. Segments have an equal size which is a function of the grid spacing. At first, the local lift and drag forces per unit area are calculated and then the lift and drag forces are projected onto the axial and tangential planes. The wind turbine module has a controller system of rotational speed [78] (originally valid only for the NREL 5 MW reference turbine). Some of the available parameters of the controller have been adjusted for the Teesside 2.3 MW bottom-fixed wind turbines.

In this study, we used the PALM model to simulate wind turbines in the neutral and stable boundary layer in the benchmark section. We also compared them with analytical models in a stable boundary layer and a crosswind case.

4.1.4. Case studies

As mentioned before, the global idea of this section is to study the uncertainties of engineering wake models. Therefore, it is proposed to explore these uncertainties for two very different offshore wind farms with two distinct technologies.

4.1.4.1. Teesside fixed offshore wind farm

The Teesside wind farm, as presented in Figure 24, is located in the northern sea, 1.5 km apart from the Northeast England coast, near the town of Redcar. It has an installed capacity of 62MW with 27 bottom fixed (monopiles) WT deployed in three rows of 9 WTs with an NW-SE orientation (Figure 24 right). The rows have a separation of around 6.2 diameters (D=93m), while the turbines within each row are 3.5D apart.

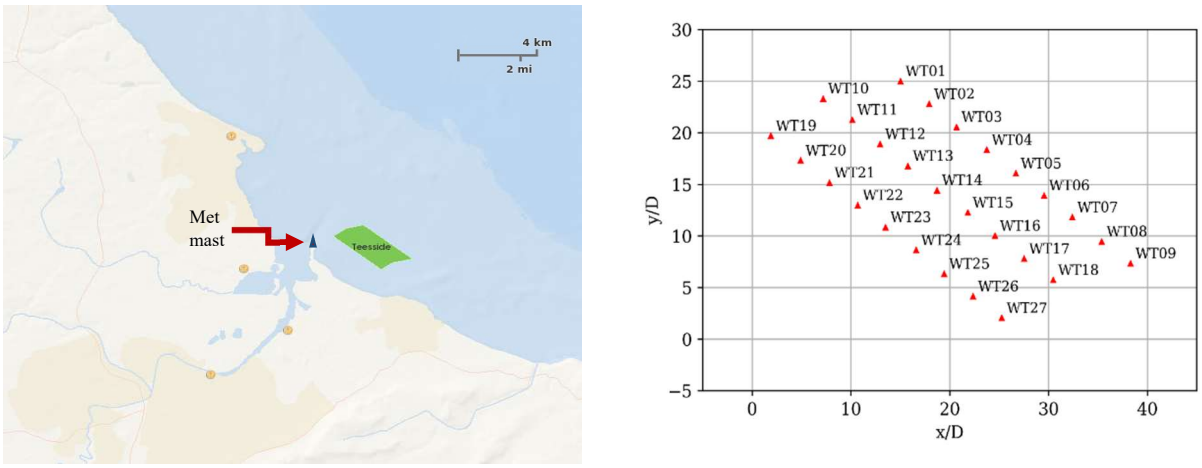

Figure 24. Teesside wind farm and met mast location (left) and layout (right).

Numerical models of the Siemens SWT 2.3MW for ASHE software have been built and validated during the first work package of HIPERWIND. Nevertheless, it was necessary to generate the numerical model of the WT for LES / AL simulations. This was done during a preliminary study, where a benchmark with DLW has been done, regarding aerodynamic loads along the rigid blade for a constant laminar flow.

4.1.4.2. South Brittany, floating offshore wind farm

The other wind farm selected for this project is a theoretical case study located offshore of South Brittany, France. A French tender plan is ongoing, to install a wind farm with a total capacity of 270 MW in the same area (Figure 25, left picture). This future wind farm is scheduled to be operational by 2029 and will be composed of FOWT with a total capacity of 270 MW. Figure 25 right picture presents the layout of our theoretical case study.

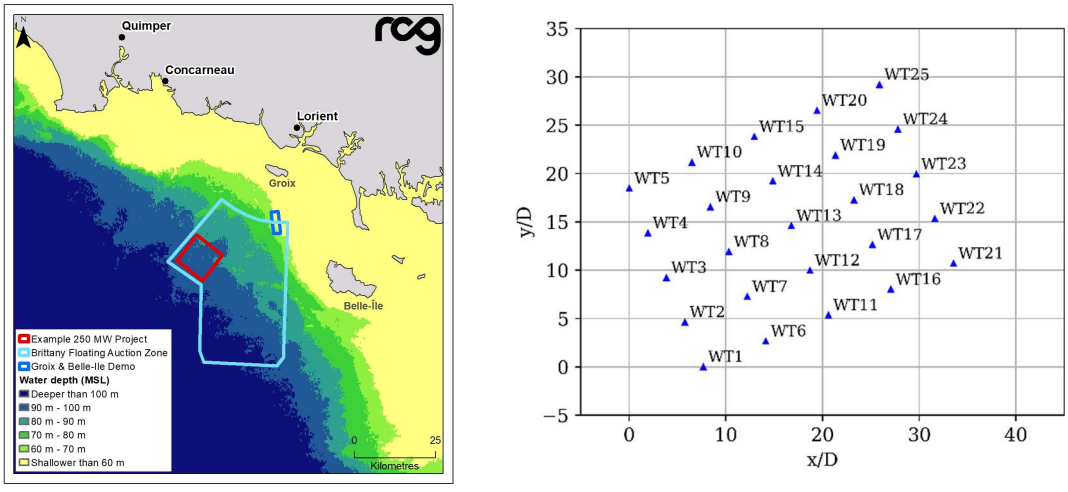

Figure 25. South Brittany wind farm location (left) and proposed layout (right).

The theoretical wind farm considered is composed of 25 IEA15MW WT on UMaine semi-submersible floaters. The turbines are arranged in 5 WSW-ENE rows with an inter-turbine distance of 7D along the dominant wind direction (WSW-ENE) and 5D along the orthogonal direction (crosswind). These values are close to the average 7.5D and 5.9D of 27 European Offshore Wind Farm indicated in [79]. The shorter distance in the crosswind direction is, however, still larger than that of existing farms like Lillgrund in Sweden (3.3*D*) or that of the previous case study of Teesside (3.5*D*).

These large turbines have a nacelle height of 145 m and a diameter of D=240 m. The choice of a regular layout with an alignment along the dominant wind direction might be not optimal for AEP. A different layout could have been chosen, for instance with an offset of one row of WT over two in the direction orthogonal to the dominant wind (e.g. offset of WT10 to WT6 and WT20 to WT16 in the WNW-ESE direction), to reduce as much as possible wake effects, both for production and fatigue. For the sake of simplicity, the choice illustrated in Figure 5 has been preferred to reduce the cost of LES computations (by the usage of symmetry) and enhance wake interactions. Similar wind farms have been built, to respect other constraints such as navigation axes.

As for Teesside, this large WT needed to be implemented and validated in Meso-NH. Therefore, an analogous preliminary study, over a simple case, was performed to compare the results against the one obtained with the ASHE solver DLW the model built during WP1.

4.2. Estimation with LES reference for a selection of wind conditions

4.2.1. Teesside case

4.2.1.1. Ambient wind conditions

To define which cases were more suitable to simulate using the LES approach, an exploratory analysis of the ambient wind conditions was first performed. On Teesside, there is a met mast installed onshore close to the wind farm. This mast is placed on a thin peninsula 2 km from the park (Figure 24). Some relevant variables reported by this met mast were used to analyse and describe the site-specific behaviour, especially the ambient wind conditions that most affect the development and evolution of a wake (such as wind speed and direction, turbulence intensity, and atmospheric stability).

Figure 26 shows the wind rose built with four years of ten-minute measurements taken at 50 meters height. It can be observed that the most frequently occurring wind directions are from the SW, with most of the measurements concentrated around a main wind direction of 225°.

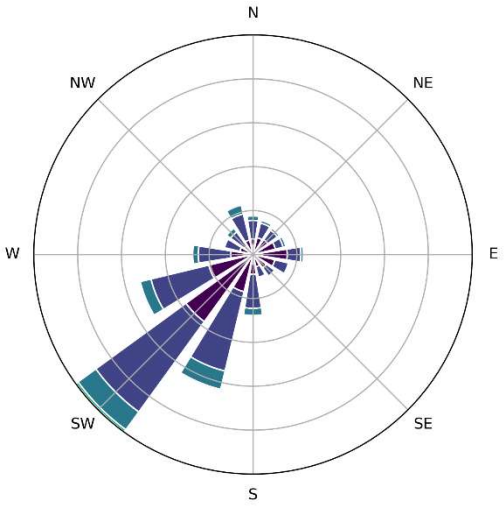

Figure 26. The wind rose of Teesside. The values are not shown for confidentiality purposes.

Another relevant ambient wind parameter for wake analysis is stability [80]. Atmospheric stability is a measure of the tendency of the atmosphere to enhance or inhibit vertical movements. The stability in the lowest layer of the atmospheric boundary layer (ABL) is largely due to thermal vertical gradients (static stability) and friction induced by wind shear (dynamic stability).

There are different methods or parameters to characterize atmospheric stability, which incorporate a greater or lesser number of variables and atmospheric processes [81]. The most widely used method to describe atmospheric turbulence in the surface layer is the one based on the Monin-Obukhov Similarity Theory (MOST). This theory introduces the dimensionless stability parameter ζ, defined as the ratio between the reference height above ground z and the length of Monin-Obukhov L:

$$\zeta = \frac{z}{L} = \frac{zg\kappa\overline{(w'\theta'_v)_s}}{\overline{\theta'_v}u_*{}^3}$$

where g is the gravity acceleration, κ is the Von Karman constant, $\overline{(w'\theta'_v)}_s$ is the vertical turbulent flux of the virtual potential temperature in the surface layer, $\overline{\theta'_v}$ is the virtual potential temperature of the mean flux and, u_* is the friction velocity. A more complete definition of L can be found in [82].

Most wind farms do not have meteorological masts with the necessary instruments to quantify the turbulent fluxes of heat and momentum. They usually have, in the best case, wind sensors (usually cup anemometers) and thermometers at different heights. Therefore, an alternative to characterize stability is through the bulk Richardson number (Rib) [82], which is obtained by approximating local gradients with observations made at discrete heights. This dimensionless parameter allows determining the stability from the relationship between the production or consumption of turbulence due to buoyancy and the production due to shear driven by the surface. Following [83], Rib can be estimated by

$$Rib = \frac{gz\Delta\theta}{\theta_0\overline{u}^2}$$

where z is taken as the mean height between the two heights of temperature measurement, and both are assumed to fall within the surface layer. $\Delta\theta$ and Rib are derived from air to surface (or the closest level to

the surface, θ_0) temperature difference, and the mean wind speed at the upper measurement height. As with L, Rib negative values will indicate unstable environments, positive values will be associated with stable stratifications and values close to zero will be related to neutral conditions. Based on [84], a five-class stability classification methodology is defined in [85]. This classification is presented in Table 4.

Table 4. Classification of atmospheric stability [84].

Stability classification	***Rib***
Very Unstable	$Rib < -0.023$
Unstable	$-0.023 \leq Rib < -0.0036$
Neutral	$-0.0036 < Rib < 0.0072$
Stable	$0.0072 \leq Rib < 0.084$
Very Stable	$Rib \geq 0.084$

To characterize the stability at Teesside, the met mast 10-min averaged observations of wind speed and temperature at 50m have been used in conjunction with 10m air temperature to estimate Rib.

Figure 27 presents the Rib frequency distribution, following the classification given in Table 4. It can be observed that most of the values are concentrated around zero indicating a higher occurrence frequency of neutral conditions. This is illustrated in the pie chart on the right, where it is shown that more than half of the time is dominated by neutral conditions, followed by a greater number of cases with stable stratifications with a percentage of occurrence of around 30% and finally the unstable conditions account for only about 10% of cases.

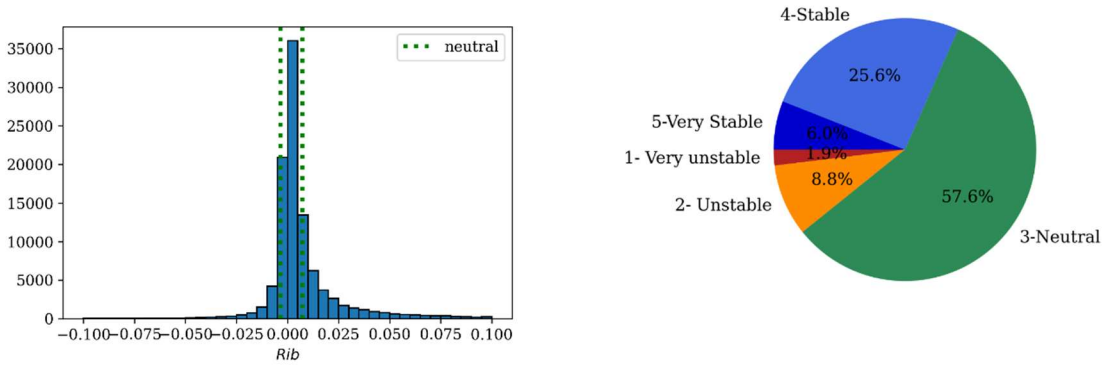

Figure 27: Rib frequency distribution Teesside (left) and occurrence percentage of each of the five stability regimes

Then, a statistical analysis of the behaviour of the different stability regimes estimated through the Rib value resulting from the measurements has been done. Figure 28 shows the frequency of occurrence of the different stability regimes for the different hours of the day, the different months of the year, and according to different wind speeds in height (50m).

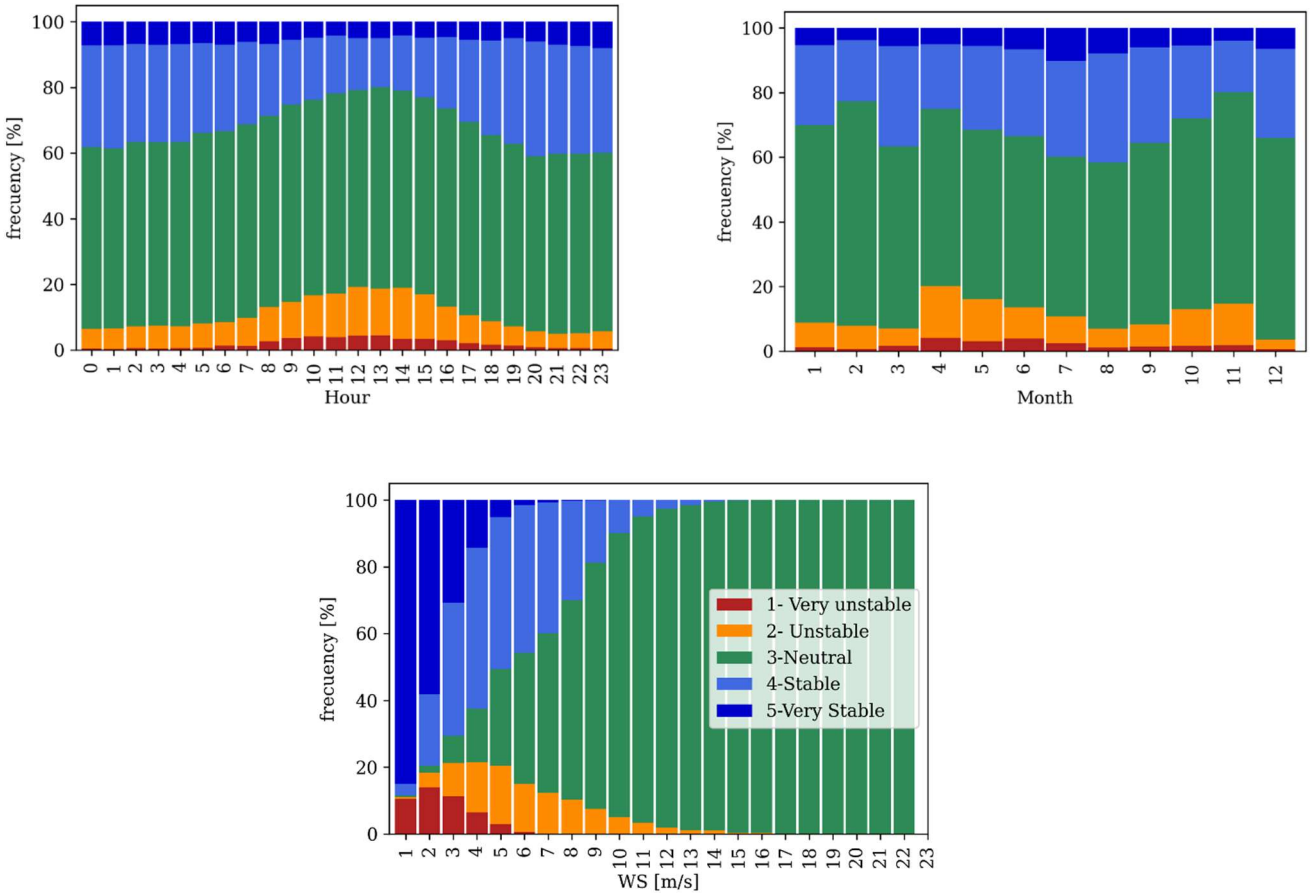

Figure 28. Frequency of occurrence of the different stability classes based on the Rib estimated from the observations. Per hour (top), per month (middle), and wind speed at 50 m height (bottom).

When analysing Figure 28, a marked diurnal cycle is observable with a predominance of neutral and stable conditions during the night and an increase in the frequency of unstable regimes during daytime hours. Regarding the variation throughout the year (Figure 28 centre), no clear intra-annual variation is observed. However, a notable reduction of unstable conditions is shown in the winter months. Concerning the distribution of frequencies for different mean wind speeds at 50m height (figure at the bottom), a marked increase in the neutral conditions with the intensity of the wind can be observed, evidencing that the mechanical production of turbulence is governing over the thermal production under high wind speed conditions. Likewise, for wind speeds between 4 and 6 m/s, the five stability conditions can occur.

4.2.1.2. Benchmark

As a first attempt to explore the capabilities of the LES model on the Teesside wind farm, a comparison between Meso-NH (coupled with the actuator line model), PALM (coupled with the actuator disc model), and SCADA data was proposed. The main idea was to compare the power outputs of both sources for different cases. Considering the study of the ambient wind conditions, it was decided to compare the model against the measurements for three different wind speeds and under neutral stability conditions, considering the most frequent ones. Regarding the wind speed, below rated, near-rated, and above rated wind speed conditions were proposed to explore different operational conditions of the WT over different regimes.

Figure 29 shows the power and the rotational speed curves for the Siemens SWT 2.3MW WT and the 3 selected wind speeds. It is important to mention that according to the wind speed, the WT controller will modify the blade pitch. Nevertheless, as we don't have the real but a generic version of the controller, we simply enforce in this section blade pitch and rotational velocity from a priori knowledge of the mean wind properties

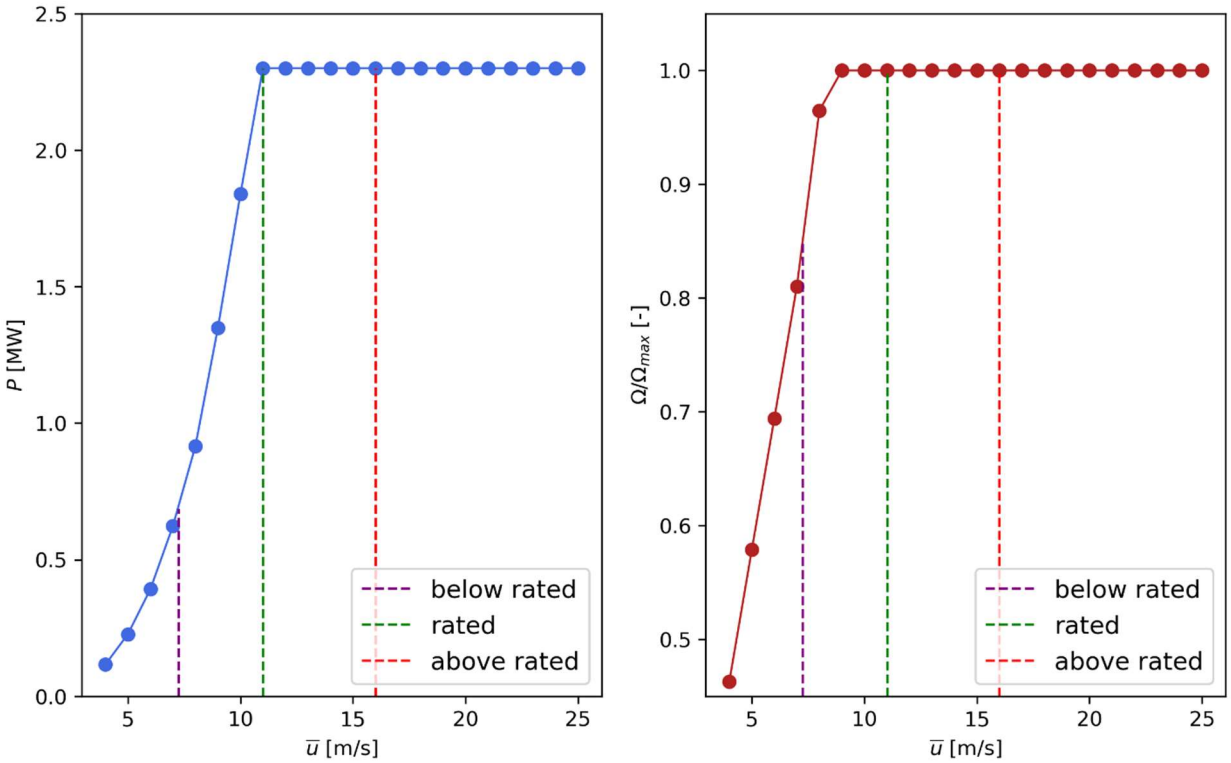

Figure 29. Power and rotational speed curve for Teesside WT.

The idea, for this first benchmark, was to study and compare the power outputs of an upstream WT, for a specific wind direction to avoid any wake interactions. The chosen wind direction is the most frequent one (see wind rose in Figure 26), to be able to collect enough data. Therefore, WT number 23 and a wind direction of 235° are selected, as shown in Figure 30. In the following work (detailed in section 4.2.1.3), this wind direction will be studied as it also leads to an important power deficit due to the alignment of the WT.

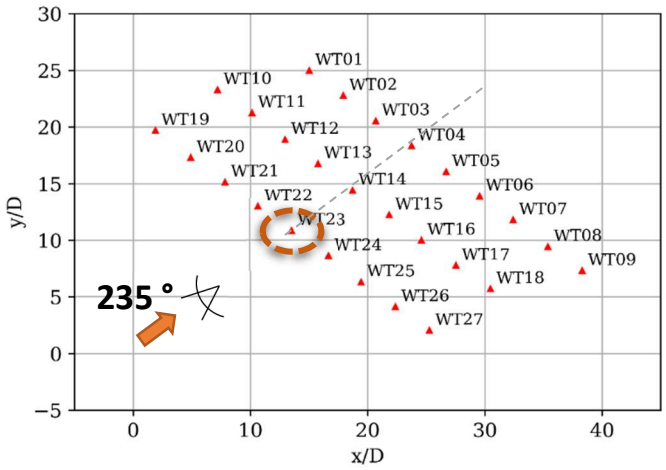

Figure 30. The layout of the Teesside wind farm. The distances are normalized by the rotor diameter D. The orange circle indicates the selected WT for the benchmark, and the orange arrow indicates the main wind direction selected.

To simulate these 3 cases the Meso-NH and PALM models under their LES framework were used, Meso-NH being coupled with the actuator line method [66] and PALM coupled with the actuator disk with rotation method.

4.2.1.2.1 Meso-NH configuration

The numerical parameters of the Meso-NH model configuration for all Teesside simulations can be found in Table 5. The horizontal and initial vertical resolution of 2.5 m was selected, leading to approximately 40 grid cells per rotor diameter, as proposed in [86]. According to the localization (shown in Figure 24), the wind is coming from the land. After a sensitivity analysis, a 0.005 m roughness length (z_0) was selected. It allows obtaining the measured turbulent intensities and corresponds to topography in between a grassland and an open sea. This simplistic choice is due to the limitations induced by the cyclic conditions of the domain. The internal boundary layer of the coastline is therefore neglected, introducing some uncertainty. To simulate a neutral boundary layer, the 3D field is initialized with a constant temperature profile (283K), considering an inversion layer at 800m. A dry ABL is considered. The time step of the precursor simulation only needs to fulfil the CFL criteria of the LES model. When the wind turbine is introduced, the time step has to be reduced: it is important, for the AL, to ensure that the blade tip does not pass through more than one grid cell. This constrain becomes stronger when using the AL of Meso-NH: a sensitivity analysis showed that a blade element has to spend several time steps in the same grid cell to avoid overestimations on the aerodynamic loads.

Table 5. Meso-NH model configuration for Teesside.

Domain size	L_x = 6 km, L_y = 1 km and L_z = 900 m
Horizontal resolution	2.5 m
Vertical resolution	2.5 m up to 200 m, and then an 8% vertical stretching until 20 m resolution is reached
Time steps	0.2 s for precursor and then 0.004 s for the simulation with the WT

Boundary conditions	Cyclic
Roughness length	$z_0 = 0.005$ m
Tip loss correction	Activated
Controller	Prescribed blade pitch imposed according to the mean wind speed
Nacelle and tower	Not considered

To achieve the desired ambient wind conditions that fit the averaged measurements for the 3 wind speed cases, first precursor Meso-NH simulations without considering the presence of the WT were performed. The precursor simulation is initiated with constant geostrophic wind and a roughness length mentioned before. After a 12-hour long simulation (physical time), the logarithmic wind profile is obtained. The obtention of the desired ambient wind conditions (wind speed, wind direction, turbulent intensity) at a certain height (hub height) is not trivial. Particular attention must be paid to define correctly the geostrophic wind (magnitude and direction) and the roughness length through an iterative procedure.

The results of both the precursor simulations and the following simulations considering the presence of the WT are detailed in the next subsections for each wind speed.

4.2.1.2.2 PALM configuration

The PALM version 21.10 revision r4901 was used in this report. Simulations are performed in two parts: (1) the precursor run: to prepare steady-state inflow profiles for the main simulations (to save computational time); and (2) the main run.

For some precursor simulations, we employed cyclic boundary conditions in both lateral directions. The grid size for the precursor runs is much smaller than the main domain (see Table 6 and Table 7). Table 6 shows the PALM model configurations for precursor simulations and the wind speed and turbulence intensity at the end of simulations. The simulations were done in a neutral boundary layer with a constant potential temperature profile of 283K and a constant humidity profile (vapour mixing ratio of 9.60E-3). We neglect Coriolis force so then there are no changes in the profiles of wind direction. A roughness length of z_0 = 0.005 m was set for all cases. We aligned the mean flow direction in the x direction.

Two domains were defined for the main simulations with horizontal and vertical grid resolutions of 10 m and 5 m. The atmospheric condition is set to neutral, like precursor run with a constant potential temperature and humidity profiles. The implemented 2.3 MW wind turbine is located at x=*750* m and y=*480* m in domain 2. The control system for the wind turbine is off in all simulations: a prescribed blade pitch and rotation speed are imposed according to the mean wind speed. Some configurations used in the main simulations are listed in Table 7.

Table 6. Configurations used in precursor simulations and wind speed (WSPD) and turbulence intensity (TI) at the end of precursor runs for benchmark simulations.

Case name	Grid size (m)	Simulation length (s)	Grid resolution (m)	WSPD at hub (m/s)	TI at hub (%)
Unrated	640×640×1600	90000	10	7.70	7.37
Rated	640×640×1600	90000	10	11.58	7.74
Above rated	640×640×1600	90000	10	15.61	7.04

Table 7. PALM Configurations used for the main simulations of benchmark cases.

Case name	Grid size (m)	Simulation length (s)	WT rot speed [rad/s]	Blade Pitch [rad]
Unrated	6000×960×960	3600	-1.6	0.017
Rated	6000×960×960	3600	-1.67	-0.013
Above rated	6000×960×960	3600	-1.67	-0.19

4.2.1.2.3 Below rated speed

For this case, a wind speed at hub height between 7 m/s and 8 m/s was targeted. Figure 31 shows the 10-min averaged wind speed ($\bar{u}$), axial turbulence intensity (I_u), and wind direction (θ_{wind}) vertical profiles for the last 10 minutes period of the precursor simulation. It can be observed in this figure that the simulation results match in fairly good agreement with the measurement, evidencing that the desired ambient wind conditions were obtained. In this figure, it can also be seen that the wind profile converged to a logarithmic neutral profile. One can note that the precursor of PALM and Meso-NH provide similar results. Nevertheless, a difference in turbulence intensity can be noticed near the ground. The wind direction profiles indicate different behaviours, as the Coriolis effect is taken into account in Meso-NH simulations, but not in PALM simulations.

For the measurements, a filtering process over the combined sets of met mats observations and SCADA data was necessary and its procedure is described hereinafter. First, the following conditions were applied on the met mast observation (at 50 m height) to filter the data:

- $\theta_{wind} = 235° \pm 0.5°$
- $\bar{u}_{50m} = 7.5 \pm 0.5$ m/s
- Neutral stability condition

After the filtering procedure, the remaining values were used to compute the averaged measurements presented in red in Figure 31. In this figure, the values of wind speed and I_u are normalized by their most frequent values (ref) for confidential reasons.

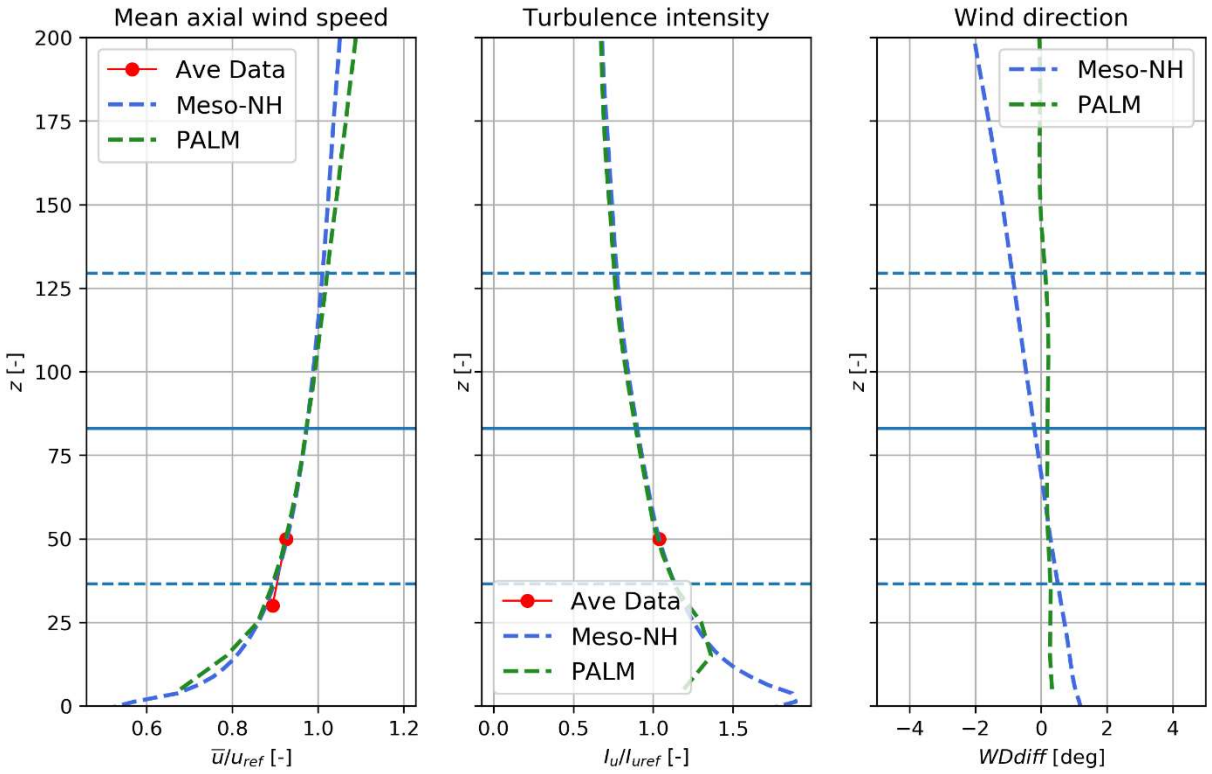

Figure 31. Wind speed, turbulence intensity, and wind direction vertical profiles for the below rated conditions. Horizontal blue lines indicate hub height and rotor tip heights. Averaged measurements (Ave Data) are presented in red.

Following the precursor simulation, a second simulation is performed, introducing the WT. This simulation is run for a physical time of 12 minutes. The first two minutes are considered as the initialisation period to establish the wake (approximately 30 rotations of the rotor), while the remaining 10 minutes are used to compute the averages presented in Figure 32 and Figure 33.

In Figure 32 the wake of the wind turbine can be observed. As the nacelle is not modelled, an overestimated Venturi effect can be noticed in the middle of the wake, close to the wind turbine. In Figure 33 the averaged power output obtained from the simulation is compared to the SCADA data. For the filtered SCADA dataset, plenty of possible values of wind speed at hub height can be observed. All these values and their corresponding power outputs are presented in the plot (black dots), as well as the power resulting from the simulation with Meso-NH (blue star), and PALM (green star). An efficiency of 0.95 has been assumed to compute the electrical power from the aerodynamic power in the numerical model, as defined in WP1 of HIPERWIND. It is possible to see in Figure 33 that the simulated power presents a good agreement with the measurements, as it follows their tendency, and stands in the middle of the cloud of points.

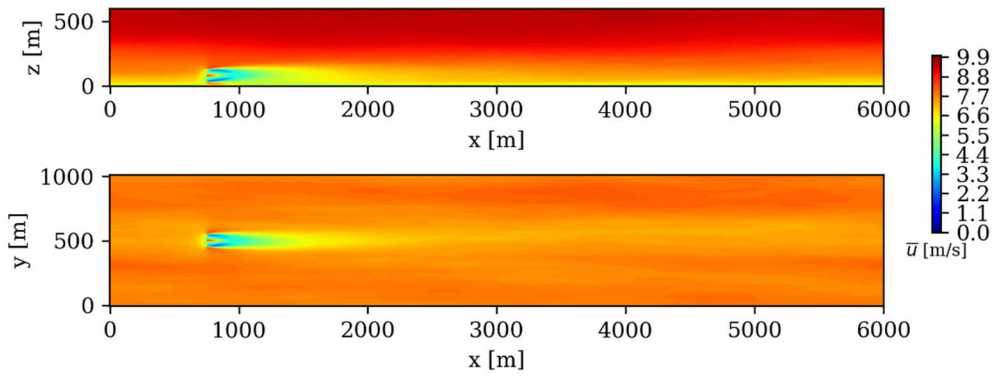

Figure 32. Vertical and horizontal cuts of wind speed obtained with Meso-NH at hub position for below rated conditions.

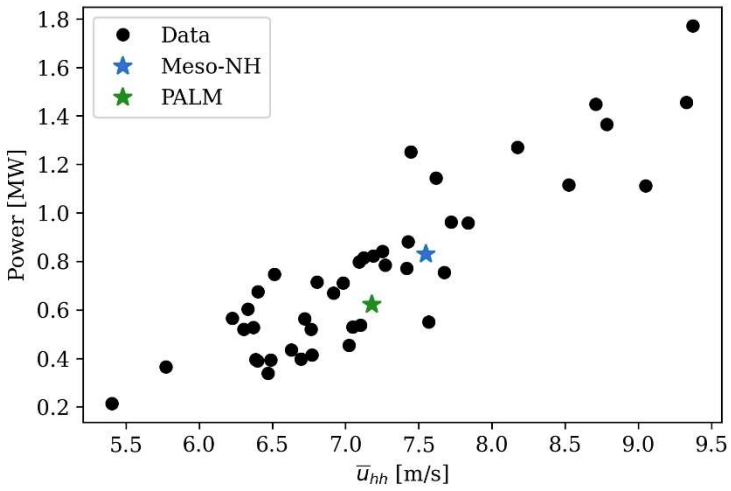

Figure 33. Electrical Power reported (black dots) and simulated (blue star) vs wind speed at hub height for conditions below rated.

4.2.1.2.4 At rated speed

Analogous to what was done in the below rated case, Figure 34, Figure 35, and Figure 36 present the profiles used as initial conditions, the average wake resulting from the simulation with the WT, and its estimated average power for the rated mean wind speed case. For this case, a mean wind speed of about 11 m/s was desired.

Figure 34 shows again a good agreement between the precursor simulation and the averaged and filtered measurements. Concerning the wind direction differences (right plot), a deviation of 2° can be observed at hub height for Meso-NH. This deviation might explainedthe slight deflection of the wake observed in Figure 35. This is due to the difficulty of the methodology mentioned earlier to obtain the desired ambient wind conditions (balance between the Coriolis effect and the rugosity). However, this small deviation is

supposed to have a negligible impact on the power output. As shown in Figure 36, the estimated power is again, for both LES models, in good correlation with the SCADA data.

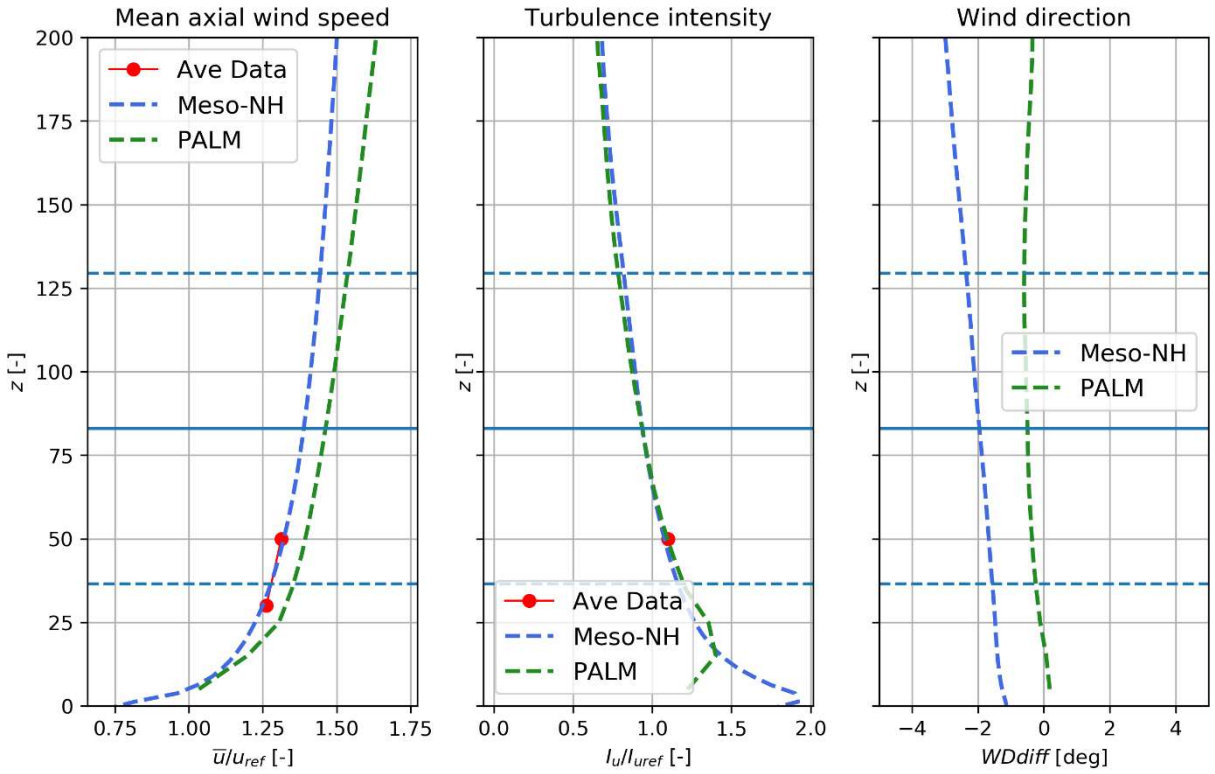

Figure 34. Wind speed, turbulence intensity, and wind direction vertical profiles for the rated case. Horizontal blue lines indicate hub height and rotor tip heights. Averaged measurements (Ave Data) are presented in red

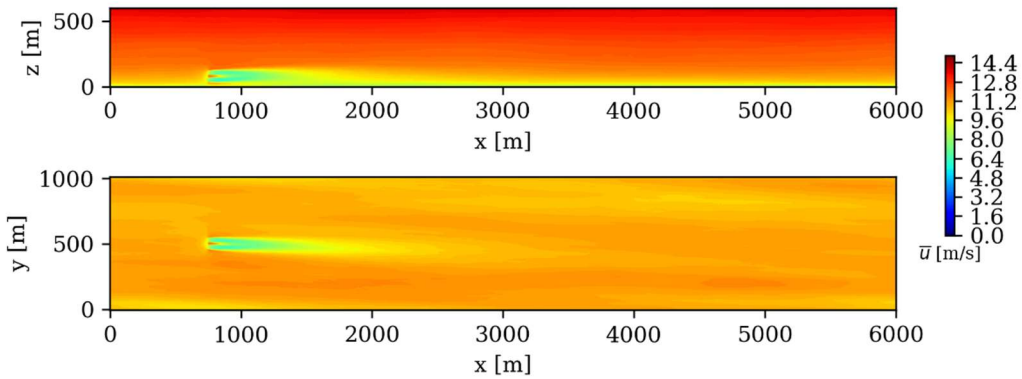

Figure 35. Vertical and horizontal cuts of wind speed obtained with Meso-NH at hub position for rated conditions.

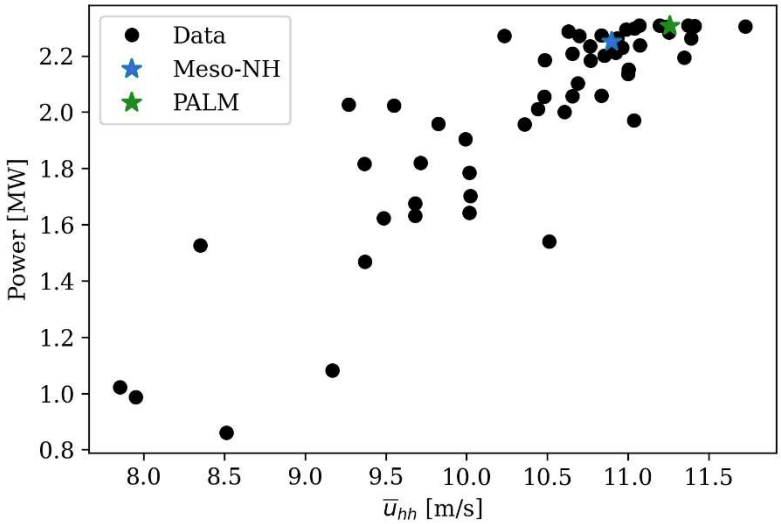

Figure 36. Electrical Power reported (black dots) and simulated (blue star) vs wind speed at hub height for below rated conditions

4.2.1.2.5 Above rated speed

As for the below rated and rated conditions, the results of the above rated case are presented in Figure 37, Figure 38, and Figure 39. As for the former cases, the initial conditions prescribed are fitting well with the filtered measurements. In Figure 38, the mean wake seems to be weaker and shorter than the one in previous cases. This is related to the reduction in thrust force due to pitch actuation for the above rated conditions (see thrust curves in [87])). In the power estimated by the models (Figure 39), a small overestimation can be observed when compared to the measurements. This might be due to the usage of a prescribed and constant blade pitch in the simulation, while active pitch control is used in real data, following wind speed fluctuations, and ensuring that the nominal power is not exceeded.

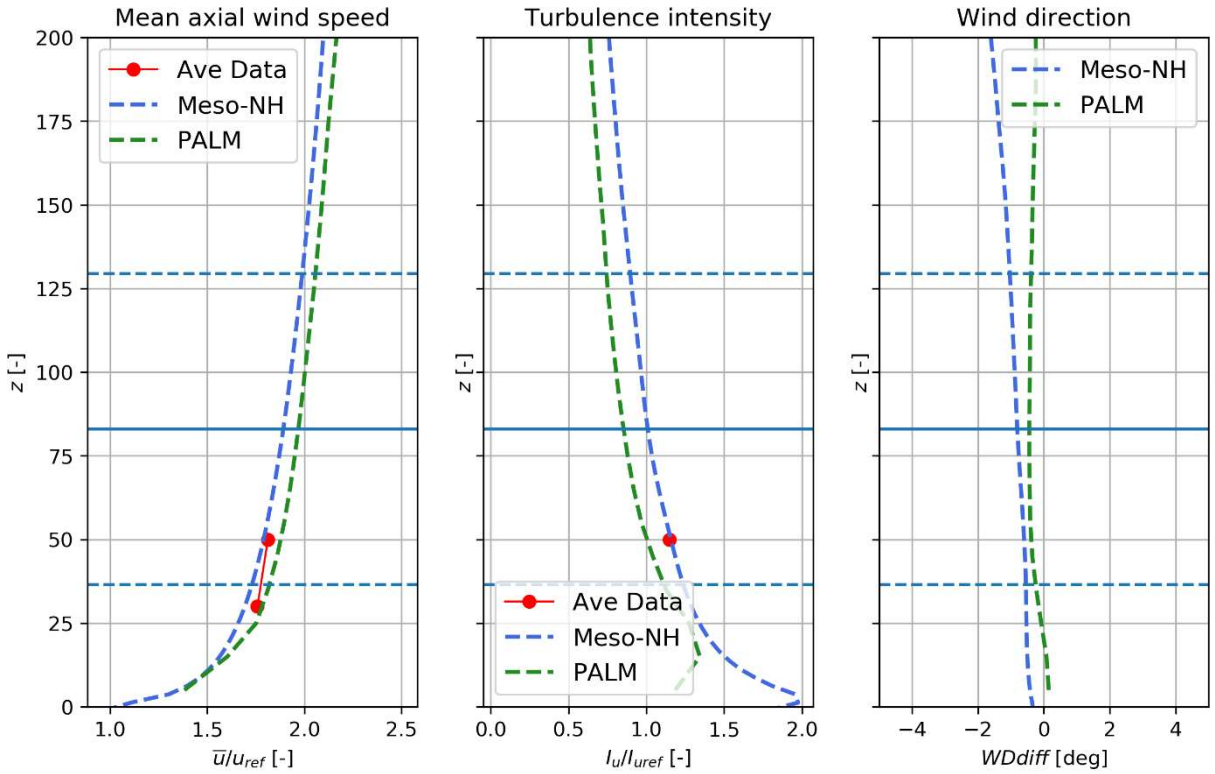

Figure 37. Wind speed, turbulence intensity, and wind direction vertical profiles for the above rated case. Horizontal blue lines indicate hub height and rotor tip heights. Averaged measurements (Ave Data) are presented in red, while the logarithmic wind profile is shown with a grey dashed line.

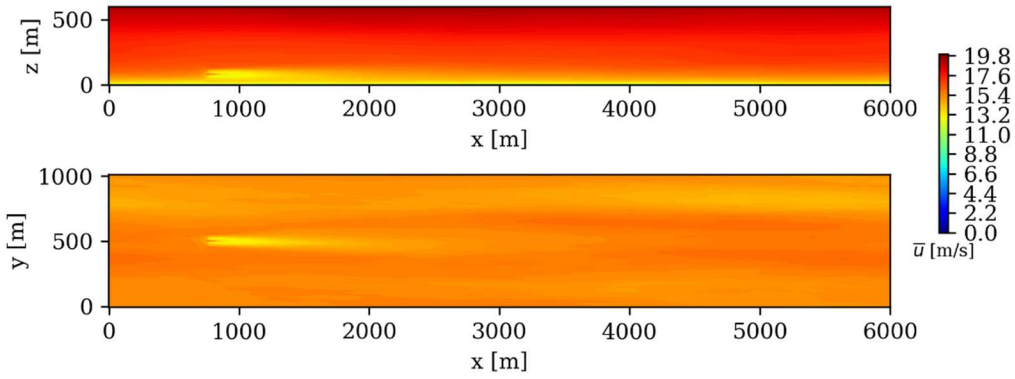

Figure 38. Vertical and horizontal cuts of wind speed obtained with Meso-NH at hub position for the above rated case.

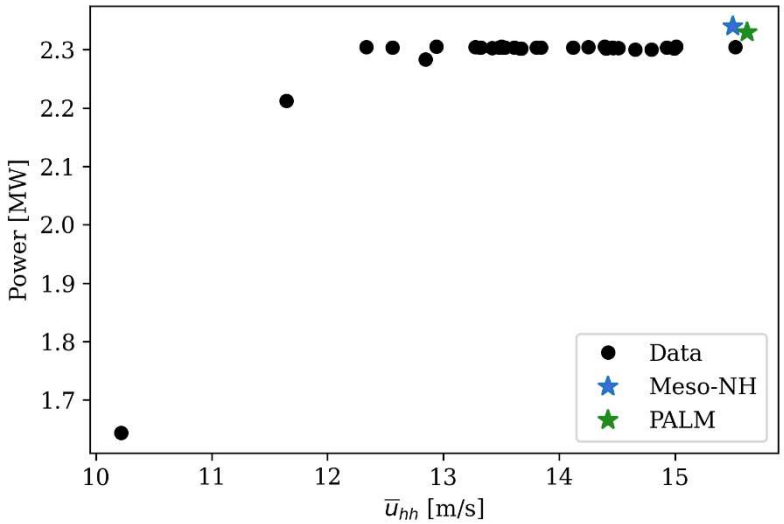

Figure 39. Electrical Power reported (black dots) and simulated (blue star) vs wind speed at hub height for the above rated case.

In the end, the benchmark shows fairly good agreements between wind farm real data (combining met mast and SCADA data) and numerical simulations, using Meso-NH and PALM. This first step was important and allows us to go further in the complexity, to investigate specific phenomena such as non-neutral conditions and non-vertical floating positions for several WT. Completing this comparison with wind speed and TI profile would have been of interest to complete the check on the model alignment but could not be done by lack of time. This comparison will be addressed in future work.

4.2.1.3. Comparisons between the analytical wake model and LES

Once the validation benchmark was done, it is proposed to do a qualitative evaluation of the uncertainties of different wake engineering models for different atmospheric stability conditions, considering the Meso-NH and PALM LES models as references. The latter allows getting a complete 3D field of variables (such as wind speed fields within the wake), that are not available in the measurements.

It can be observed in Figure 28 that the possibility of the occurrence of any atmospheric stability condition is higher for low wind speed situations, consistent with [88] and [103]. Therefore, for these comparison analyses, it is proposed to work with very low wind speeds, around 5 m/s at hub height.

In these cases, the wake development for the 3 WT alignment condition presented in Figure 30 is studied for two different atmospheric stabilities, neutral and unstable. The main ambient wind conditions for both cases are listed in Table 8. With the aim of following industrial standards, we decided to use the power law function as an approximation for the wind speed profile. To this end, the wind shear exponent at hub height, α_h, was estimated using a fit to a power law curve: $u(z) = u_h \left(\frac{z}{z_h}\right)^{\alpha_h}$ [88] on the area of the rotor, where "h" index indicates the quantity computed at the hub height. Note that another choice, like the logarithmic profile, could be chosen for better representativeness of the wind conditions.

Table 8. Ambient wind conditions for the 3 WT simulations.

Cases	$\bar{u}_h$ [m/s]	I_{u_h} [%]	θ_h [°]	α_h	Surface heating (SH)
Neutral	4.8	7.5	235	0.095	0 W/m2
Stable	5.7	10.9	235	0.669	-15K/h
Unstable	5.2	10.1	235	0.021	30 W/m2

The methodology explained before, using a precursor simulation to obtain the desired ambient wind condition is applied.

To perform the analytical wake model simulations, the FarmShadow™ code introduced in section 4.1.3.1 was used. The idea was to compare different wake models with different levels of complexity with the high-fidelity LES simulation. The different configurations are listed in Table 9. Note that Qian [63] was developed for the wake downwind of only 1 WT. More generally, in the analytical models known in the literature, the turbulence superposition in the case of multiple wakes at the same location is not established and validated. Following [89], based on [90], when considering at a given location multiple wakes produced by upwind turbines, only the wake which has the most significant impact is considered for the added turbulence intensity. As there is no controller in FarmShadow™, we use a look-up table, giving the Cp/Ct coefficients as a function of the wind speed (see Figure 26 of [92]).

Table 9. Analytical wake model configurations.

Simulations	Wake deficit	Wake superposition method	Wake-added turbulence	Blockage
1	Jensen [59][60]	Local linear [61][62]	Qian [63]	Vortex cylinder [64]
2	Gaussian [91]	Local linear [61][62]	Qian [63]	Vortex cylinder [64]
3	Super Gaussian [57]	Local linear [61][62]	Qian [63]	Vortex cylinder [64]
4	Super Gaussian [57]	Bastankhah [61]	Qian [63]	Vortex cylinder [64]

4.2.1.3.1 Neutral case

Table 10. Meso-NH model configuration for the Teesside wind farm.

Domain size	$L_x = 6$ km, $L_y = 1$ km and $L_z = 900$ m
Horizontal resolution	2.5 m
Vertical resolution	2.5 m up to 200 m, and then an 8% vertical stretching until 20 m resolution is reached
Time steps	0.2 s for precursor and then 0.008 s for the simulation with the WT
Boundary conditions	Cyclic
Roughness length	$z_0 = 0.005$ m
Tip loss correction	Activated
Controller	Based on a look-up table, providing blade pitch and rotation speed as a function of wind speed.
Nacelle and tower	Not considered

The model configuration for this case is similar to the one used for the single WT simulations and provided in Table 10. In this domain, 3 parallel rows of WT were simulated, as illustrated in the horizontal mean wind field, given in Figure 41. The usage of boundary conditions on the lateral side of the domain makes it possible to consider an infinite wind farm (laterally), allowing lateral wake interactions and blockage effects of the wind farm. As the aim is to study the row in the middle of the wind farm (as shown in Figure 30), it is a way to reduce the computational cost by simulating only a part of the wind farm.

After 12 hours of precursor simulation, the profiles are illustrated in Figure 40. The vertical profile on the left indicates the wind speed averaged over the last 10 minutes of the precursor simulation. A typical "power law" shape can be observed for such neutral conditions. The fit to the power law has been applied (considering the same wind speed at hub height and $z_0 = 0.005$ m): it provides a power law exponent about $\alpha = 0.095$. This value will be used later as input for analytical wake models. The turbulence intensity profile shows a regular shape for neutral conditions, with low turbulence intensities in the upper part of the ABL, which increases closer to the surface because of the friction of the ground. An important change of direction of the wind is indicated in the right profile. As the Coriolis effect is considered in Meso-NH, the neutral condition produces the Ekman spiral: a variation around 2.5° can be observed over the rotor.

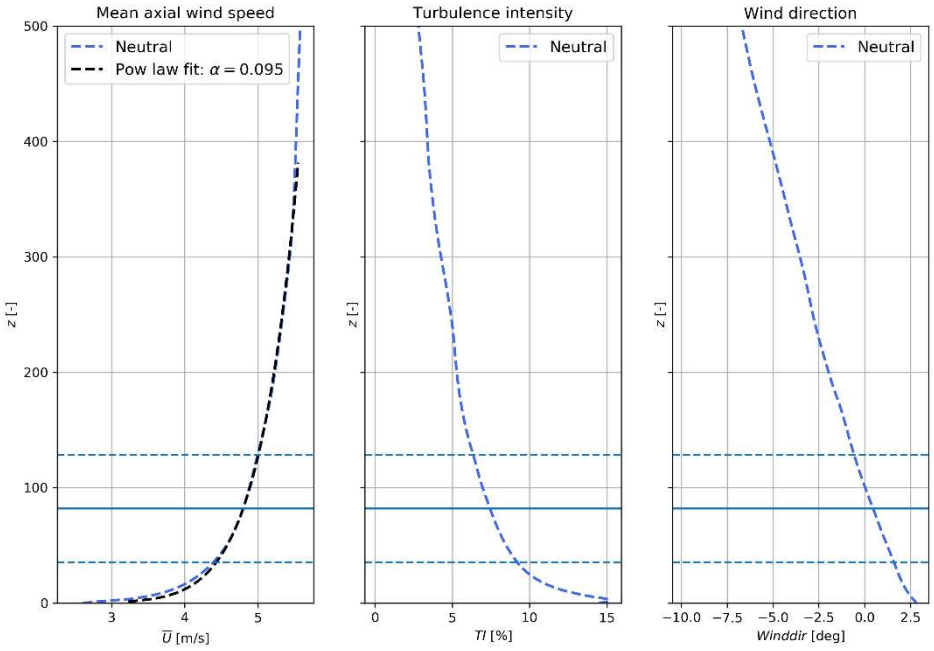

Figure 40. Wind speed, turbulence intensity, and wind direction vertical profiles for the neutral case obtained after the precursor. Hub height and rotor top/bottom are indicated by solid and dashed horizontal lines, respectively.

Then, wind turbines have been introduced. An initialisation of 14min has been considered to let the establishment of the wake. In the end, the results are analysed over the next 10min. Because of the simulation time length, the domain size, and the cyclic conditions, a weak signal of wake re-entering in the domain is observable, but the consequence in the wake analysis is neglectable. For these simulations, a simple controller is used to enforce blade pitch and rotation speed. The controller is based on a look-up table from data provided in WP1. The configuration of these simulations is provided in Table 10.

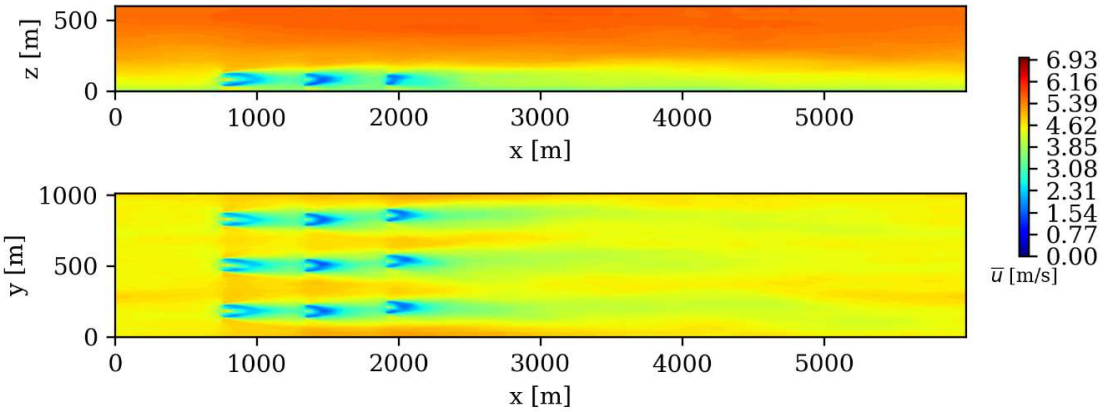

Figure 41. Vertical and horizontal cuts of mean wind speed at the middle row position and at hub height, respectively.

The objective was to explore the behaviour of the different models (listed in

Table 9) several diameters downstream of the first WT. To do so, vertical, and horizontal profiles of wind speed and turbulence intensity every 2D downstream were extracted from the different simulations. The positions of the different profiles are presented in Figure 42, while their results for wind speed are shown in Figure 43 and Figure 44. In these plots, a generally good agreement can be noticed between the analytical wake model and LES results concerning the wind speed: both the amplitude and the width of the wake deficit are, overall, well evaluated. Analytical wake models fail at estimating the bi-modal shape at the very near wake (2D), but they are not intended to. The wakes predicted by LES seem to be slightly larger. Surprisingly, in the horizontal profiles, it is possible to note that, in the far wake, the deficit tends to triangular shapes (12D and 18D) for LES results. As mentioned before, the wind speed profile imposed in the analytical wake model is fitted from the last moment of the LES precursor simulation. Nevertheless, in the vertical profiles, one can note that the wind speed in the upper part of the ABL is lower for LES simulations.

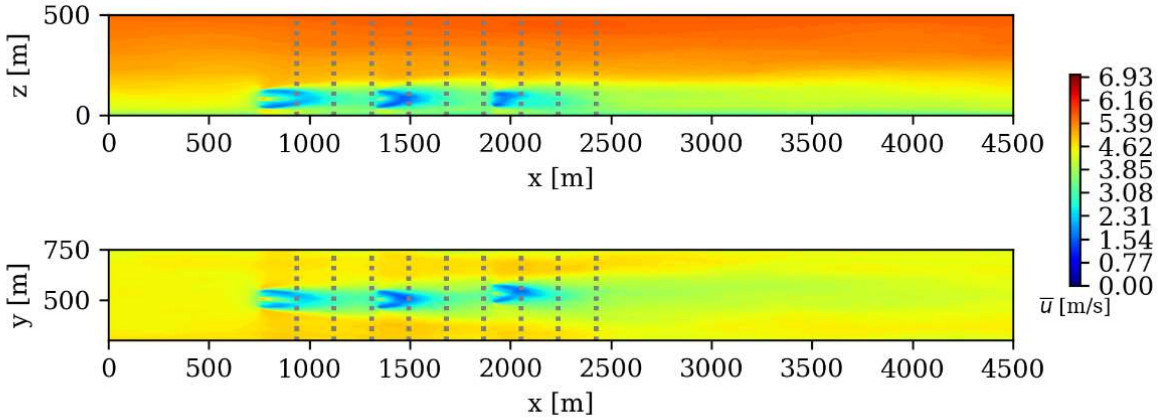

Figure 42. Selected positions to extract vertical and horizontal profiles downstream of the first WT.

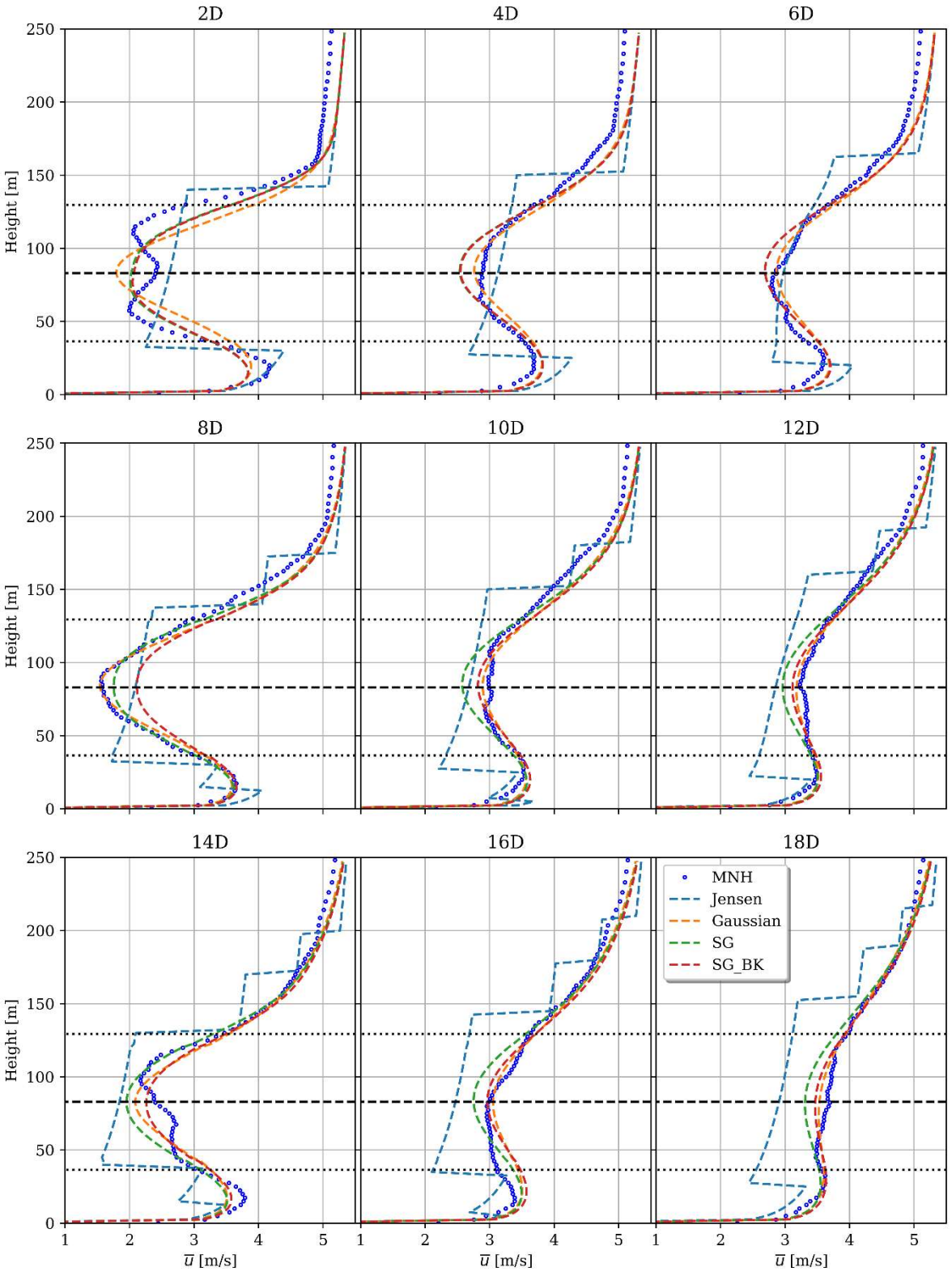

Figure 43. Vertical profiles of 10-min averaged wind speed downstream of the first WT considering the neutral case of Teesside, provided by different models.

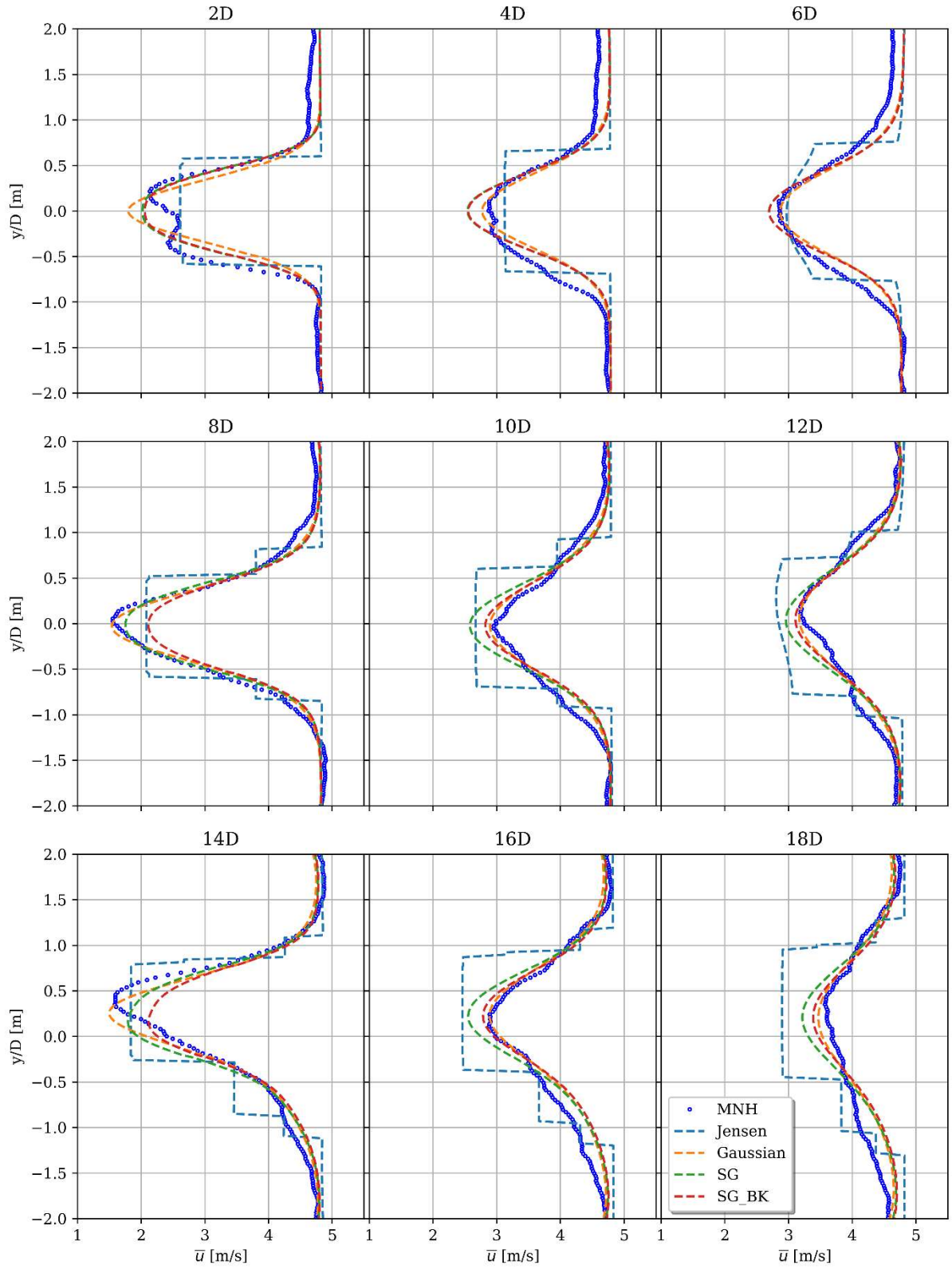

Figure 44. Horizontal profiles of 10-min averaged wind speed several diameters downstream of the first WT considering the neutral case of Teesside, provided by different models.

For the analytical models, it seems that the Gaussian wake model coupled with the local linear sum method behaves the best, while super-Gaussian wakes provide fairly good results. One can note that the momentum conservation of Bastankah avoids the potential overprediction of the local linear sum. If the results after the 2nd wind turbine (8D) show some discrepancies (as mentioned by the author [61]), the deficit is improved in the far wake. The Jensen model is, as expected for its simplified formulation, the farthest to the high-fidelity simulations all along the wake.

A similar analysis downstream of the wake was performed for the turbulent intensity. Figure 45 presents the horizontal and vertical cuts for this magnitude and the points selected to extract the profiles. It can be observed that within the wake, the turbulence shows an important increase compared to the ambient turbulence in the regions near the WT, but these values are rapidly reduced a few diameters downstream.

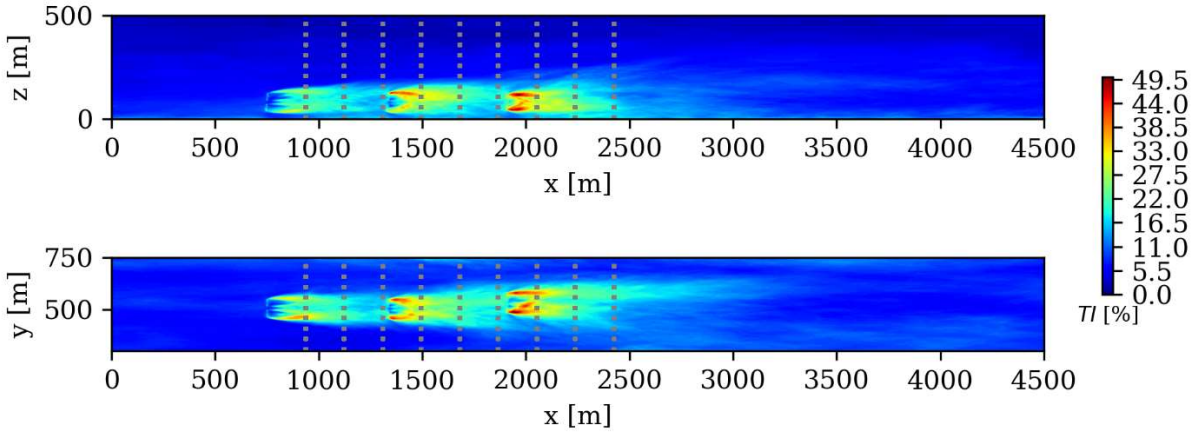

Figure 45. Vertical and horizontal fields of turbulence intensity at middle row position and hub height, respectively. Selected positions to extract vertical and horizontal profiles downstream of the first WT (dashed grey lines).

Regarding the vertical and horizontal I_u profiles, Figure 46 and Figure 47, it can be first noticed that even though the turbulence-added model is the same for all FarmShadow™ configurations (see

Table 9), the TI variable is modulated by the mean wind speed, $TI = \sigma_u/\overline{u}$. Therefore, important differences in the velocity field between the analytical models and the LES simulations (Figure 46 and Figure 44) may lead to important differences in the turbulence intensity fields. For example, an important overestimation appears in the regions near the blade tip for the case of the FarmShadow™ configuration with the Jensen model. In general, overestimations by the analytical models can be noticed. The other configurations present an overall good correspondence with the values resulting from the high-fidelity simulation. The horizontal profiles show that the LES predicts wider shapes in the far wake of wind turbines (especially 12D and 18D). In the vertical profiles, more important differences are observed after the third wind turbine (14D, 16D, and 18D): an overestimation of the analytical wake model is noticeable. At the moment of the writing of the report, the authors discovered that a mistake in the added TI formulation of FarmShadow™ is the reason for a major part of these overestimations. For the sake of coherence with the following parts, the results are not updated with the correction.

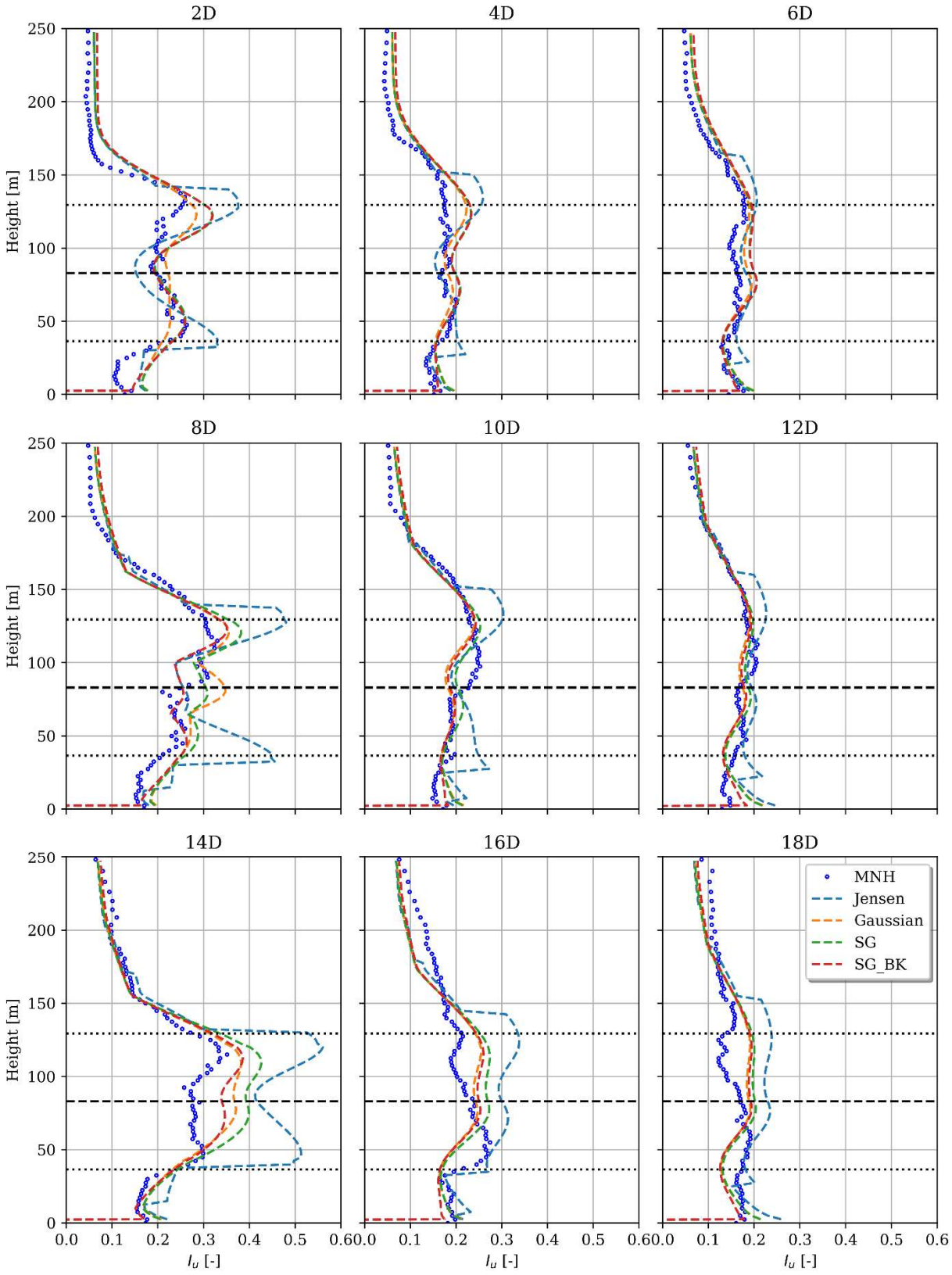

Figure 46. Vertical profiles of turbulence intensity several diameters downstream of the first WT and for different models.

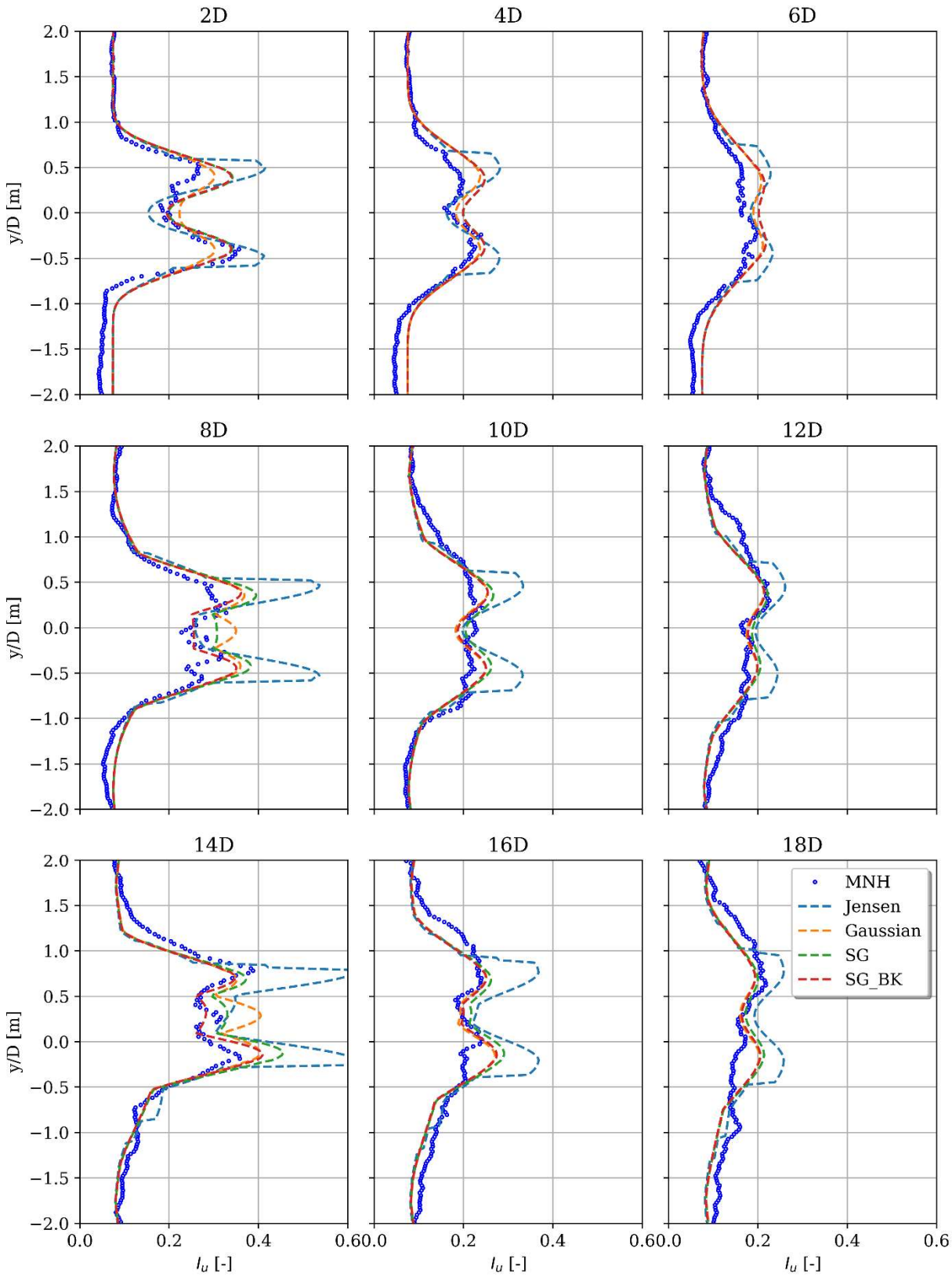

Figure 47. Horizontal profiles of turbulence intensity several diameters downstream of the first WT and for different models.

4.2.1.3.2 Stable case

We used the PALM model to simulate wakes in a row of three 2.3 WTs in a stable boundary layer condition. Like benchmark simulations, we made a precursor run to generate steady-state profiles and initialize the main run. The precursor domain configuration is similar to the benchmark setup for the under-rated case. However, we imposed a negative surface cooling rate to generate stable conditions. A surface heating rate equal to -0.15 K/h was defined to produce strong wind shear and turbulence in the flow field. For the main run, the domain size is 6000×1280×960 in *x*, *y,* and *z* dimensions, respectively, with a grid resolution of 5 m both in horizontal and vertical directions. The speed control is on, but the pitch angle is set to a constant value in this experiment for wind speeds below 10 m/s. It is worth mentioning that to keep pitch control activated for a 2.3 WT, a list of operational and technical specifications would be required. At the time of the study, it was not possible to define them all.

The profiles obtained at the end of the precursor simulation are illustrated in Figure 48. In this stable case, important wind shear and a low-level jet are noticeable. The power law fit fails at providing an acceptable value, introducing a potential uncertainty for the following computation with the analytical wake model. Instead of using the power law exponent as input for FarmShadow™, one can think about using directly the profiles extracted from LES for better estimation. For the sake of the evaluation of the uncertainty of industrial methods (that may not have access to wind profiles for every condition), the power law will be considered in this study. The turbulence shows quite high intensities near the ground, mainly due to the mechanical production of turbulence. The wind direction is constant over the vertical levels as the Coriolis effects as been deactivated in PALM.

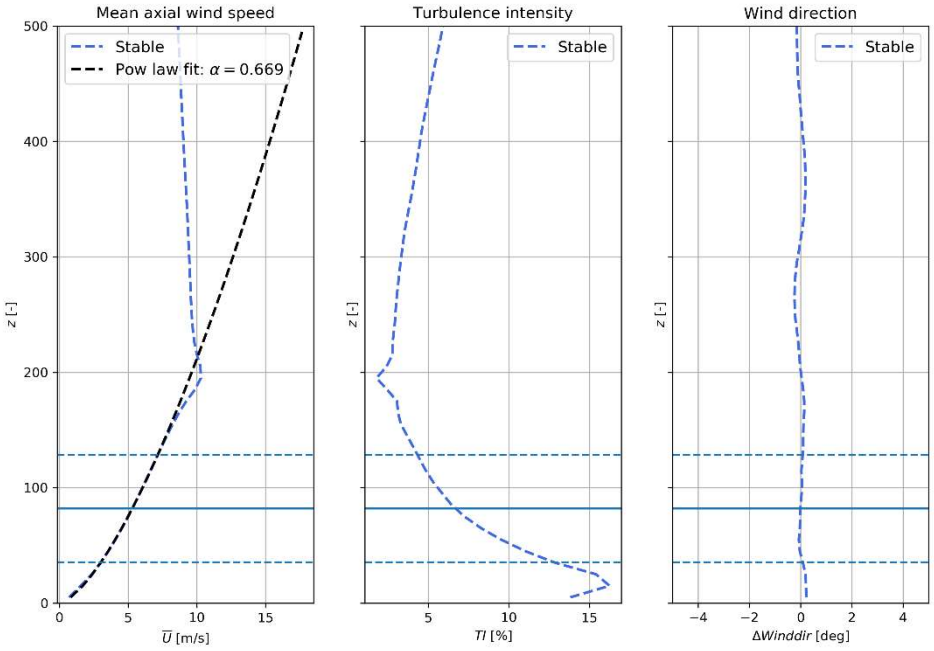

Figure 48. Wind speed, turbulence intensity, and wind direction vertical profiles for the stable case obtained after the precursor. Hub height and rotor top/bottom are indicated by solid and dashed horizontal lines, respectively.

Figure 49 shows the vertical and horizontal cross-sections of a 10-minute average wind speed. As seen in this figure, the wake is stronger than the neutral case (see Figure 42), and the velocity deficit is propagated farther downstream of the wind turbines compared to the neutral cases (as expected for the stable condition due to a significant decrease in the momentum fluxes, and turbulence lateral/vertical mixing).

Vertical and horizontal wind speed profiles at several diameters (from 2D to 18D) downstream of the first WT are presented in Figure 50 and Figure 51. A stronger wind speed deficit is observed in both vertical and horizontal profiles for LES results when compared to analytical models. For near wake conditions, LES simulation represents a bimodal shape which is not shown in analytical models. By going farther downwind from the wind turbines (especially at 4D and 6D), stronger wake effects can be seen in the LES results, indicating that wake recovery is weaker than in analytical models, as expected for stable conditions. In the upper layers, the wind speed shows important discrepancies as the power law fails to represent the low level-jet. In the bottom layers, a Venturi effect between the surface and the rotors induces acceleration of the wind speed, which is not included in analytical models, and maybe slightly overestimated by the rotative actuator disk.

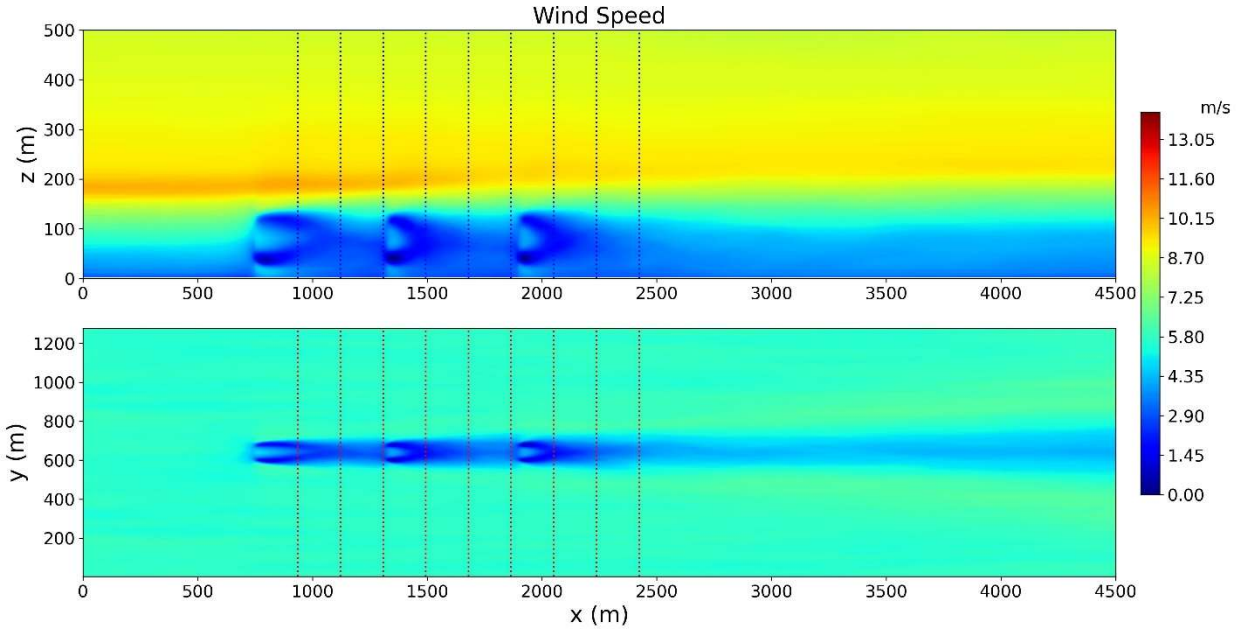

Figure 49 Vertical (up) and horizontal (down) cuts of mean wind speed at the middle row position and hub height, respectively. The vertical lines show selected positions to extract vertical and horizontal profiles downstream of the first WT.

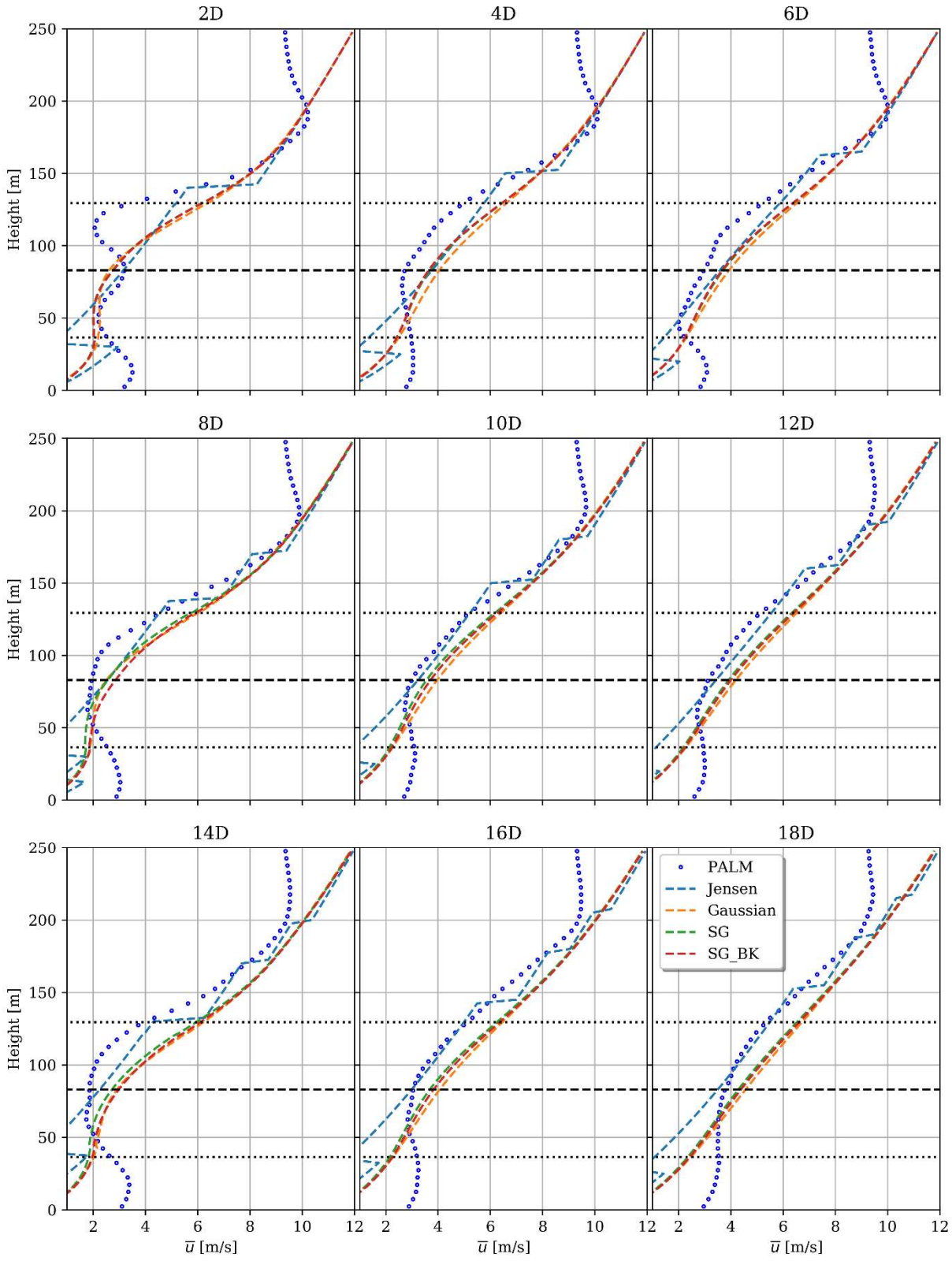

Figure 50. Vertical profiles of 10-min averaged wind speed, several diameters downstream of the first WT for the stable case. Comparison of the PALM LES (blue points) and analytical models (dashed lines).

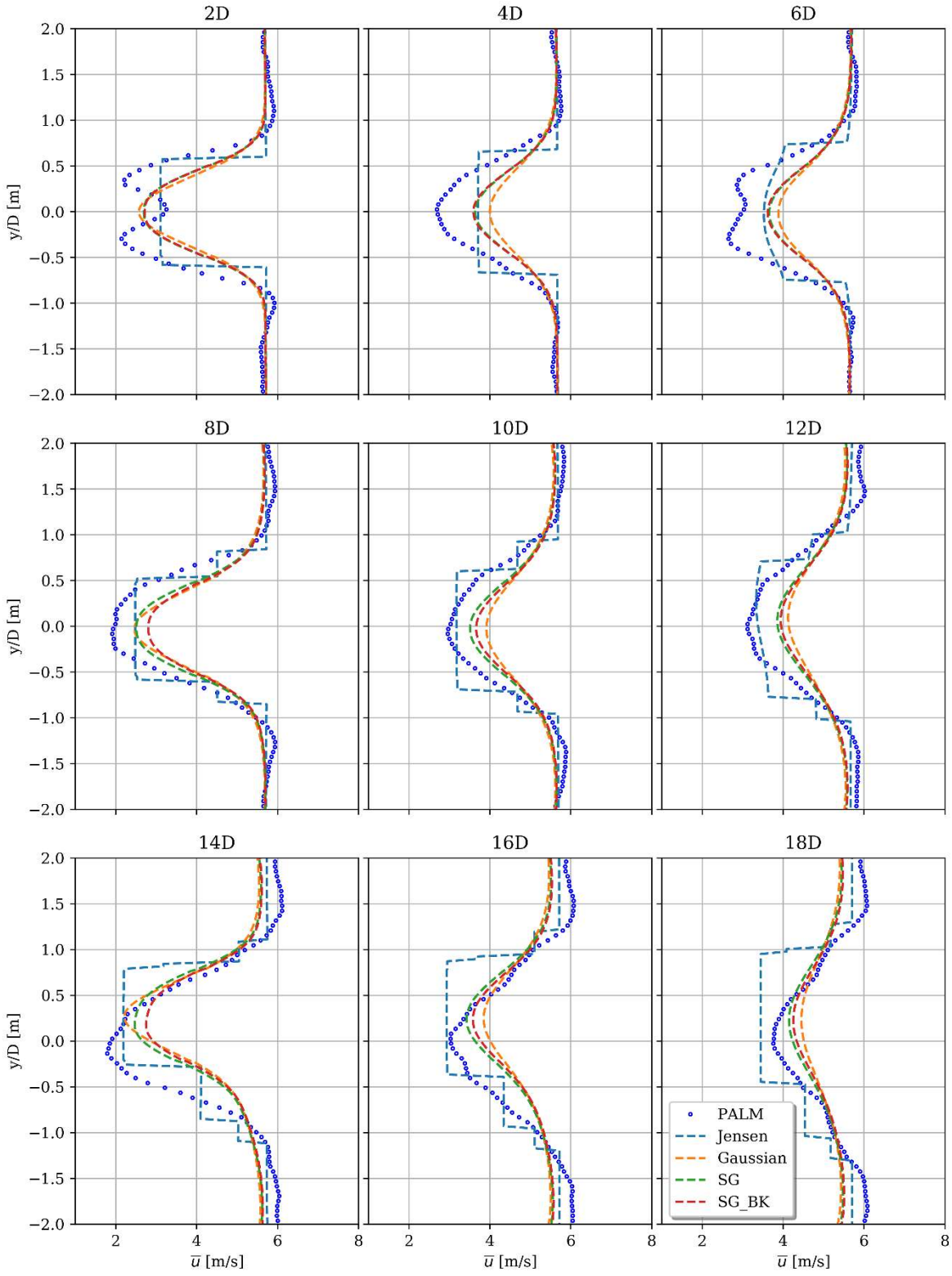

Figure 51. Horizontal profiles of 10-min averaged wind speed several diameters downstream of the first WT for the stable case. Comparison of the PALM LES (blue points) and analytical models (dashed lines).

Figure 52 shows cross-section plots of turbulence intensities in the *x-z* plane (top panel) and *x-y* plane at hub height (bottom panel) respectively. In general, wakes are stronger in stable conditions than in neutral conditions (see Figure 42) and can be expanded farther from the turbine row. Vertical profiles of turbulence intensity at the different ranges are shown in Figure 53 and Figure 54. The differences between LES and analytical models are important in this case, more than in other cases proposed in this report. The stable boundary layer with a low-level jet is a tricky condition for not only analytical wake model, but also high-fidelity simulations. It is then hard to conclude about the behavior of the turbulence intensity. Important discrepancies are noticeable below the rotor: they might be due to the very low wind speed estimated near the ground in analytical wake models.

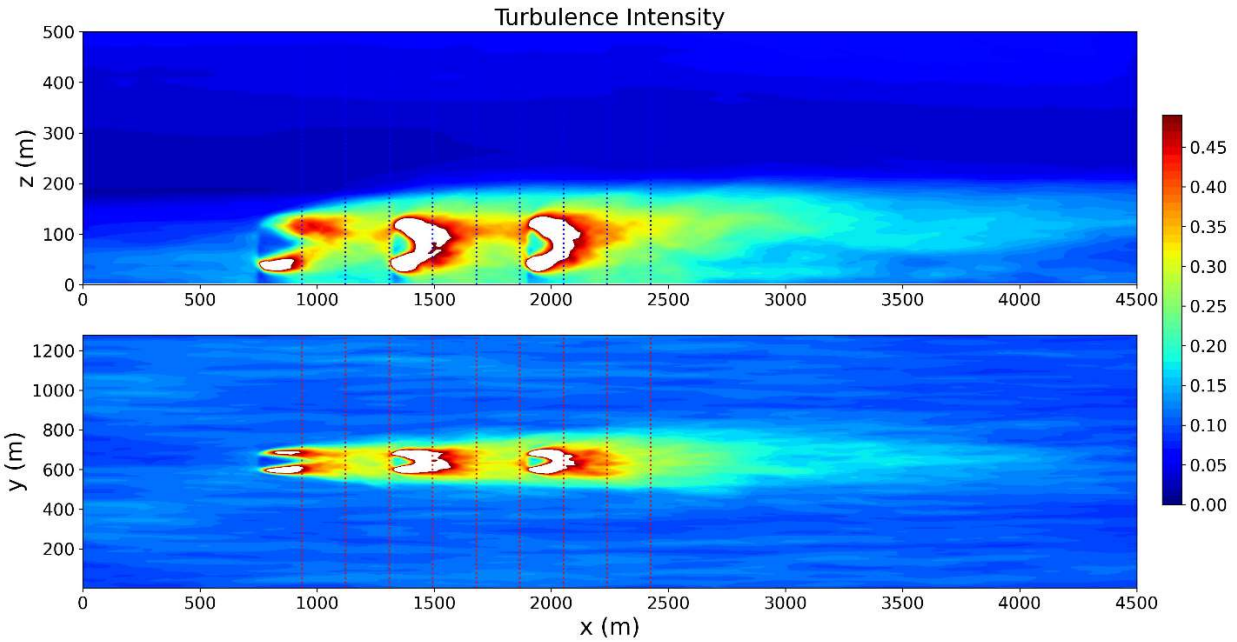

Figure 52. Vertical and horizontal cuts of turbulence intensity at the middle row position and hub height, respectively. The vertical dashed lines show selected positions to extract vertical and horizontal profiles downstream of the first WT.

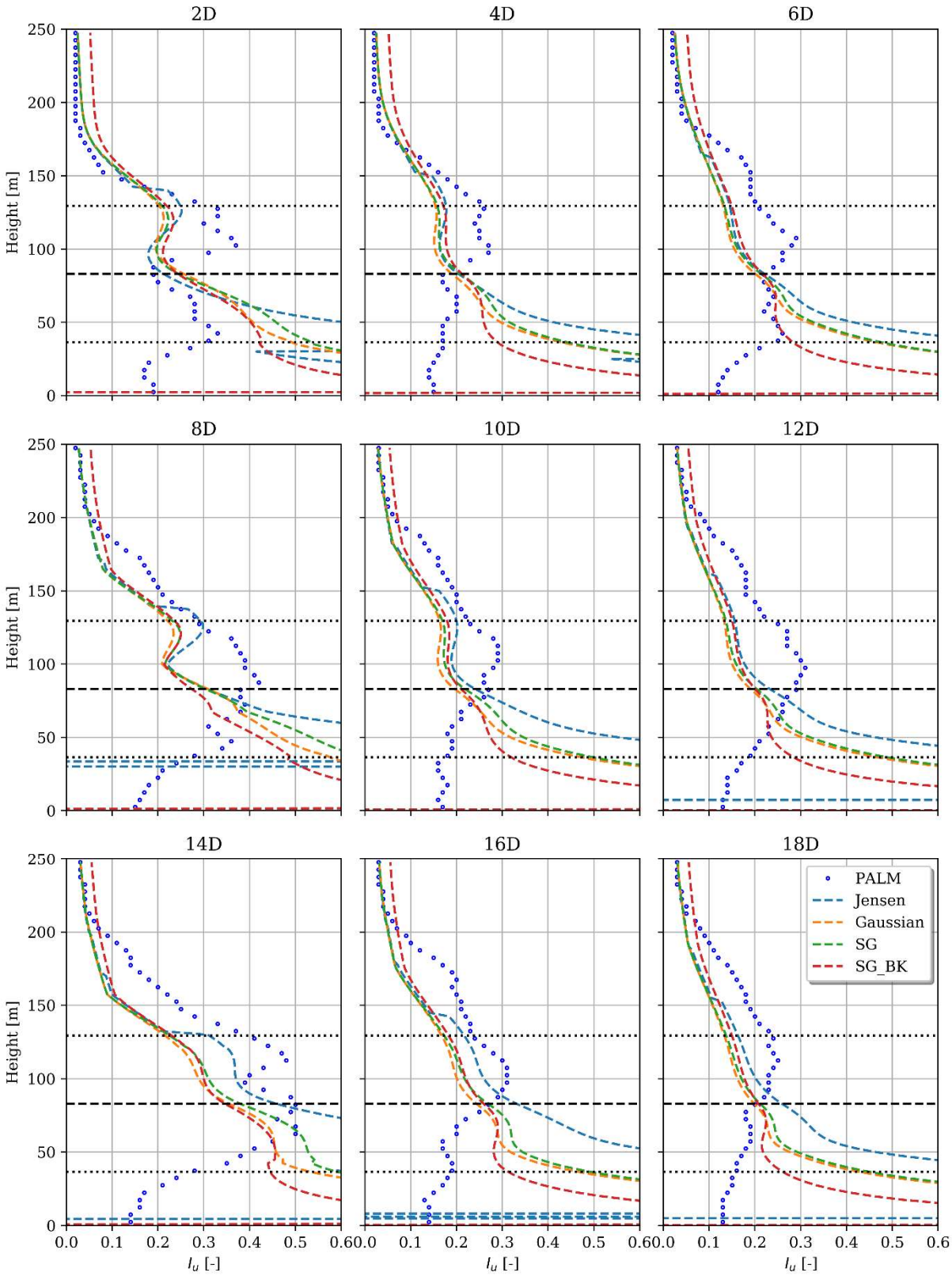

Figure 53 Vertical profile of Turbulence intensity at several diameters downstream of the first WT for stable case. Comparison of the PALM LES (blue points) and analytical models (dashed lines).

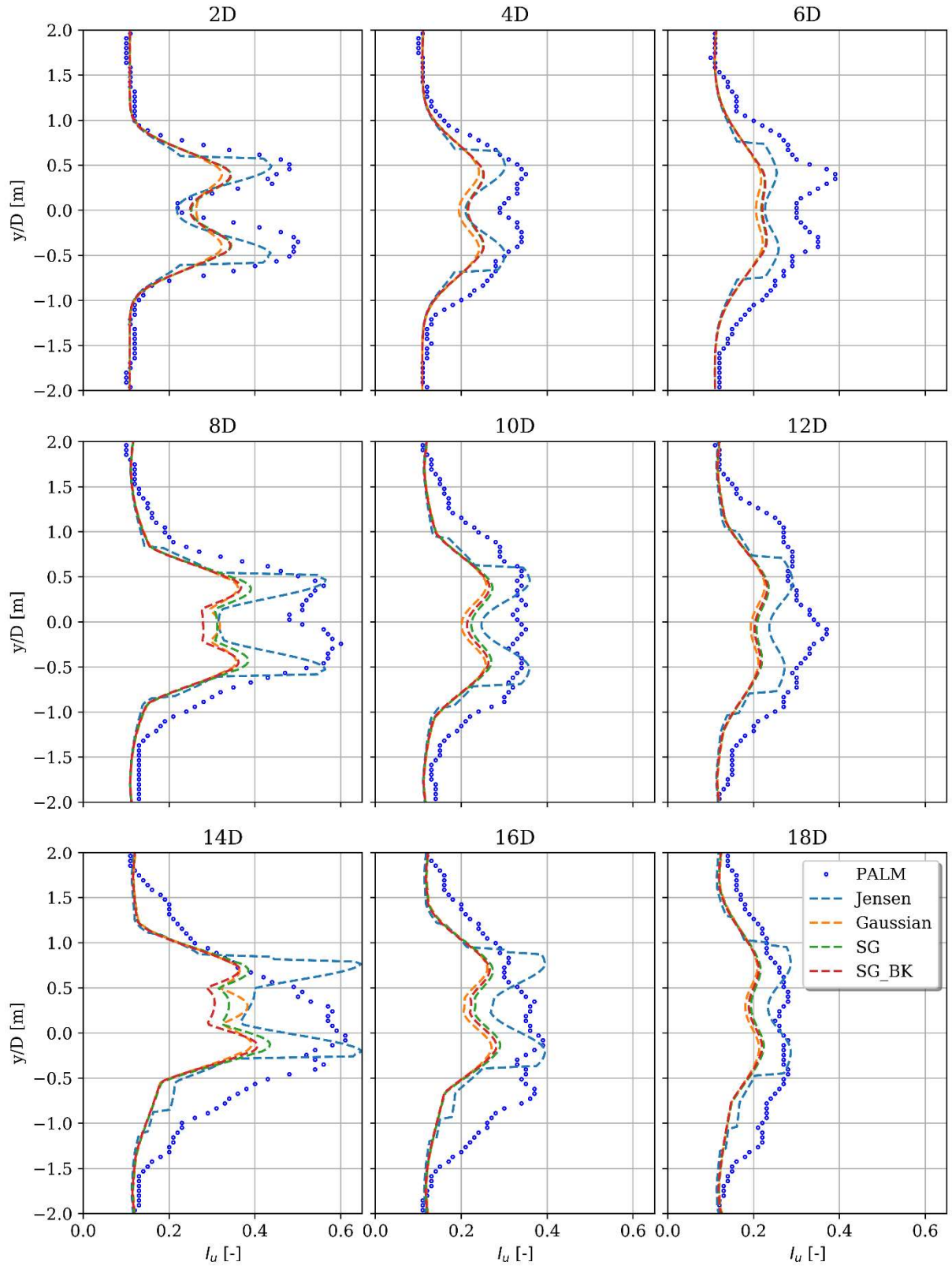

Figure 54 Horizontal profiles of turbulence intensity at several diameters downstream of the first WT for the stable case. Comparison of the PALM LES (blue points) and analytical models (dashed lines).

4.2.1.3.3 Unstable case

For the unstable case, Meso-NH was used. As one of the objectives of the project was to use reduced configuration, we wanted to see if it is possible to generate a convective boundary layer by using a domain as small as the neutral boundary layer: $L_x = 6$ km, $L_y = 1$ km and $L_z = 900$ m, using cyclic conditions. For this case, a surface heat flux of 30 W/m2 was imposed during the entire simulation to enhance buoyancy. After 9h of precursor simulation (relatively long for a CBL), the profiles illustrated in Figure 55 have been obtained. This duration was necessary to reach a moment showing low variations of wind speed and wind direction.

In a convective boundary layer, the behaviour is quite different from the previous cases. For each variable, the profiles are more uniform in a major part of the ABL because of the important mixing. Variations are mainly observed near the ground, in the so-called "surface layer". For the wind speed (averaged over the last 10 minutes of the precursor simulation), the "power law" shape is not obtained anymore. The fit provides the value of $\alpha = 0.021$, but shows some discrepancies, especially in the bottom part of the rotor. The power law profile underestimates the shear of the wind speed in the surface layer. As expected, important values of turbulence intensity are measured, even at high altitudes. However, almost no differences in wind direction are observed thanks to the mixing.

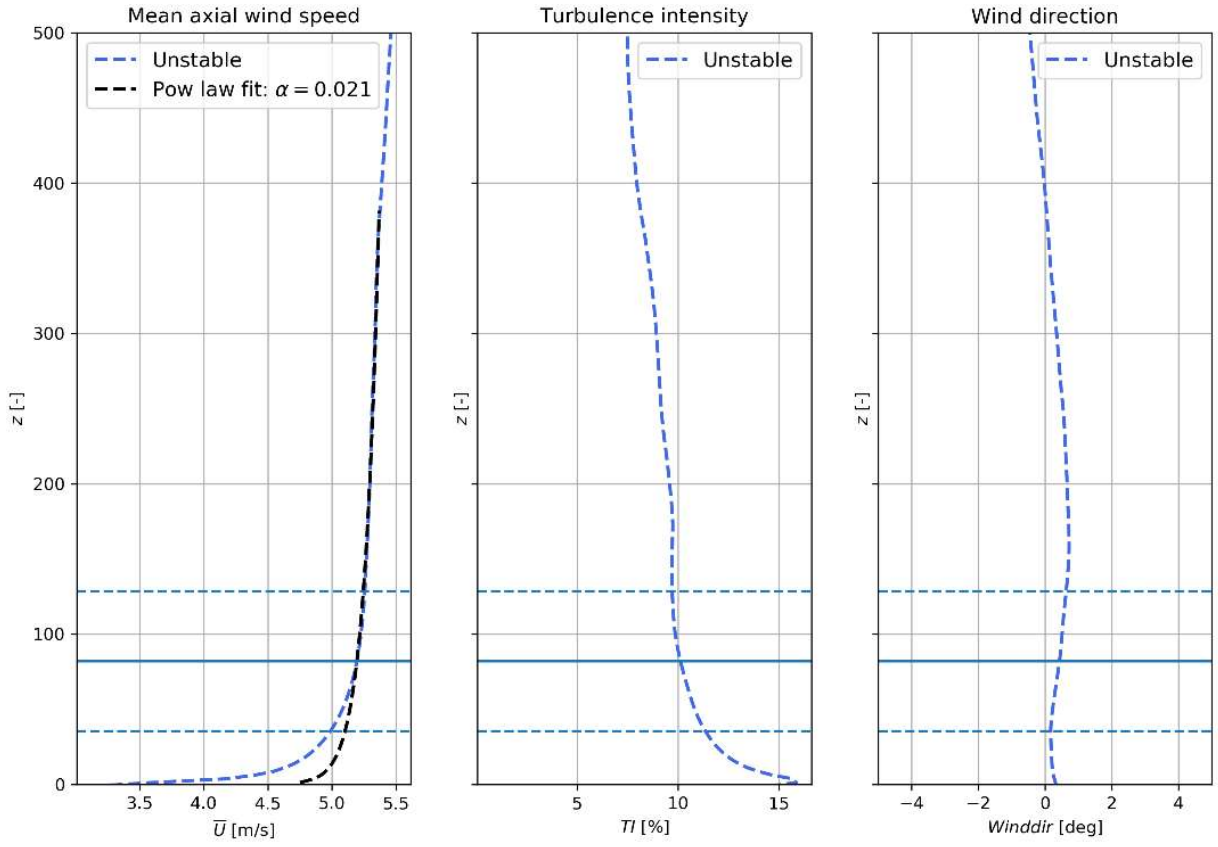

Figure 55. Wind speed, turbulence intensity, and wind direction vertical profiles for the unstable case. Hub height and rotor top/bottom are indicated by solid and dashed horizontal lines, respectively.

Unfortunately, after the precursor simulation, important thermal convection appears, as illustrated in Figure 56. This figure shows a vertical plane of a vector field. The vector field is time-averaged (denoted as $\bar{\cdot}$) over 10-min, and spatially averaged on the x-axis (denoted as $<\cdot>$). The main x-axis component $< \bar{u} >$ has been removed: only $(< \bar{v} >, < \bar{w} >)$-components of the wind are displayed. The colours indicate the intensity of the vertical component $< \bar{w} >$ to highlight the thermal cell. The updraft motion took place at around $y = 400m$, while the downdraft motion took place at around $y = 900m$. Near the ground, one can see a convergence of the flow below the updraft and a divergence below the downdraft. The opposite is observed at the top of the boundary layer. Such important and stationary thermal was not expected and might show the limits of the methodology applied.

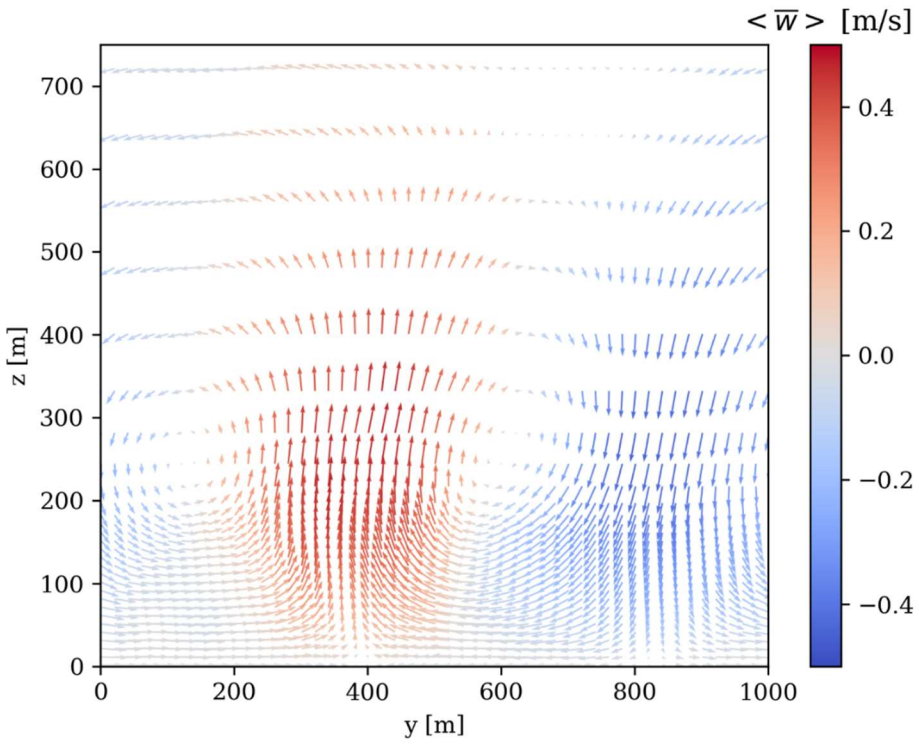

Figure 56: Time (10-min) and spatial (x-axis) average of $(< \bar{v} >, < \bar{w} >)$-wind components. The colour bar indicated the vertical component intensity.

After the precursor, the wind turbines can be introduced, but the thermal has a strong impact on the wakes. Figure 57 presents the mean wind fields for the last 10 minutes of the simulation with the WT. The wakes of the line in the middle are interacting with the updraft motion and are convected upwards: an important vertical wake deflection is observable in the vertical cut. On the other side, the wakes of the line near $y = 850m$ are pushed downward (not shown), as they are interacting with the downdraft motion. The wakes of the last line, near $y = 200m$, are strongly deflected along positive y-direction. In the horizontal plane, it is possible to see a convergence of the wake: the wakes are interacting with the convergence of the flow below the thermal illustrated in Figure 56.

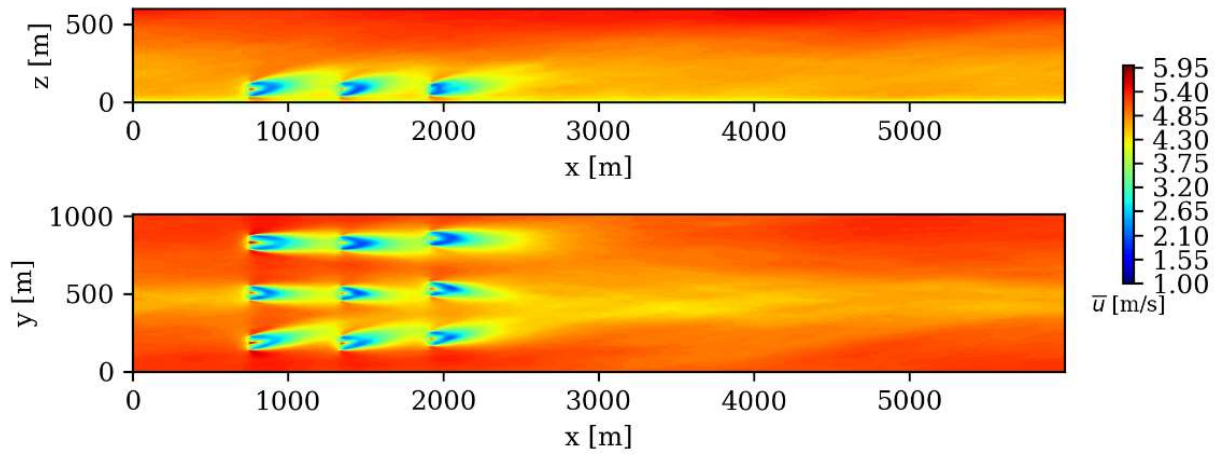

Figure 57. Vertical and horizontal cuts of mean wind speed at the middle row position and hub height, respectively, for the unstable case of Teesside.

As mentioned before, the limits of the methodology are maybe highlighted for this case. Firstly, the reduced domain using cycling conditions seems irrelevant to study a convective boundary layer: it should be at least 10 times wider than the boundary layer height. In such conditions, the eddies do not have enough space for their development. One can note that the size of the main eddies is perfectly equal to the half-width of the domain. Secondly, the usage of the precursor simulations aiming at reaching quasi-stationary flow, for comparisons with analytical wake models, loses its sense, especially for unstable conditions. Indeed, the 9h of precursor simulation with a constant heat flux is not representative of a diurnal cycle and brings a lot of energy to the flow.

In the end, the authors have doubts about the physical representativeness of the flow generated. For all these reasons, a comparison with analytical models is not provided. To make sure about the physical behaviour obtained, a wider domain should be simulated. It would allow us to see if the spatial dimension of the previously observed thermal is representative. If not, a bigger domain is necessary for this study, leading to the need to simulate the entire wind farm, which seems infeasible with the resolution used. Another discussion could be opened about the comparisons between stationary models and high-fidelity models for a convective boundary layer. Indeed, trying to reach a stationary state of an unstable case seems unrealistic and leads to specific problems such as statistical representativeness.

4.2.1.3.4 Crosswind simulations

In this section, we simulated 5 WT in a row in the middle of the Teesside wind farm when the wind blows from 304-312˚ (i.e. the crosswind case). PALM simulation contains a precursor and then a main run. We used the same grid configuration for the precursor as the one employed in the benchmark under-rated case (see Table 6). A neutral stability condition is considered for this case. At the end of the precursor simulation, wind speed, turbulence intensity, and wind direction reached 7.1 m/s, 9.6%, and 308˚ respectively. The domain size for the main run is 6000m×960m×960m in x, y, and z directions respectively with a grid size of 5 m in both horizontal and vertical directions. Same as the stable case, speed control is on, and the pitch angle is set to the constant value.

Figure 58 illustrates the profiles obtained at the end of the precursor simulations. Again, for this neutral case, the typical "power law" shape can be observed. The fit to the power law provided $\alpha = 0.14$ and shows a slight uncertainty. This value will be used as input for analytical wake models. The turbulence intensity profile shows a regular shape for neutral conditions. As the Coriolis effect is not considered, a different behaviour of wind direction is observed when compared to Figure 40: the wind direction is nearly constant at each vertical level.

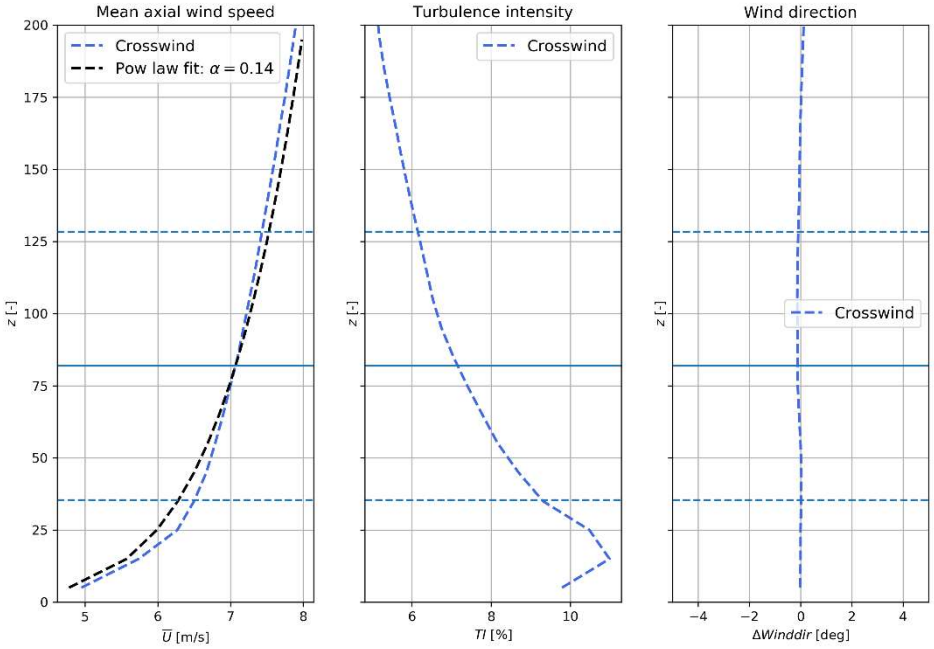

Figure 58. Wind speed, turbulence intensity, and wind direction vertical profiles for the crosswind case obtained after the precursor. Hub height and rotor top/bottom are indicated by solid and dashed horizontal lines, respectively.

Figure 59 shows a simulated 10-minute averaged wind speed, and we can observe the wake evolution patterns downstream of the domain. From the second wind turbine, wakes are stronger because downwind turbines are exposed to the wakes of their upwind ones. Figure 59 (top) shows that wind is deflected to upper layers to heights even more than 300 m at distances way farther from the row of turbines (say x>4 km). Figure 60 shows the variation of turbulence intensity in the x-z and x-y planes. The deflection of turbulence intensity in the wake area reaches higher heights (see Figure 60 (top)). Such deflection explains the discrepancies between the LES and analytical model profiles in the upper layers (see Figure 61 and Figure 63), also observed in the neutral case (section 4.2.1.3.1). Vertical profiles of wind speed and turbulence intensity show further differences between LES and analytical models at heights upper than 150 m, especially from 6D and farther distances. Figure 62 and Figure 64 show horizontal profiles of wind speed and turbulence intensity at distances from 1.5D to 13.5D from the first wind turbine. As mentioned in section 4.2.1.3.1, the turbulence intensity is, in general, over-estimated by this version of FarmShadow™ (now corrected). It can be seen that the shape of the wakes in the PALM simulation and analytical models are very similar.

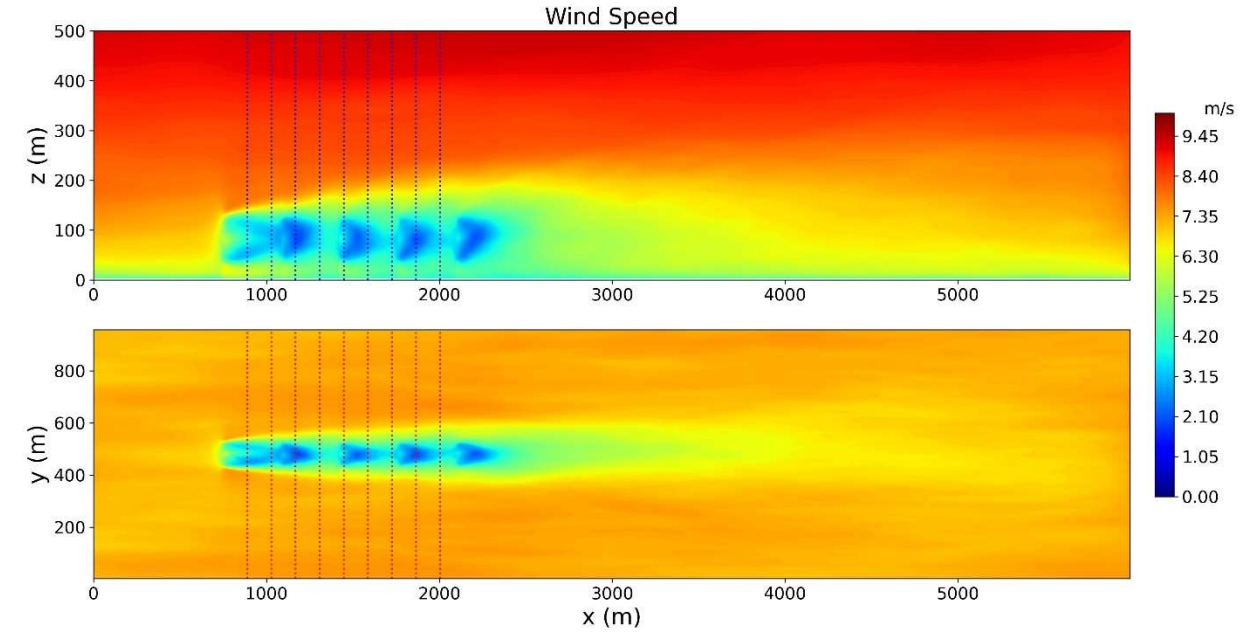

Figure 59 Vertical and horizontal cuts of mean wind speed for crosswind simulation. Selected positions (from 1.5D to 13.5D) to extract vertical and horizontal profiles downstream of the first WT are shown by dashed lines.

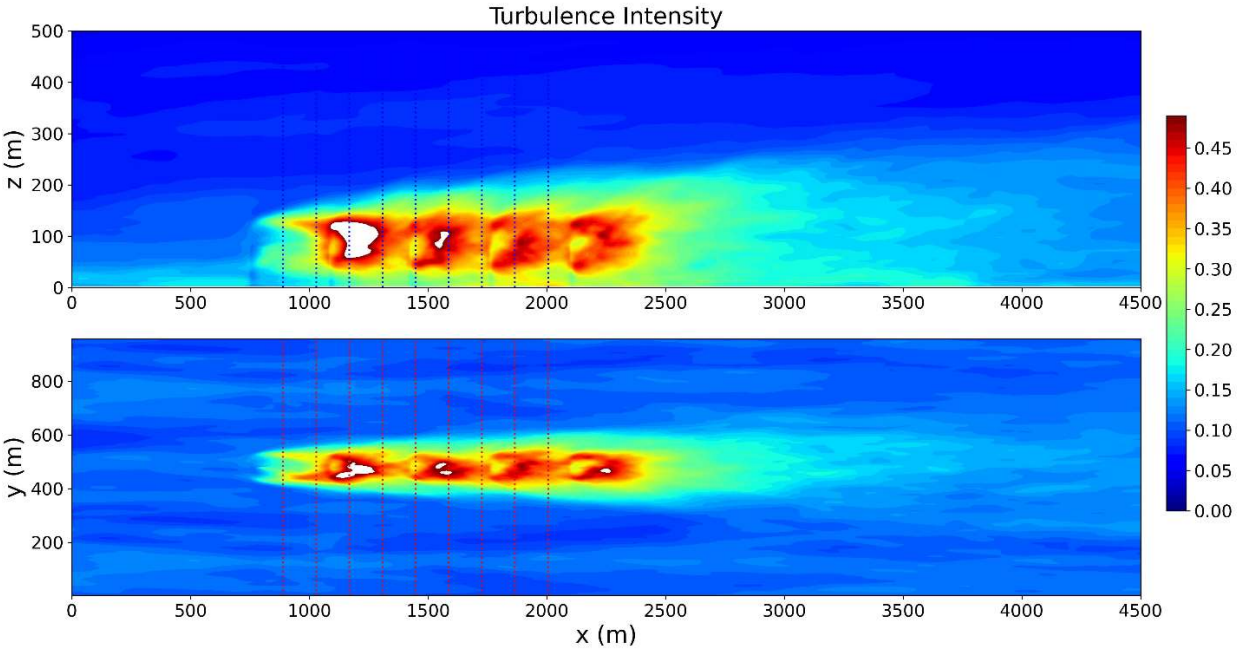

Figure 60 Vertical and horizontal cuts of turbulence intensity for crosswind case. Selected positions (from 1.5D to 13.5D) to extract vertical and horizontal profiles downstream of the first WT are shown by dashed lines.

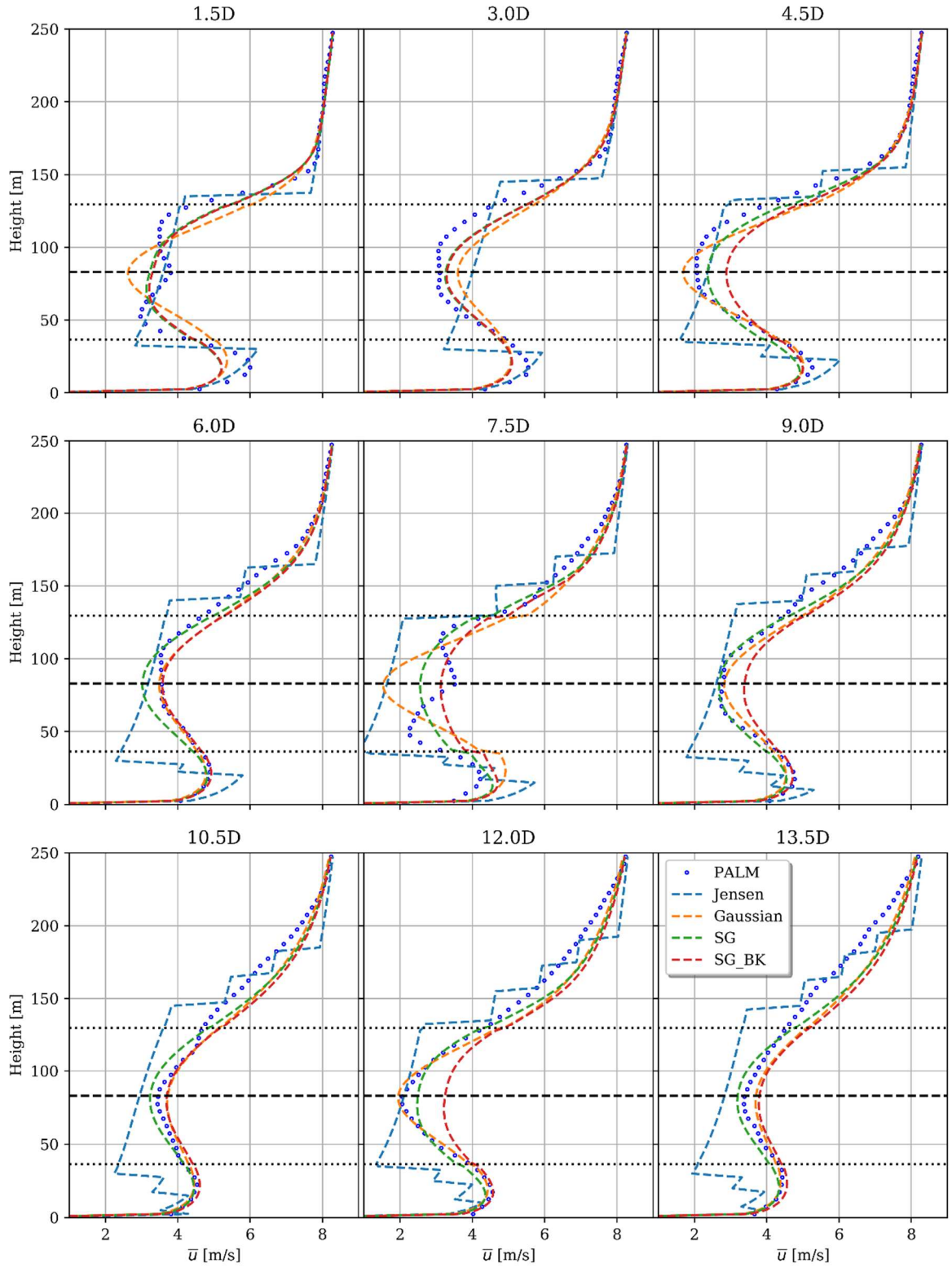

Figure 61 Vertical profile of wind speed downstream of wind turbines; several diameters (from 1.5D to 13.5D) downstream of the first WT. Comparison of the PALM LES (blue points) and analytical models (dashed lines).

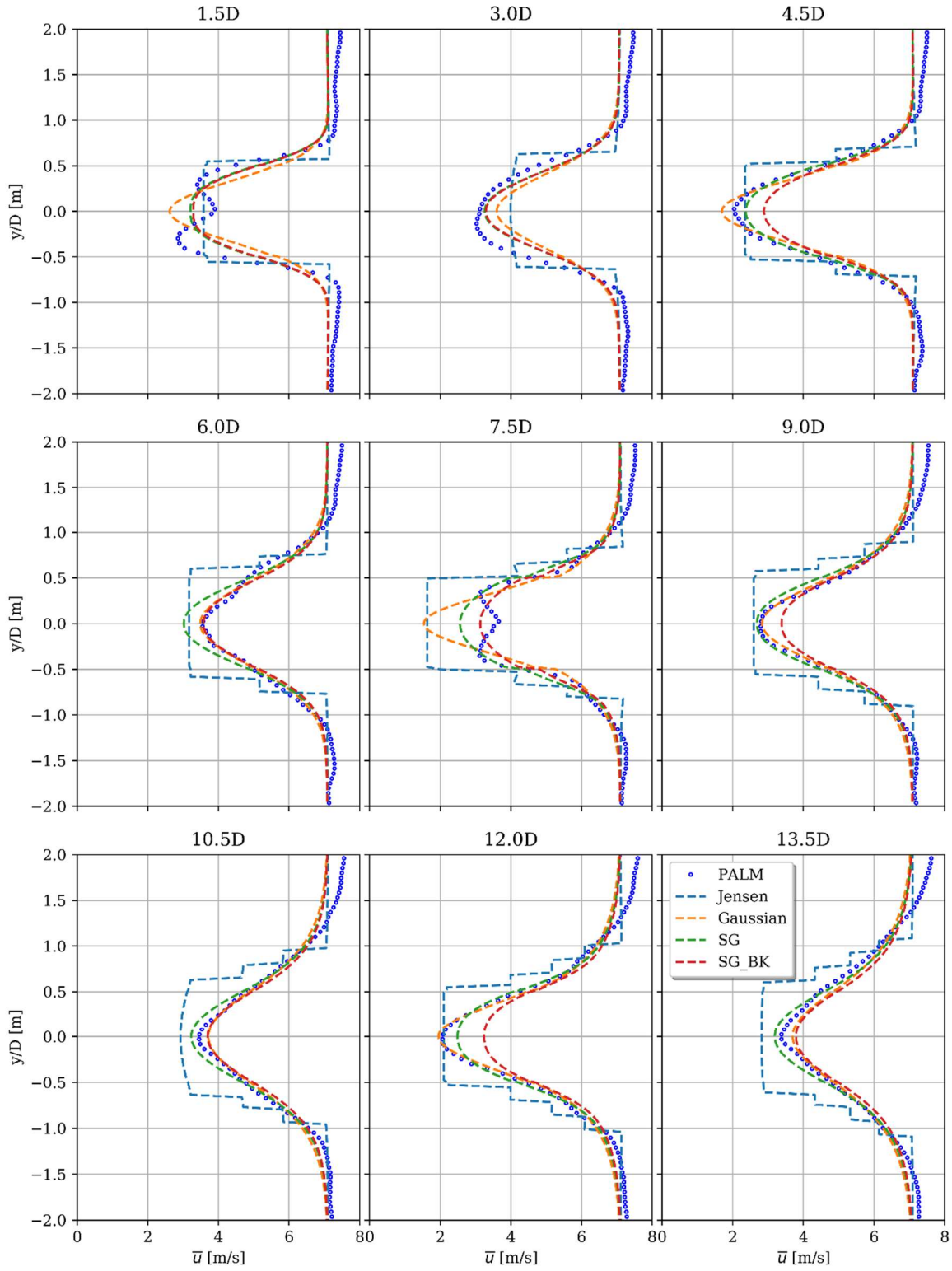

Figure 62 Horizontal profiles of 10-min averaged wind speed; several diameters (from 1.5D to 13.5D) downstream of the first WT. Comparison of the PALM LES (blue points) and analytical models (dashed lines).

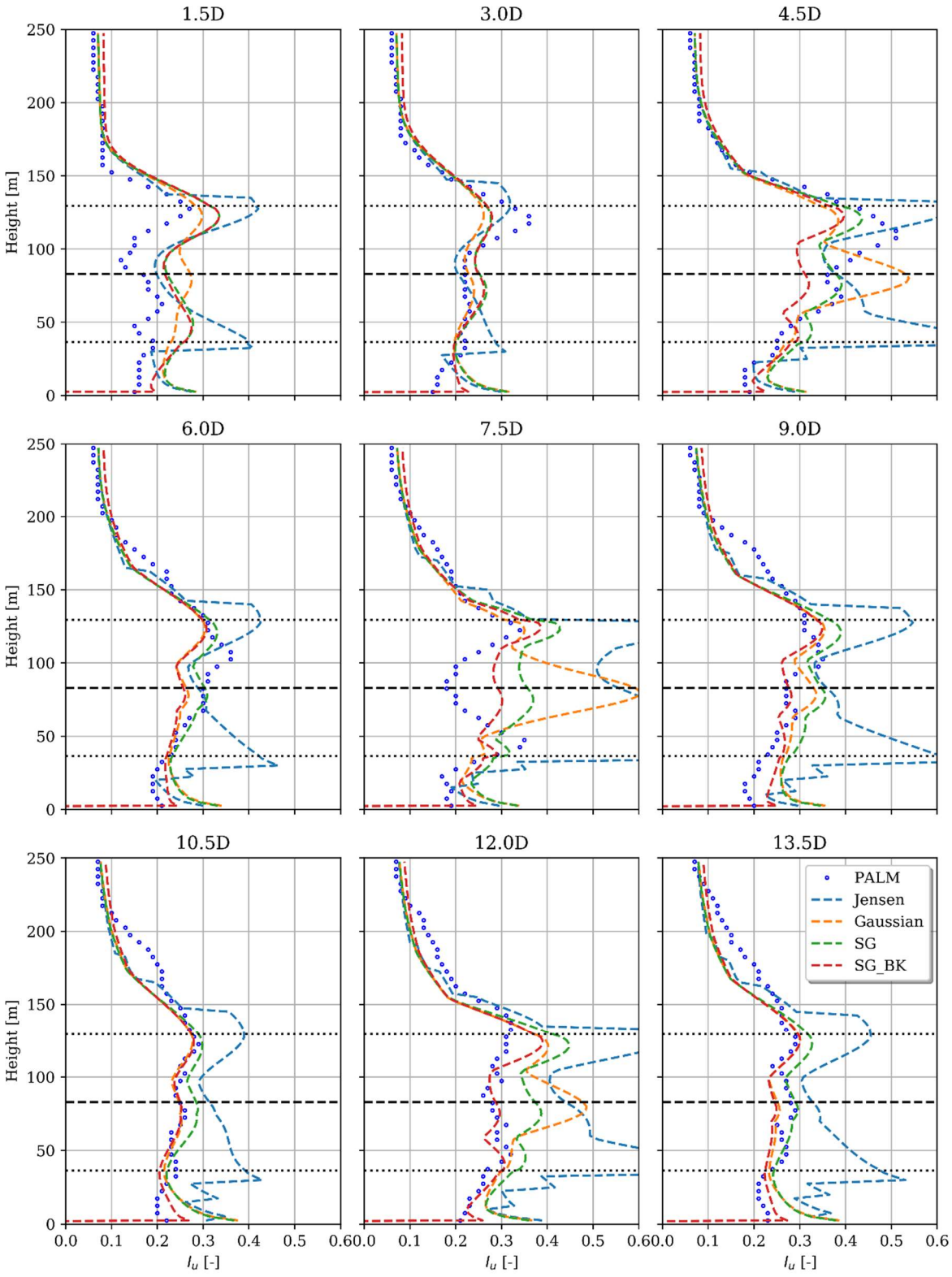

Figure 63 Vertical profile of Turbulence Intensity downstream of wind turbines; several diameters (from 1.5D to 13.5D) downstream of the first WT. Comparison of the PALM LES (blue points) and analytical models (dashed lines).

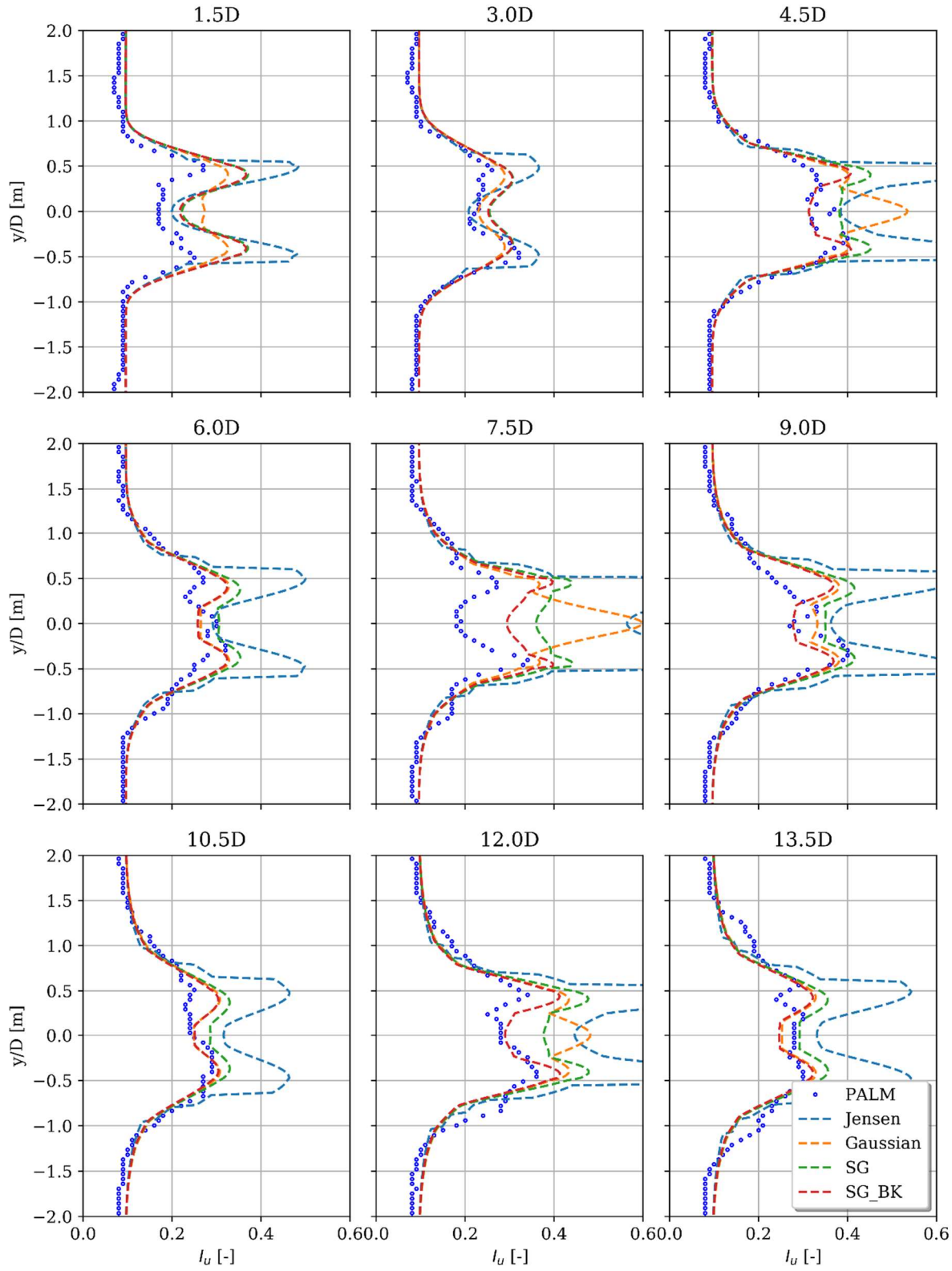

Figure 64 Horizontal profiles of 10-min averaged Turbulence Intensity; several diameters (from 1.5D to 13.5D) downstream of the first WT. Comparison of the PALM LES (blue points) and analytical models (dashed lines).

4.2.2. South Brittany case

4.2.2.1. Ambient wind conditions

Because South Brittany is composed of FOWT, the main idea for this wind farm was to explore its behaviour under several wind speeds, to enhance various static positions of the WT. Different wind speeds will generate different thrusts applied on the rotor, leading to different layouts (horizontal 2D position) and inclinations (non-vertical position), according to the reaction of the floating system (mooring lines and floater).

Therefore, a qualitative evaluation of the uncertainties of different wake engineering models but for different wind speeds is proposed, considering the Meso-NH LES model as a reference.

In these cases, the wake development for the 5 WT alignment condition presented in Figure 65 is studied for two different wind speeds, below rated and rated. The main wind conditions for both cases are listed in Table 11.

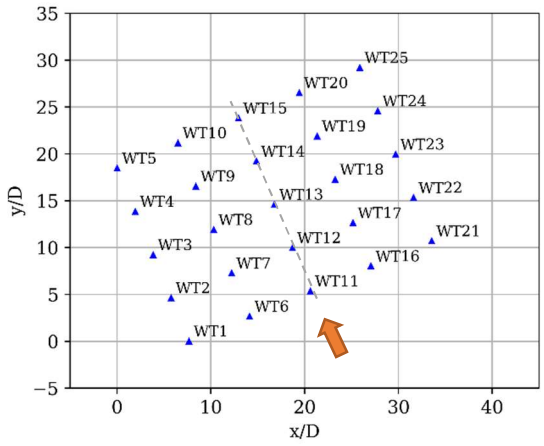

Figure 65. The layout of the South Brittany wind farm. The orange arrow indicates the wind direction selected to study the 5 WT alignment.

Table 11. Ambient wind conditions for the 5WT simulations.

Cases	$\bar{u}_h$ [m/s]	I_{u_h} [%]	θ_{wind_h} [°]	α_h	SH [W/m2]
Below rated	8.27	6.7	157	0.102	0
Rated	11.17	6.9	157	0.096	0

The methodology explained in the previous cases for Meso-NH simulations, using a precursor simulation to obtain the desired ambient wind condition was applied.

4.2.2.2. Comparisons between the analytical wake model and LES

The configuration of the Meso-NH model, provided in Table 12, is slightly different than for Teesside. Note however that the same roughness length was chosen for this case by simplicity, which could reduce its representativeness for far offshore sites. As South Brittany WT are larger, it is possible to have the same number of grid elements per blade with a lower resolution; This also allows an increase of the time step. In the end, the rotor diameter is covered by 48 grid elements. The time step, about 0.4sec during precursor simulation to respect the CFL constrain, is set to 0.012 sec when the wind turbines are simulated.

Table 12. Meso-NH model configuration for South Brittany.

Domain size	$L_x = 18$ km, $L_y = 1.6$ km and $L_z = 900$ m
Horizontal resolution	5 m
Vertical resolution	5 m up to 300m, and then an 8% vertical stretching until 20 m resolution is reached
Time steps	0.4 s for precursor and 0.012s for the simulation with the WT
Boundary conditions	Cyclic
Roughness length	0.005 m
Tip loss correction	Activated
Controller	Based on a look-up table, providing blade pitch and rotation speed as a function of wind speed.
Nacelle and tower	Not considered

Before performing the Meso-NH simulations including the 5 WT, the specific layout, and pitch of the floater turbines have to be determined, according to the ambient wind conditions presented in Table 11. For this, the HiperSAMI tool presented in section 3 was used, under an offline coupling: this information, both for the under and rated cases has been computed using a reference combination of analytical models (‘‘SG_BK’’). Then, the new layout was incorporated as input settings into the Meso-NH model and the other analytical setups (‘‘Jensen’’, ‘‘Gaussian’’, and ‘‘SG’’). The differences in position and pitch for the first WT (the most affected one), are presented in Table 13. In FarmShadow™, a look-up table is used, giving the Cp/Ct coefficients as a function of the wind speed (see section 3.3). For LES computations, a simple controller is used to enforce blade pitch and rotation speed. The controller is based on a look-up table from data provided in WP1. The simulation period was 24 physical minutes, and the first 14-min segment was discarded as spin-up time. The last 10-minute average results for both cases are shown below.

Table 13. Differences in position and pitch for the first WT obtained with HiperSAMI.

1st WT	x diff [m]	Pitch diff [°]
Below rated	18.8	3.6
Rated	31.8	6.2

Regarding FarmShadow™, the same four model configurations presented in

Table 9 was explored.

4.2.2.2.1 Below rated

The resulting vertical and horizontal mean wind fields, at the WT position and hub height, respectively, are presented in Figure 66. As for section 4.2.1.3, vertical and horizontal profiles of wind speed and turbulence intensity were extracted from these simulations. In the same way, for each 2D downstream of the wake, the profiles were extracted to be compared with those resulting from the different FarmShadow™ simulations. The location of these profiles is also presented in Figure 66 and the resulting profiles are shown in Figure 67 and Figure 68.

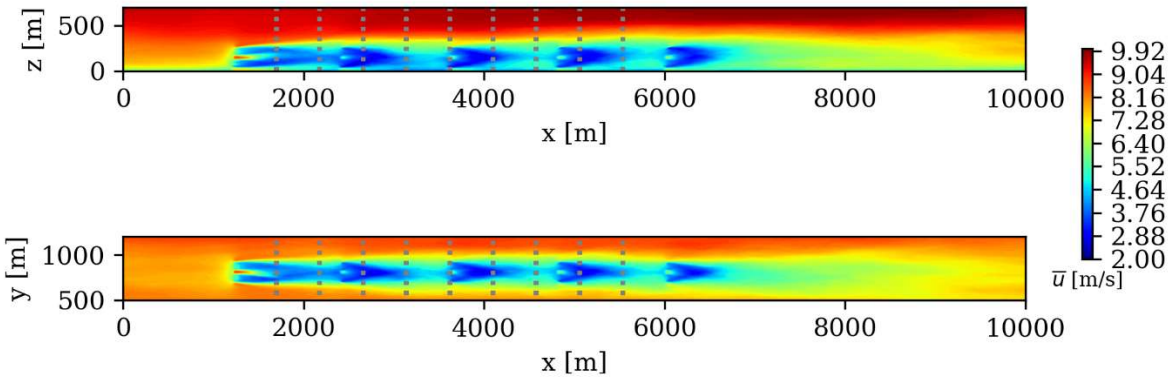

Figure 66. South Brittany vertical and horizontal fields of mean wind speed at row position and hub height, respectively. Selected positions to extract vertical and horizontal profiles downstream of the first WT (dashed grey lines).

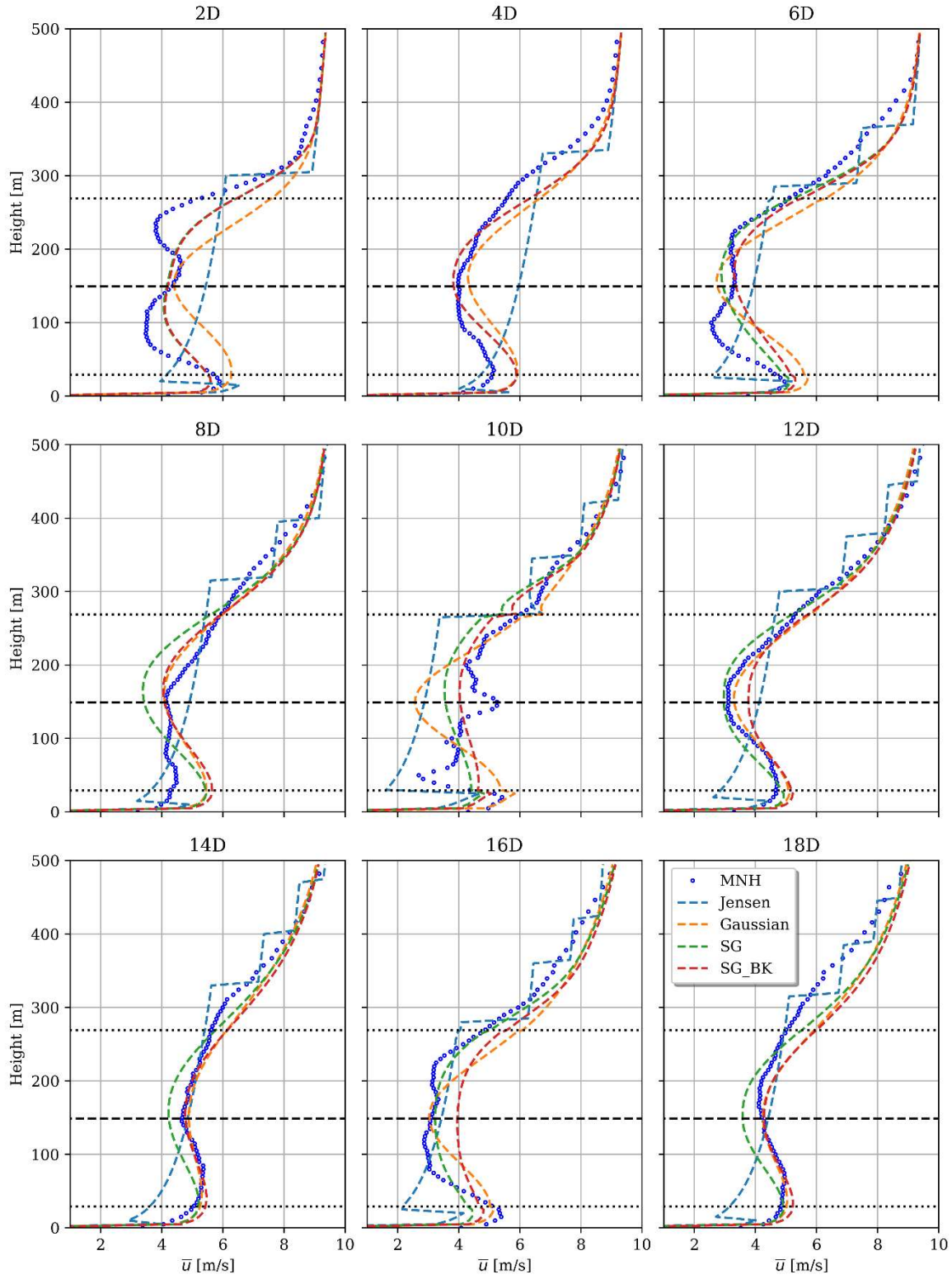

Figure 67. Vertical profiles of 10-min averaged wind speed several diameters downstream of the first WT and for different models for South Brittany at below rated conditions.

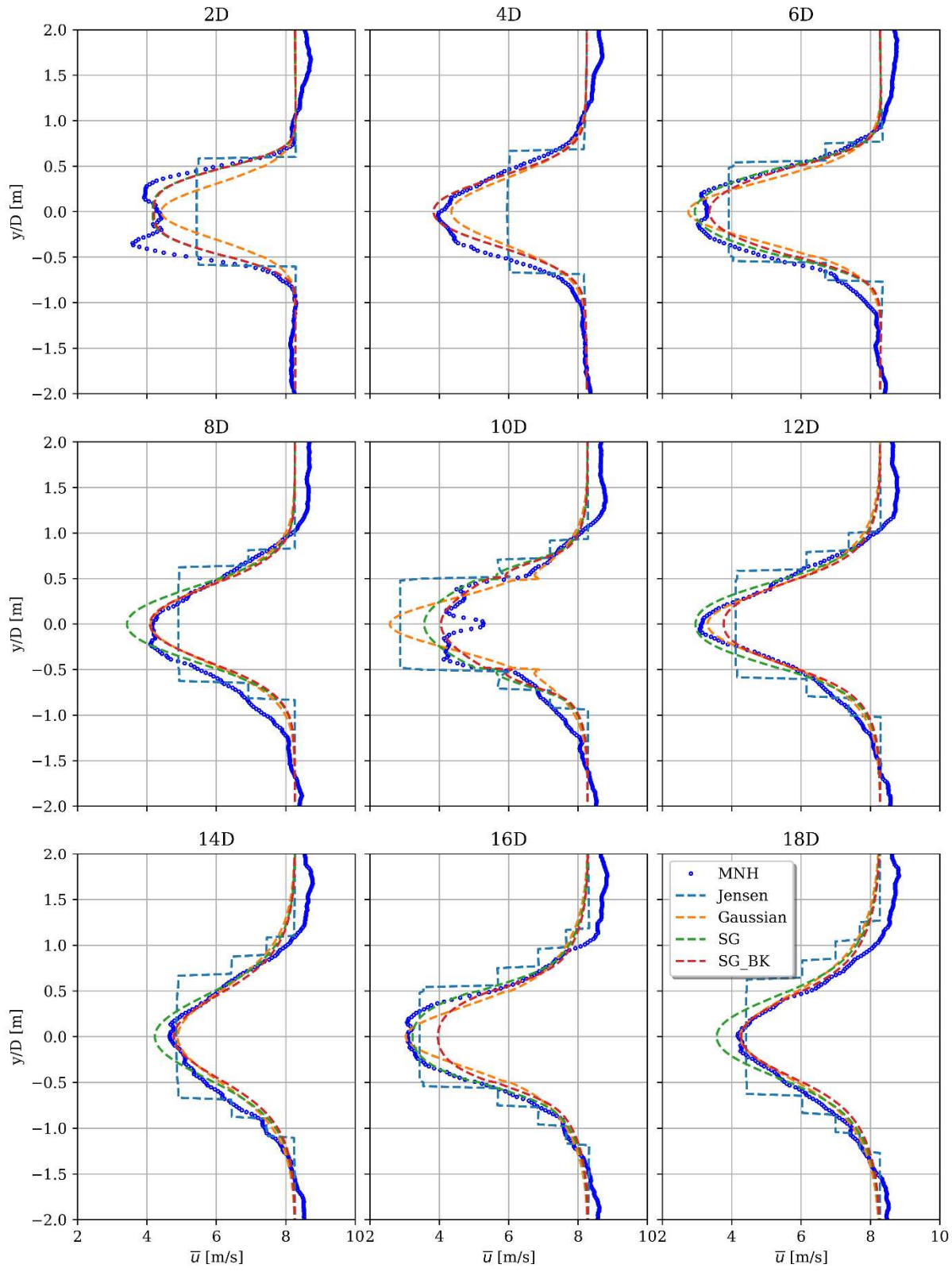

Figure 68. Horizontal profiles of 10-min averaged wind speed several diameters downstream of the first WT and for different models for South Brittany at below rated conditions.

Overall, on the wind speed profiles, a good correspondence can be observed between the LES results and the different analytical models, except in the wake of the first wind turbine where the deficit is thinner (at 2D and 4D), and weaker (at 2D) in analytical wake models. It can also be seen that the configuration considering the Jensen model is the one that differs the most from LES profiles, while the configuration that uses the Super Gaussian wake deficit model and the Bastankhah solver is the one that gives an overall best fit in that case. Higher wind speed values can be observed in the near wake centre of LES results because of nacelle absence. The wake recovery seems to be well evaluated by analytical models. In the vertical wake profile, an extension of the wake can be seen above the rotor area. This might be due to the vertical wake deflection of the wind turbines (mainly from the first one) that is maintained, or interactions with the upper part of the ABL.

The same analysis was performed for the turbulence intensity fields, sampled during the last 10-min of the simulation. The result for LES results is presented in Figure 69, while the combined profiles results are shown in Figure 70 and Figure 71. The regions with the greatest difference between the different analytical models coincide with the greatest differences in the velocity field. Regarding the differences between analytical models and the LES results, a general overestimation of analytical wake models can be noticed again, especially at 10D, when the position corresponds to the 3rd wind turbine. Near the ground, the TI is also overestimated. However, the TI estimation shows fairly good agreement when compared to LES results.

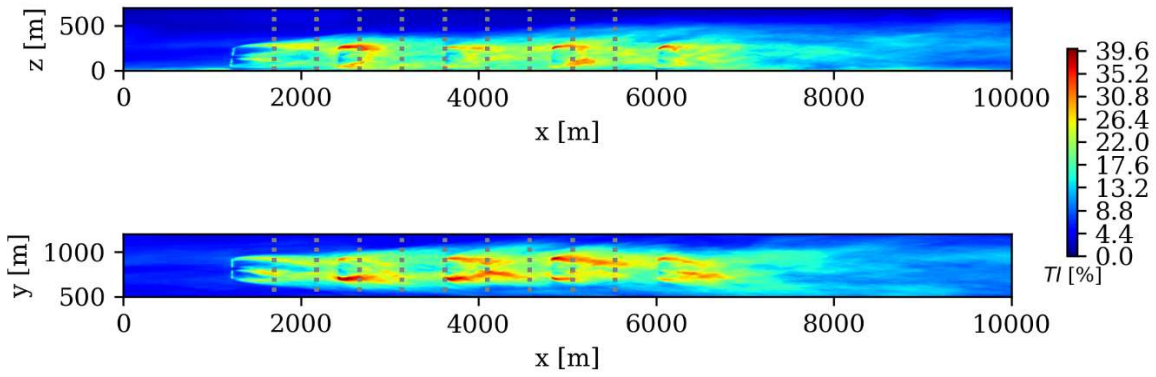

Figure 69. South Brittany vertical and horizontal fields of mean TI at row position and hub height, respectively. Selected positions to extract vertical and horizontal profiles downstream of the first WT (dashed grey lines).

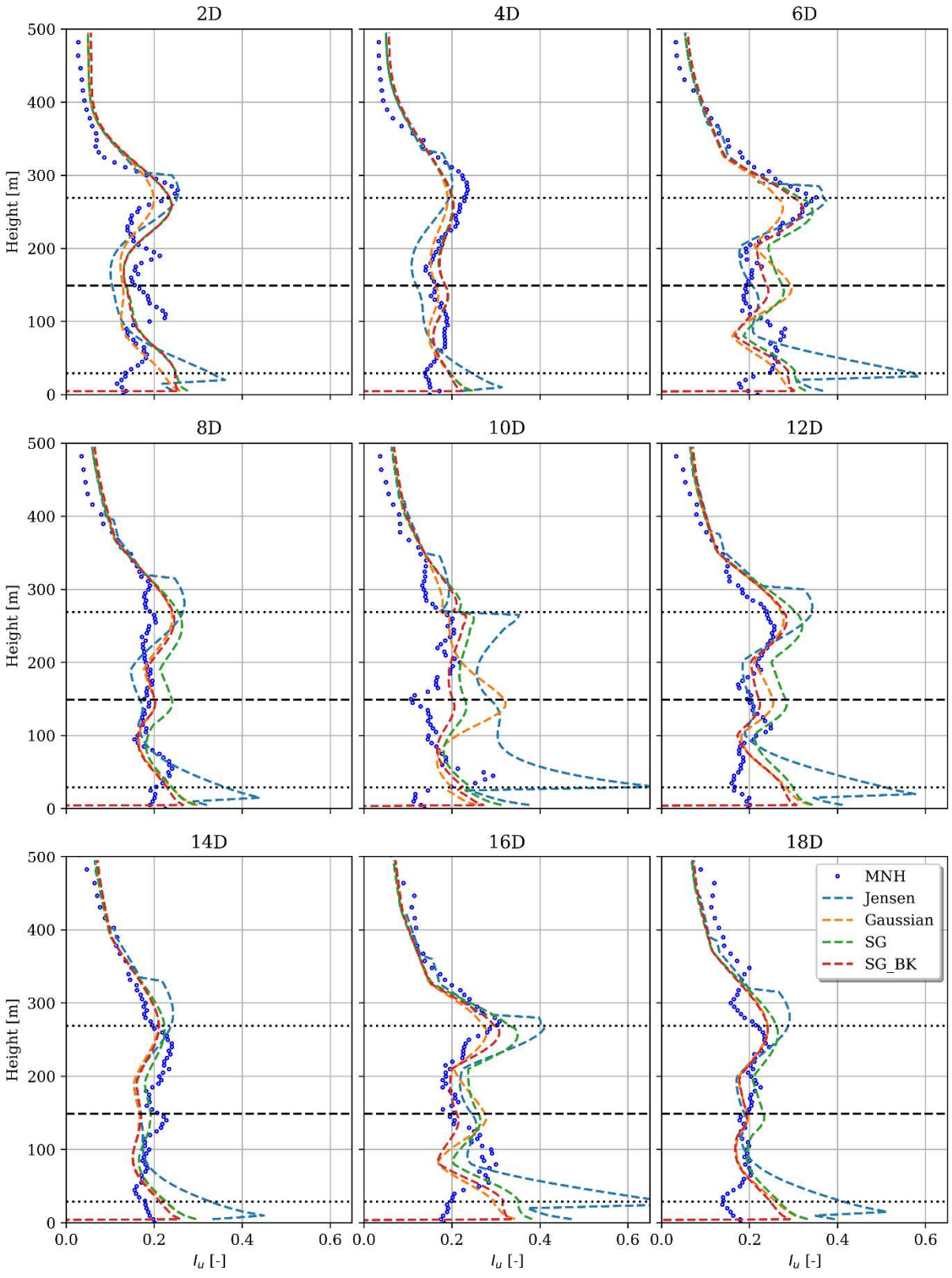

Figure 70: TI vertical profiles several diameters downstream of the first WT and for different models for South Brittany at below rated conditions

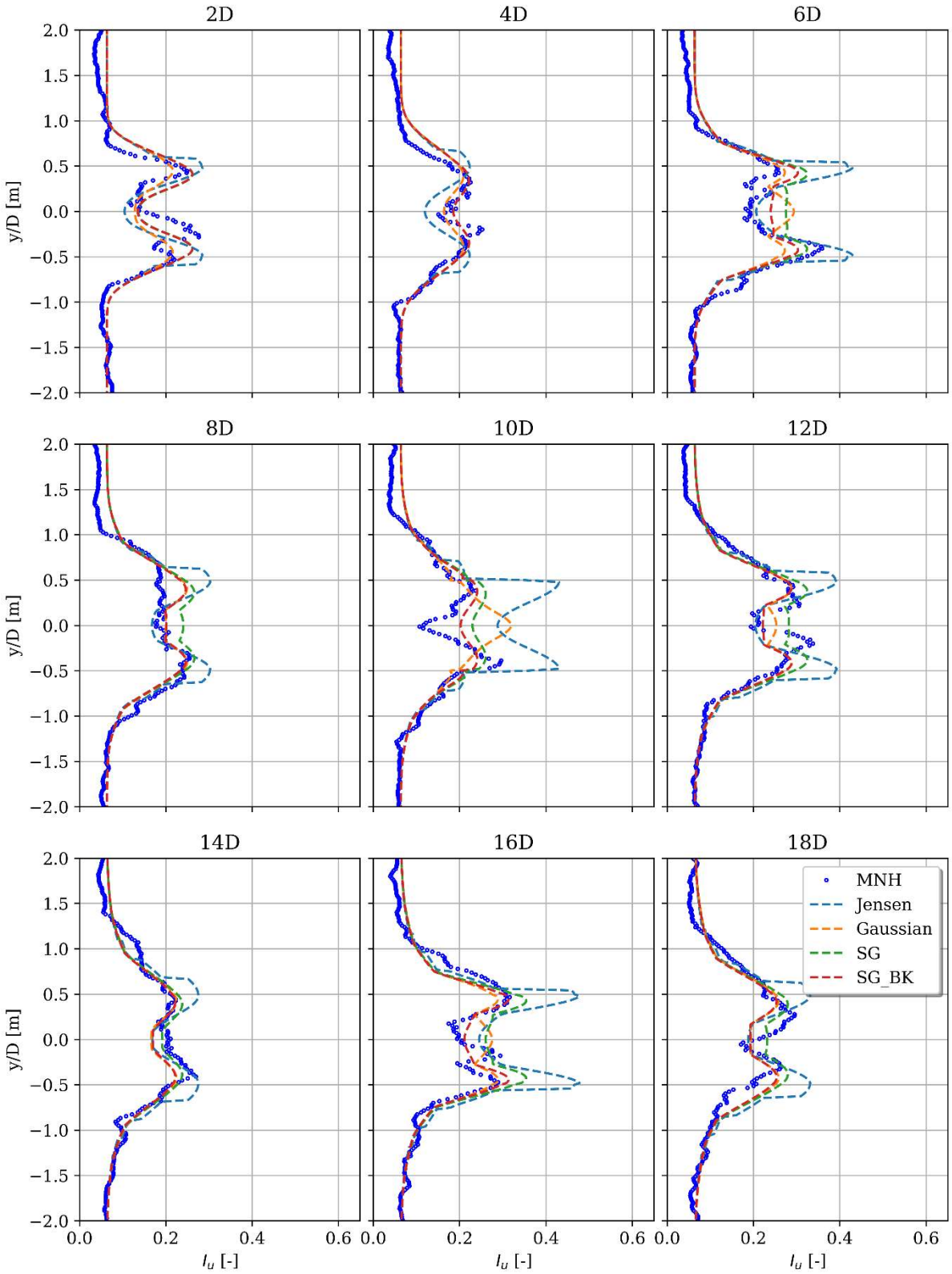

Figure 71: TI horizontal profiles several diameters downstream of the first WT and for different models for South Brittany at below rated conditions.

4.2.2.2.2 Rated

For the rated case (around 11 m/s at hub height) a similar analysis to the previous one has been performed. All the results for mean wind speed and *TI* are presented below, from Figure 72 to Figure 77. Both the results and the behaviours of these variables for this rated case are practically analogous to those found for the below rated case. While it is hard to conclude about the best analytical wake model combination, one can note that all the results show overall good correspondence.

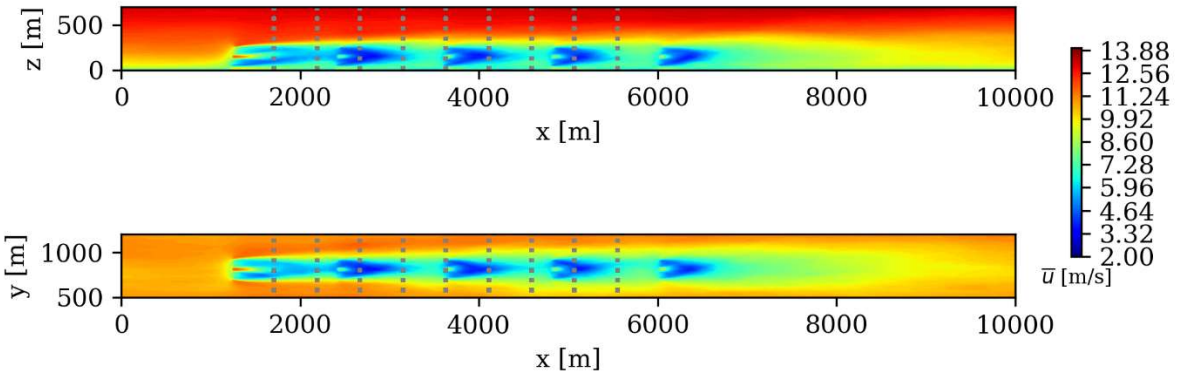

Figure 72. South Brittany vertical and horizontal cuts of mean wind speed at row position and hub height, respectively. Selected positions to extract vertical and horizontal profiles downstream of the first WT (dashed grey lines).

The pitch angle difference of the floater is slightly higher (see Table 12), as the thrust force is more important. By comparing the wind speed and turbulence intensity vertical profiles of Figure 73 and Figure 70, only a modestly greater vertical wake deflection can be observed for the rated case, especially for the first wind turbine (ie. at 2D and 4D). The same differences are observed at 2D and 4D, with a wider and stronger deficit predicted by Meso-NH. The extension of the wake above the rotor, mentioned before, seems less important in this case, indicating that the pitch of the floater may be not sufficient to explain it for the below rated case. However, if the width of the wake deficit was well evaluated by analytical models for the Teesside case, here, for this floating case, the width is underestimated when comparing against LES results. It is especially visible for the first wind turbine (2D, 4D for both below rated and rated), which is the one with the highest pitch of floater.

The TI profiles, shown in Figure 76 and Figure 77 are showing again reasonably good results, as mentioned for the rated case. The overestimation near the ground is still present.

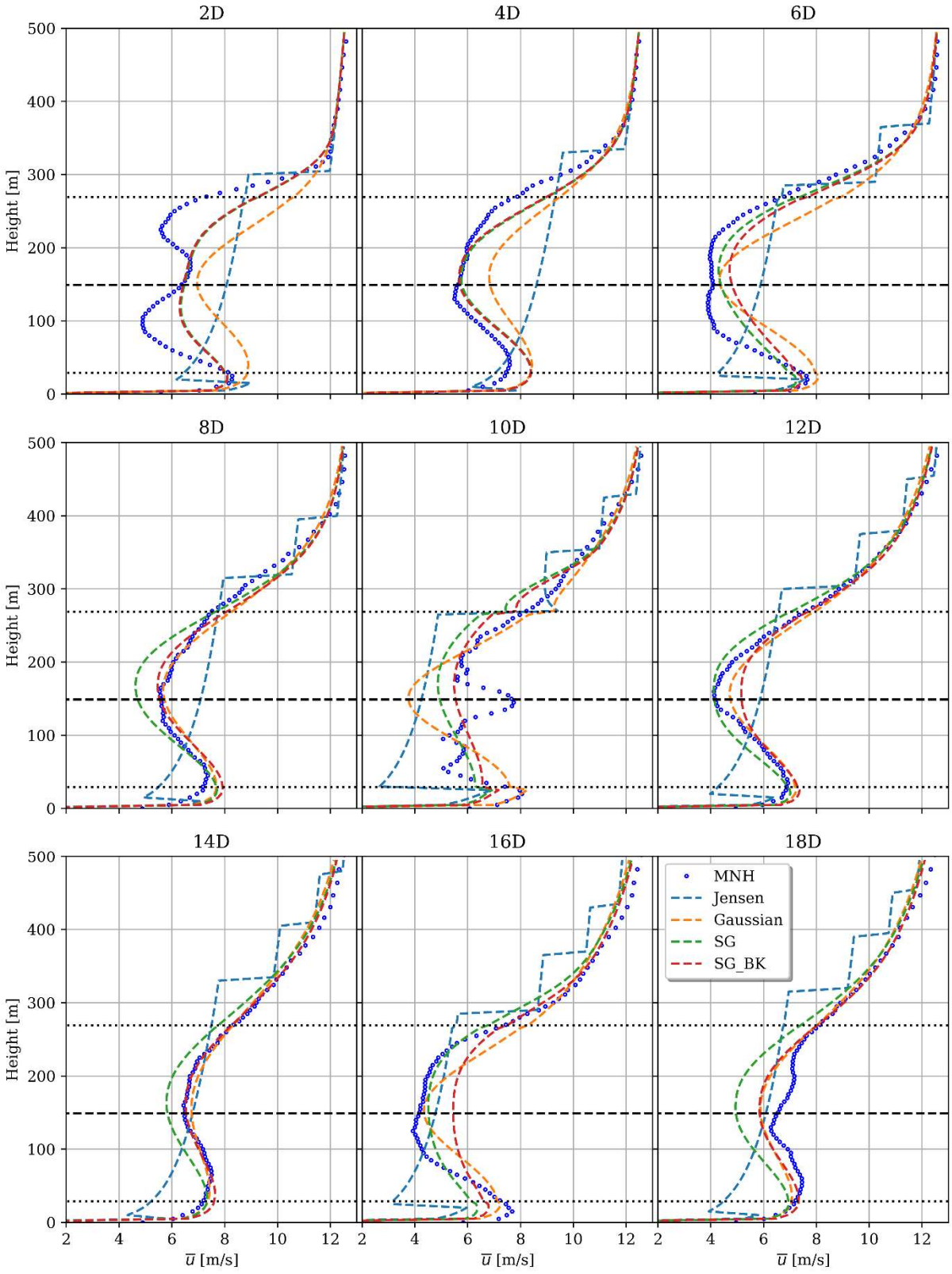

Figure 73. Wind speed vertical profiles several diameters downstream of the first WT and for different models for South Brittany at rated conditions.

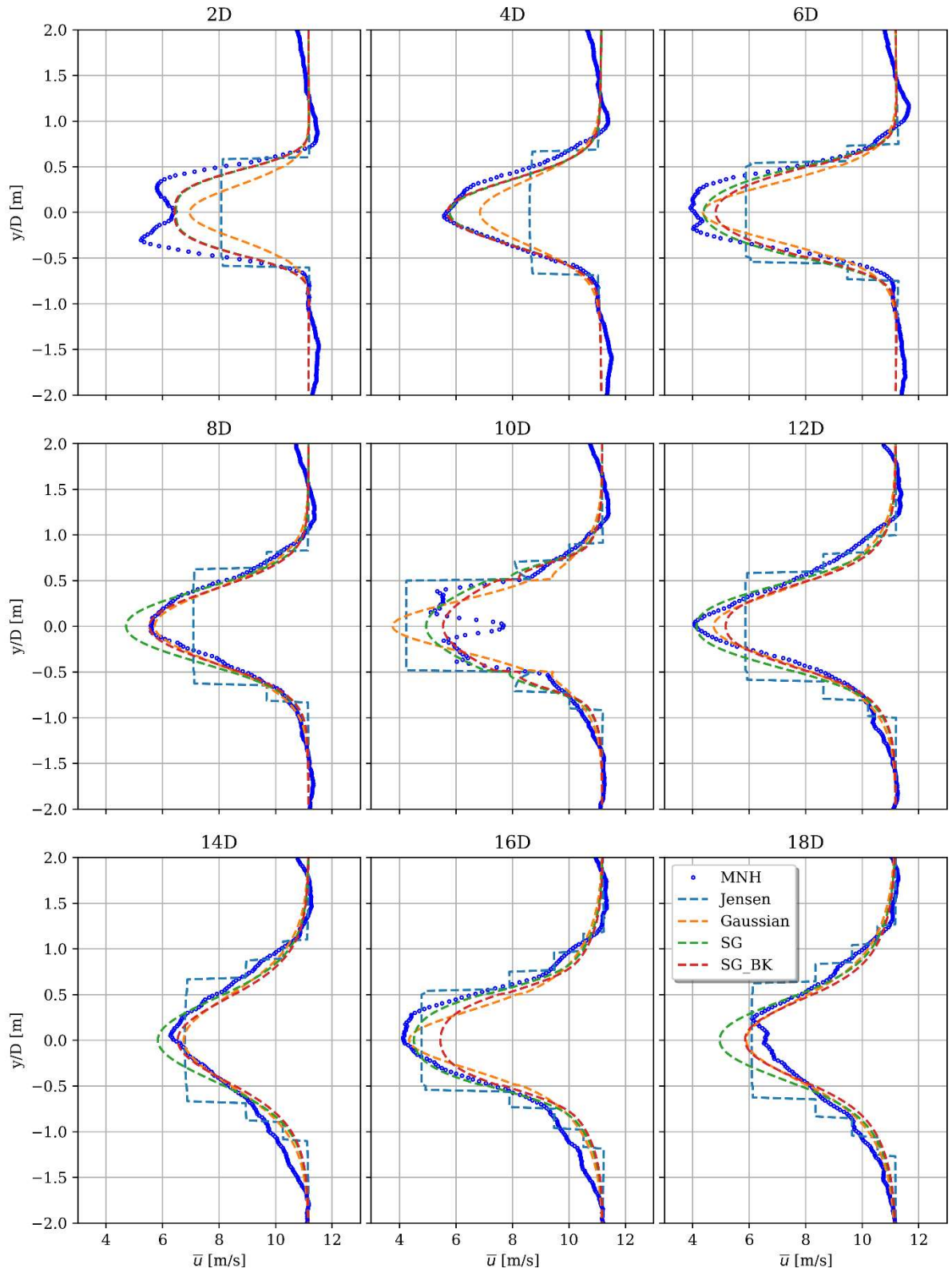

Figure 74. Wind speed horizontal profiles several diameters downstream of the first WT and for different models for South Brittany at rated conditions.

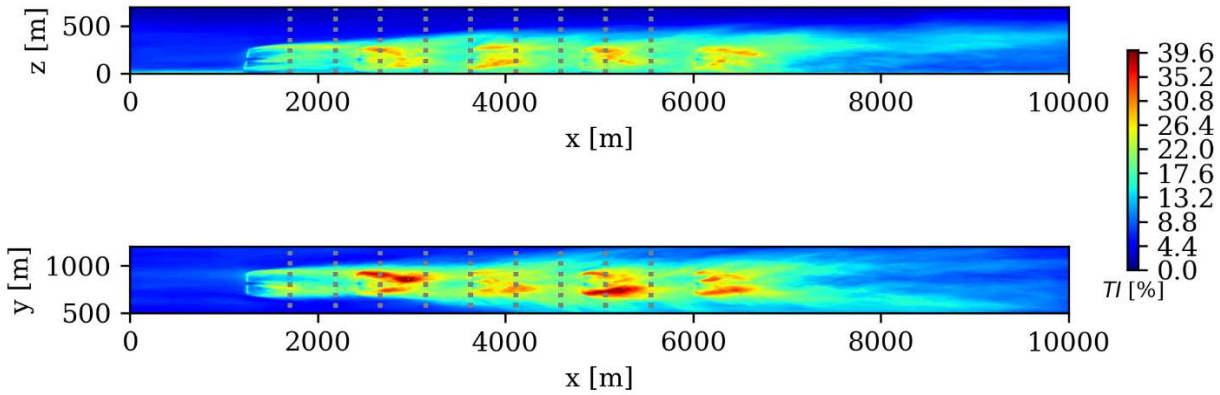

Figure 75. South Brittany vertical and horizontal cuts of mean TI at row position and hub height, respectively. Selected positions to extract vertical and horizontal profiles downstream of the first WT (dashed grey lines).

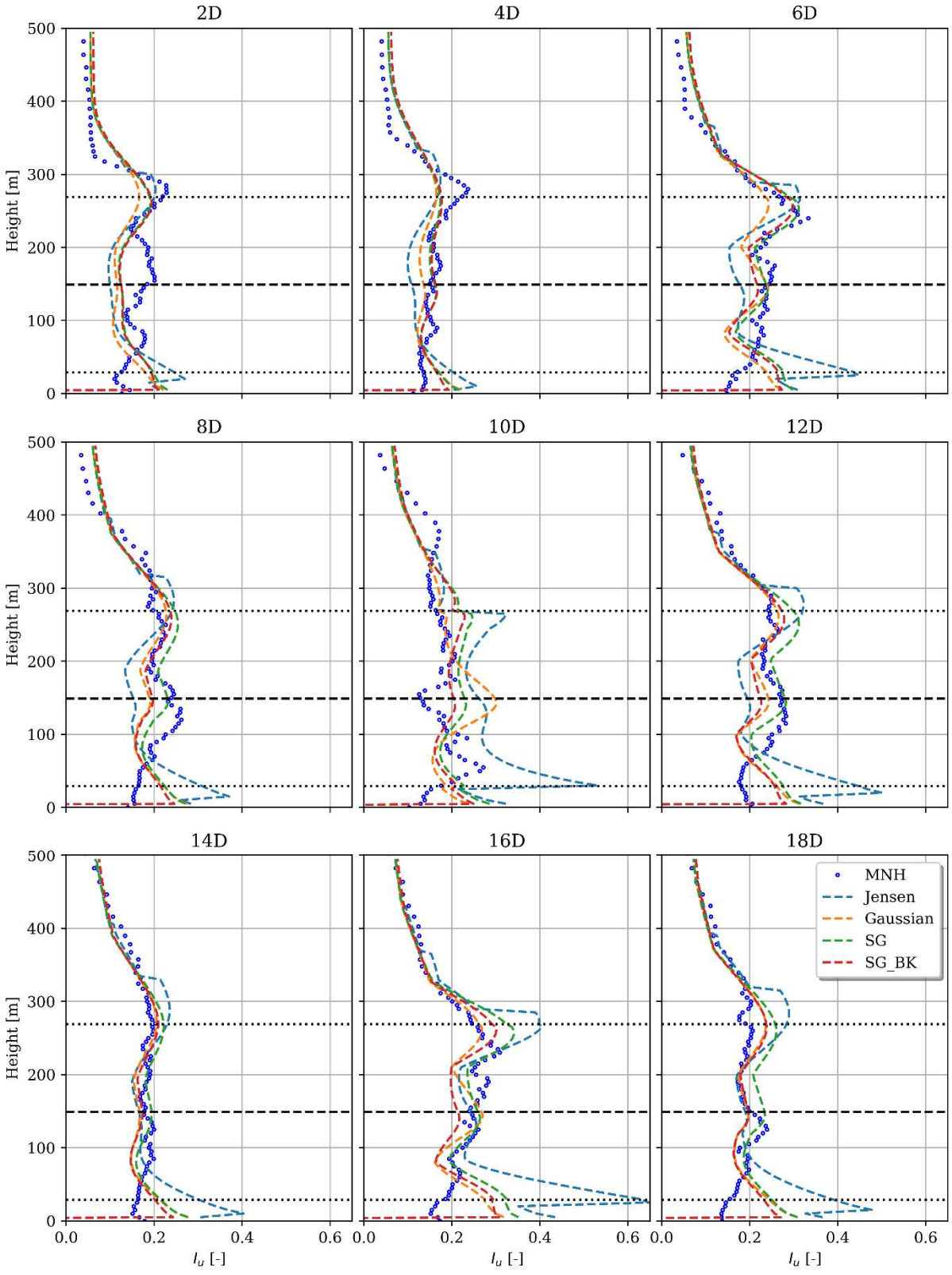

Figure 76: TI vertical profiles several diameters downstream of the first WT and for different models for South Brittany at rated conditions.

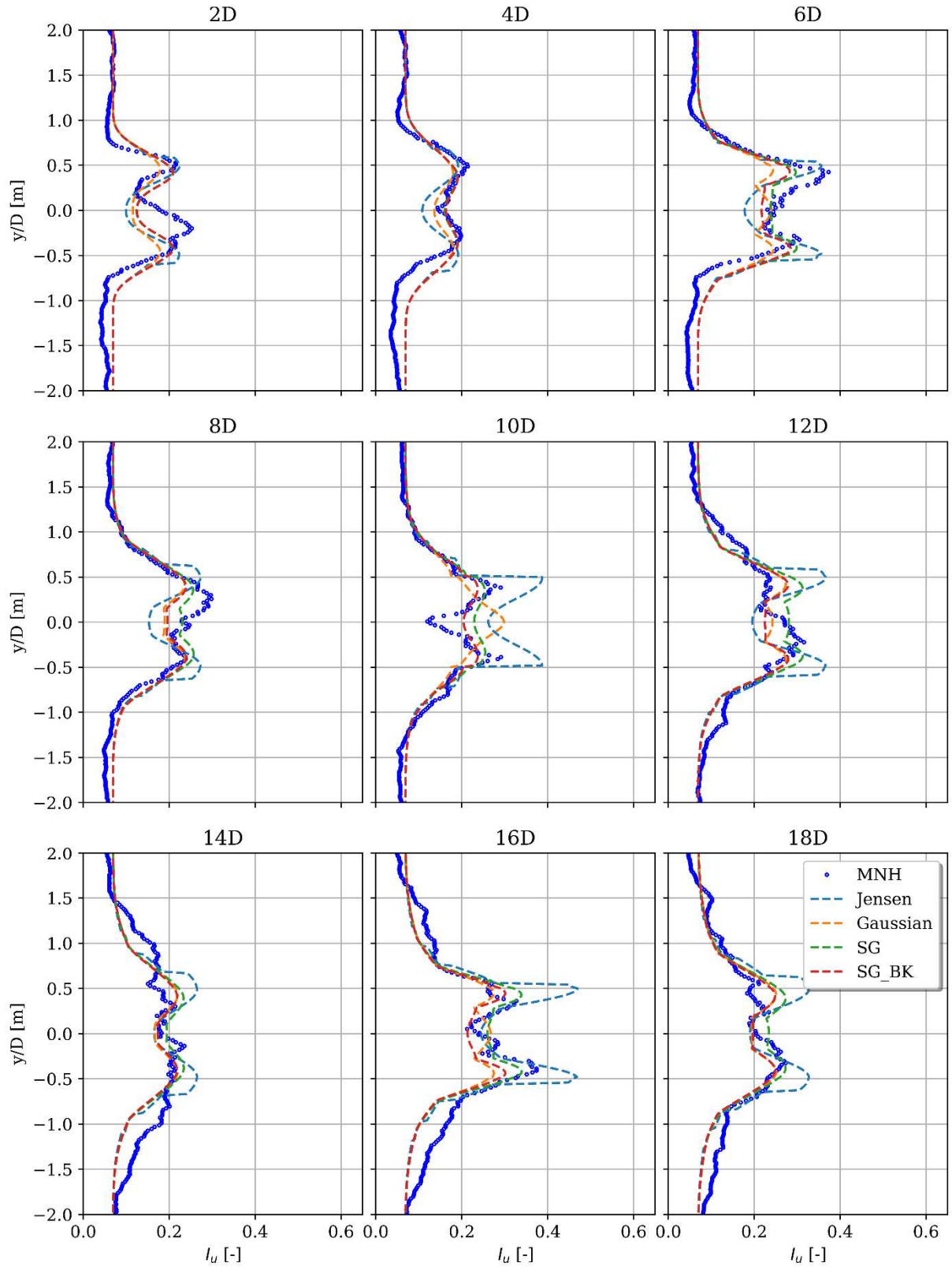

Figure 77. TI horizontal profiles several diameters downstream of the first WT and for different models for South Brittany at rated conditions.

4.3. Estimation with DWM reference for an extensive sampling of environmental conditions

Because of the tremendous computational cost of high-fidelity LES simulations, only a limited number of configurations was studied, to highlight the qualitative effects in wakes (atmospheric stability for Teesside use case, floater position for South Brittany). In this section, LES models are replaced by a less costly simulation but are still considered more representative than engineering models for wake physics. The DWM of DTU has been selected (see details in sections 2 and 4.1.3.3) which adds the low-frequency meandering variation in the wake model. Because of the additional stochastic effects present with the DWM (a realization-to-realization uncertainty due to the random seeds used in obtaining the wake meandering paths and the ambient turbulence fields), it is required to run several n_{DWM} replications of DWM simulations and compute a mean of the quantities of interest over the n_{DWM} simulations. In the following of this section, choice has been to select $n_{DWM} = 12$ which is expected to reduce the uncertainty in the mean of the quantities of interest by about 350% compared to the variance due to realization-to-realization uncertainty.

4.3.1. DoE generation

It is well known that the wake effect is firstly driven by the number of upstream wind turbines, and so by the horizontal direction (i.e. azimuth) of wind θ, as shown in the results of fatigue and extreme load on a WT within a farm in [92]. For this reason, a hybrid DoE will be built by considering first a regular sampling in θ and then for each θ value, a space filling sampling in two other dimensions which are ambient wind mean speed $\bar{u}$ and turbulence intensity $TI = \sigma_u/\bar{u}$. It would have also been of interest to add the atmospheric stability as an additional parameter, e.g. continuous parameter like the bulk Richardson number defined in section 4.2.1.1, to investigate the dependency of wake meandering on this stability. This additional dimension will not be considered here for lack of time but may be addressed to enrich the uncertainty quantification in future works.

This space-filling based on [93] is presented in section 5.2.1.1 of [87] and allows us to take into account a constraint of the domain with a joint dependence. For the sake of reducing the computational cost of DWM, it is also possible to take advantage of the symmetry of the wind farm layout for the two case-study of Teesside and South Brittany. When looking in detail at the Teesside layout 4.1.4.1, it appears that one row over two of WT is slightly offset in the crosswind direction so we have selected θ in $[180°, 360°]$ for Teesside. Then a Latin Hypercube Sampling (LHS) of 60 points has been computed to sample points in the $(\bar{u}, TI)$ domain. Two nonlinear boundaries, lower and upper, have been considered, to sample points in the most probable domain of $TI|\bar{u}$, including a part of the distribution tail (see Figure 78).

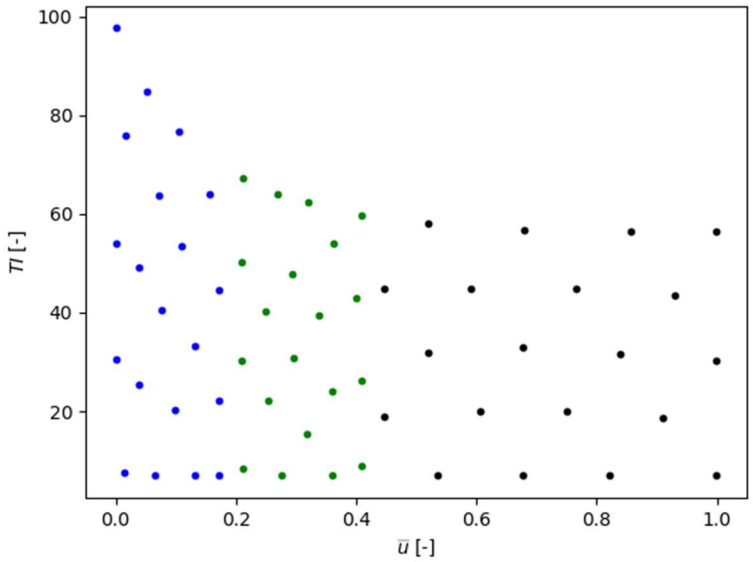

Figure 78: 60 points of the DoE in normalized $(\bar{u}, TI)$ space for DWM vs FarmShadow™ comparison of Teesside. Colours indicate 3 zones in $\bar{u}$ for which the 60 points have been equally distributed.

A similar hybrid DoE construction has been computed for the South Brittany use-case with the following distinctions. Firstly, in that case, the layout is perfectly regular. To account for the rectangle symmetry and encompass the crosswind direction at which maximum wake occurs, the θdomain has been chosen as [230°, 355°]. Secondly, for this case-study the distribution of $TI|\bar{u}$ has been chosen to follow the IEC-61400-1 recommendation of log-normal distribution defined by:

$$\mathbb{E}(\sigma_u|U) = I_{ref}(0.75\,\bar{u} + 3.8)\ m/s$$

$$Var(\sigma_u|U) = I_{ref}(1.4)^2\ m^2/s^2$$

with $I_{ref} = 0.14\ m/s$ for the IEA15MW class IB WT. We have then chosen to sample between Q1 and Q99 quantiles of $TI|\bar{u}$ with a constrained LHS methodology. Also to ensure enough sampling around the rated wind speed of the IEA15MW which is at 10.59 m/s, 3 zones in $\bar{u}$ domain have been defined with a predefined ratio of points: 24 points for $\bar{u}$ in [3m/s, 8m/s], 24 points for $\bar{u}$ in [8m/s, 13m/s] and the left 12 points for $\bar{u}$ in [13m/s, 25m/s]. The resulting DoE is shown in Figure 79.

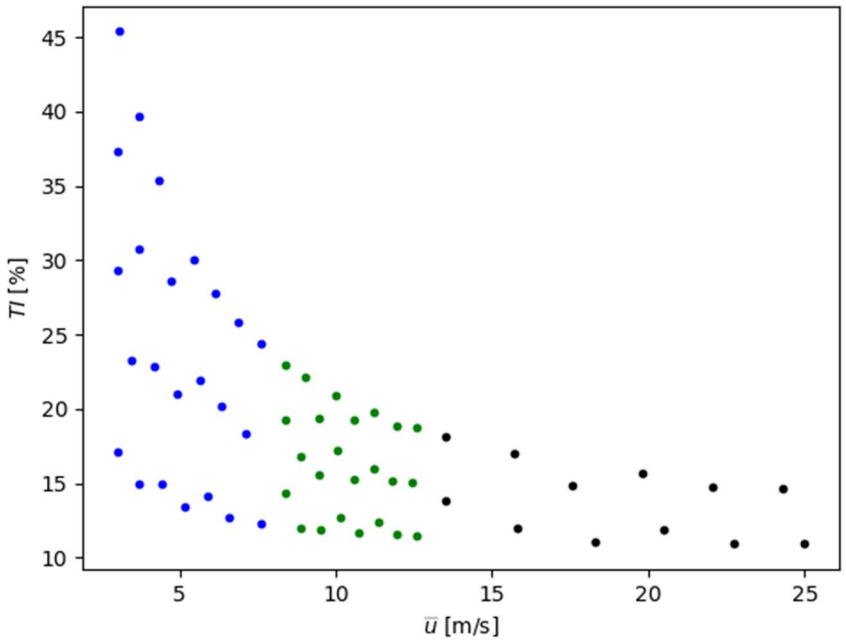

Figure 79: 60 points of the DoE in $(\bar{u}, TI)$ for DWM vs FarmShadow™ comparison of South Brittany. Colours indicate a preferential sampling according to 3 zones in $\bar{u}$ with 40%, 40% and 20% of total points respectively.

4.3.2. Comparisons between the analytical wake model and DWM

It is not practically feasible to explore the infinite set of all relevant scenarios through simulations to compare wake models with different fidelities. However, as many physical processes exhibit a smooth behaviour (i.e. differentiable), a regression model can be trained on a set of simulations and then used as a fast-running approximation, or surrogate model, for scenarios not explicitly simulated. That is, we want to approximate the costly simulation function f with an approximative function $\hat{f}$ such that:

$$\hat{y} = \hat{f}(\boldsymbol{x}) \approx y = f(\boldsymbol{x}_{sim}),$$

where $\hat{y}$ is the estimated response of the surrogate model at the input vector $\boldsymbol{x}$. The components of the vector $\boldsymbol{x}$ are the components of the full input vector of the simulator $\boldsymbol{x}_{sim}$ that dominate the response. Hence, $\boldsymbol{x} \in \mathbb{R}^{n_x}, \boldsymbol{x}_{sim} \in \mathbb{R}^{n_{x_{sim}}}$ with $n_x < n_{x_{sim}}$, where n_x is the number of parameters that are assumed to dominate the response and $n_{x_{sim}}$ is the number of input parameters of the simulator. Referring to the wake simulation problem, $n_{x_{sim}}$ represent the full set of parameters representing the ambient wind condition, with the assumption that OWT configuration is homogenous in the wind farm (see section 4 for more details on wind parameters). In this section, n_x represents the limited set of parameters $(\bar{u}, \sigma_u, \theta)$ which are the time averaged mean and standard deviation of ambient wind speed at hub height and the wind azimuth respectively (see section 4 for details on their definition).

Gaussian Process (GP), also known as Kriging, is one type of surrogate model that provides an estimate of the response and an empirical estimate of the uncertainty in this estimate. This section presents the GP regression models trained on both the FarmShadow™ and DWM simulations, quality metrics of the cross-validation, and quantification of the discrepancy between the two simulation models.

A GP is a stochastic process indexed by the input $\boldsymbol{x}$, where any finite set of outputs (corresponding to a finite set of inputs) is jointly normal. A GP $\hat{f} \sim \mathcal{GP}\big(\mu(\boldsymbol{x}), K(\boldsymbol{x}, \boldsymbol{x}')\big)$ can be viewed as a prior probability distribution over function $f: \mathbb{R}^{n_x} \rightarrow \mathbb{R}$ and is fully defined by its mean and covariance functions:

$$\mu(\boldsymbol{x}) = \mathbb{E}\big[\hat{f}(\boldsymbol{x})\big]: \mathbb{R}^{n_x} \rightarrow \mathbb{R},$$

$$\mathrm{K}(\boldsymbol{x}, \boldsymbol{x}') = \mathbb{E}\left[\Big(\hat{f}(\boldsymbol{x}) - \mu(\boldsymbol{x})\Big)\Big(\hat{f}(\boldsymbol{x}') - \mu(\boldsymbol{x}')\Big)\right]: \mathbb{R}^{n_x \times n_x} \rightarrow \mathbb{R}.$$

Here $\boldsymbol{x}$ is a vector in $\mathbb{R}^{n_x}$ which corresponds to a point in the input space. Let $\boldsymbol{X}$ be the $n_x \times N$ matrix of N input vectors, while $\boldsymbol{Y} = [\boldsymbol{y}_1, \ldots, \boldsymbol{y}_N]^T$ is the vector of the corresponding observations (in our case observation means simulations). The vector $\hat{\boldsymbol{f}}(\mathbf{X}) \sim \mathcal{N}(\boldsymbol{\mu}(\boldsymbol{X}), \boldsymbol{K}(\boldsymbol{X}, \boldsymbol{X}))$ is then multivariate Gaussian. Let's assume a noise on the outputs evaluated at $\boldsymbol{X}$ represented by a gaussian random vector with distribution $\mathcal{N}(\mathbf{0}, \sigma^2 \boldsymbol{I}_N)$. The distribution of function values at new observations (i.e., not yet computed simulation) inputs $\boldsymbol{X}^*$ can then be predicted as:

$$\mathbb{E}\big[\hat{\boldsymbol{f}}(\boldsymbol{X}^*) | \, \boldsymbol{X}, \boldsymbol{Y}\big] = \boldsymbol{\mu}(\boldsymbol{X}^*) + \boldsymbol{K}(\boldsymbol{X}^*, \boldsymbol{X})[\boldsymbol{K}(\boldsymbol{X}, \boldsymbol{X}) + \sigma^2 \boldsymbol{I}_N]^{-1}\big(\boldsymbol{Y} - \boldsymbol{\mu}(\boldsymbol{x})\big),$$

$$cov\big(\hat{\boldsymbol{f}}(\boldsymbol{X}^*) \,\big|\boldsymbol{X}, \boldsymbol{Y}\big) = \mathrm{K}(\boldsymbol{X}^*, \boldsymbol{X}^*) - K(\boldsymbol{X}^*, \boldsymbol{X})[K(\boldsymbol{X}, \boldsymbol{X}) + \sigma^2 \boldsymbol{I}_N]^{-1} K(\boldsymbol{X}, \boldsymbol{X}^*),$$

where $\hat{\boldsymbol{f}}(\boldsymbol{X}^*)|\boldsymbol{X}, \boldsymbol{Y}$ is the predictive posterior of $\boldsymbol{f}(\boldsymbol{X}^*)$ given the observed data $\boldsymbol{X}, \boldsymbol{Y}$ and $\boldsymbol{I}_N$ is the identity vector of dimension N

For a physical system with a continuous response, it is reasonable to select a covariance (kernel) function which is at least once differentiable. A much-used covariance function for physical systems is the Matérn5/2 kernel which is twice differentiable:

$$K(\boldsymbol{x}, \boldsymbol{x}') = \sigma_K^2 \left(1 + \sqrt{5}r + \frac{5r^2}{3}\right) exp\big(-\sqrt{5}r\big)$$

where:

$$r = \sqrt{\sum_{i=1}^{n_x} \frac{\big(x_i - x_i'\big)^2}{l_i}}$$

and l_i is the anisotropic length scale for each of the i dimensions. The length scale is an important hyperparameter that is optimized when training the GP so as the a priori kernel variance σ_K^2. See [94] for more details.

One alternative to an exact GP with a Gaussian noise model is the Stochastic Variational GP regression described in [95] and implemented in [96]. This approach has some advantages when it comes to data sets where there are a lot of data points that are in proximity, in the input space. However, one should note that it might also smoothen out the response as it is an approximative method that works by approximating the response around a set of selected inducing points.

The comparisons between the wake models were performed for the two different study case wind farms of HIPERWIND: the Teesside (UK) wind farm of EDF composed of OWT on monopiles, and the theoretical South Brittany (France) wind farm composed of IEA15MW OWT on UMaine semi-submersible floater.

4.3.2.1. Teesside results

To facilitate the reading of the following results, illustrates once again the layout of the Teesside wind farm, with the convention that wind direction is an azimuth (trigonometric and 0 at North).

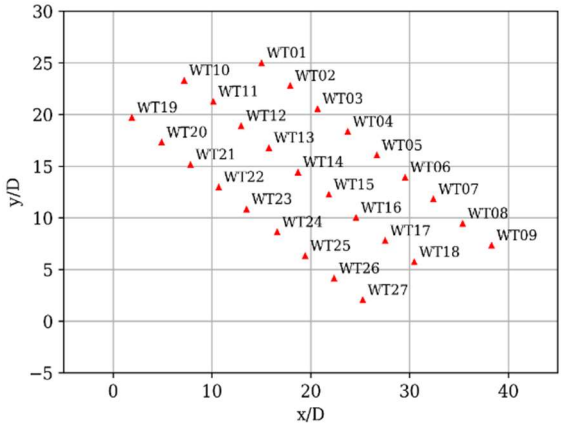

Figure 80: Teesside wind farm layout with North upward.

The input space Ω is defined as the set of $(\bar{u}, \sigma_u, \theta)$, see section 4.3.1 for details on the DoE. The quantities of interest are $\bar{u}_{rotor}$ and $\sigma_{u_{rotor}}$ which are the mean and standard deviation of wind speed averaged over the rotor surface respectively. The outputs are a result of a wake simulation with FarmShadow ™ analytical and stationary model and the DWM dynamic model (see section 4.1 for details on these models). Let us remind you that the DoE was run at the central WT no 14 which was selected to get a representative distribution of $\bar{u}_{rotor}$ and $\sigma_{u_{rotor}}$. The DWM model uses random realizations of turbulence, leading to a statistical (realization-to-realization) uncertainty where different average wind fields are obtained with each realization. To reduce the statistical uncertainty, the simulator has been run for 12 different seeds sampling the dynamic meandering distribution. For comparison with the deterministic FarmShadow™ model, the quantities of interest have been taken as the mean response of each DWM replication (i.e. set of 12 seeds results). In both models, the same power law is used for the ambient wind conditions. Last, for this case study, DWM superposition rules follow the recommendation of [70] with a single (closest WT) deficit for below rated wind speeds and a summation of deficits for above rated wind speeds.

Two independent GPs were built to represent the responses from the two simulation models FarmShadow™ and DWM. The quantity of interest is the effect of the mean wind speed and turbulence on a wind turbine rotor inside the wind farm, compared to the free-field (i.e. ambient) wind speed and turbulence. To accommodate a zero-mean GP, the response was normalized by the free-field wind speed $\bar{u}$ and turbulence, i.e., for the resulting wind speed

$$f_u = \frac{\bar{u}_{rotor}}{\bar{u}} - 1$$

and similarly for the turbulence

$$f_{\sigma_U} = \frac{\sigma_{u_{rotor}}}{\sigma_u} - 1$$

The dataset consists of 5460 simulations for each model. Figure 81 shows the FarmShadow™ and DWM model normalized quantities of interest. The two model predictions are close except for a few points at crosswind direction (θ around 308°) and low $\bar{u}$, for which DWM points seems to predict very high wind speed deficit and added turbulence. This may be suggesting additional investigations of the wake superposition empirical assumptions for that configuration.

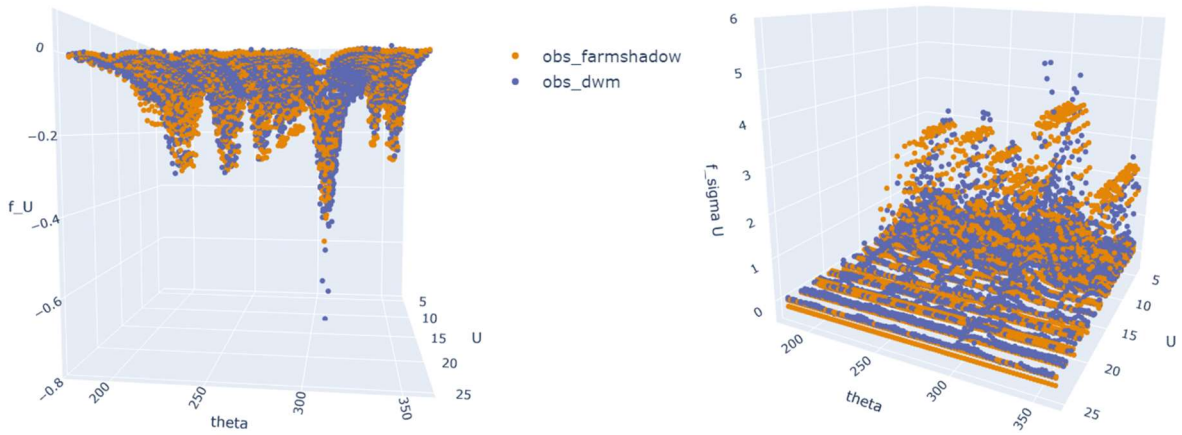

Figure 81 : Teesside: FarmShadow™ and DWM model results: f_u on the left, and f_{σ_u} on the right.

A GP is fully defined by the selected mean function, kernel function, the optimized (trained) hyperparameters, and the data used to optimize it.

In Figure 82 below, each input scenario simulated by both the FarmShadow™ and DWM simulator has been plotted. In the $\bar{u}$ and σ_u input dimensions, both simulators have been run at 60 unique input combinations. For each of these 60 unique combinations of $\bar{u}$ and σ_u, the simulators have been run for every 2 degrees between 180 and 360, resulting in 91 unique wind directions. This results in a DoE which is much denser in the wind direction dimension (θ) compared to the wind speed ($\bar{u}$) and turbulence (σ_u) dimensions. This can be seen as "cylinders" of simulation results that are very close to their neighbour observations in the θ dimension in Figure 82.

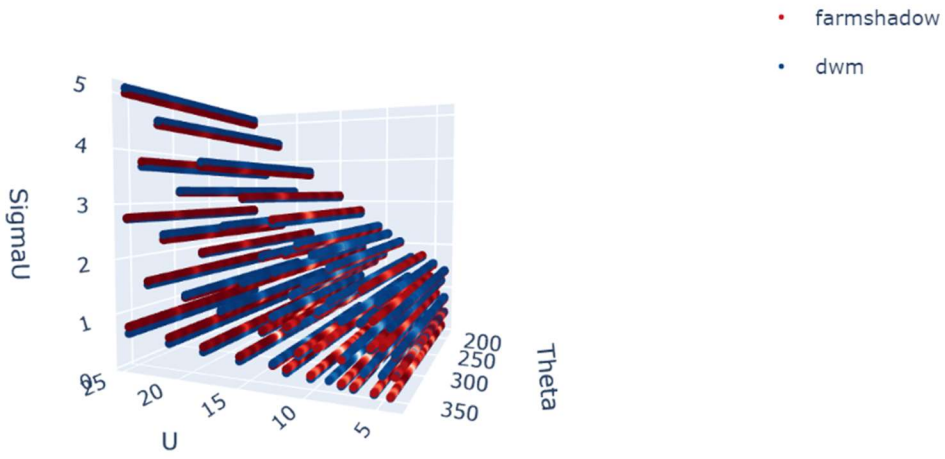

Figure 82: Input space for all simulation runs from the FarmShadow™ simulator (reds) and the DWM simulator (blues).

This “clustering” of data in one dimension may lead to the optimization of the GP hyperparameters relying too much on the covariance between the training data. To avoid this, a stochastic variational approach to estimate a GP has been used. This method approximates the response close to a set of inducing points and uses these as part of the hyperparameters to optimize the GP. To train a stochastic variational GP (SVGP), one has to select a variational distribution and variational strategy. The SVGP in this work has been optimized using the python package GPyTorch [96] and the optimization routines of the tensor package PyTorch [97]. The SVGPs have been optimized using a Natural Variational distribution and the standard variational strategy as described in [95]. The Adam optimizer with variational evidence lower bound (ELBO) has been used to approximate the Marginal log-likelihood loss function to optimize the GP. The parameters that have been optimised are 1) the location of the inducing points, 2) the likelihood (variance) at the inducing points, and 3) the kernel hyperparameters.

Figure 83 shows a trained SVGP fitted to the normalized f_u and Figure 84 a trained SVGP fitted to the normalized f_{σ_u}, together with the original observations (i.e. simulation results). On the left is the model for the FarmShadow™ simulator and on the right for the DWM simulator. Note that the input space is normalized using a standard scaler to remove the mean and scale it to unit variance before training. New predictions must be done using the same scaling, and results must be re-scaled for comparison with the original simulation results.

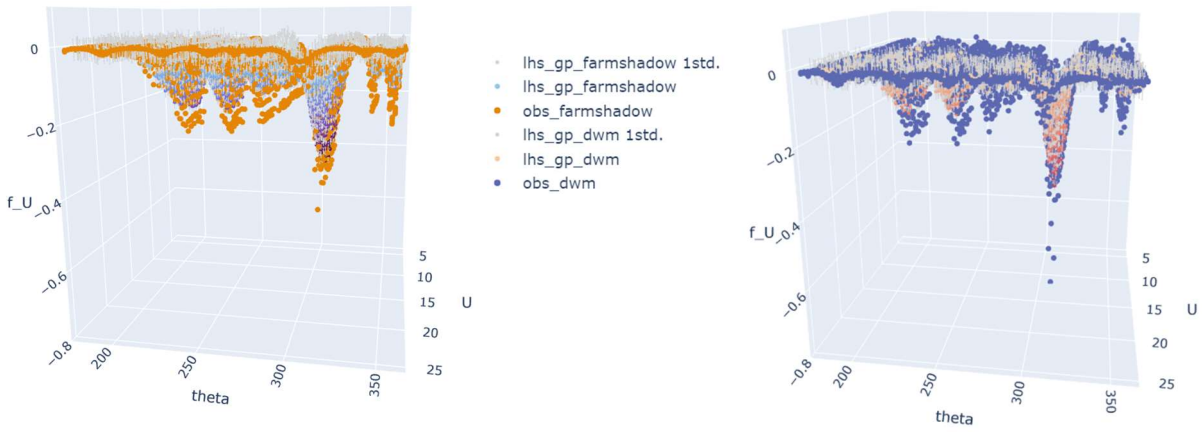

Figure 83 : Teesside: GP prediction of the f_u for a large LHS. Error bars (grey) correspond to the standard deviation (std) of the GP. Orange and purple points correspond to simulated responses from FarmShadow™ and DWM simulations, respectively. Left: GP for the FarmShadow™ simulator. Right: GP for the DWM simulator.

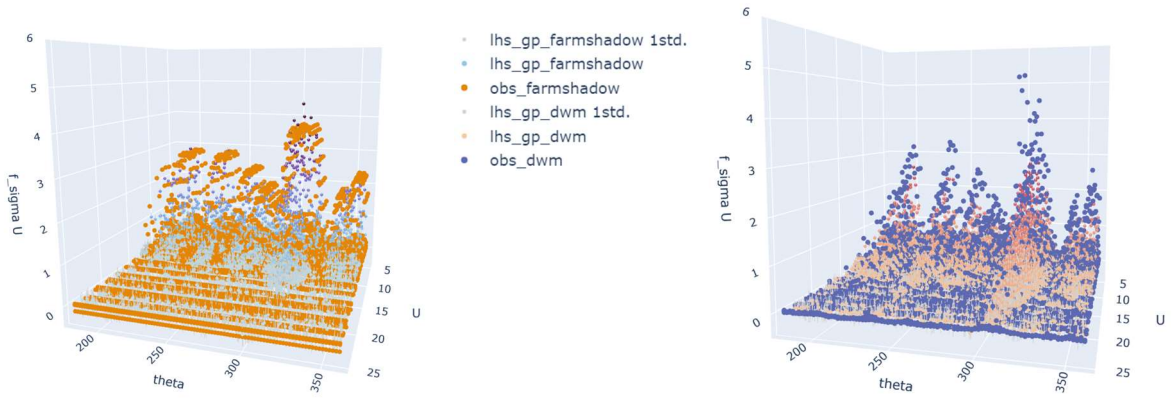

Figure 84 : Teesside: GP prediction of the f_{σ_u} for a large LHS. Error bars (grey) correspond to the std of the GP. Orange and purple points correspond to simulated responses from FarmShadow™ and DWM simulations, respectively. Left: GP for the FarmShadow™ simulator. Right: GP for the DWM simulator.

As can be seen in Figure 83 and Figure 84, the fitted SVGP fits reasonably well with the observations it is trained on. However, as a lot of the observations, or simulation results, are in proximity to the input space, it is important to check that the GP is not overfitting. To validate how well the model generalizes and avoids overfitting, prediction residuals have been calculated using the leave-one-(group)-out cross-validation (CV) technique.

For each unique combination of $\bar{u}$ and σ_u (see Figure 82), there will be 91 simulations where only the wind direction is varying. Simulations that are close together in the input space must be excluded together to avoid overconfident cross-validation. The simplest way to ensure this is to exclude the entire set of 91 simulations that share the same input combination in the $(\bar{u}, \sigma_u)$ input space when doing the cross-validation. The cross-validation has been done with the optimized hyper-parameters according to the formulation in [98] and the implementation in [99], where each fold contains the entire set of simulations with unique input combinations of $\bar{u}$ and σ_u.

In Figure 85 three plots illustrate the prediction accuracy of the GP for each of the selected responses. On the left, a Quantile-Quantile (QQ) plot shows the standardized CV residual plotted as quantiles against the theoretical quantiles of a standard normal distribution. In the middle, the distribution of the CV residuals (histogram) and the corresponding estimated probability density using kernel-density-estimate (KDE) are compared to the probability distribution of the standard normal distribution. On the right, the CV normalized predictions are plotted against the true normalized observations in a unity plot. In the right-most plot, all points that are on the dashed black diagonal indicate a "perfect" prediction. The GPs are generally accepted as good models when the predictions including their uncertainty are close to the unity line, and when the prediction uncertainty is sufficiently small (i.e. where the uncertainty is less than what is needed to discriminate between the relevant decisions based on the predictive responses).

For both f_u and f_{σ_u}, the distribution of residuals is narrower than what is expected from a Gaussian distribution. From Figure 83, Figure 84, and Figure 85, it is clear that most of the observations have f_u and f_{σ_u} of small amplitudes corresponding to a small wake effect. The GP is generally representing this part of the input space quite well, and thus a quantile plot will be dominated by the low uncertainty/high accuracy of these observations. Note that for a few points with higher wake effects, i.e. where f_u is close to 0.8, the GP underpredict the wind speed deficit (Figure 83) and the added turbulence (Figure 84). This can also be

noticed in the prediction vs observations plots on the right column of Figure 85 for which the large wake points are the smallest for f_u and the highest for f_{σ_u}.

These GPs are thus a reasonable approximation for the lower response values, but one needs to be cautious when approximating more high wake effects.

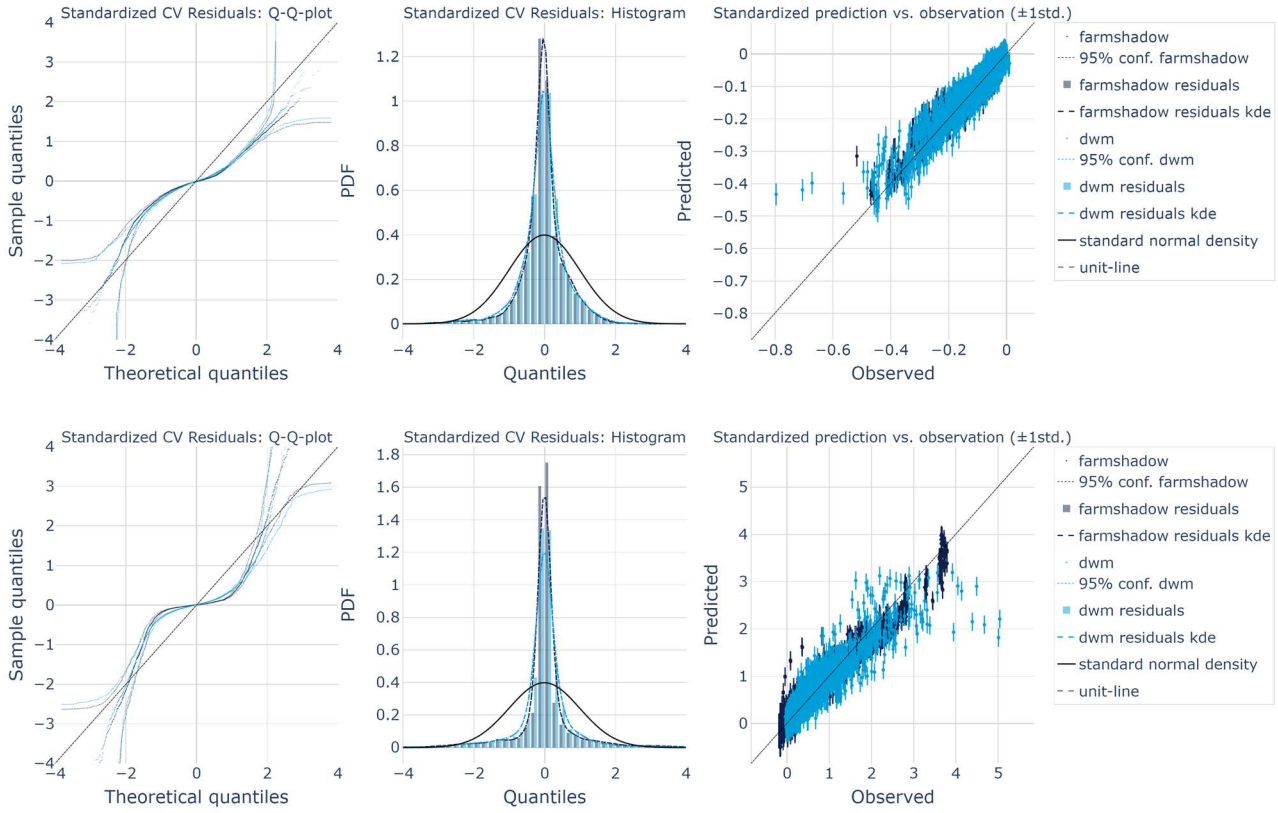

Figure 85 : Teesside: For each of the standardized quantities of interest: (left): plot of the Theoretical vs. Sample quantiles of the CV residuals, (middle): corresponding distribution of CV residuals, (right): CV prediction vs true observation including 1 std. From top to bottom, the plots represent the distribution of f_u and f_{σ_u}.

Figure 86 presents the difference between FarmShadow™ GP minus and DWM GP for both quantities of interest. It helps for instance to see that despite f_{σ_u} may be greater for DWM than for FarmShadow™ on observations for a few points at low wind speed and crosswind direction (Figure 84), the dominant trend for GP at that location is the contrary. It may be noted however that Figure 86 does not enable us to distinguish the difference in the 3rd dimension of turbulence.

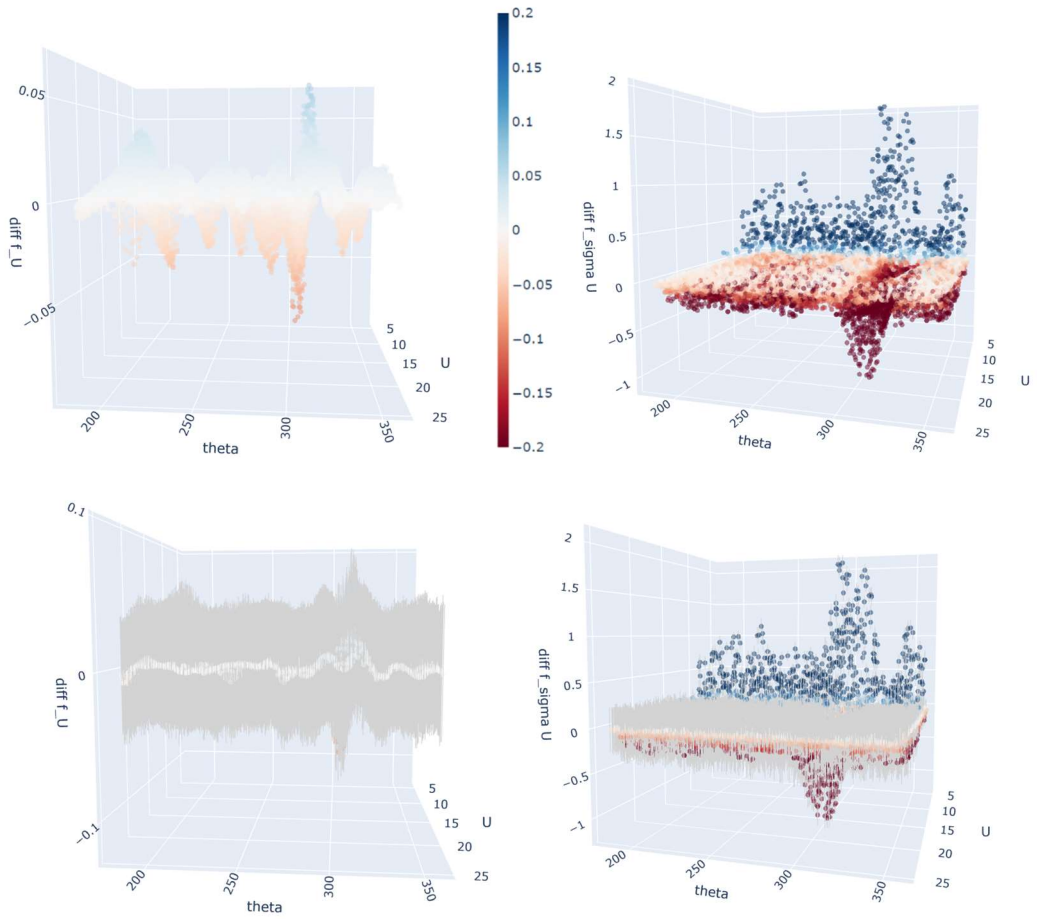

Figure 86 Teesside: Difference between GP predictions from FarmShadow™ and DWM coloured from red to blue (top). Error bars (grey) correspond to the std of the GP (bottom). Left: f_u. Right: f_{σ_u}.

To facilitate the view of GP uncertainty, Figure 87 and Figure 88 show 2D slices of GP predictions for both normalized quantities of interest as plotted in Figure 83 and Figure 84. In these plots, two input parameters are fixed and one is varying (see legends of the figures for detail). The highest difference between DWM and Farmashadow™ models occurs at mean wind speed U lower than 15 m/s and wind azimuth θ around 308° for both f_u and $\mathrm{f}_{\sigma_\mathrm{u}}$ but most significantly to $\mathrm{f}_{\sigma_\mathrm{u}}$. These values correspond to the crosswind direction (orthogonal to the dominant wind direction), for which the number of upstream wind turbines is the highest, and the inter-turbine distance is the smallest. The larger difference in turbulence prediction may derive from the different assumptions of the models (see section 2 and section 4.1.3) and suggest future work for checking these model turbulence predictions against data or LES simulations.

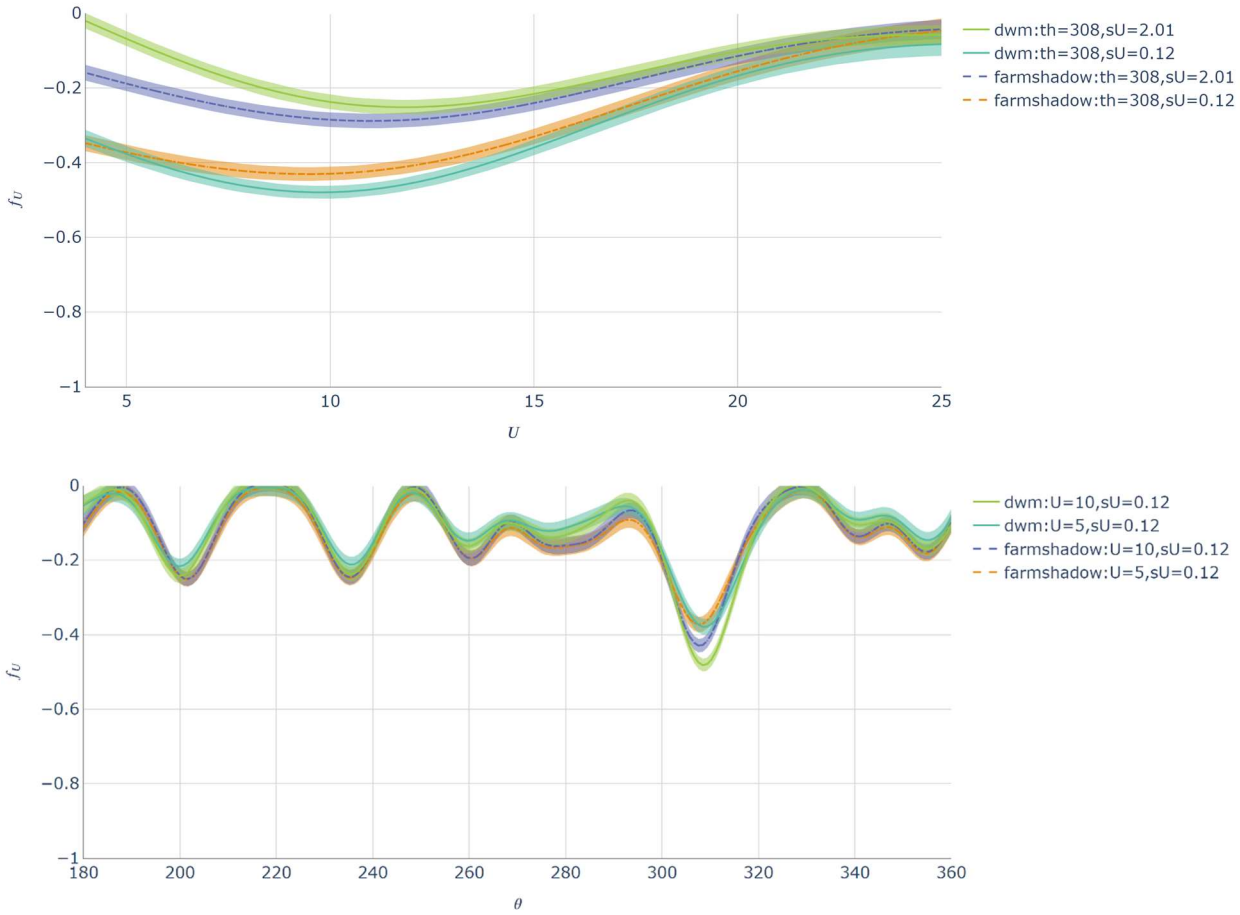

Figure 87 : Teesside: f_U GP predictions from FarmShadow™ and DWM. Top: fixed input parameters θ=308°, σ_u set to 0.12 and 2.01 and varying $\overline{u}$. Bottom: fixed input parameters $\overline{u}$ set to 5 and 10, σ_u=0.12 and varying θ.

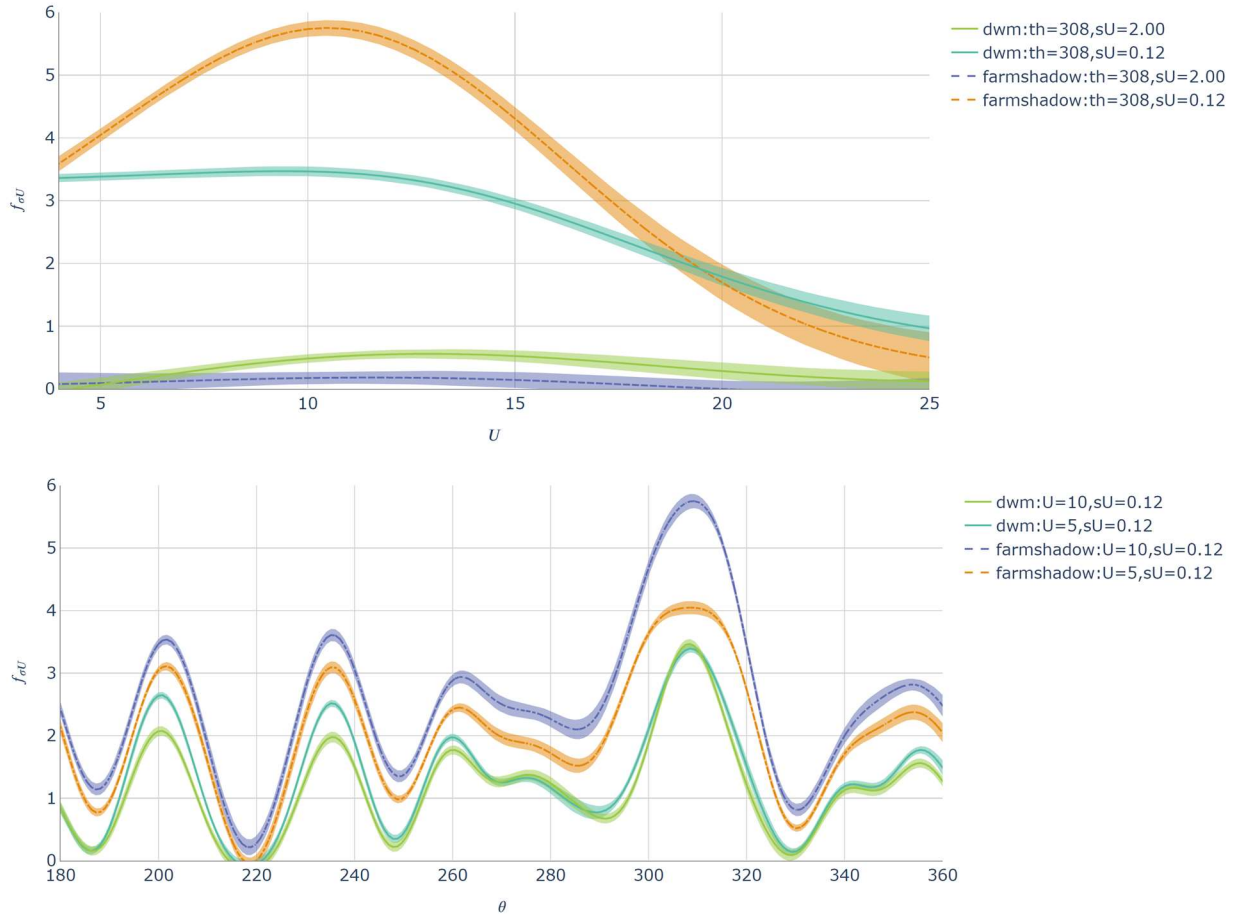

Figure 88 : Teesside: f_{σ_u} GP predictions from FarmShadow™ and DWM. Top: fixed input parameters θ equal 308°, σ_u equal 0.12 and 2.00 and varying $\overline{u}$. Bottom: fixed input parameters $\overline{u}$ equal 5 and 10, σ_u equal 0.12 and varying θ.

Let us note $\hat{f}_{\mathrm{u}}^{\mathrm{F}}(\boldsymbol{x})$ (resp. $\hat{f}_{\sigma_u}^{\mathrm{F}}(\boldsymbol{x})$) the GP on f_u (resp. f_{σ_u}) from FarmShadow™ simulations at a point $\boldsymbol{x}$ of the 3D input space. Similarly, a D superscript will denote the same GP built from DWM simulations. Then if denoting the parameters as:

$$\hat{f}_{\mathrm{u}}^{\mathrm{F}}(\boldsymbol{x}) \sim \mathcal{N}\left(\mu^{\mathrm{F}}(\boldsymbol{x}), K^{\mathrm{F}}(\boldsymbol{x},\boldsymbol{x})\right) \quad \text{and} \quad \hat{f}_{\mathrm{u}}^{\mathrm{D}}(\boldsymbol{x}) \sim \mathcal{N}\left(\mu^{\mathrm{D}}(\boldsymbol{x}), K^{\mathrm{D}}(\boldsymbol{x},\boldsymbol{x})\right),$$

Eq 2

the difference between the two models is also a GP which can be written as:

$$\hat{f}_{\mathrm{u}}^{\mathrm{F-D}}(\boldsymbol{x}) = \hat{f}_{\mathrm{u}}^{\mathrm{F}}(\boldsymbol{x}) - \hat{f}_{\mathrm{u}}^{\mathrm{D}}(\boldsymbol{x}) \sim \mathcal{N}\left(\mu^{\mathrm{F}}(\boldsymbol{x}) - \mu^{\mathrm{D}}(\boldsymbol{x}), K^{\mathrm{F}}(\boldsymbol{x},\boldsymbol{x}) - K^{\mathrm{D}}(\boldsymbol{x},\boldsymbol{x})\right).$$

Eq 3

The same summation rule holds for the difference on f_{σ_u} GP which is denoted $\hat{f}_{\sigma_{\mathrm{u}}}^{\mathrm{F-D}}(\boldsymbol{x})$.

Let us now try to provide some quantitative information on $\hat{f}_u^{F-D}(\boldsymbol{x})$ which could be used if one wants to apply an RBD in this case study. The following figures display histograms based on a large Latin Hypercube Sample (LHS) with approximately 30k points across the entire input space. Each histogram represents a series corresponding to a bin of a dimension of the input space or a bin of $\hat{f}_u^{F}(\boldsymbol{x})$. Each histogram is normalized by the number of observations in the series while the fraction of all observations in each series is specified in the legend. Each figure is composed of two plots. The left-hand side plot represents $\hat{f}_u^{F-D}(\boldsymbol{x})$ or $\hat{f}_{\sigma_u}^{F-D}(\boldsymbol{x})$ GP. The right-hand plot represents the corresponding std of this GP which gives and empirical estimate of the GP uncertainty.

As can be seen in Figure 89, the largest absolute values of $\hat{f}_u^{F-D}(\boldsymbol{x})$ occur where the wind speed deficit is most prominent (orange and purple histograms on the left plot) with a 95th percentile at 4.9% (where DWM predicts more wind deficit than FarmShadow^{TM}) and a 5th percentile of -6.4% (where DWM predicts less wind deficit than FarmShadow^{TM}). Such differences are however limited in occurrence (see n/N in the right legend) and correspond to a wind direction θ around the crosswind direction, between 300° and 320° (Figure 91). The largest differences are negative and correspond to the low wind speed of fewer than 5 m/s, as indicated by Figure 90, and moderate turbulence (when compared to the maximum turbulence plotted in Figure 82) as shown by the top plot (crosswind direction) of Figure 87.

However, for 89.4% of the observations, where $\hat{f}_u^{F}(\boldsymbol{x}) \in [-0.11, 0.02]$, with the 5th and 95th percentiles equals to -1.2% and 1.7%. The associated uncertainty is measured by the std of $\hat{f}_u^{F-D}(\boldsymbol{x})$ which is between 3.9% and 2.4% (5th and 95th percentiles respectively). Also, Figure 90 represents the same histograms but according to bins of $\bar{u}$. The std ordering, between the different bins in $\bar{u}$, is related to the choice of the percentage of simulation which was done in the initial DoE (see section 4.3.1).

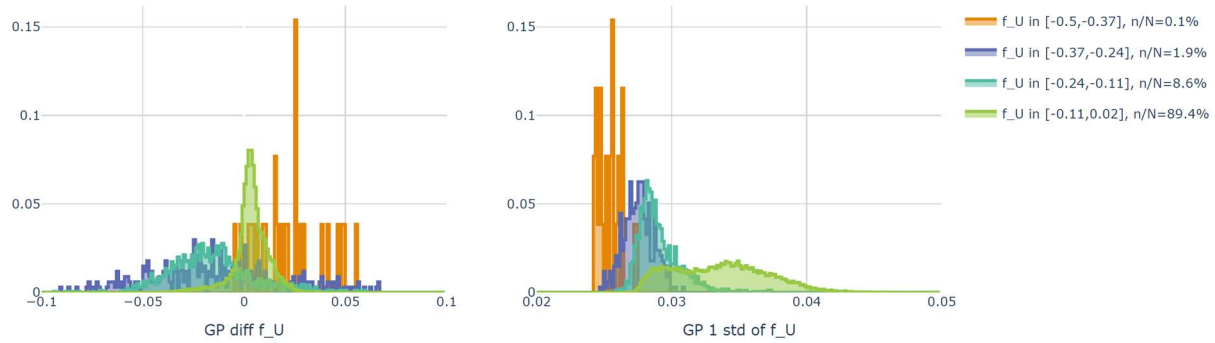

Figure 89 : Teesside: Histograms of $\hat{f}_u^{F-D}(\boldsymbol{x})$ (left) and of its std (right). Each histogram is normalized by the number of observations of the $\hat{f}_u^{F}(\boldsymbol{x})$ bin indicated by the color in the total LHS.

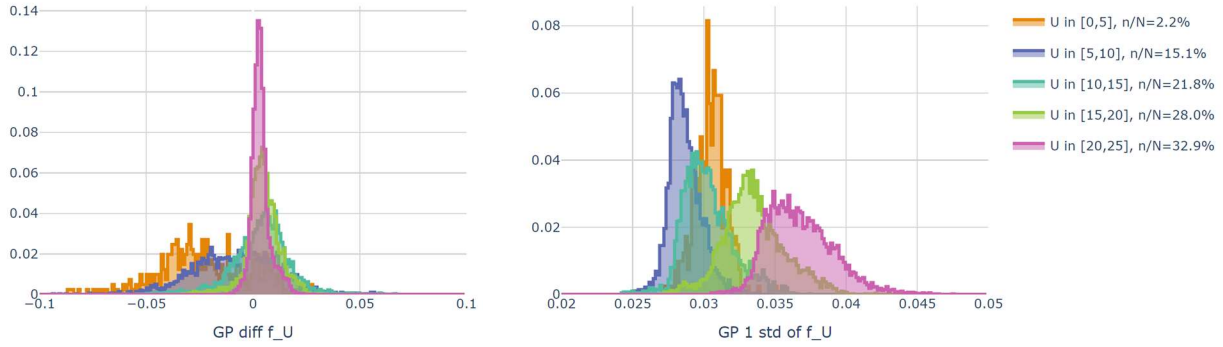

Figure 90 : Teesside: Histograms of $\hat{f}_u^{F-D}(\boldsymbol{x})$ (left) and of its std (right). Each histogram is normalized by the number of observations of the $\bar{u}$ bin indicated by the color in the total LHS.

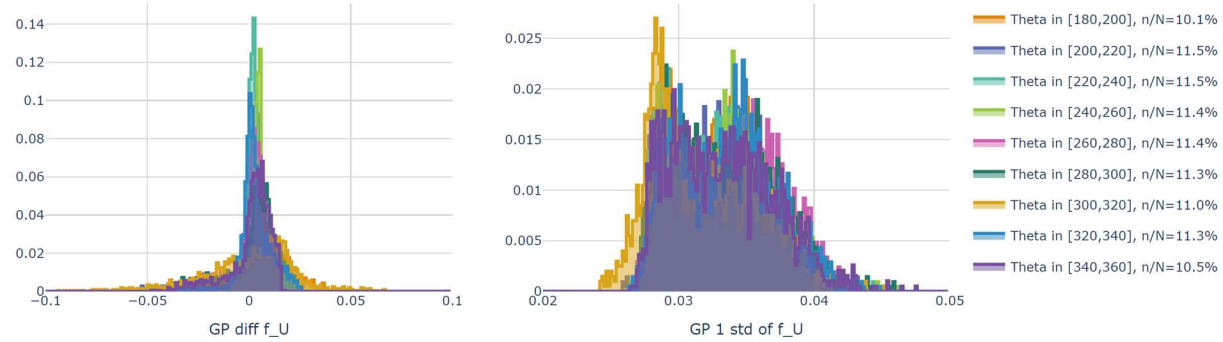

Figure 91 : Teesside: Histograms of $\hat{f}_u^{F-D}(\boldsymbol{x})$ (left) and of its std (right). Each histogram is normalized by the number of observations of the θ bin indicated by the color in the total LHS.

Figure 92 (resp. Figure 93) shows similar histograms for $\hat{f}_{\sigma_u}^{F-D}(\boldsymbol{x})$ according to bin in $\hat{f}_{\sigma_u}^{F}(\boldsymbol{x})$ (resp. according to bin in θ). For 90.4% of the samples, where $\hat{f}_{\sigma_u}^{F}(\boldsymbol{x}) < 0.68$, the difference $\hat{f}_{\sigma_u}^{F-D}(\boldsymbol{x})$ is between -23.5% and 1.4% (5th and 95th percentiles, respectively) with an estimated uncertainty between 10% and 24% (5th and 95th percentiles, respectively). For the samples with larger prediction in added turbulence, the difference goes down to -40% and up to 184% (5th and 95th percentiles, respectively). The largest differences are positive (i.e. DWM predicts less turbulence than FarmShadow^{TM}) and correspond to rarely occurring high turbulence cases (green and pink histograms in Figure 92) close to rated mean wind speed. Note that a value around 2 for σ_u is close to maximum near rated $\bar{u}$ in Figure 82. The largest negative values (i.e. DWM predicts more turbulence than FarmShadow^{TM}) are also rare and correspond to directions close to the crosswind direction, between 300° and 320° (Figure 93).

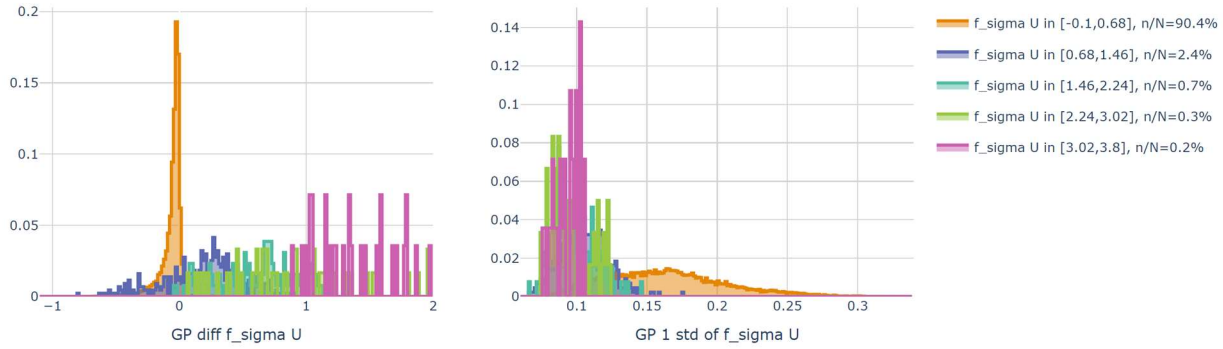

Figure 92 : Teesside: Histograms of $\hat{f}_{\sigma_u}^{F-D}(\boldsymbol{x})$ (left) and of its std (right). Each histogram is normalized by the number of observations of the $\hat{f}_{\sigma_u}^{F}(\boldsymbol{x})$ bin indicated by the color in the total LHS.

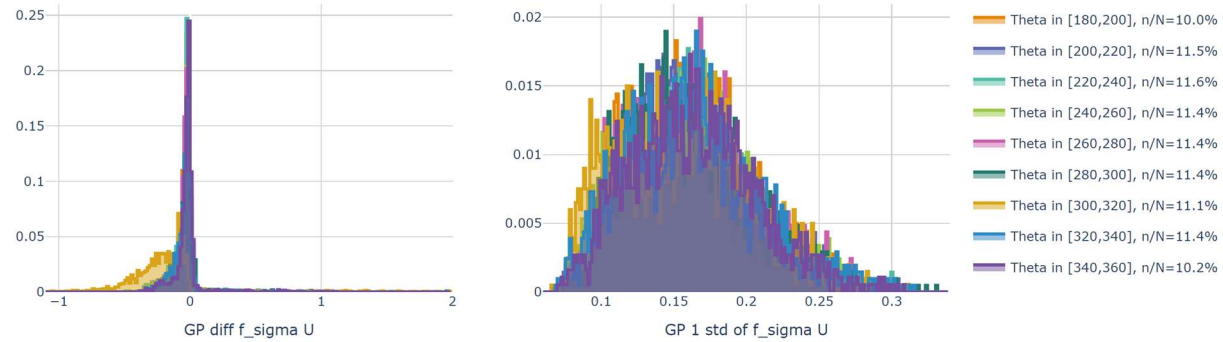

Figure 93 : Teesside: Histograms of $\hat{f}_{\sigma_u}^{F-D}(\boldsymbol{x})$ (left) and of its std (right). Each histogram is normalized by the number of observations of the θ bin indicated by the color in the total LHS.

4.3.2.2. South Brittany results

To facilitate, the reading of the following results, Figure 94 illustrates once again this theoretical wind farm layout, with the convention that wind direction θ is an azimuth (i.e. clockwise and 0 at North). Also, let us specify that for this case study, contrary to the Teesside case study, only the summation of deficit rules has been selected for DWM superposition rules. This choice which could be updated by lack of time may lead to an overestimation of wind speed deficit and added turbulence which should however remain small when considering the small number of WT and the larger inter-turbine distance in this theoretical wind farm than for the Teesside wind farm.

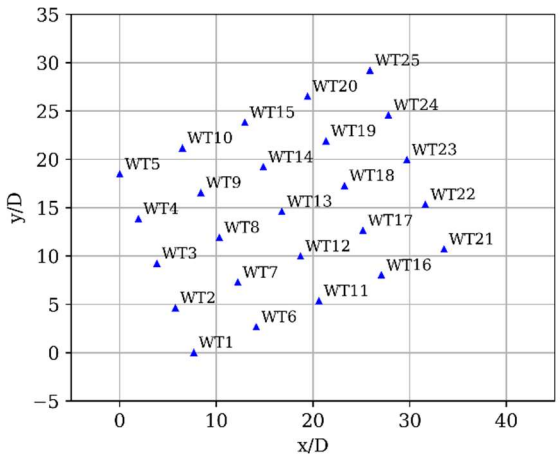

Figure 94: layout of South Brittany wind farm with North upward.

Following the same approach as documented for the Teesside simulations in section 4.3.2.1, the South Brittany simulations from both the FarmShadow™ and DWM simulator and the corresponding fitted SVGP and the differences between them are plotted in the following. For this comparison, the average floater pitch (induced by the wind) has not been taken into account for the sake of simplification.

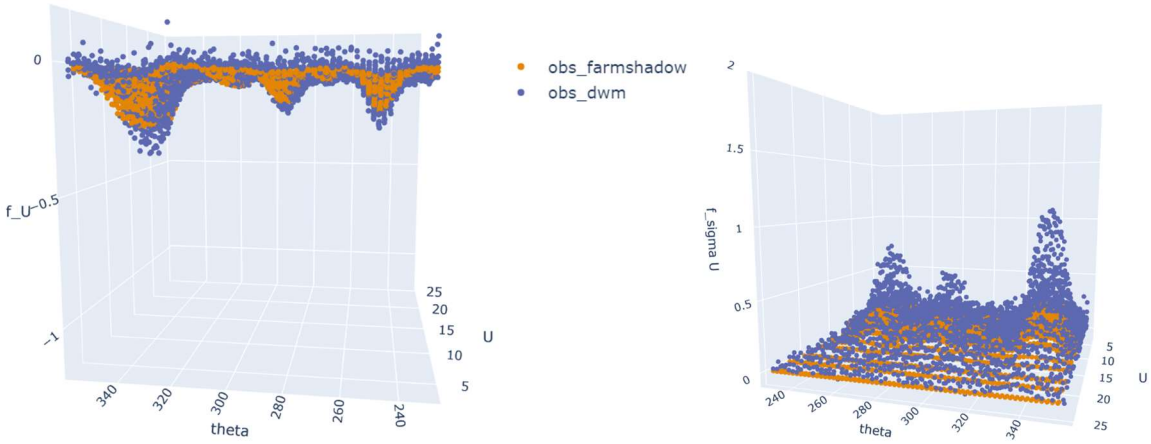

Figure 95: South Brittany: FarmShadow™ and DWM model results of the normalized f_u and f_{σ_u}.

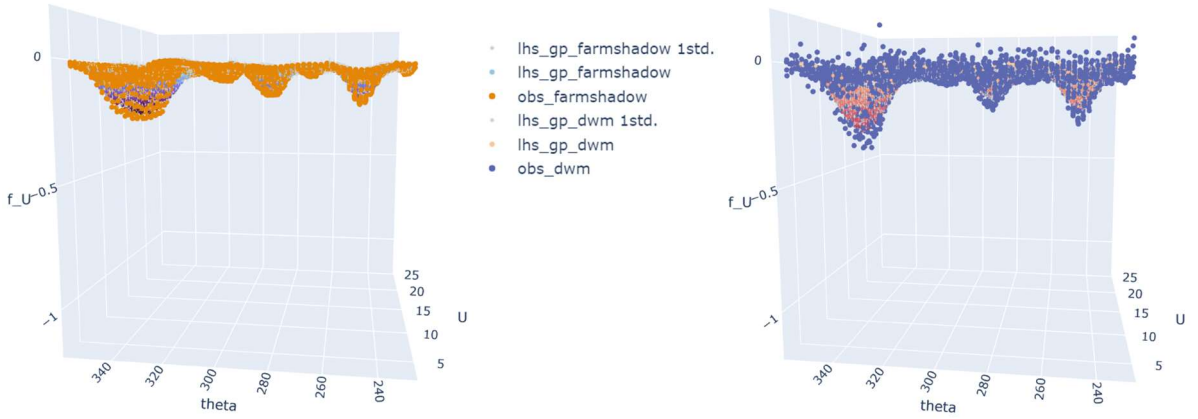

Figure 96: South Brittany: GP prediction of f_u for a large LHS. Error bars (grey) correspond to the standard deviation of the GP. Orange and purple points correspond to simulated responses from FarmShadow™ and DWM simulations, respectively. Left: GP for the FarmShadow™ simulator. Right: GP for the DWM simulator.

Figure 97 shows, each input scenario simulated by both the FarmShadow™ and DWM. Similar to the Teesside case, the $\bar{u}$ and σ_u input dimensions, both simulators have been run at 60 unique input combinations. For each of these 60 unique combinations of $\bar{u}$ and σ_u, the simulators have been run for every 2 degrees between 230 and 354 for Farmshadow™, resulting in 63 unique wind directions, and between 230 and 356 for DWM, resulting in 64 unique wind directions. As explained in section 4.3.1, let's remind that this θ domain has been chosen to encompass the [247.5°, 337.5°] quarter of symmetry of the wind farm layout and to avoid getting the strongest wake effects at the θ domain boundaries.

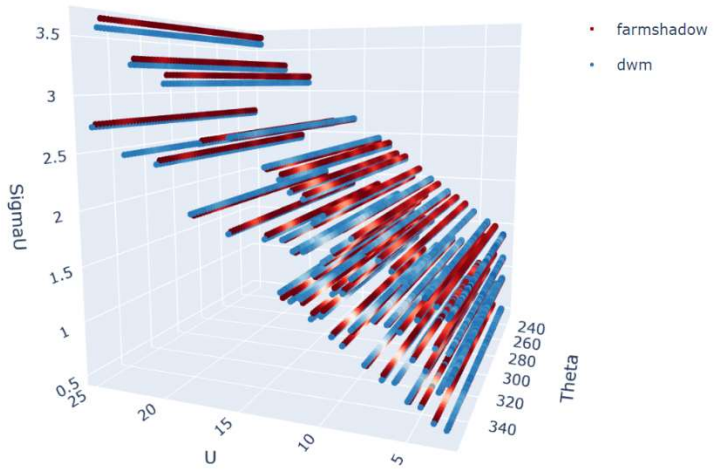

Figure 97: South Brittany: Input space for all simulation runs from the FarmShadow™ simulator (reds) and the DWM simulator (blues).

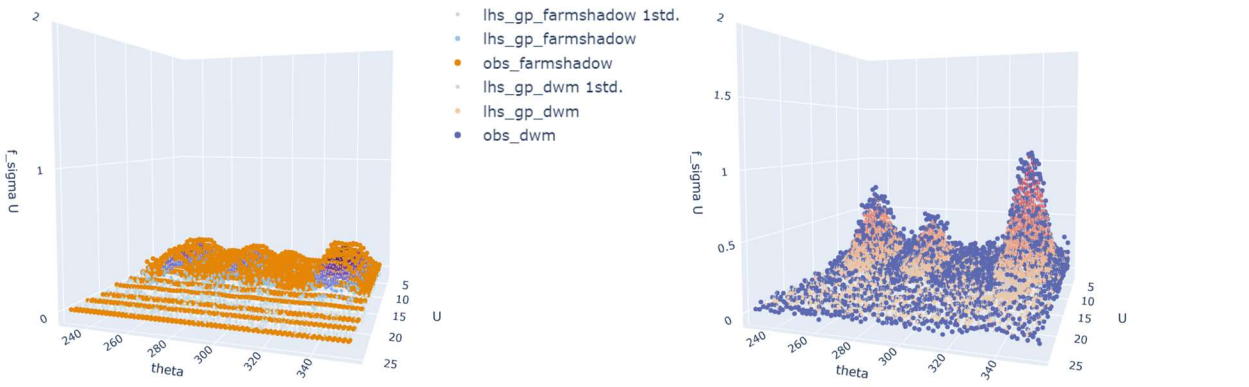

Figure 98: South Brittany: GP prediction of the normalized f_{σ_u} for a large LHS. Error bars (grey) correspond to the std of the GP. Orange and purple points correspond to simulated responses from FarmShadow™ and DWM simulations, respectively. Left: GP for the FarmShadow™ simulator. Right: GP for the DWM simulator.

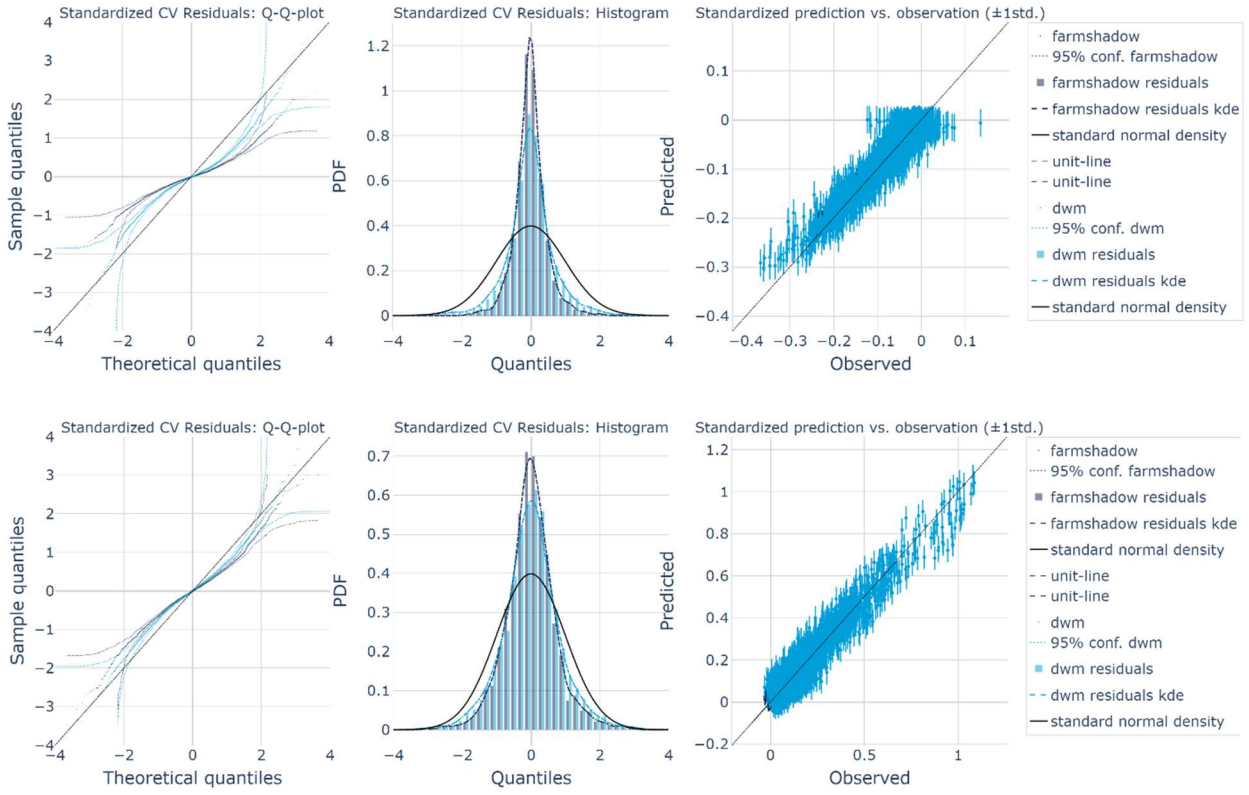

Figure 99: South Brittany: For each of the standardized quantities of interest: (left): plot of the Theoretical vs. Sample quantiles of the CV residuals, (middle): corresponding distribution of CV residuals, (right): CV prediction vs true observation including 1 std. From top to bottom, the plots represent the distribution of f_u and f_{σ_u}.

Figure 99 shows the CV results for f_U (top) and $f\sigma_u$ (bottom). These plots show that the GPs for the wake effect at the South Brittany field need the same considerations as those for the Teesside field. The GPs are generally good for most of the input space, but one needs to consider the effect of potential underprediction

of the wake superposition effect (mean wind speed deficit and added turbulence) due to GP approximation for the most extreme wake effects. This deviation is however much smaller than for Teesside, which can be explained by the fact the inter-turbine distances are generally largest for South Brittany (such distance is varying with wind direction). Consequently, the wake effects are smaller as can be seen by the fact that f_u is always much larger than -0.5 for both models (Figure 96).

Note however that for the DWM simulator, the f_u response has a higher variability for low wind speeds. See the red circle in Figure 100. In Figure 99, this leads to the wide variation of observed responses that correspond to a 0-prediction (top right plot). The same effect is not observed in the FarmShadow™ simulations.

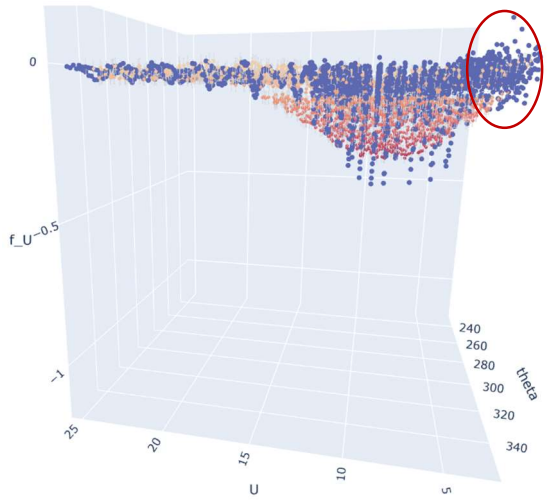

Figure 100: South Brittany: View of the f_u response where the high variability of the DWM simulator for low values of $\bar{u}$ is highlighted.

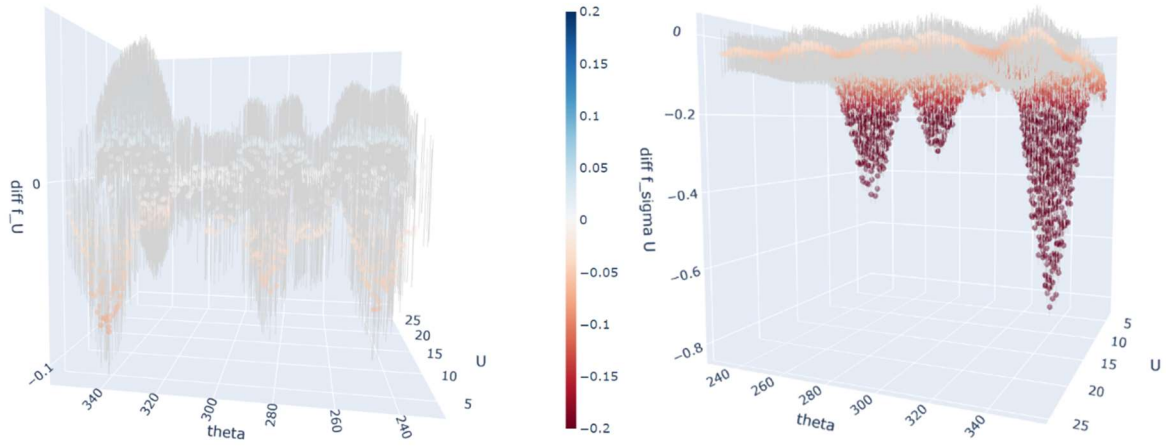

Figure 101: South Brittany: Difference between GP predictions from FarmShadow™ and DWM coloured from red to blue. Error bars (grey) correspond to the std of the GP. Left: f_u. Right: f_{σ_u}.

Figure 102 and Figure 103 show 2D slice views of GP predictions for both normalized quantities of interest and models. In these plots, two input parameters were kept fixed and one was left varying. The difference between f_u results from Farmshadow™ and DWM is less significant than the Teesside results as already explained. However, for: f_{σ_u}, the differences between the Farmshadow™ and DWM simulations are significant at $\bar{u} = 10\ m/s$ for the slice at $\theta = 340°$ and $\sigma_u = 1.2\ m/s$, respectively. This zone corresponds to a crosswind case with the smallest inter-turbine distance and a near-rated mean speed.

For some regions of the input space, there is a higher uncertainty in the predictions. Some of these regions do not have any data samples from the simulated data (see Figure 97). Note also that for the South Brittany case, no simulation data exists for wind directions (θ) less than 230°.

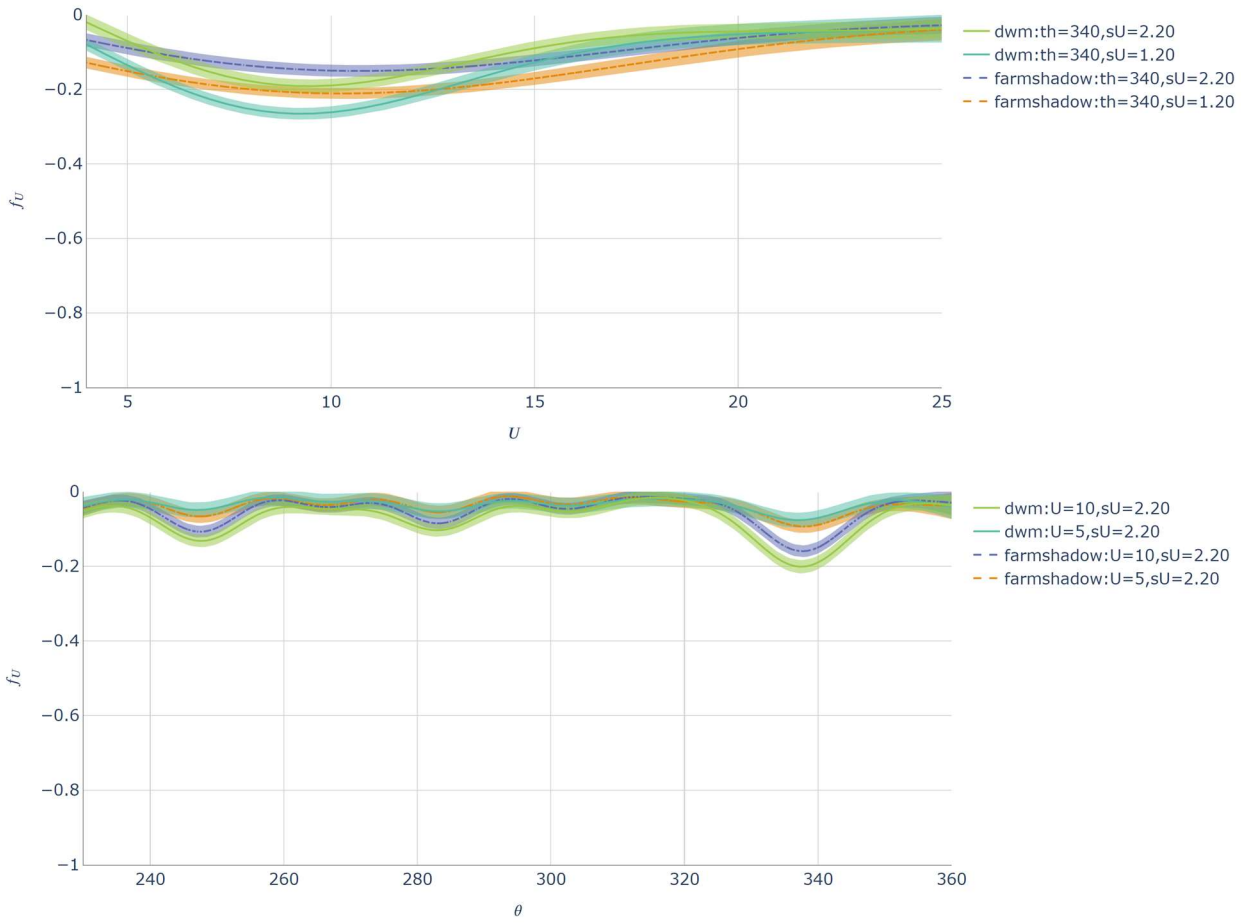

Figure 102: South Brittany: f_U GP predictions from FarmShadow™ and DWM. Top: fixed input parameters θ = 340°, σ_u set to 1.20 and 2.20 and varying $\bar{u}$. Bottom: fixed input parameters $\bar{u}$ set to 5 and 10, σ_u=2.20 and varying θ.

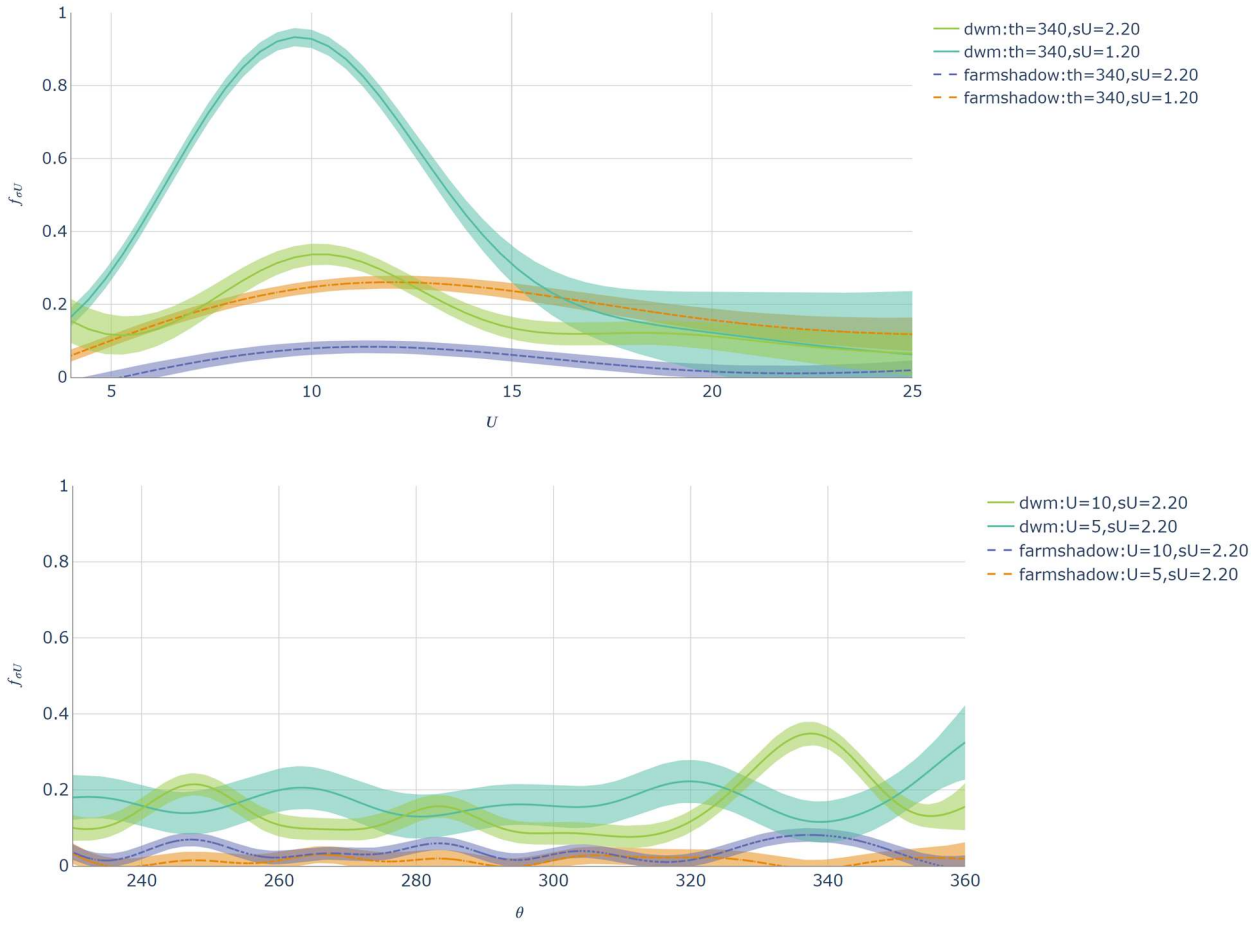

Figure 103: South Brittany: GP predictions from FarmShadow™ and DWM. Top: fixed input parameters θ = 340°, σ_u set to 1.20 and 2.20 and varying $\bar{u}$. Bottom: fixed input parameters $\bar{u}$ set to 5 and 10, σ_u = 2.20 and varying θ.

As proposed during the study of the Teesside wind farm, let us now try to provide some quantitative information on $\hat{f}_u^{F-D}(\boldsymbol{x})$ which could be used if one wants to apply an RBD on the theoretical South Brittany wind farm. The following figures display histograms based on a large Latin hypercube sample (LHS) of about 15k points across the entire input space. Each histogram is normalized by the number of observations in the series while the fraction of all observations in each series is specified in the legend. The range of the difference is similar to that of Teesside, as can be seen from the left-hand side plot in Figure 104, with 5th and 95th percentiles at -4% and 6% respectively. The largest values are still occurring when the direction is near the crosswind direction at 345° (Figure 105). For about 90% of the samples, this range is slightly reduced in amplitude, with the 5th and 95th percentiles at -2% and 2% respectively. The empirical uncertainty is also similar when compared to Teesside: it lies between 2.2 and 3% (5th and 95th percentiles). It may be noticed that this similarity in the difference of the amplitude is obtained despite a non-optimal assumption of the superposition rule that has been used here for DMW with below rated wind speeds. This may confirm the fact that the slight overestimation of DWM wind speed deficit and added turbulence due to this choice remains small due to the smaller number of WT and the larger inter-turbines distance in general for the South Brittany layout when compared to the Teesside layout.

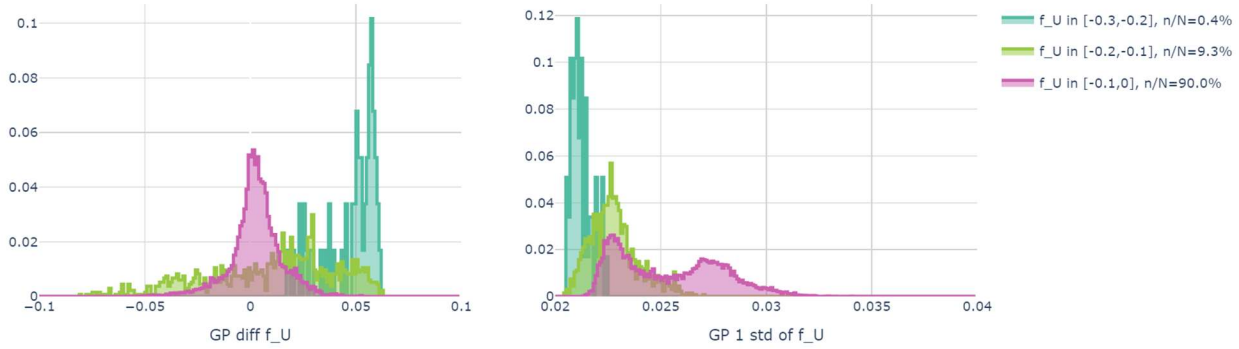

Figure 104: South Brittany: Histograms of $\hat{f}_u^{F-D}(\boldsymbol{x})$ (left) and of its std (right). Each histogram is normalized by the number of observations of the $\hat{f}_u^{F}(\boldsymbol{x})$ bin indicated by the color in the total LHS.

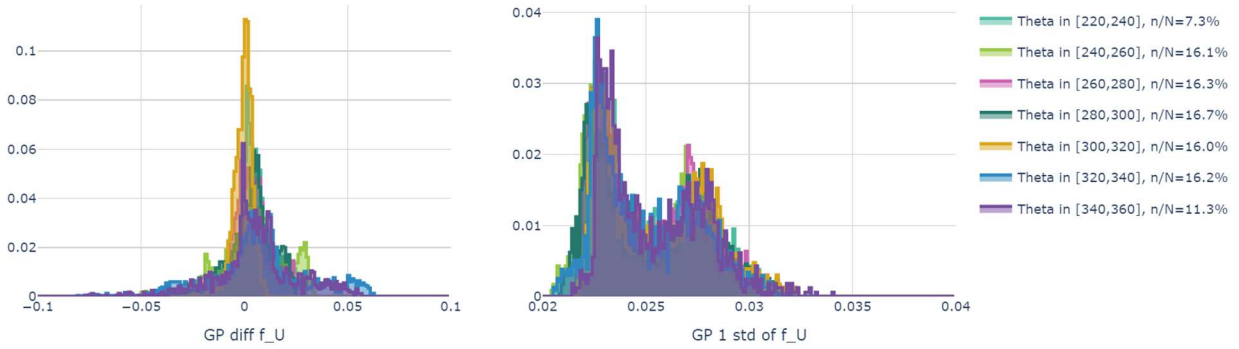

Figure 105: South Brittany: Histograms of $\hat{f}_u^{F-D}(\boldsymbol{x})$ (left) and of its std (right). Each histogram is normalized by the number of observations of the θ bin indicated by the color in the total LHS.

Figure 106 (resp. Figure 107) shows similar histograms for $\hat{f}_{\sigma_u}^{\mathrm{F-D}}(\boldsymbol{x})$ according to bin in $\hat{f}_{\sigma_u}^{\mathrm{F}}(\boldsymbol{x})$ (resp. according to bin in θ). The biggest difference is for the scenarios which have the largest added turbulence. Farmshadow™ generally predicts a lower increase in turbulence than DWM. For 91.4% of the scenarios, where $\hat{f}_{\sigma_u}^{\mathrm{F}}(\boldsymbol{x})$ <10%, the difference is negative (i.e. FarmShadow™ predicts less turbulence than DWM) with a magnitude less than 13.8% (5th percentile). The 5th percentile of the difference in $\hat{f}_{\sigma_u}^{\mathrm{F-D}}(\boldsymbol{x})$ is at -75%. As illustrated in Figure 107, it is also associated to the directions close to the crosswind direction.

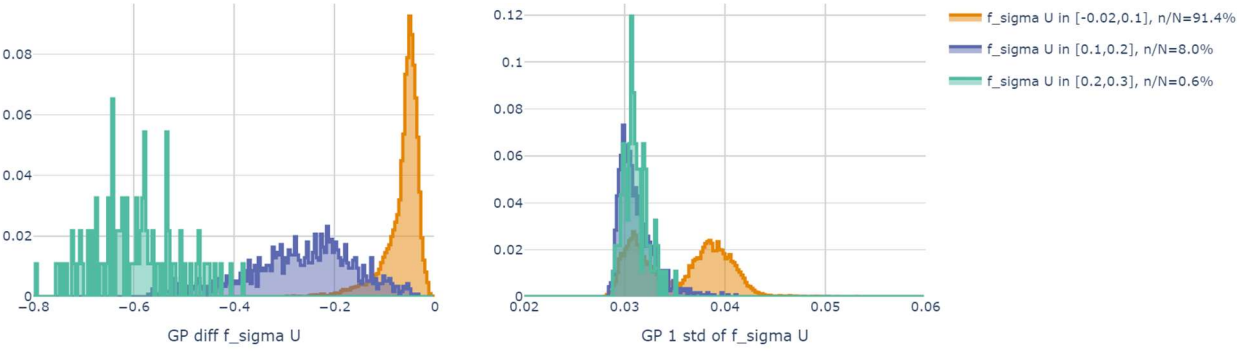

Figure 106: South Brittany: Histograms of $\hat{f}_{\sigma_u}^{F-D}(\boldsymbol{x})$ (left) and of its std (right). Each histogram is normalized by the number of observations of the $\hat{f}_{\sigma_u}^{F}(\boldsymbol{x})$ bin indicated by the color in the total LHS.

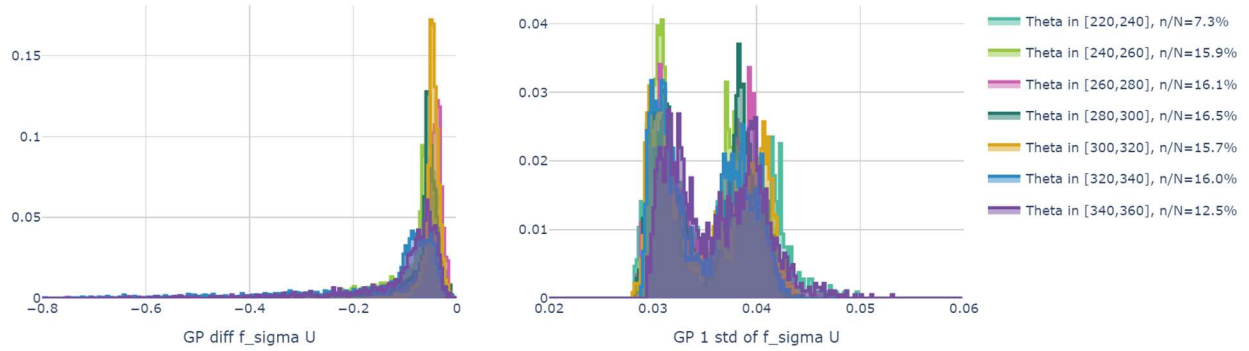

Figure 107: South Brittany: Histograms of $\hat{f}_{\sigma_u}^{F-D}(\boldsymbol{x})$ (left) and of its std (right). Each histogram is normalized by the number of observations of the θ bin indicated by the color in the total LHS.

4.4. Summary of section 4

The objective of this task was double. First, a qualitative uncertainty evaluation of engineering methology for wake modeling under specific conditions, such as non-neutral thermal stratification and non-vertical static position of FOWT has been done (section 4.2). Secondly, an extensive and quantitative uncertainty estimation of engineering wake modeling for usual wind parameters has been provided (section 4.3).

Successive steps were needed to fulfil the above-mentioned objectives. As a preliminary study, the high-fidelity models Meso-NH and PALM based on an LES framework have been successfully compared against SCADA power data of the Teesside wind farm, especially for rated and below rated conditions. The interesting comparison of wind speed and turbulence profile to check the two LES model alignments is however left for future work. Then, high-fidelity simulations from Meso-NH and PALM were compared to the results from the engineering methodology of wake modelling. To follow industrial workflow, the latter considers a power law to represent the vertical wind profile of initial ambient conditions and uses analytical wake model of FarmShadow™. Wind speed and turbulent intensity profiles were analysed. The aim was to study specific cases leading to the limit of low-fidelity models. On the Teesside wind farm, the analysis of the effect of different thermal stratifications (stability) was performed. The engineering approach provides good estimations in neutral conditions, especially for Gaussian and super-Gaussian models, emphasizing the robustness of such models. However, it shows its limit in stable cases: the wake deficit and the turbulence intensity are underestimated. For the unstable case, the methodology for LES computations aiming at considering a reduced domain makes it impossible to provide a fair conclusion. One should note that the wind profiles used as inputs to low-fidelity models were directly interpolated from high-fidelity simulations, including then some specific characteristics of atmospheric stability. To the authors, it seems that this simple way of proceeding could contribute to reduce the modelling uncertainty. Afterward, the effect of the static position (mean drift and pitch of the floater) on the wake was studied for the floating South Brittany wind farm constituted of larger 15MW WTs. Vertical wake deflections remain small, even during rated conditions which are leading to the highest inclination of the floater. Nevertheless, wider and stronger wakes were mainly observed downstream of the first wind turbine. Again, the overall prediction of wake deficit was in good agreement with the high-fidelity model. In general, if the wake deficit estimation showed good correlations, the difference between low-fidelity and high-fidelity models seems to be comparable to the difference among the various low-fidelity models used during this study. The

turbulence intensity estimation showed good correlations with LES results too. A slight overestimation (quite important near the ground) from analytical models has been noticed and underlines the need for further research concerning this quantity, even if a correction in FarmShadow™ (not used in this report) improved the results.

To provide a quantitative estimation of uncertainty, analytical models of FarmShadow™ were compared to the Dynamic Wake Meandering (DWM) of HAWC2 which is more affordable in terms of computational cost than LES simulations. It enables the estimation over an exhaustive DoE covering an entire set of ambient wind conditions. The uncertainty estimation was computed for the Teesside and the South Brittany wind farms using the Kriging approach. The results are provided as normalized mean speed deficit (see section 4.3.2) f_u and f_{σ_u}. GPs are trained on these two quantities for both the FarmShadow™ and DWM simulations, to provide an estimate of the difference between the two models and of the uncertainty of this difference. Statistic on this difference is given in Table 14. Let us remind you that $\hat{f}_q^{\,A}(\boldsymbol{x})$ represents the GP where the lower index q indicates the wind parameter ($\bar{u}$ or σ_u) and the upper index A indicates the simulator (F stands for FarmShadow™ while D stands for DWM), or the difference between the two models (F-D stands for FarmShadow™ minus DWM).

Table 14 : 5th and 95th percentiles for GP $\hat{f}_q^{\,F-D}(\boldsymbol{x})$ or its std function denoted $\sigma(.)$. Ω^F denotes about 90% of the LHS samples. The wind parameter ($\bar{u}$ or σ_u) corresponding to the lower q index in the GP corresponds to the normalized function f_u or f_{σ_u} indicated at the top of each column, after the case study name. See section 4.3.2 for the definition of f_u and f_{σ_u}.

Quantity on which 5th and 95th percentiles are computed	Teesside f_u	Teesside f_{σ_u}	South Brittany f_u	South Brittany f_{σ_u}
$\hat{f}_q^{\,F}(\boldsymbol{x})\ \forall x \in \Omega^F$	[-8.8%, 0%]	[-4.6%, 24.5%]	[-8%, 0%]	[-0.8%,8%]
$\hat{f}_q^{\,F-D}(\boldsymbol{x})\ \forall x \in \Omega^F$	[-1.2%, 1.7%]	[-23.5%, 1.4%]	[-2%, 2%]	[-13.8%, -2.9%]
$\sigma\left(\hat{f}_q^{\,F-D}(\boldsymbol{x})\right)\ \forall x \in \Omega^F$	[3.9%, 2.4%]	[10%, 24%]	[2.2%, 3%]	[3%, 4.2%]
$\hat{f}_q^{\,F-D}(\boldsymbol{x})\ \forall x$	[-6.4%, 4.9%]	[-40%, 184%]	[-4%, 6%]	[-75%, 0%]

A striking feature of these results is that the difference in prediction of wind speed deficit between the two models is very similar for the two case studies of the real (Teesside) and theoretical (South Brittany) wind farms, despite the difference of WT (2.3 MW WT for Teesside and 15MW WT for South Brittany). This may be explained by the fact that the potentially stronger wake effect of large WT in South Brittany is compensated by the larger inter-turbine mean distance of the layout. This difference (for about 90% of scenarios) is almost symmetrical to 0, meaning that there is about the same number of scenarios for which FarmShadow™ predicts more or less wind speed deficit when compared to DWM. The larger differences are for very few cases, at directions close to the crosswind directions (which maximizes wakes superposition effects), showing a lower wind speed deficit predicted by DWM when compared to FarmShadow™. A difference between the two wind farms is that these larger difference values are for very low wind speed (<5 m/s) for Teesside while they are near-rated for South Brittany (compare Figure 88 and Figure 102).

There is more difference in the prediction of turbulence intensities between the two models and this difference is not similar when comparing Teesside and South Brittany results. One may note in particular for the Teesside case study more scenarios for which FarmShadow™ predicts more added turbulence than DWM, while the larger differences for South Brittany correspond to the opposite ranking on the model

predictions. The larger differences correspond to rarely occurring scenarios with wind directions close to the crosswind direction, a near-rated wind speed, and a large turbulence intensity. However, for Teesside, the larger differences are for cases with more added turbulence predicted by FarmShadow™ than by DWM while they correspond to cases with more added turbulence predicted by DWM than by FarmShadow™ for South Brittany. For below rated wind speed, the latter may be partly because a non-optimal choice of turbulence superposition was used in the South Brittany case for DWM (see previously detailed explanations).

As one may notice, DWM could not be included in the comparison with Meso-NH and PALM LES results presented in section 4.2 for selected ambient wind conditions, because of lack of time. Although the DTU implementation of DWM was previously successfully fitted against full-scale wind flow data in [100], [101], and [102], this missing information will be investigated in future work to make the link between the quantitative and qualitative results and also to check the choice of DWM as a reference for FarmShadow™.

References of Section 4

[57] Blondel, F., Cathelain, M. (2020). "An alternative form of the super-Gaussian wind turbine wake model". Wind Energy Science, 5(3), 1225-1236.

[58] Blondel, F. (2022). "Brief communication: A momentum-conserving superposition method applied to the super-Gaussian wind turbine wake model". Wind Energy Science Discussions, 1-8.

[59] Jensen, N. (1983). "A Note on Wind Generator Interaction", RISOE-M-2411, Risø National Laboratory, https://books.google.fr/books?id=5w3tvgEACAAJ.

[60] Katic, I., Højstrup, J., Jensen, N. O. (1986). "A simple model for cluster efficiency". In European wind energy association conference and exhibition, v. 1, 407-410. Rome, Italy.

[61] Bastankhah, M., Welch, B. L., Martínez-Tossas, L. A., King, J., Fleming, P. (2021). "Analytical solution for the cumulative wake of wind turbines in wind farms". Journal of Fluid Mechanics, 911.

[62] Zong, H., Porté-Agel, F. (2020). "A momentum-conserving wake superposition method for wind farm power prediction". Journal of Fluid Mechanics, 889.

[63] Ishihara, T., Qian, G. W. (2018). "A new Gaussian-based analytical wake model for wind turbines considering ambient turbulence intensities and thrust coefficient effects". Journal of Wind Engineering and Industrial Aerodynamics, 177, 275-292.

[64] Branlard, E.,Meyer Forsting, A. R. (2020). "Assessing the blockage effect of wind turbines and wind farms using an analytical vortex model". Wind Energy, 23(11), 2068-2086.

[65] Lac, C., Chaboureau, J. P., Masson, V., Pinty, J. P., Tulet, P., Escobar, J et al. (2018). "Overview of the Meso-NH model version 5.4 and its applications". Geoscientific Model Development, 11(5), 1929-1969.

[66] Joulin, P. A., Mayol, M. L., Masson, V., Blondel, F., Rodier, Q., Cathelain, M., Lac, C. (2020). The actuator line method in the meteorological LES model Meso-NH to analyze the horns rev 1 wind farm photo case. Frontiers in Earth Science, 7, 350.

[67] Jézéquel, E., Cathelain, M., Masson, V., Blondel, F. (2021). "Validation of wind turbine wakes modeled by the Meso-NH LES solver under different cases of stability". In Journal of Physics: Conference Series, v. 1934, No. 1, p. 012003. IOP Publishing.

[68] Joulin, P. A. (2019). « Modélisation à fine échelle des interactions entre parcs éoliens et météorologie locale ». Doctoral thesis of Toulouse INPT.

[69] Reinwardt, I., Schilling, L., Steudel, D., Dimitrov, N., Dalhoff, P., Breuer, M. (2021). "Validation of the dynamic wake meandering model with respect to loads and power production". Wind Energy Science, 6(2), 441-460. https://doi.org/10.5194/wes-6-441-2021

[70] Larsen, T. J., Larsen, G. C., Aagaard Madsen , H., Petersen, S. M. (2015). ”Wake effects above rated wind speed. An overlooked contributor to high loads in wind farms”. In Scientific Proceedings. EWEA Annual Conference and Exhibition 2015 (pp. 95-99). European Wind Energy Association (EWEA).

[71] Maronga, B., Banzhaf, S., Burmeister, C., Esch, T., Forkel, R., Fröhlich, D., Fuka, V., Gehrke, K.F., Geletič, J., Giersch, S. and Gronemeier, T., (2020). Overview of the PALM model system 6.0. Geoscientific Model Development, 13(3), pp.1335-1372.

[72] Deardorff, J. W., (1980), Stratocumulus-capped mixed layers derived from a three-dimensional model, Bound.-Lay. Meteorol., 18, 495–527, https://doi.org/10.1007/BF0011950.

[73] Moeng, C.-H. and Wyngaard, J. C., (1988), Spectral Analysis of Large-Eddy Simulations of the Convective Boundary Layer, J. Atmos. Sci., 45, 3573–3587, https://doi.org/10.1175/1520-0469(1988)045<3573:SAOLES>2.0.CO;2.

[74] Saiki, E. M., Moeng, C.-H., and Sullivan, P. P., (2000). Large-Eddy Simulation Of The Stably Stratified Planetary Boundary Layer, Bound.-Lay. Meteorol., 95, 1–30, https://doi.org/10.1023/A:1002428223156.

[75] Steinfeld, G., Witha, B., Dörenkämper, M., and Gryschka, M., (2015). Hochauflösende Large-Eddy-Simulationen zur Untersuchung der Strömungsverhältnisse in Offshore-Windparks, promet – Meteorologische Fortbildung, 39, 163–180.

[76] Martínez-Tossas, L.A., Churchfield, M.J. and Leonardi, S., 2015. Large eddy simulations of the flow past wind turbines: actuator line and disk modeling. Wind Energy, 18(6), pp.1047-1060.

[77] Martinez, L., Leonardi, S., Churchfield, M. and Moriarty, P., 2012, January. A comparison of actuator disk and actuator line wind turbine models and best practices for their use. In 50th AIAA Aerospace Sciences Meeting including the New Horizons Forum and Aerospace Exposition (p.900)

[78] Jonkman JM, Butterfield S, Musial W, Scott G., (2009). Definition of a 5-MW reference wind turbine for offshore system development. Technical Report NREL/TP-500-38060, National Renewable Energy Laboratory, Golden, Colorado.

[79] The Renewables Consulting Group LLC (2018). “Analysis of Turbine Layouts and Spacing Between Wind Farms for Potential New York State Offshore Wind Development”. NYSERDA Report 18-20, New-York (USA).

[80] Porté-Agel, F., Bastankhah, M., Shamsoddin, S. (2020). Wind-turbine and wind-farm flows: a review. Boundary-Layer Meteorology, 174(1), 1-59.

[81] Sedefian, L., Bennett, E. (1980). A comparison of turbulence classification schemes. Atmospheric Environment (1967), 14(7), 741-750.

[82] Stull, R. B. (1988). An introduction to boundary layer meteorology (Vol. 13). Springer Science & Business Media.

[83] Rodrigo, J. S., Cantero, E., García, B., Borbón, F., Irigoyen, U., Lozano, S. et al (2015). “Atmospheric stability assessment for the characterization of offshore wind conditions”. In Journal of Physics: Conference Series, v. 625, No. 1, p. 012044. IOP Publishing.

[84] Mohan, M., Siddiqui, T. A. (1998). “Analysis of various schemes for the estimation of atmospheric stability classification”. Atmospheric Environment, 32(21), 3775-3781.

[85] Cantero, E., Sanz, J., Borbón, F., Paredes, D., García, A. (2022). “On the measurement of stability parameter over complex mountainous terrain”. Wind Energy Science, 7(1), 221-235.

[86] Joulin, P.A., Mayol, M.L., Blondel, F., Masson, V., Rodier, Q., Lac, C. (2019). “Coupling the actuator line method to the high order meteorological LES model Meso-NH to study wind farm wakes impacts on local meteorology”. Journal of Physics: Conference Series, 1256, pp.012019.

[87] Peyrard, C., Robaux, F., Borras-Nadal, A., Joulin, P.-A., Mayol, L., Eldevik, S., Guiton, M., Cousin, A, Benoit, M., Dimitrov, N., Lovera, A., Fereira, C. (2022). "Aero-servo-hydroelastic model uncertainty". D3.3. Rep. of HIPERWIND H2020 project (agreement No. 101006689), https://hal-ifp.archives-ouvertes.fr/hal-04033056.
[88] Kelly, M., Larsen, G., Dimitrov, N.K., Natarajan, A., (2014). "Probabilistic Meteorological Characterization for Turbine Loads". J. Phys.: Conf. Series, 524, 012076, DOI 10.1088/1742-6596/524/1/012076.
[89] Niayifar, A., Porté-Agel, F. (2016). "Analytical Modeling ofWind Farms: A New Approach for Power Prediction". Energies, 9, 741 11.
[90] Frandsen, S.; Thogersen, M.L. (1999). "Integrated fatigue loading for wind turbines in wind farms by combining ambient turbulence and wakes". Wind Eng., 23, 327–340.
[91] Bastankhah, M., Porté-Agel, F. (2014). "A new analytical model for wind-turbine wakes". Renewable energy, 70, 116-123.
[92] McWilliam, M., Bonfils, N., Dimitrov, N., Dou, S. (2022). "Wind farm parameterization and turbulent wind box generation". D3.1 Tech Rep. of HIPERWIND H2020 project, Grant Agreement No. 101006689, https://hal-ifp.archives-ouvertes.fr/hal-04033050.
[93] Auffray, Y., Barbillon, P., & Marin, J. M. (2012). Maximin design on non hypercube domains and kernel interpolation. Statistics and Computing, 22(3), 703-712.
[94] Williams, C. K., Rasmussen, C. E. (2006). "Gaussian processes for machine learning", v. 2, no. 3, 4. Cambridge, MA: MIT press.
[95] Hensman, J., Matthews, A., Ghahramani, Z. (2005). "Scalable Variational Gaussian Process Classification", arXiv:1411.2005v1
[96] Python package GPyTorch documentation: https://docs.gpytorch.ai/en/stable/
[97] Python package PyTorch documentation: https://pytorch.org/docs/stable/index.html
[98] Ginsbourger, D., Schaerer, C. (2021). "Fast calculation of Gaussian Process multiple-fold cross-validation residuals and their covariances" , https://arxiv.org/abs/2101.03108
[99] DNV, (2022). "RaPiD-models python package", https://github.com/RaPiD-models/rapid_models
[100] Bingöl, F.; Mann, J. and Larsen, G.C. (2010). Light detection and ranging measurements of wake dynamics. Part I: one-dimensional scanning. Wind Energy; 13(1): 51–61.
[101] Trujillo, J.; Bingöl, F.; Larsen, G.C. and Mann, J. (2011). Light detection and ranging measurements on wake dynamics. Wind Energy; 14: 61–75.
[102] Keck, R.-E. (2014). Validation of the standalone implementation of the dynamic wake meandering model for power production. Wind Energy.
[103] Kelly, M. and van der Laan, M.P. (2023). From shear to veer: theory, statistics, and practical application. Wind Energy Sci., DOI 10.5194/wes-2022-119.

5. Quantifying the wake-induced perturbations within a wind farm

Previous sections documented the models used to simulate the wake effect (i.e. modification of the wind flow due to operating WT with generally downstream wind speed deficit and added turbulence), distinguishing engineering models generally composed of analytical static approaches, and high fidelity models with CFD (cf. section 2). Section 3 discussed the specific problem of the static floater motion influence for FOWT including its impact on AEP. Section 4 provides results on an engineering wake model uncertainty by comparing the static model FarmShadow^{TM} of IFPEN to higher fidelity models (DWM and LES approach with PALM and Meso-NH), see details on these models in section 4.1.3.1.

Given these preliminary works, we are now able to present the perturbations of the free wind conditions (see [104] for an example of the joint probabilistic distribution of long-term, i.e., pluriannual, parameters) by the wake effect of the wind turbines inside a wind farm. The uncertainty propagation is done through the FarmShadow^{TM} wake model. A choice has to be done on a finite number of output parameters representing the wake effects. In section 4 of [105], a parameterization of the local wind seen by a WT has been suggested. The same reference also provides results of a Global Sensitivity Analysis with Sobol indices, concluding that the average over-rotor surface of the time average wind speed, $\bar{u}_{rotor}$ and of the wind speed standard deviation $\sigma_{u_{rotor}}$ are the most influent parameters on both extreme and fatigue load on WT main components. For the sake of simplification, we will consider only these two scalars for carrying the uncertainty propagation.

To quantify the wake modification of ambient wind, it is useful to introduce metrics. We will present such a metric, with Maximum Mean Discrepancy [106] to measure the discrepancy between free and perturbed wind conditions. With such a metric, the wind conditions seen by the wind turbines within a wind farm can be clustered using various methods. This information can later be exploited to limit the number of reliability studies to the number of clusters built.

5.1. Uncertainty propagation in a wake model

The engineering stationary and analytical wake models which are based on the FarmShadow^{TM} software, and which are used in this section, are described in more detail in section 4.1.3.1. However, let us recall that these models have a rather low fidelity, making their execution fast (about 6 seconds per simulation for the Teesside model and 3 minutes for the floating case of South Brittany). On the other hand, models of higher fidelity can also simulate the wake effect in an operating wind farm as described in sections 4.1.3.2 and 4.1.3.3. However, these models are intractable in our uncertainty propagation study. For the LES Meso-NH solver, the computational cost is about 2 days to initialize the ambient atmospheric state and then 4 days per each simulation with WT with a parallelization on 2160 CPU. From the qualitative comparison of the analytical stationary wake FarmShadow^{TM} models with LES simulations in section 4.2, we consider in this section that the modelling error committed by FarmShadow^{TM} is reasonable. Therefore, the uncertainty propagation is carried out on the FarmShadow^{TM} model only. Further investigations should be done on the integration of the different fidelity levels in uncertainty propagation. Note that the influence of the waves on the wake effect is considered secondary and out of the scope of this work.

A FarmShadow™ model (e.g. of the Teesside WF) takes as input a set of variables describing the free wind conditions $\boldsymbol{x} \in \mathbb{R}^3$and computes the perturbed wind conditions at each wind turbine represented by the vector $\boldsymbol{x}_l', l \in (1, \cdots, n_{WT})$:

$$g : \mathbb{R}^3 \to \mathbb{R}^{3\,n_{WT}}$$
$$\boldsymbol{x} \mapsto g(\boldsymbol{x}) = (\boldsymbol{x}_1', \ldots, \boldsymbol{x}_{n_{WT}}')$$

The uncertainties associated with the free wind conditions are represented by a random vector $\boldsymbol{X}$ following the distribution $\boldsymbol{p}_0$. Note that the index 0 is a reference to the fact that these conditions are not perturbed by the wake. A parametric model has been fitted by DNV for each case study using conditional probability density functions to capture the dependence structure, as illustrated for example in [104]. As shown in previous sections of this report, wake output is varying strongly according to wind direction. Consequently, the random vector $\boldsymbol{X}$ is described by the omnidirectional wind parameter distribution. Finally, the input random variables considered in the wake analysis are the following:

Table 15: Description of the environment random variables

Mean wind speed	$\bar{\boldsymbol{u}}$	m/s	10-min average horizontal wind speed at hub height in wind propagation direction
Wind turbulence	σ_u	m/s	10-min wind speed turbulence (standard deviation) at hub height
Wind direction	θ	deg.	10-min average wind direction

When perturbed by the wake effect of the wind farm, the wind turbine i sees a wind flow represented by the random vector $\boldsymbol{X}_l', l \in (1, \cdots, n_{WT})$, following the distribution $p_l{}'$. As introduced before, we chose to select only two scalars, $\bar{u}_{rotor}$ and $\sigma_{u_{rotor}}$ to represent this modified wind flow on a vertical plane located at each wind turbine. These two quantities of interest are computed from the cell values of a FarmShadow™ model (see section 4.1.3.1). Horizontal maps of the local mean wind speed and turbulence at the hub height are shown in Figure 108 for one simulation on the Teesside site (see section 4 for details on the simulation settings).

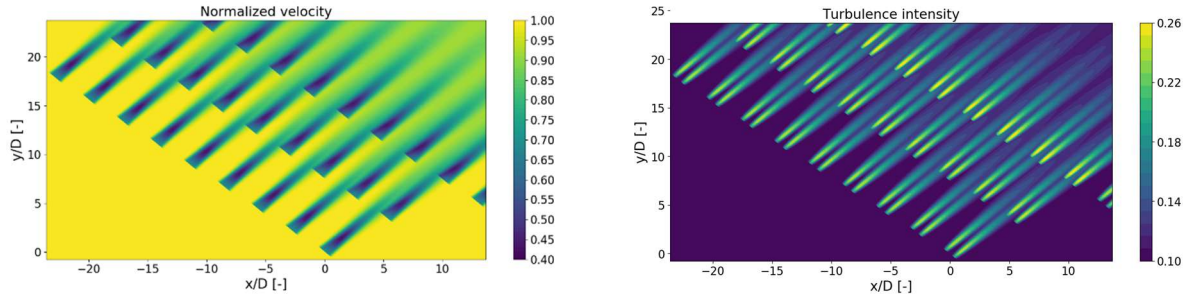

(a) (b)

Figure 108: FarmShadow™ simulation example for the dominant South-West wind direction. The pictures show the field of (a) wind speed deficit and (b) added turbulence intensity at hub height within the meshed domain.

Everything is set up for an uncertainty propagation of the random vector $\boldsymbol{X}$ through the wake model FarmShadow™, giving as outputs a set of perturbed environmental distributions $p_l', l \in (1, \cdots, n_{WT})$.

A Monte-Carlo sample $\boldsymbol{X}_n = \{\boldsymbol{x}^{(1)}, \cdots, \boldsymbol{x}^{(n)}\}$ of the three random inputs defined in Table 15 is generated by directly subsampling from a large, independent, and identically distributed dataset (with wind speeds truncated between the cut-in and cut-out of the turbines). Then, considering a farm layout and a constant wind shear exponent, FarmShadow™ is launched for every environmental condition from the Monte Carlo

DOE. The outputs of the code consist of a multivariate joint distribution for each turbine. As the Monte Carlo simulation is known to converge slowly but surely, it was chosen to perform this uncertainty propagation because of its simplicity and the low computational cost of the FarmShadow™ simulations. Figure 109 is a schematic representation of the methodology.

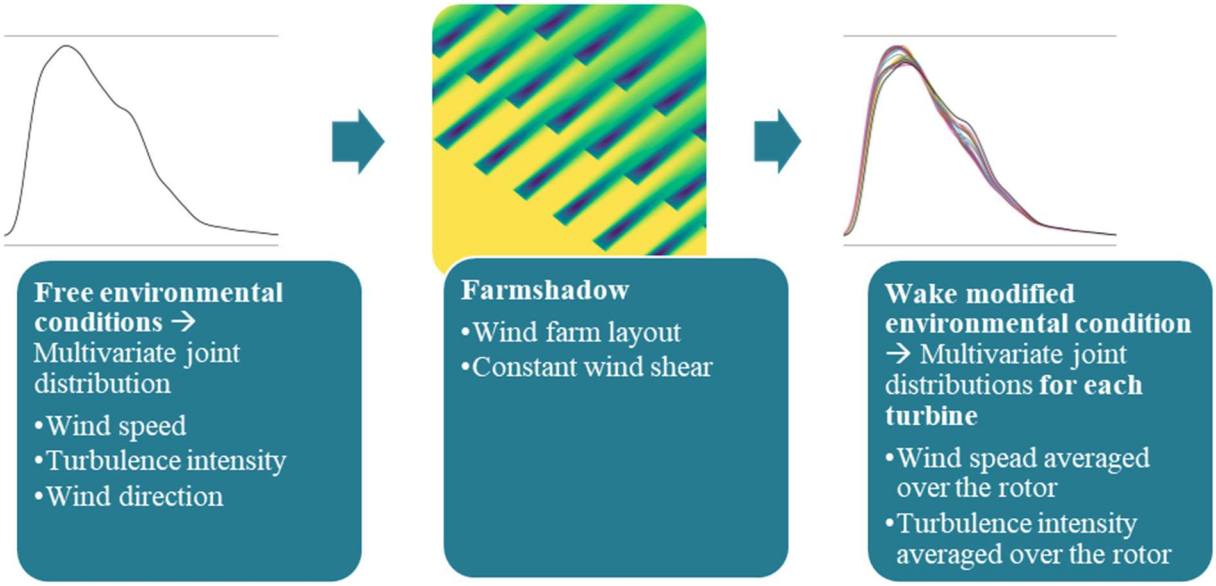

Figure 109: Illustration of the methodology

This uncertainty propagation in the FarmShadow™ wake model allows us to define the wind parameter distribution seen by each turbine of a farm. However, the analysis requires at this step a general metric of the discrepancy between free and perturbed wind parameter distribution.

5.2. The statistical metric of wake-induced perturbations

As previously mentioned, note that initial quantities are defined at hub height while output quantities are mean over the rotor surface. We will neglect this difference in what follows, to consider the uncertainty propagation $\boldsymbol{X}' = g(\boldsymbol{X})$ as a simple perturbation of $\boldsymbol{X}$. For conciseness, we will abusively denote $\bar{u}$ and σ_u both the input and output quantities. Similarly, TI will denote both the input $(\sigma_u/\bar{u})$ and wake modified $(\sigma_{u_{rotor}}/\bar{u}_{rotor})$ normalized turbulent intensities. Furthermore, the wind direction is not modified by the wake model so that we can consider it independently of the uncertainty propagation and reduce the input space of $\boldsymbol{X}$ to 2. The uncertainty propagation is then simplified in what follows:

$$g : \mathbb{R}^2 \to \mathbb{R}^{2\,n_{WT}}$$
$$\boldsymbol{x}(\bar{u}_x, \sigma_{u_x}) \mapsto g(\boldsymbol{x}) = (\boldsymbol{x}_1', \dots, \boldsymbol{x}_{n_{WT}}')$$

5.2.1. Maximum Mean discrepancy: a distance between distributions

Considering a positive-definite kernel $k: \mathbb{R}^d \times \mathbb{R}^d \to \mathbb{R}, d \in \mathbb{N}$ generating a unique Hilbert space $\mathcal{H}_k$ of functions equipped with inner products $\langle \cdot, \cdot \rangle_{\mathcal{H}_k}$ and norms $\|\cdot\|_{\mathcal{H}_k}$ (also called reproducing kernel Hilbert space when the function $k(\boldsymbol{x}, \cdot)$ satisfies the reproducing property). Let us define the *kernel mean embedding* of the distribution P in the function space $\mathcal{H}_k$:

$$\mu_P(\boldsymbol{x}) := \int_{\mathbb{R}^d} k(\boldsymbol{x}, \boldsymbol{y}) dP(\boldsymbol{y}) \approx \frac{1}{n} \sum_{i=1}^{n} k\left(\boldsymbol{x}, \boldsymbol{x}^{(i)}\right), \boldsymbol{x}^{(i)} \in \boldsymbol{X_n}$$

The kernel mean embedding is approximated on samples $\boldsymbol{X_n} = (\boldsymbol{x}^{(1)}, \ldots, \boldsymbol{x}^{(n)})$ following the distribution P. Note that the kernel is defined as a product of 1D Matérn 5/2 kernels (see section 4.3.2 for definition):

$$k(\boldsymbol{x}, \boldsymbol{y}) = k_u\left(\bar{u}_x, \bar{u}_y\right) k_{\sigma_u}\left(\sigma_{u_x}, \sigma_{u_y}\right).$$

Figure 110 illustrates the kernel mean embedding of two distributions in the function space $\mathcal{H}_k$ defined previously. Note that the distribution P is continuous while the distribution Q is discrete.

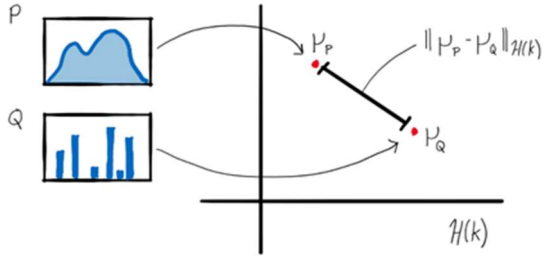

Figure 110 Kernel mean embedding of two probability distributions P and Q mapped in the RKHS $\mathcal{H}_k$ after [108].

The distance between the two kernel mean embeddings μ_P and μ_Q is called the *Maximum Mean Discrepancy* (MMD) [106]. This distance between two distributions P and Q is initially defined by the worst-case error for any function within a unit ball of a Hilbert space $\mathcal{H}_k$, generated by the kernel k:

$$MMD_k(P, Q) := \sup_{\|g\|_{\mathcal{H}_k} \leq 1} \left| \int_{\mathbb{R}^d} g(\boldsymbol{x}) dP(\boldsymbol{x}) - \int_{\mathbb{R}^d} g(\boldsymbol{x}) dQ(\boldsymbol{x}) \right| = \left\| \mu_P(\boldsymbol{x}) - \mu_Q(\boldsymbol{x}) \right\|_{\mathcal{H}_k}$$

Using the reproducing property of the kernel, one can demonstrate that

$$MMD_k(P, Q) = \left\| \mu_P(\boldsymbol{x}) - \mu_Q(\boldsymbol{x}) \right\|_{\mathcal{H}_k},$$

meaning that the MMD fully relies on the difference of kernel mean embeddings. Moreover, according to [109], a kernel is called a "characteristic kernel" when the following equivalence is true, $MMD_k(P, Q) = 0 \iff P = Q$, making the MMD a metric on $\mathbb{R}^d$. For its good convergence behaviour, the squared MMD has been used for multiple other purposes than numerical integration: statistical testing [110], and sensitivity analysis [111]. When elevated to the square, it can be estimated using one n-sized representative sample of P denoted $\left\{\boldsymbol{x}^{(i)}\right\}_{i \in (1, \cdots, n)}$ (and respectively one m-sized sample of Q denoted $\left\{\boldsymbol{y}^{(i)}\right\}_{i \in (1, \cdots, m)}$):

$$\widehat{MMD_k}(P,Q)^2 = \frac{1}{n^2}\sum_{i,j=1}^{n} k(\boldsymbol{x}^{(i)},\boldsymbol{x}^{(j)}) - \frac{2}{nm}\sum_{i=1}^{n}\sum_{j=1}^{m} k(\boldsymbol{x}^{(i)},\boldsymbol{y}^{(j)}) + \frac{1}{m^2}\sum_{i,j=1}^{m} k(\boldsymbol{y}^{(i)},\boldsymbol{y}^{(j)})$$

In the following, the idea is to compare the free environmental distribution p_0 to the wake-perturbed environmental conditions $p_l{}'$at the wind turbine l using the previously defined squared MMD.

It should be noticed that MMD belongs to the more general family of Integral Probability Distance [107]. The interested reader may find in [106] many other choices of metrics by changing the class of real-valued bounded measurable functions (unit ball of a Hilbert space $\mathcal{H}_k$ in MMD), including the Kolmogorov distance or the Wasseirstein distance (also known as Earth Moving Distance).

5.2.2. Application to the South Brittany wind farm project

The South Brittany theoretical study case of HIPERWIND is a farm composed of 25 FOWT off the French coast (see details in Section 3 for the layout and wind rose diagram). A dedicated FarmShadow™ model was developed, and a Monte Carlo DOE was simulated (size $n = 6000$). As already explained, the wind orientation variable θ is considered to be independent of the wake. Consequently, we can plot in the other 2 dimensions of $\boldsymbol{X}$, a preview of the wake perturbations on the joint distribution (mean wind speed and turbulence).

Figure 111 illustrates this perturbation at three WT differently affected by the wake depending on their position on the farm. One can notice that the WT 25 distribution (in orange) is very close to the free distribution (in black), as expected, this WT being located on the edge of the farm and facing the dominant wind direction. Meanwhile, the WT 13 distribution (in red) seems more affected by the wake, by getting higher wind turbulence with lower wind speed. This analysis can be completed with the two marginals in Figure 112 and Figure 113, both describing the free marginal distributions (on the left) and wake-disturbed distributions (on the right). In general, a small wind speed deficit is noticed as indicated by the small shifts of pdfs to the left in Figure 112. Also, a small added turbulence is indicated by the small shifts of pdf to the right in Figure 113.

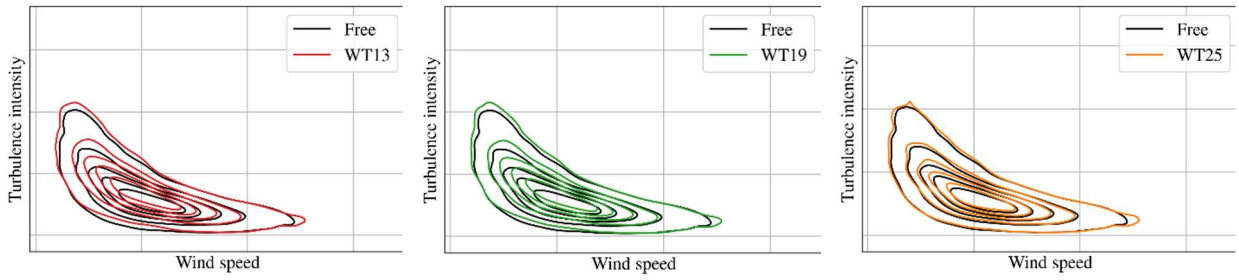

Figure 111: Modification of joint probability in $(\bar{u}, TI)$ at wind turbines 13, 19, and 25

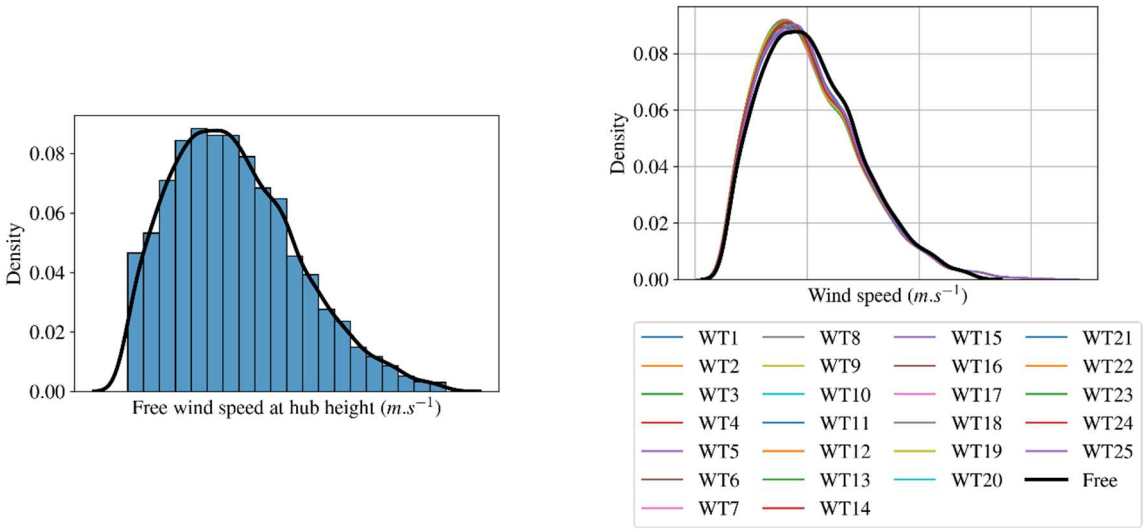

Figure 112 : $\bar{u}$ marginal distribution: on the left free, and on the right wake modified, distributions.

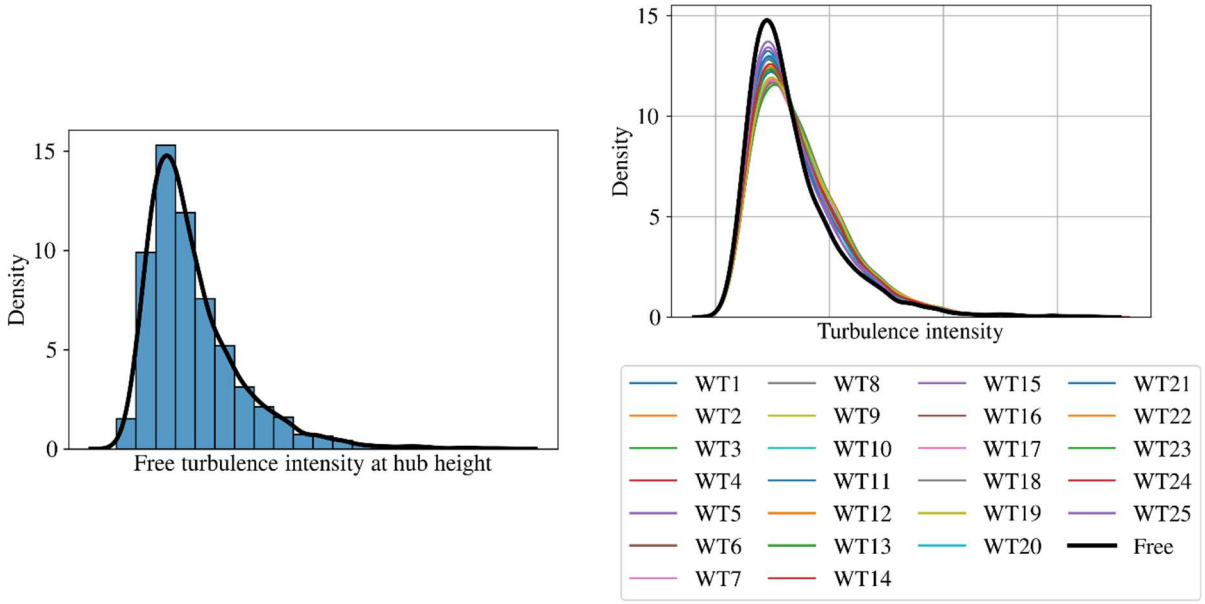

Figure 113: TI marginal: on the left free distribution, and on the right wake modified distribution

Once the joint perturbed distributions of each WT are approached by a large Monte Carlo sample, the MMD with the free conditions can be computed. Figure 114 illustrates the layout planned for the South Brittany project, for each wind turbine MMD is computed to measure the wake-induced perturbation. Note that the vertical direction on this plot does not represent the north direction. The lower this metric gets, the closer to the free environmental distribution. Quite logically, the turbines in the centre are more affected by the wake in general since they are subject to the wake regardless of the wind direction. On the right, the wind rose of this site gives a distribution of the wind speed per direction.

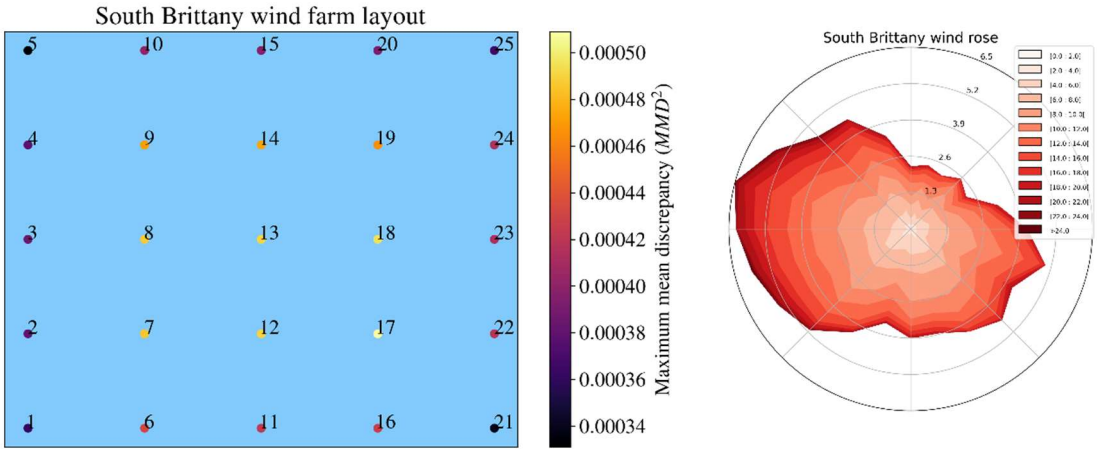

Figure 114: South Brittany layout and wake effect on environmental conditions (left). South Brittany wind rose (right).

The values of squared MMD given in the previous figure are estimated between two samples:

1- the Monte Carlo sample of the free environmental distribution: $\boldsymbol{X}_n$,
2- the wake-perturbed Monte Carlo sample at the WT l: $\boldsymbol{X'}_{n,l}$ (output of the FarmShadow™ numerical model).

To ensure that this estimation converged, Figure 115 plots the squared MMD between the sample $\boldsymbol{X}_n$ and the increasing samples $\boldsymbol{X'}_{i,l}, i \in \{400, \cdots, 6000\}$. After a few thousands of simulations, the MMD of each WT tends to converge towards a stable value, as expected. This exercise was useful to confirm that the DOE size was sufficient to estimate this quantity by Monte Carlo sampling.

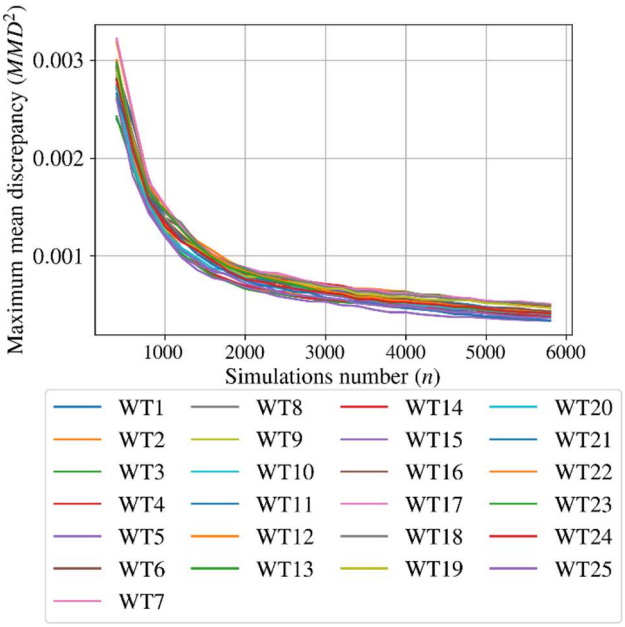

Figure 115: Convergence of the squared MMD estimation

5.2.3. Application to the Teesside wind farm project

This section illustrates the same results on the Teesside operating wind farm. Unlike the South Brittany site, Teesside is very close to shore which increases the localization of wind orientation in a narrow sector with dominant land coming wind (see the wind rose illustrated in Figure 119). In Figure 116, the perturbations seen by three WT are plotted. This time, the distribution for the WT 20 (in orange) is the closest to the free distribution (in black). The WT presenting the distribution with the strongest perturbation is WT 14 (in green). As in the previous conclusions, the perturbations induced by the wake tend to reduce the wind speed while increasing the wind turbulence. This analysis is also carried out for the marginals, as indicated by the shift of pdf to the left in Figure 117, and by the shift to the right in Figure 118, respectively.

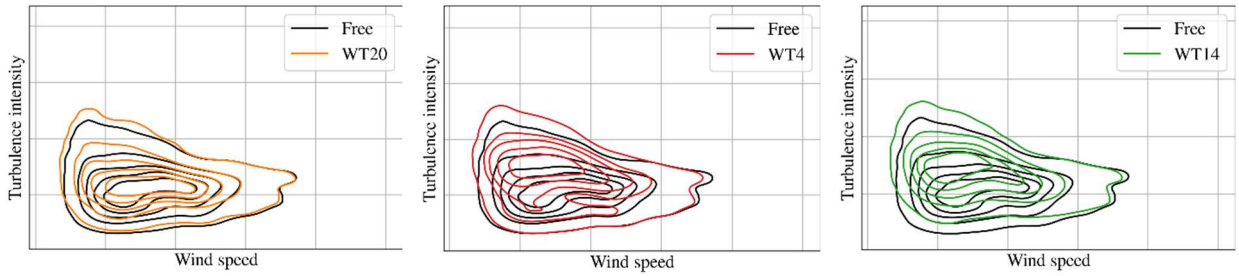

Figure 116: Joint perturbation at wind turbines 20, 4, and 14

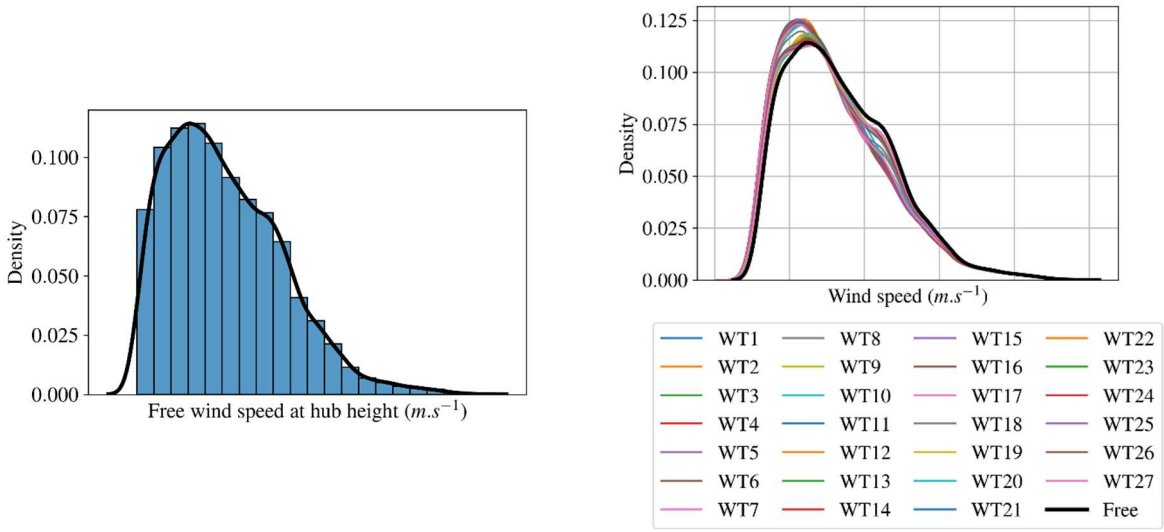

Figure 117: Free wind speed distribution (on the left) and Perturbed wind speed distributions (on the right)

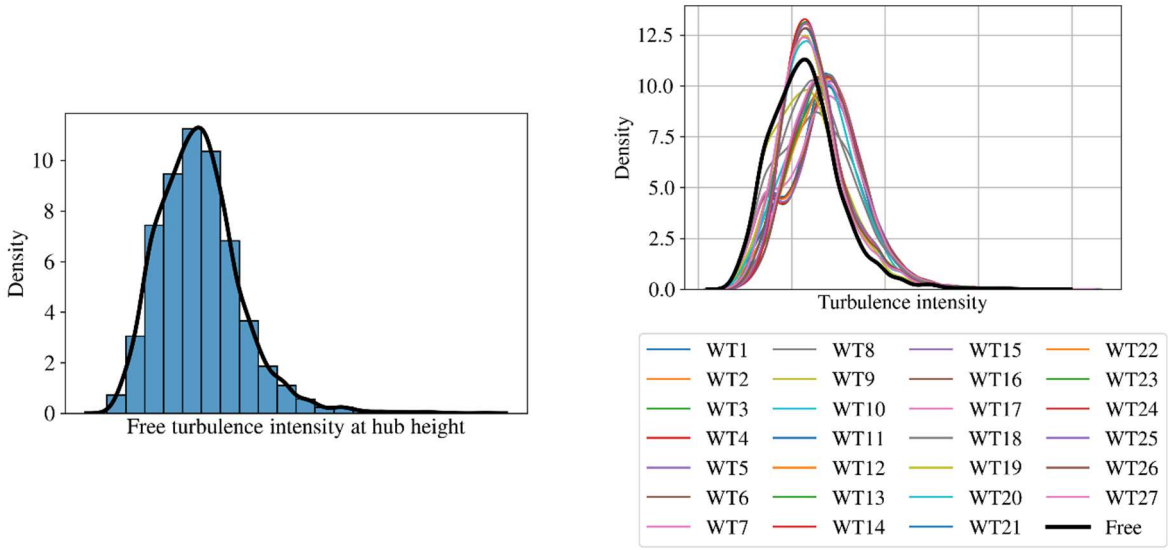

Figure 118: Free wind turbulence intensity distribution (on the left) and Perturbed wind turbulence intensity distributions (on the right)

Identically, Figure 119 shows the Teesside layout and the respective squared MMD with the free distribution. Since the wind mostly comes from the southwest direction, the south row of turbines is behaving quite differently from the north one.

Note that an important factor of the wake is the distance between wind turbines. The closest they operate, the more wake perturbations they create. At the Teesside wind farm, the turbines are spaced by 6 times the rotor diameter in one direction and 4 times the rotor diameter in the other. Meanwhile, for South Brittany, the turbines are spaced 5 times the rotor diameter in one direction and 7 times the rotor diameter in the other. Thus, the layout of the South Brittany wind farm is generally generating fewer wake effects than the Teesside wind farm.

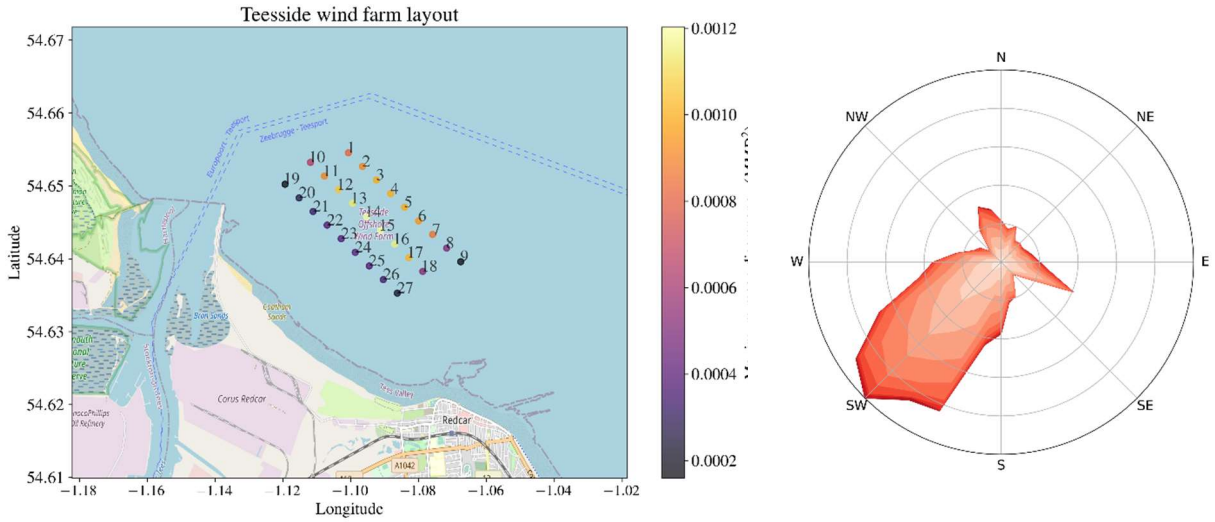

Figure 119 Teesside layout and wake effect on environmental conditions (left). Teesside wind rose (right).

Identically to the previous section, the convergence of the squared MMD estimation is plotted in Figure 120. With the Teesside FarmShadow^{TM} model being quicker to run, more simulations were computed. We consider that the convergence is reached, making the estimation of this DOE accurate.

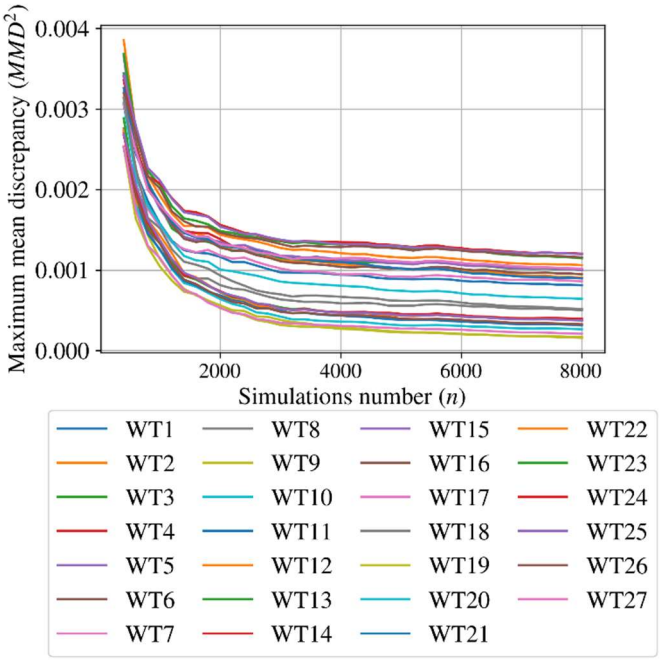

Figure 120 Convergence of the squared MMD estimation

5.3. Clustering output data to limit RBD analysis

A clustering between wake-modified environmental conditions is performed, to gather wind turbines that are exposed to similar wind conditions, leading to similar structural responses. This analysis is essential to ensure the practical feasibility of reliability analysis requiring a high number of simulations to sample the small target failure probability required by international standards (e.g. the target nominal annual failure probability in structural design is set to5e-4 in annexe K of IEC61400-1:2019).

Note that we are looking for a final clustering solution that does not depend on wind direction. This simplification, motivated by practical feasibility, leads to potentially higher errors compared to a clustering made for several wind sectors. Nevertheless, these errors are shown to be reasonable for the two study cases considered here.

Several methods classically used for clustering are explored, as well as a method allowing us to assess the optimal number of clusters. Finally, a few numbers of clusters (i.e., representative turbines) allows for representing the total number of turbines of the wind farm. Moreover, the choice of the representative turbine for each cluster is discussed in section 5.3.4.

5.3.1. Global methodology

At the end of the previous section, we obtained for each turbine a wake-modified joint environmental condition, in other words, a perturbed multivariate joint distribution including the wind speed and the turbulence intensity. Those quantities of interest are averaged over the rotor surface.

The MMD is chosen as the metric for the following clustering analysis. The choice of this metric is justified by the fact that we are looking for a clustering solution valid for all wind directions. Indeed, this metric is a distance between two distributions and concatenates information for all wind sectors.

This metric is used to build the matrix of distances of our system. The component d_{ij} of this matrix is the distance between the perturbed multivariate joint distribution of turbines i and j. The size of this square matrix hence corresponds to the number of turbines in the farm.

Once the selection of the representative turbine is fixed (cf. section 5.3.4), the relative error for a turbine in a particular cluster is defined as:

$$\varepsilon_i = \frac{|x_i - x_r|}{x_r} \qquad \text{Eq. 5-1.}$$

where:

- x refers to the quantity of interest (either $\bar{u}_{rotor}$ or $\sigma_{u_{rotor}}$)
- the subscript i refers to any turbine i belonging to this cluster
- the subscript r refers to the representative turbine of this cluster

For each cluster, the criterion allowing to evaluate its representativity is based on the average value of ε_i for all turbines belonging to a given cluster. Those errors are looked at for all environmental conditions. Note that those errors could have been looked at for a restricted domain of the free wind field corresponding to the most critical conditions when looking for instance at fatigue damages. In that case, given the damage in design is an expectation over environmental conditions, a restricted domain could have been built (for instance with the Adaptive Kriging approach, see e.g. section 5.3.4), with the $(\bar{u}, \sigma_u)$ pairs contributing the most. This restricted domain would have led to lower errors than the ones presented thereafter.

5.3.2. Existing methods for clustering

The matrix of distances introduced before is chosen as the input of our clustering analyses. This kind of data guides the type of clustering methods that can be used. We chose among the most classical methods compatible with this input.

Hierarchical clustering is a common class of methods. It consists in building clusters incrementally either by starting with as many clusters as the number of elements and then merging two clusters at each step (agglomerative), either starting with one cluster containing every turbine and splitting a cluster in two at each step (divisive). There is a multitude of criteria for defining which clusters to merge or split, leading to a multitude of hierarchical clustering methods.

Among hierarchical methods, we looked at three agglomerative clustering methods:

- Ward [112], whose criterion is to merge the two clusters for which the increase of internal inertia (defined as the sum of the square of the distance between two turbines of the merged cluster) is minimal,
- Complete-linkage, whose criterion is to merge two clusters for which the maximum distance between any pair of turbines of this pair of clusters is minimal,

- Single-linkage, whose criterion is to merge two clusters for which the minimum distance between any pair of turbines of this pair of clusters is minimal.

Single-linkage did not seem suitable, as it gave solutions with clusters containing a single turbine for low numbers of clusters, which didn't seem relevant. It was then excluded from our analyses. The other two methods are discussed.

Another type of widely used method is k-means [113]. It consists in finding the optimum solution which minimizes internal inertia between points of the cluster and its centroid. The solution is obtained for a given initial condition and is then a local optimum. It is then necessary to run the method for several initial conditions, to find the global optimum. It is to be noted that the number of clusters is an input of the method. Due to the nature of the input data (matrix of distance), k-means cannot compute the centroid of the cluster which is an element that does not initially exists. Application of k-means in our case requires an initial predictor of cluster centroids. A simple approach would be to select a random point but may converge relatively slowly. To fasten the clustering process, it may be possible to use an interpolating kernel to build a density map of the distance and then find local maxima with a gradient descent algorithm like that in [114]. To avoid this additional work, we chose in the following to use the k-medoids method [115][116] which is similar to k-means except that it uses the medoid of the cluster which is an element from the initial data set (i.e. a turbine). To find the global solutions for k-medoids, we run the method 5,000 times with random initial conditions and keep the solution with minimal inertia.

Finally, we chose the spectral method as the last method for comparison. This method uses eigenvalues and eigenvectors of the similarity matrix (which can be obtained from the distance matrix) to perform a reduction before making a cluster analysis by the mean of spectral embedding. Implementation of all methodologies is made using the Scikit-learn python package [117].

5.3.3. Choice of the representative WT of a cluster

The representative turbine of a cluster could be an existing turbine or a virtual turbine (whose distribution of environmental conditions can be computed afterwards using distributions of other turbines of the cluster).

We chose to use an existing turbine as a representative. For a cluster C that contains n turbines, the representative turbine T_r is taken as the medoid of the cluster, which is defined as follows:

$$T_r = \arg\left\{min_{T\in C}\sum_{i=1}^{n} d(T,T_i)\right\}$$

In other words, it is the turbine that minimizes the sum of distances of the turbine of this cluster to its representative.

The selection of the representative turbine of a cluster should follow reliability considerations. Indeed, we compute the reliability of the wind farm, which is system reliability, and for this, we have to define what is understood as wind farm failure, i.e. for instance how many WT failures are necessary to consider the global wind farm failure. Several possibilities exist. For example, it could be considered that all turbines have to fail (parallel system), which seems excessive. On the opposite, it could be considered that at least one WT has to fail (series system). It is the most conservative definition of wind farm failure. Intermediate cases are possible. This should be determined later in the HIPERWIND project.

If it is considered that at least one turbine has to fail, it corresponds to the probability of a union of failure events (case of a series system):

$$P_{f,WF} = P\left(\bigcup_{i=1}^{N_{WF}} \text{fail}(WT_i)\right)$$

where:

- N_{WF} is the number of wind turbines
- WT_i is wind turbine n°i.
- $\text{fail}(WT_i)$ is the failure set of events corresponding to WT_i.

Or, equivalently,

$$P_{f,WF} = P\left(\bigcup_{j=1}^{N_C}\left(\bigcup_{i=1}^{N_j} \text{fail}(WT_i)\right)\right)$$

where:

- N_C is the number of clusters
- N_j is the number of wind turbines in cluster n°j.

The following inequalities can be obtained (see for example [118]):

$$\max_{i=1\ldots N_{WF}} P_f(WT_i) \leq P_{f,WF} \leq \sum_{i=1}^{N_{WF}} P_f(WT_i)$$

where $P_f(WT_i)$ is the probability of $\text{fail}(WT_i)$. Similarly for each cluster with index *j*:

$$\max_{i=1\ldots N_j} P_f(WT_i) \leq \text{Pf,j} \leq \sum_{i=1}^{N_j} P_f(WT_i)$$

Note that the lower bound corresponds to the case where the failure events are fully dependent. More generally, the independence assumption for the failure events is conservative compared to the case where the events are positively correlated [118], and one gets for example in this case:

$$\max_{i=1\ldots N_j} P_f(WT_i) \leq \text{Pf,j} \leq 1 - \prod_{i=1}^{N_j}(1 - P_f(WT_i)) \leq \sum_{i=1}^{N_j} P_f(WT_i) = N_j.\overline{P_f(WT_\iota)_{\iota=1\ldots N_j}}$$

The term $1 - \prod_{i=1}^{N_j}(1 - P_f(WT_i))$ corresponds to the failure probability under the independence assumption.

For low failure probabilities, the last two terms (on the right) are almost identical, and the exact expression of the failure probability under the independence assumption should not reduce the conservatism significantly. If the wind farm pre-design is acceptable enough, failure probabilities should be low, and the WT failures should be positively correlated (all WTs experience the same wind global environmental conditions) but not fully correlated (e.g. material properties are independent).

Therefore, considering a representative leading to the mean failure probability and multiplying it by the number of represented WTs is a conservative analysis in the case of a series system (union of WT failures), which is itself the most conservative definition of wind farm failure, and maybe highly conservative due to the positive correlation of WT failures. In future reliability assessments, it could be interesting to investigate the difference between the lower and upper bounds of the WF failure probability.

5.3.4. Comparison between clustering solutions

First, clustering for the Teesside wind farm is done and then the clustering for the South Brittany wind farm is briefly described.

The solutions obtained for each method, for a number of clusters N varying from 2 to 6, are presented in the following tables. For the enumeration of the turbines and their location on the farm, see Figure 119.

Table 16: Solutions obtained with Ward for N=2 to 6 (Teesside).

N	1-7	8, 10, 18	9	11-17	19, 27	20-26
2						
3						
4						
5						
6						

Table 17: Solutions obtained with k-medoids for N=2 to 6 (Teesside).

N	1-7	8	9	10	11-12	13-17	18	19-27
2								
3								
4								
5								
6								

Table 18: Solutions obtained with the Spectral method for N=2 to 6 (Teesside).

N	1	2-7	8	9	10	11	12, 13	14	15-16	17	18	19, 20	21-26	27
2														
3														
4														
5														
6														

Table 19: Solutions obtained with the Complete-linkage method for N=2 to 6 (Teesside).

N	1-7	8-18	9	10	11-17	19-27
2	●	●	●	●	●	●
3	●	●	●	●	●	●
4	●	●	●	●	●	●
5	●	●	●	●	●	●
6	●	●	●	●	●	●

The first observation made when looking at the solutions obtained is that some groups of turbines emerge. The following groups are turbines that are almost always in the same cluster:

- {1, 2, 3, 4, 5, 6, 7},
- {8, 18},
- {12, 13, 14, 15, 16, 17},
- {19, 27},
- {21, 22, 23, 24, 25, 26}.

We also observe that methods sometimes lead to the same solution. It is the case for:

- N=2 with Ward and Complete-linkage on one side and k-medoids and Spectral on the other side,
- N=3 with k-medoids and Spectral,
- N=4 with Ward and k-medoids,
- N=5 with Ward, k-medoids and Complete-linkage.

We observe that for the Spectral method and N=6, turbine 14 is not with turbines 12, 13, 15 and 16, which looks suspicious.

To have information about what could be gained by increasing the number of clusters, we decide to look at average errors made in each cluster for different solutions. We derive it for the Ward method since the building of solutions is incremental and cluster structures remain from step to step. For a given clustering solution with N clusters, the average error of cluster C containing n turbines is defined as:

$$mean_{s\in\Omega,i\in C}(\varepsilon_{i,s})$$

With $\varepsilon_{i,s}$ the error defined in Equation 5-1 and Ω the set of all Farm Shadow simulations run for this study. It must be noted that this error is defined from absolute errors for a specific free wind speed condition. Hence, it does not take into account possible symmetries in wind distribution which could balance errors of specific simulations and then lead to lower global errors.

Table 20 shows the solutions obtained with the Ward method and a varying number of clusters. Table 21 and Table 22 respectively show the errors in $\bar{u}$ and $TI = \frac{\sigma_u}{\bar{u}}$ obtained for each solution.

Table 20 Cluster solutions obtained using the Ward method for the Teesside wind farm

N	Clusters and representative turbine							
2	{1-5-8, 10-18}					{9, 19-21-27}		
3	{1-5-8, 10, 18}			{11-14-17}				
4	{1-5-7}	{8, 10, 18}						
5				{9}	{19-26, 27}			
6					{19, 27}	{20-23-26}		
7		{8, 18}	{10}					
8				{11, 12}	{13, 14-17}			

Table 21 Mean errors in perturbed wind speed for Teesside wind farm

N	Errors in U							
2	3.56%					1.98%		
3	2.50%			1.56%				
4	1.18%	3.81%						
5				0%	1.82%			
6					2.44%	1.11%		
7		2.13%	0%					
8				0.78%	1.32%			

Table 22 Mean errors in perturbed turbulence intensity for Teesside wind farm

N	Errors in TI							
2	5.91%					3.04%		
3	3.39%			2.28%				
4	1.18%	7.55%						
5				0%	2.81%			
6					4.79%	1.37%		
7		4.68%	0%					
8				1.61%	1.76%			

Note that for the step from 3 to 4 clusters, the mean error of the group of turbines {1-8, 10, 18} decreases from 2.50% to 1.97% in U and from 3.39% to 3.09% in TI. Since the representative remains the same (i.e. turbine 5) for group {1-7}, the gain is obtained for the group {8, 10, 18} which have a better representativity. This last group contains turbines located at different extremities of the layout and would benefit from wind distribution symmetries discussed above. Thus, these turbines are expected to face lower errors than the ones presented here. We have a similar case for step 5 to 6 clusters for turbines {19, 27}.

The previous results were derived for the Ward method but if we want to compare these solutions to those obtained with other methods, we must define a simple indicator which does not rely on a specific cluster. We take the previously defined error but instead of averaging it over one cluster, we average the error over all the turbines of the farm for a specific clustering solution. Table 23 summarizes the mean absolute errors in U and TI made for solutions obtained with the 4 methods and N varying from 2 to 8.

Table 23 Mean absolute errors (in %) in wind speed and turbulence intensity over the full domain for every clustering solution for Teesside

N	Ward		Complete-linkage		k-medoids		Spectral	
	U	TI	U	TI	U	TI	U	TI
2	2.97	4.85	2.97	4.85	2.92	4.71	2.92	4.71
3	2.06	2.97	2.78	4.74	1.94	2.78	1.94	2.78
4	1.87	2.86	2.65	4.55	1.87	2.86	1.83	2.73
5	1.74	2.67	1.74	2.67	1.74	2.67	1.64	2.76
6	1.6	2.45	1.47	2.18	1.46	2.17	1.71	2.55
7	1.34	1.95	1.32	1.83	1.24	1.85	1.68	2.53
8	1.24	1.81	1.25	1.75	1.08	1.5	1.8	3.24

It must be kept in mind that the errors defined here are not a perfect indicator of the real differences faced by turbines as discussed above. Ward and k-medoids have the same evolution and give good results, the k-medoids method seems to give slightly better results. Complete-linkage method gives poor results for a low number of clusters (N=2 to 4). It is because, for these solutions, turbines of the 2nd and 3rd row are grouped but face different wakes. The Spectral method seems to perform well, for a low number of clusters but poorly as the number of clusters grows (for N greater than 6). This observation can be linked to a previous we made about turbine 14 not being with 12, 13, 15 and 16 for the solution N=6.

For N=3, the difference between Spectral and k-medoids on one side and Ward and Complete on the other side is made on whether turbine 18 is regrouped with {1-8, 11-17} or {9, 19-27}.

For N=4, the difference between Spectral on one side and Ward and k-medoids on the other side is that the first one regroups turbine 9 with {8, 10, 18} instead of the first row {19-27}.

For N=5, the differences between Spectral on one side and the other 3 methods on the other side are made for 2 groups of turbines. Spectral regroups {8, 9, 27} and {10, 17, 18} while the others regroup {8, 10, 18} and {9}.

Computing solutions taking a slightly different metric, which is not presented here, we also observed solutions with regrouping of turbines {9, 19, 27}. Globally, these differences remain marginal. What is mainly observed is the similarities between obtained solutions and the robustness of the methods. Either solution of Ward, k-medoids and Spectral (for low N) is expected to give suitable results.

The main question remains the choice of the number of clusters. To have an insight on what would be a good number of clusters, basic reasoning upon free wind distribution, farm layout and wake phenomenon would be sufficient for the case of Teesside. The wind rose and farm layout are shown in Figure 123. First, the wind distribution is composed of a major wind sector coming from SW and 2 minor approximately symmetric wind sectors from NW and SE (perpendicular to the major sector). The layout is constituted of 3 rows of turbines aligned in a perpendicular direction from the dominant wind direction, turbines are spaced from 4 diameters in the row alignment and 6 in the perpendicular direction. Wake would have a great influence on up to 2 turbines downwind. There are essentially 2 modes of wake, one in the major wind sector and the other in the perpendicular direction.

The solution is then expected to be driven from the SW sector and at least 3 clusters are needed to extract the levels of wake in this major direction. The 2 other quasi-symmetric sectors would induce some wake in the alignment of the rows. Turbines in the extremities of the row are then expected to face lower wakes than the ones in the middle. To take this lower mode into account, increasing the number of clusters to 4 or

5 would be necessary. Increasing the number of clusters would probably slightly reduce the errors by catching lower modes of wake but in terms of clustering and complexity reduction, it is not expected to improve the solution. Some more justifications for this basic reasoning could be found in the next section 5.3.5 where errors against wind directions are analysed.

We propose to keep the following solution candidates:

- N=3 of k-medoids and Spectral
- N=4 of Ward and k-medoids
- N=5 of Ward, Complete and k-medoids (a group {9, 19, 27} could be used)

These solutions are represented in Figure 121 below.

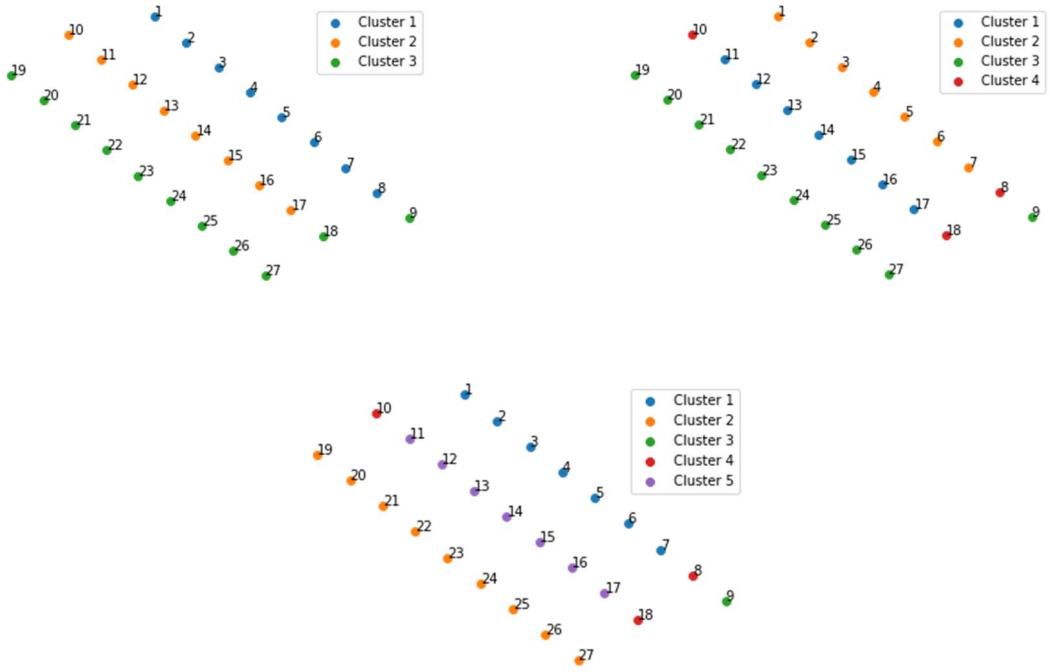

Figure 121: Clustering solutions proposed for the Teesside wind farm.

For South Brittany, the observations about strong similarities in solutions of different methods are less true. This is due to the less strong wake modes that could be observed for Teesside. Referring to Figure 114 for the layout and wind distribution of South Brittany, we see that the wind sectors are sparse and that turbines are more spaced in terms of rotor diameter than Teesside. Among these methods, we can easily identify core groups but there are turbines which do not belong to one group. This results in differences in clustering solutions between the various methods which are now explored.

The comparison of the different clustering solutions in terms of mean errors is shown in Table 24. We can notice that the errors are lower than those of Teesside, which is due to the higher spacing of turbines in South Brittany.

Table 24: Mean absolute errors (in %) in wind speed and turbulence intensity over the full domain for every clustering solution for the South Brittany wind farm

N	Ward		Complete		k-medoids		Spectral	
	U	TI	U	TI	U	TI	U	TI
2	1.53	1.01	1.53	1.01	1.43	0.96	1.50	1.08
3	1.31	0.88	1.31	0.88	1.15	0.78	1.21	0.89
4	0.95	0.62	0.95	0.62	0.89	0.56	0.92	0.60
5	0.84	0.53	0.84	0.54	0.70	0.43	0.84	0.54
6	0.73	0.46	0.76	0.50	0.6	0.32	0.88	0.62
7	0.83	0.37	0.64	0.41	0.52	0.27	0.71	0.47
8	0.57	0.35	0.57	0.35	0.46	0.23	0.80	0.56

Here, the k-medoids method seems to give better results. For the choice of the number of clusters, after analysing the core groups emerging from solutions, we propose the following solution candidates:

- N=4 of k-means,
- N=6 of k-means.

These solutions are represented in Figure 122.

Figure 122: Clustering solutions proposed for the South Brittany wind farm.

5.3.5. Clustering approximation versus wind sector analysis

As the clustering solution does not depend on wind sectors, some questions remain on the errors (i.e. clustering approximation) that could be made for some wind directions. We decide to analyse extreme errors that could occur in each cluster for the Teesside wind farm.

We decide to study the k-medoids 5-cluster solution illustrated in Figure 123. To give insights on wake interactions between turbines, the wind rose of Teesside is presented to its side.

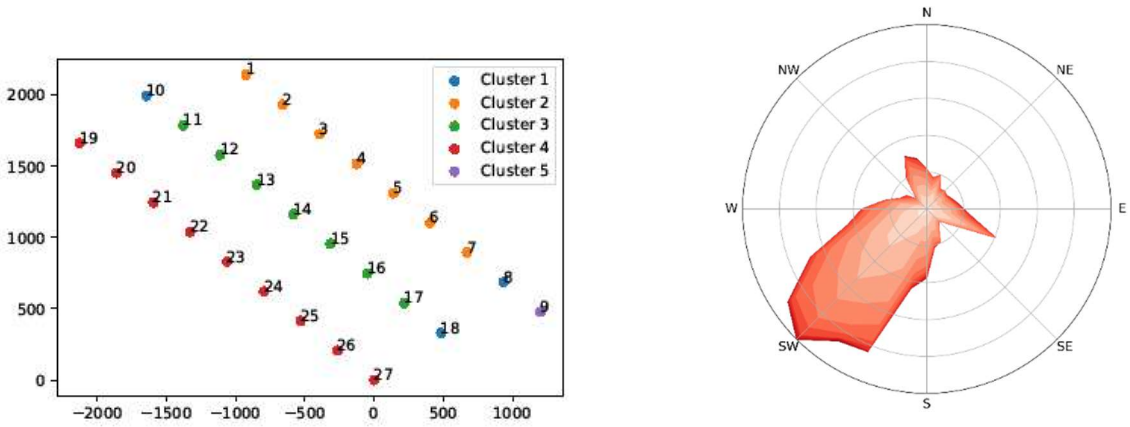

Figure 123 Ward 5 clusters solution and wind rose at Teesside wind farm

Figure 124 below gathers graphs of errors for all clusters. What these graphs represent is the counting of FarmShadow™ wake simulations for which the maximal error in the cluster is in a specific range of error and it is plotted against wind sectors. Since we are looking at extremal values, we defined a threshold error of 10% below which simulations are ignored. Cluster {9} is not represented as it contains only 1 turbine.

Cluster {1-5-7}

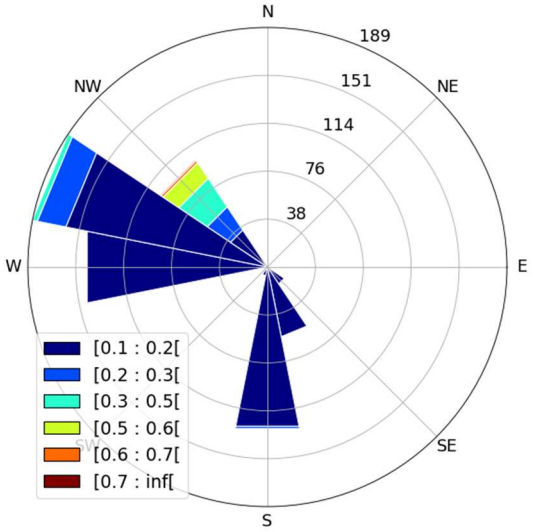

Cluster {11-14-17}

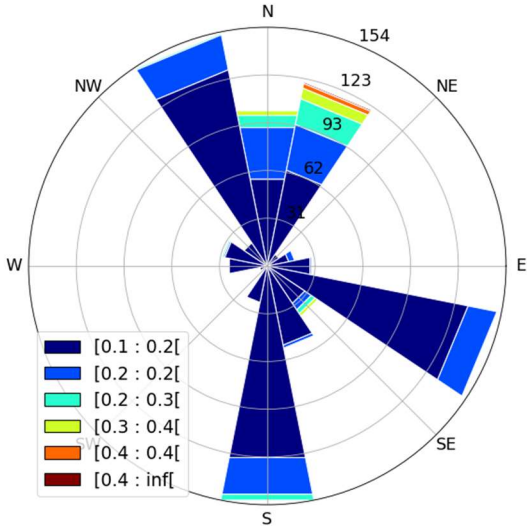

Cluster {19-26-27}

Cluster {8, 10, 18}

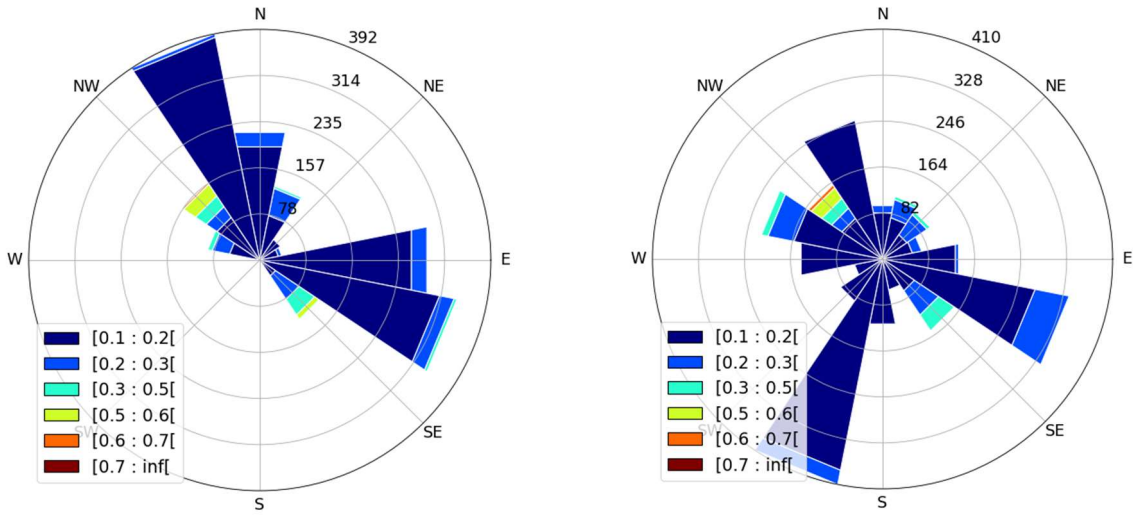

Figure 124 Roses of maximal errors for each cluster for solution k-medoids 5-clusters. The representative turbine of each cluster is specified in red. Each bar represents the number of simulations for which the maximal relative wind speed error in the cluster is in a given range and it is plotted against the corresponding upward wind direction, as in wind rose. The simulations, initially representative of Teesside wind conditions and at the number of 8000, are filtered to consider only simulations where maximal errors > 10%.

For cluster {1-5-7}, larger errors come from the North-West direction where turbine 1 is upwind and faces no wake while other turbines of the cluster are shadowed by turbines of this same cluster. Two other wind sectors are the source of errors: first in the West direction where turbine 1 faces lower wakes than the turbines of its group; second in the South direction where it is turbine 7 that faces lower wakes. An example of this last case is illustrated in Figure 125.

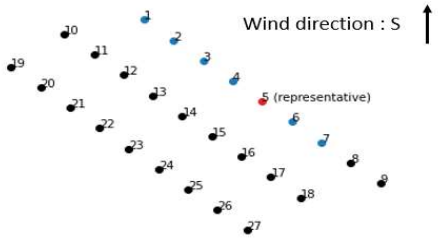

WT	Error in U (%)
1	-2.11
2	-1.19
3	-1.06
4	1.15
5	0
6	6.84
7	10.17

Figure 125: Relative errors in wind speed in cluster {1-7} for a single simulation with the wind coming from the south. Free wind conditions: U_{free}=5.58m/s, TI_{free}=0.11. Representative wind conditions: U_r=5.05m/s, TI_r=0.148.

For cluster {11-14-17}, larger errors come from the N-NE direction where turbine 11 faces no wake. Errors also occur in SE-E and S directions where turbine 17 faces lower wakes.

For cluster {19-26-27}, larger errors come from NW and SE directions where the wind is aligned with the row formed by the turbines. In this case, one turbine of the cluster faces no wake while others do. This case is illustrated in Figure 126.

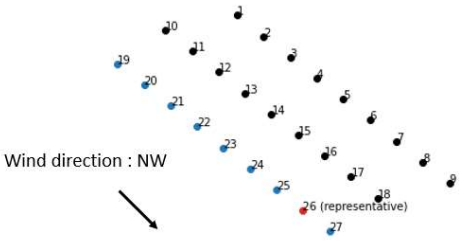

WT	Error in U (%)
19	26.01
20	2.07
21	4.14
22	1.83
23	3.35
24	0.05
25	-0.25
26	0
27	2.73

Figure 126: Relative errors in wind speed in cluster {19-27} for a single simulation with the wind coming from the north-west. Free wind conditions: U_{free}=6.04m/s, TI_{free}=0.17. Representative wind conditions: U_r=4.78m/s, TI_r=0.207.

The case of cluster {8, 10, 18} is a bit different since turbine 10 is spatially distant from 8 and 18 and turbine 8 is not in the same row as the two others. Still, the errors observed can be explained with the same reasoning made earlier. Here we are looking at errors, simulation per simulation, but the symmetries in wind distribution and layout would lead to similar distributions for turbines 10 and 18, as can also be expected at some point in cluster {19-27}. Generally, it is the same scheme that generates these larger errors: in one or several specific wind directions, one or two turbines are upwind and see less wake than the rest of its cluster. It is a phenomenon that cannot be avoided when making a clustering that does not depend on wind direction.

Let us remind you that to simplify the subsequent reliability design, we chose a clustering that is not depending on the wind orientation. Consequently, some WT may present significant errors for specific wind orientation which may lead to a large conservatism when the design is driven by a limit state which is strongly dependent on this wind orientation. However, in our study case, the occurrence of such local errors is quite low.

5.4. Summary of section 5

The propagation of uncertainties is made for the two study cases; the bottom-fixed and the floating wind farms on two parameters for each WT which are the mean over rotor surface of the 10 min averaged wind speed $\bar{u}_{rotor}$ and of the wind speed standard deviation $\sigma_{u_{rotor}}$. A metric has then been defined to measure the distance between the pdf of these two parameters between different WT. Those results are then used to obtain using a clustering approach a limited number of WTs representing the farm for reliability designs.

For the Teesside wind farm, three solutions involving three, four and five clusters are given. For the South Brittany wind farm, two solutions involving four and six clusters are given. Note that the clustering solution obtained for South Brittany leads to lower errors (i.e., a measure of the distance between the uncertainty of $(\bar{u}_{rotor}, \sigma_{u_{rotor}})$ pairs of each WT in a cluster) than the solution obtained for Teesside. If we want to have the same errors for both wind farms, a solution would be to consider fewer clusters for South Brittany or more clusters for Teesside.

References of Section 5

[104] Kelly, M., Vanem, E. (2022). "Environmental joint probability distributions and uncertainties" D2.3 Tech Rep. of HIPERWIND H2020 project, Grant Agreement No. 101006689, https://www.hiperwind.eu/.

[105] McWilliam, M., Bonfils, N., Dimitrov, N., Dou, S. (2022). "Wind farm parameterization and turbulent wind box generation". D3.1 Tech Rep. of HIPERWIND H2020 project, Grant Agreement No. 101006689, https://hal-ifp.archives-ouvertes.fr/hal-04033050.

[106] Sriperumbudur, B. K., Gretton, A., Fukumizu, K., Schölkopf, B., Lanckriet, G.R.G. (2010) "Hilbert space embeddings and metrics on probability measures". J. Mach. Learn. Res., 99:1517-1561.

[107] Müller, A. (1997). "Integral probability metrics and their generating classes of functions". *Advances in Applied Probability*, 29:429–443, 1997.

[108] Oates, C. (2021). "Minimum Discrepancy Methods in Uncertainty Quantification," Lecture at Ecole Thématique sur les Incertitudes en Calcul Scientifique (ETICS21).

[109] Sriperumbudur, B., Gretton, A., Fukumizu, K., Schölkopf, B., Lanckriet, G. (2010). "Hilbert space embeddings and metrics on probability measures," Journal of Machine Learning Research, v. 11, 1517-1561.

[110] Gretton, A., Borgwardt, K., Rasch, M., Schölkopf, B., Smola, A. (2006). "A kernel method for the two sample-problem," In Proceedings of the19th International Conference on Neural Information Processing Systems, 513-520.

[111] Da Veiga, S. «Global sensitivity analysis with dependence measures», Journal of Statistical Computation and Simulation, vol. 85, pp. 1283-1305, 2015

[112] J. Ward, "Hierarchical Grouping to Optimize an Objective Function," Journal of the American Statistical Association, vol. 58, pp. 256-244, 1963

[113] Bock, H. «Clustering Methods: A History of k-Means Algorithms», 2007.

[114] Kittler, J., (1976). A locally sensitive method for cluster analysis. Pattern Recognition 8, 23–33.

[115] Maranzana, F. (1963). "On the location of supply points to minimize transportation costs," IBM Systems Journal, v. 2, 2, 129-135.

[116] Park, H., Jun, C. (2009). "A simple and fast algorithm for K-medoids clustering," Expert systems with applications, v. 36, 2, 3336-3341.

[117] Pedregosa, F., Varoquaux, G., Gramfort, A., Michel, V., Thirion, B., Grisel, O., Blondel, M., Prettenhofer, P., Weiss, R., Dubourg, V., Vanderplas, J., Passos, A., Cournapeau, D., Brucher, M., Perrot, M., Duchesnay, E. (2011). "Scikit-learn: Machine Learning in Python," Journal of Machine Learning Research, v. 12, 2825-2830.

[118] Lemaire, M., (2009). "Structural Reliability", Ed. by Jacky Mazars. London ISTE Ltd, Wiley.

6. General conclusions and Perspectives

The importance of accounting for the wake of wind turbines is well known for the design of offshore wind farms, both for the AEP evaluation at early stages and for the design of wind turbine components. Several analytical wake models have been developed in the literature and validated against experimental and/or in-site data, or high-fidelity CFD simulations. They have been used for a long time for AEP evaluation and are increasingly used in recent years to optimize wind farm layouts and to provide input wind conditions for the design of WT in the farms. Based on this context, these analytical models are qualified in this report as engineering wake models. If their computational cost is low, such models are based on strong assumptions that might show limitations, especially for specific conditions. To quantify their uncertainty, more advanced methods have been considered in this study as references.

Firstly, a new model has been developed in section 3 with a coupling between a static wake model and a hydrostatic solver to consider the static motion of the floater induced by the thrust of the wind. A study based on the South Brittany theoretical wind farm (composed of IEA15MW UMaine generic WT) has been performed with a systematic computation over 3 dimensions: mean wind speed, turbulence intensity, and wind direction. The influence on the mean wind speed and turbulence seen by the rotor of the different WT remains small, the main driving effect being the inclination of the floater, depending on the vertical shear of the wind speed. The noticeable effects are observed for crosswind directions with about $D/6$ vertical uplift of the wake centre for a distance of ~$6D$ downwind. The floater static motion impact on the mean speed and turbulence seen by each WT remains lower than the uncertainty in the static wake model (see section 4). Also, the AEP estimation, conducted overall wind orientations, has been compared to a fixed case. The main effect, leading to 0.5% power reduction, seems to be due to the misalignment of the rotor because of the pitch of the floater, suggesting that the effect of vertical deflection of the wake is less significant.

A few perspectives can be noted from these first results. First, one should be careful with the conclusions of the small influence of floater motion, because of several limitations in the implementation which has been done for the hydrostatic coupling with the engineering wake model. Indeed, the consequence of the floater inclination on the wake is based on the yaw misalignment correction. There is no resolution of the flow behaviour associated with the interactions between the wakes and the sheared inflow of the wind or even the Dynamic Wake Meandering, the latter playing an important role in the fatigue of WT components [119]. A reliable investigation of these interactions would require experimental measurements. Then, only the static motion has been considered, based on previous results of the literature, and the controller has not been fully taken into account when computing the floater motion which should have underestimated the latter. Also, the power and thrust coefficient curves according to mean wind speed could be improved by taking into account the effect of wind direction due to the anisotropy of the mooring system. Last, one should keep in mind that the floater motion amplitude is strongly dependent on the floater and mooring design. A generalisation of the conclusion would thus require studying the effects of different technologies like TLP or SPAR (e.g. [120][119]).

In section 4, a comparison between semi-industrial workflow and high-fidelity simulations (based on LES) of wakes is proposed to estimate the uncertainty of this prediction during the design of wind farms and WT. This comparison is analysed for several representative configurations of ambient wind conditions. For

neutral cases (dominant wind direction and crosswind), a qualitatively good correlation has been observed regarding the mean wind speed, especially for Gaussian and super-Gaussian models, when compared to LES results at several locations downwind WTs. The same conclusion can be drawn for TI with however a slight overprediction of the engineering model. This overestimation seems to be reduced with a correction introduced in FamShadow™ after the writing of this report. In stable conditions, the engineering methodology was shown to underpredict the wake deficit and turbulence intensity, as the approach does not consider the interactions with the atmospheric boundary layer thermal stratification. It was impossible to conclude about the unstable case as the LES domain was too small. Last, when using one analytical wake model, the user may consider that depending on the model setting and combinations of models (i.e. wake deficit, added turbulence, and wake superposition), the prediction may also significantly vary. Concerning the influence of floater averaged motion for the FOWT case study, the LES shows again a small influence of the mean floater position (pitched away) on wakes: if a stronger and wider wake is observed downwind the first wind turbine in LES results, the vertical wake deflection is well predicted by analytical models.

To help future RBD, engineering models have also been compared over the whole space of wind parameters (mean speed, turbulence intensity, and direction) to the medium fidelity DWM, at a single wind turbine located at the centre of the wind farm for each of the two case studies. The results are provided with GP interpolations in the whole 3D space. For most of the scenarios, the difference between FarmShadow™ and DWM remains small, between -2% and 2%, for the normalized wind speed deficit f_u, which is in line with the small differences between FarmShadow™ and LES wind speed profiles in the qualitative study. However, for most of the scenarios, the difference between the DWM GP and the FarmShadow™ GP for the normalized standard deviation f_{σ_u} is larger, between –25% and 2% (see Table 14 for details). FarmShadow™ generally predicts larger turbulence when compared to DWM, in particular for Teesside, while the prediction of FarmShadow™ was relatively close to the LES one. Furthermore, for a few cases of ambient wind parameters with a wind direction near crosswind, the differences are larger and rise to 200% more prediction by FarmShadow™ of added turbulence for Teesside. One should keep in mind that crosswind events are specifically the ones for which the number of upwind turbines is the largest and the inter-turbine distance is the lowest.

From this study, few perspectives can be suggested. To complete the study on atmospheric stability, it would also be interesting to compare the engineering wake model to LES for an unstable configuration, by simulating a larger domain to generate all the scales of turbulence in the ABL. A perspective to this work could also be to enlarge the comparison to a monitored event or with some forcing conditions given by a mesoscale model with reanalysis like in [121]. The results obtained for stable conditions highlight the need of improvements in engineering methodology. The vertical wind profile should be enriched for non-neutral conditions, by using the log wind profile or, if available, direct LES or in-situ profiles. Furthermore, analytical wake models should also be enriched with interactions of the wind flow and the ABL, as introduced in [124].

The DWM cannot be considered as a fully validated reference, hence motivating further investigations to clarify the differences between the different fidelity models, with a focus on the models for the added turbulence with wake superposition, and for crosswind events. Last, one should keep in mind that the quantitative analysis of the engineering wake model approximation was evaluated at a single wind turbine only. The resulting difference to high-fidelity predictions is composed of a deterministic part plus another part measuring the uncertainty of this difference (see the columns of Table 14). We will assume, in the next step of the project, that this difference function can be applied to any other WT of the wind farm. To do so, a mapping to local wind parameters (e.g. mean wind speed over the rotor and mean turbulence over the rotor) should be used, instead of a mapping to the input ambient wind parameters. Additional post-

treatments of the different fidelity models on different WT within the farm could be used to check the validity of this assumption. Last, DWM results should also be compared against the LES profiles to link the quantitative and the qualitative study on the same selected ambient wind conditions.

To perform RBD computations, one should consider a model chain and related uncertainty on both input data and output prediction of the models. Most of the literature on RBD for offshore WT considers one WT in ambient wind conditions and does not include the wake effect. To do so, a first way would be to consider a model chain including both the wake analysis plus an ASHE solver, for instance with the surrogate model encoding layout that was developed in [122]. Section 5 of this report chose an alternative where the model chain is only the ASHE solver, including the turbulence box generator, which has the advantage of better control of the different sources of uncertainty, specifically due to each model approximation. Consequently, the uncertainty on long-term varying wind and wave parameters at a given site has to be propagated on wake-modified parameters defining the local wind seen by each WT in the farm. We chose to select the mean and standard deviation of wind speed, both integrated over each WT rotor surface as these outputs. A new method has then been proposed to quantify the wake modification through a dedicated metric, i.e. the MMD. To reduce the number of cases for costly RBD, a clustering method has also been detailed, which computes the minimum number of clusters (groups of WT) that are globally submitted to similar wind conditions. An application on Teesside (resp. South Brittany) wind farm shows that only 5 (resp. 4) clusters are sufficient to achieve this goal with less than 1% mean absolute error in MMD.

A first perspective to this work could be to add the influence of the wake model uncertainty that has been quantified in section 4 but which may require further investigations (cf. hereabove comments). One could also consider the uncertainty in the input joint probability distributions for the ambient wind and wave long-term parameters (see [123] for more details). Other output quantities can also be included with additional parameters on the local wind conditions (e.g. the centres of Gaussian wakes in [122]) or even uncertainty on the wind spectrum (e.g. Mann 3 parameters) which could be provided by comparison to LES simulations. Whatever these possible enrichments, the most important perspective is to follow the uncertainty propagation with RBD analysis both in ULS and FLS. This will be the topic of the next Work Package (WP4) of HIPERWIND, with the final objective to compare to standard IEC DLC design for possible cost reduction or even identification of unsafe design.

References of Conclusions and Perspectives

[119] Wise, A.S., Bachynski, E.E. (2020). “Wake meandering effects on floating wind turbines”. Wind Energy, 23:1266–1285.

[120] Johlas, H.M., Schmidt, D.P., Lackner, M.A., (2022). “Large eddy simulations of curled wakes from tilted wind turbines”. Renewable Energy 188, 349-360.

[121] Bakhoday-Paskyabi, M., Bui, H., Penchah, M., (2022). “Atmospheric-Wave Multi-Scale Flow Modelling”. D2.1 Tech Rep. of HIPERWIND H2020 project, Grant Agreement No. 101006689, https://www.hiperwind.eu/.

[122] McWilliam, M., Bonfils, N., Dimitrov, N., Dou, S. (2022). “Wind farm parameterization and turbulent wind box generation”. D3.1 Tech Rep. of HIPERWIND H2020 project, Grant Agreement No. 101006689, https://hal-ifp.archives-ouvertes.fr/hal-04033050.

[123] Kelly, M., Vanem, E. (2022). "Environmental joint probability distributions and uncertainties" D2.3 Tech Rep. of HIPERWIND H2020 project, Grant Agreement No. 101006689, https://www.hiperwind.eu/.

[124] Jezequel, E. (2022). “Simulations of wind turbine wakes in realistic atmospheric conditions: from large eddy simulations to analytical models”. Doctoral thesis of Institut National Polytechnique de Toulouse.

Acknowledgements:

The authors acknowledge the GENCI for providing super-computational resources (DARI A0112A12965) on the “Très Grand Centre de Calcul” of the Commissariat à l'Energie Atomique, used to run high fidelity simulations with Meso-NH.